CRANFIELD UNIVERSITY

Fan Xu

Damage Tolerance Characteristics of Carbon Fibre Composites: Behaviour under Impact Loads and Post-Impact Fatigue

SCHOOL OF AEROSPACE, TRANSPORT AND MANUFACTURING

Ph.D. in Aerospace Engineering

PhD

Academic Year: 2013 - 2017

Supervisor: Dr. Wenli Liu

Associate Supervisor: Prof. Phil Irving

Jan 2018

CRANFIELD UNIVERSITY

SCHOOL OF AEROSPACE, TRANSPORT AND MANUFACTURING
Ph.D. in Aerospace Engineering

PhD

Academic Year 2013 - 2017

Fan Xu

Damage Tolerance Characteristics of Carbon Fibre Composites: Behaviour under Impact Loads and Post-Impact Fatigue

Supervisor: Dr. Wenli Liu
Associate Supervisor: Prof. Phil Irving
Jan 2018

This thesis is submitted in partial fulfilment of the requirements for the degree of PhD

ABSTRACT

One of the critical issue restraining the fully application of carbon fibre reinforced polymer (CFRP) composites to aircraft structures is barely visible impact damage (BVID) caused by low-velocity impact (LVI). Consequent internal damage, such as delamination, which is difficult to find by regular inspection, raising a great concern for the damage tolerance performance of CFRP.

The main objective of this research study was to investigate the damage tolerance behaviour of carbon fibre composites under impact loads and post-impact fatigue. The project aims to explore and identify delamination growth and failure processes in impact-damaged carbon fibre epoxy composites under compressive cyclic loading and to explain the behaviour in the fracture mechanics method.

Low velocity drop weight impacts were used to create the initial damage. There were four levels from 12J-25J. Maximum compressive loads during fatigue were between 70% and 80% of the nominal residual strength in compression after impact (CAI) tests. Delamination propagation was monitored at intervals during the test using DIC and C-scan techniques. It was found that compressive fatigue failure can be categorised into three phases: (1) local bending at impact damage site (2) local buckling mode change and (3) buckling propagation. Monitoring of local normal displacement at the impact damage site provided earlier indications of fatigue induced changes in delamination buckling than observations of delamination area growth. A three-dimension analytical model was developed and revealed that deep delamination has higher strain energy release rates at crack tip than delaminate at the surface of laminate.

Keywords: Composites, Post-impact fatigue, Damage tolerance

ACKNOWLEDGEMENTS

I would like to express my deepest gratitude towards my two remarkable supervisors, Dr. Wenli Liu and Prof. Phil Irving. It is truly with your patient and thoughtful supervision I could overcome the difficulties in the study. I would also like to thank you for your mentoring not only in the research but also in how to become a better person.

I want to thank my beloved wife, Yuqing without whose determined support I could never end with this. Your company is the best thing I could ever imagine.

My sincere thanks also go to Mr. Barry Walker, Mr. Jim Hurley, Mr. Ben Hooper and Mr. Jarryd Braithwaite. Deeply gratitude towards all of you to give me help and assistance during this project.

I am grateful to my ex-supervisor, Prof. Xiang Zhang. Thanks for your first-year supervision and the warming encouragement even when you have left Cranfield.

I would like to thank my parents who are supporting me mentally and financially. Thank you for letting me have this opportunity to develop and dedicate recent years in researching.

Last but not least, I would like to thank the friends I met in Cranfield, Hanlin Niu, Hao Li, Jean-Michael Ipock, Shuoyuan Xu, Ye Xie, Shirley Leng, Si Chen and Xin Chen. It is my luck to know you and thanks for the good time we had together and the inspiration you gave me.

TABLE OF CONTENTS

LIST OF FIGURES

LIST OF TABLES

LIST OF ABBREVIATIONS

ASTM	American Society for Testing and Materials
BVID	Barely Visible Impact Damage
CAI	Compression After Impact
CFRP	Carbon Fibre Reinforced Polymer
CP	Cross-Ply
DCB	Double Cantilever Beam
DIC	Digital Image Correlation
FEM	Finite Element Method
LEFM	Linear Elastic Fracture Mechanics
LVI	Low Velocity Impact
MMB	Mixed Mode Bending
NDI	Non Destructive Inspection
NDT	Non Destructive Test
PTFE	Polytetrafluoroethylene
QI	Quasi-isotropic
RCS	Residual Compressive Strength
SERR	Strain Energy Release Rate
SIF	Stress Intensity Factor
UT	Ultrasonic Test
VCCT	Virtual Crack Closure Technique

1 INTRODUCTION

1.1 Background

The aerospace industry has evolved to achieve the critical balance between safety and efficiency. Researchers and engineers are looking at cutting-edge technologies to reduce the cost of operations and to increase the efficiency and reliability of commercial aircrafts.

The adaptation of composites for aircrafts seems to have improved over the last half century. Figure 1-1 shows the trend of composite application from barely used on DC-9 in the early 1960s to application in over half of the components in B787s and A350s recently. Among the various kinds of composites, carbon fibre reinforced polymer (CFRP) is, currently, the most widely utilised one owing to its high specific stiffness and strength compared to its metallic counterparts.

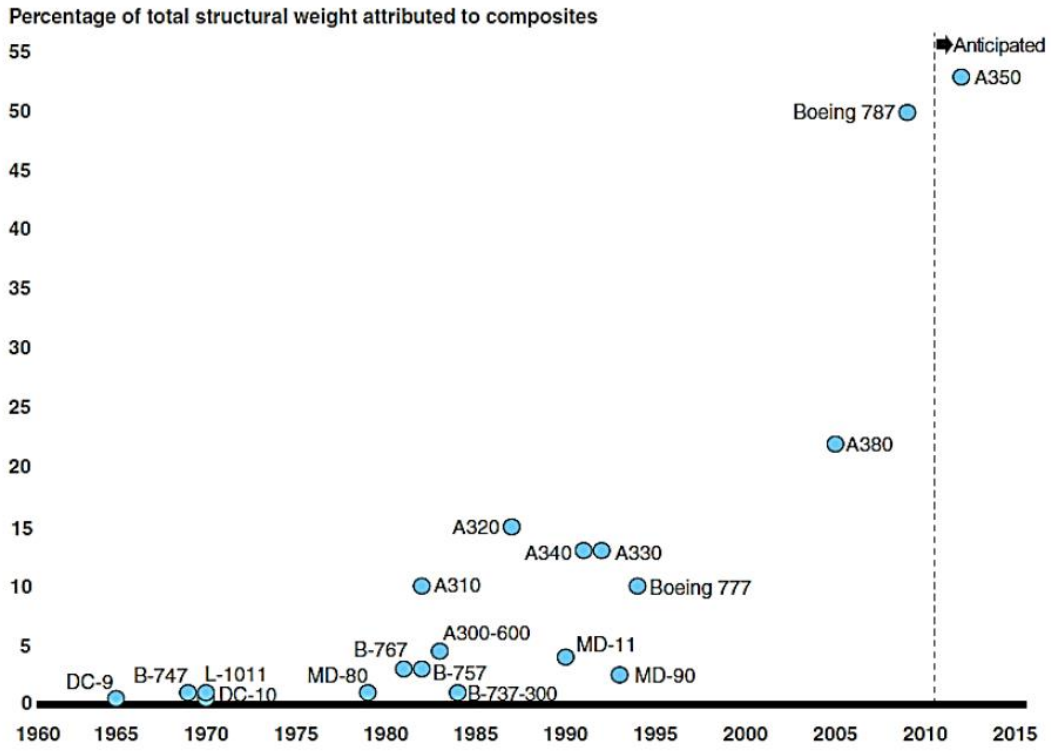

Figure 1-1 Percentage by weight of composites used by commercial aircrafts from the 1960s to 2010s (Source: US GAO., 2011)

Although CFRP has many advantages over the metallic alternative, one drawback that can never be neglected is that, concerning impact-induced

damage, carbon fibre composites have lower residual strength than their pristine status, which is an essential factor in the damage tolerance design of aircrafts nowadays.

Damage of composites can be attributed to many sources. Among the different types of damage, impact damage is one of the most prominent and crucial problems. Dropping tools, hail, runway debris, and general maintenance are all sources of impact damage that an aircraft would suffer during its long service life. High-velocity impact (HVI) that leads to penetration of the components can be easily found and repaired. Barely visible impact damage (BVID), however, caused by low-velocity impact (LVI) is a major problem for composites since the damage is usually initiated by internal damage, such as delamination, which is difficult to find by regular inspection. These flaws significantly reduce the static strength of composites.

Although it is accepted that fatigue performance of an undamaged carbon fibre laminate is superior to that of metals, the introduction of delamination via impact can lead to the onset of fatigue damage at stress levels as low as 20% of the laminate's ultimate strength (Sala, 1997; Mitrovic et al., 1999). Fatigue damage growth is also critical under compression loads and may cause catastrophic failure of the structure via local and global buckling at stress levels well below the undamaged fatigue limit of the material.

Damage tolerance, as a design philosophy, has various definitions, coined by many researchers. For instance, Miracle et al. (2001) defined damage tolerance as "a critical structure's ability to withstand a level of damage induced while in service or during manufacture while ensuring functional maintainability". The philosophy allows slow or no growth of the defects or cracks in aircraft structure and components during their service life. Approaches to damage tolerance certification of carbon fibre polymer composite aircraft structures are radically different from the equivalent of metallic aircraft structures. Demonstration of damage tolerance in an aluminium aircraft is checked via slow a fatigue crack growth coupled with regular inspections to ensure a high probability of detection of fatigue cracks before any catastrophic event. In contrast, damage tolerance in

polymer composite aircraft structures require demonstration of zero delamination growth, as once a propagation starts, crack growth can be so fast that there is no practical window for inspection to detect growing cracks. Current regulations such as Certification Specification (CS) 25 and accepted criteria from industry require no growth of damage in composite structures. During the service life of the airplane, the damaged composite components require for an instant replacement once the internal damage is spotted, which represents a conservative approach to ensure the structural integrity and flight safety due to the lack of knowledge in the delamination growth in composite structures. Thus, a better understanding on how the delamination will propagate when it's damaged is with high importance for better material usage.

An important category of defects from which delaminations can propagate is the local arrays of delaminations formed subsurface after impacts to the structure. This leads to the possibility of prior detection and a resulting extended window rather than late detection by C-scan using comparative strain and displacement data from a relatively new method of digital image correlation (DIC). In some previous studies, DIC was used by researchers to compare the surface strain and displacement data for predicting the damage propagation and failure pattern. The results were usually compared with analytical results, numerical outputs, and data extracted from a strain gauge. Former instances of application were to characterise the stress fields around the crack tip of an aluminium test piece for determining the stress intensity factors (K), T-stress, and crack tip opening angle (CTOA). Previous studies found that the DIC is suitable for the elastic field of the material but was deficient in the accurate observation of anisotropy and plasticity behaviour (Yates et al., 2010; Mathieu et al., 2012). The limitations of DIC do not seem to be an obstacle for its usage with composites, which exhibit an almost pure elastic behaviour. A study (Gong et al., 2015) was conducted to observe the progression during a compression in the impact test for carbon fibre composites; at a certain point, there was a change in the results, due to the delamination propagation.

Although the DIC technique seems very practical for the detection of propagation of inner delamination of composites, not many researchers focused on applying the technique to the fatigue process.

Under compression-compression in-plane fatigue, these delaminations can grow under local mode I/mode II displacement once a threshold stress of around 70% of the static compression strength is exceeded. Despite a few previous investigations, factors controlling the onset of delamination growth and the stress and life at which growth begins are poorly understood. Some previous research related the growth initiation and propagation criteria to the strain energy release rate (SERR). FEA is used for theoretical analysis of delamination growth in composite materials. Selection of crack growth technique is an important consideration in the numerical analysis of delamination growth when using any finite element package. Two popular crack growth techniques are used for modelling delamination growth in composite materials: virtual crack closure technique (VCCT) and cohesive zone model (CZM).

For the wide application of a material, the properties and performance of the material should be certified through the pyramid structure (see Figure 1-2) to the final application of the aircraft component. The experimental tests in this project could validate a material's performance at the coupon level.

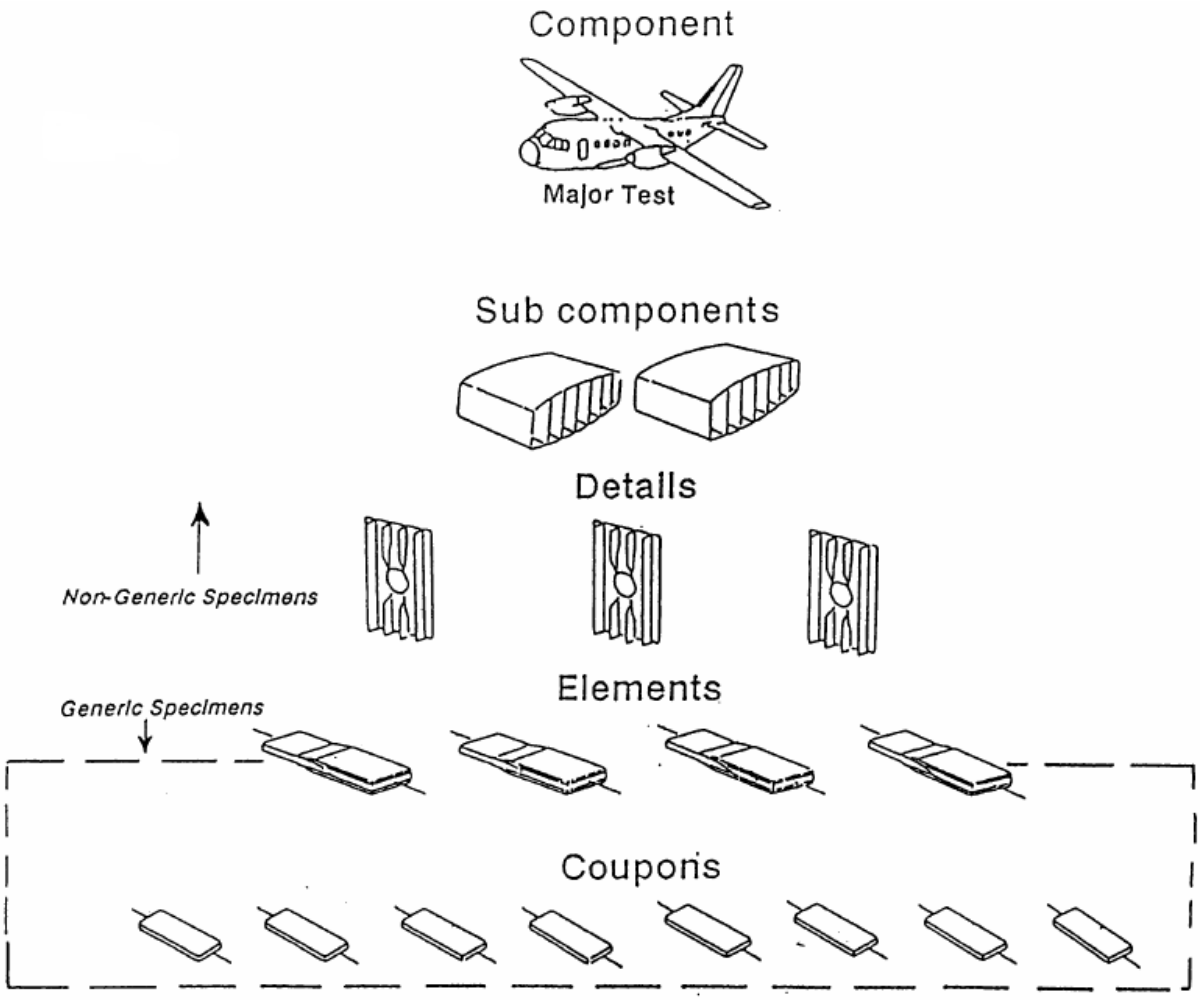

Figure 1-2 Certification levels for aircraft structures (source: EASA, 2014)

1.2 Scope, Aim, and Objectives

This scope of this project is to investigate the damage tolerance behaviour of carbon fibre composites under impact loads and post-impact fatigue. The project aims to explore and identify delamination growth and failure processes in impact-damaged carbon fibre epoxy composites under compressive cyclic loading and to explain the behaviour in the fracture mechanism method.

The objectives of this project are:

(1) To identify gaps in the current research and perform experimental testing: The literature review will cover the existing relevant work to find the data on damage tolerance of carbon fibre composites.

(2) To acquire the mechanical and fracture properties of the testing material from the literature and basic testing: The data will be collected by both literature review and experimental testing for measuring G_{IC} and G_{IIC}, such as double cantilever beam (DCB) and mixed-mode bending (MMB) test.

(3) To produce BVID on specimens by conducting a series of LVI tests and characterising the data: The BVID and the tests will be carried out within the CS25 requirement and based on the relevant ASTM standards on impact testing.

(4) To perform static and fatigue testing on damaged specimens and observe the delamination growth and mechanical behaviour: A static compression test will be conducted within the testing standard. Fatigue testing will be based on the static standard by adding some modifications.

(5) To perform and detect delamination initiation and propagation in both non-destructive and destructive approaches

(6) To characterise the FAI results by both the S-N curve approach and fracture mechanics-based approach

(7) To study the effect of strain energy release rate (SERR) on the development of delamination growth pattern by developing a multi-delamination model

1.3 Structure of the Thesis

The thesis is structured in ten chapters. Firstly, the problem of fatigue after impact for composites is outlined; then, a literature review is carried out to identify current research progress and the gaps in the knowledge. The methodology includes the techniques and methods involved in the project. The experimental part consists of the preparation for the test, low-velocity impact test, subsequent compression after impact test, and compressive fatigue after impact test. Several destructive and non-destructive evaluation methods are adapted herein. The numerical model to extract the SERR value distribution is presented. The results are presented and analysed in the following chapter to illustrate the damage tolerance behaviour of impacted composites. A summary of each chapter is given below:

Chapter 1 states the background and the importance of studying the post-impact fatigue behaviour of carbon fibre composites.

Chapter 2 introduces the reader to the purpose of this project. The review consists of three major parts: LVI, compression after impact, and post-impact fatigue. These are the three aspects of the damage tolerance performance of the carbon fibre composites. A review of LVI and compression after impact will look at the delamination caused by impact load, which is one of the major concerns causing fatal failure of the structures; also, such delamination would reduce the residual strength significantly. The propagation of these existing delaminations would cause failure under fatigue load and the strain energy released at the delamination front is considered the driving factor here.

Chapter 3 explains the experimental and numerical methods and techniques used in this project. The drop weight impact and compression after impact testing had some standards to follow while fatigue after impact testing was performed with some modifications to the compression after impact test. Two major modes of detection and measurement, i.e. phased array ultrasonics and DIC, were introduced in the chapter. Virtual crack closure technique, a widely accepted and efficient way to obtain the SERR value from numerical modelling was introduced in the later part of the chapter.

Chapter 4 explains the experimental testing setups from sample fabrication to the calibration of phased array ultrasonics and DIC.

Chapter 5 is addressed to explore the response of CFRP under LVI load. Further data presented the difference in the responses of cross-ply (CP) and quasi-isotropic (QI) layups and the relation between three key index forces of impact response. The measured delamination morphology was compared between the two different layups and different impact energies. A computed tomography scan was used to present the whole-field delamination distribution after impact.

Chapter 6 presents the results of measured residual strength after certain impact levels and of the application of DIC on capturing the specific surface pattern during the progression of the compression test.

Chapter 7 presents the compression-compression fatigue testing results for the samples impacted at different levels of energy. The relation between maximum compressive load, ratio of maximum compressive load to its residual compressive strength, fatigue life, and damage area is discussed. NDT/NDE results from the C-scan and DIC are presented for typical samples at every impact energy. The out-of-plane displacement in z-direction best describes the progression in fatigue.

Chapter 8 explains the method of finite element modelling. The content starts from the validation of basic fracture testing for mode I and II in double cantilever beam (DCB) and mixed mode bending (MMB). Strain energy release rate (SERR) at delamination front and local buckling load are presented as well. A further model with two embedded delaminations is developed to explain the experimental observation.

Chapter 9 draws specific conclusions on the research work. The accomplishment of thesis objectives is explained and the mechanism of post-impact fatigue behaviour is discussed.

Chapter 10 gives the conclusions based on the previous chapters and some future work is also recommended.

2 LITERATURE REVIEW

2.1 Low-Velocity Impact

Higher specific strength and modulus make the CFRP an ideal alternative to the currently used metal structures. The trend is composite dominant or even full composite for many structural parts in the aerospace industry. It is inevitable to encounter some impacts from foreign objects during the manufacturing process, maintenance, and entire service life of an aerospace structure. The two types of impact damages, HVI and LVI, are defined on the basis of impact velocity, whose classification threshold is 20 m/s (Davies and Zhang, 1995). LVIs can be expected from most common situations. Impact from objects may come from the runway debris bouncing onto the fuselage during take-off and landing and accidental fall of service tools during a maintenance inspection.

Many studies have looked into LVIs because they may result in BVID which is almost invisible to the naked eyes, as the name implies. As far as inspection is concerned, there are mainly two types of impact damages: dent on the impact face and internal delamination. A dent caused by LVI usually has a depth of less than 1.25 mm (Cartié and Irving, 2002). Hence, the damage below BVID threshold is often easier to be neglected during the manufacture and service of an aircraft. Furthermore, under the dent, there is usually delamination damage that is invisible on visual inspection, which can be quite big and cause degradation in the strength. Therefore, those damages must be carefully considered during aircraft design owing to their huge influence on the integrity and safety of the structures.

2.1.1 Damage Mechanism

Impact can cause four types of damages to composites: (a) matrix cracking, (b) delamination, (c) fibre failure, and (d) penetration (Richardson, 1996). The damage is due to the interaction between local indentation and global deformation. Penetration is the result of high local stress due to high energy impact, which is visible. In this review, the focus is on the BVID; hence, only the

first three types of mechanisms will be considered. Figure 2-1 shows the morphology of three types of damages induced by an impact.

Matrix cracks

Matrix cracking is the first stage of impact damage as a result of LVI load (Richardson and Wisheart, 1996). The damage is usually concentrated near the impact indentation and is perpendicular to the laminate thickness. The contact force of the impact strike, causing in-plane normal stress, can result in tensile cracks, and the subsequent transverse shear stress is attributed to the shear cracks. Richardson and Wisheart (1996) made a sketch of matrix cracking of a CP laminate under impact force (see Figure 2-2). Shear cracks are more likely to be observed in the viewpoint at a perpendicular angle to the fibre direction.

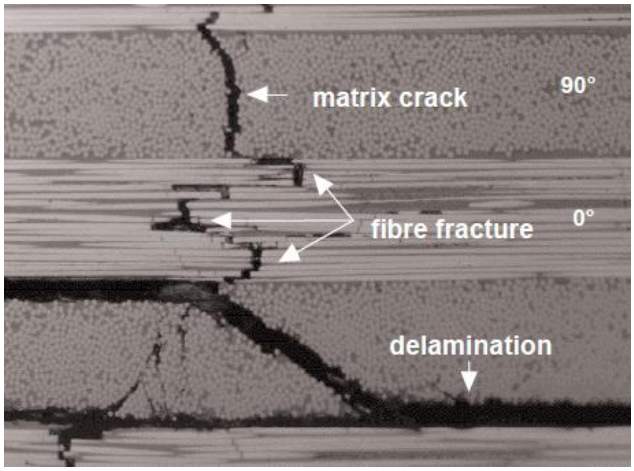

Figure 2-1 Types of damages in impacted fibre-reinforced laminates (Source: Davis and Olsson, 2004)

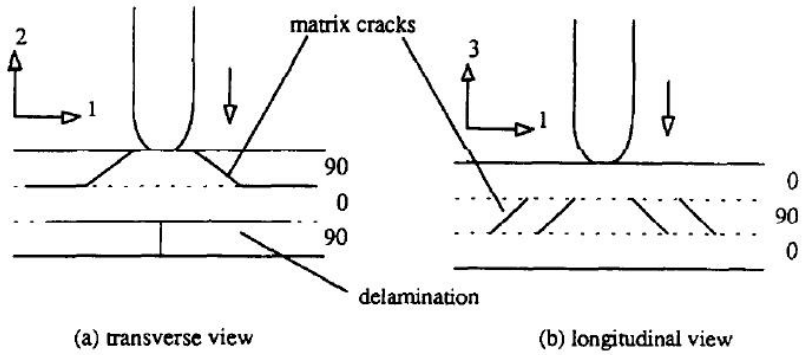

Figure 2-2 Initial damage of matrix cracking (Source: Richardson and Wisheart, 1996)

Abrate (1998) investigated the distribution of matrix cracks in thick and thin laminates in response to impact strike (see Figure 2-3). It was found the thick laminate shows a “pine tree” distribution as the laminate has higher bending stiffness than the thin laminate. The near contact point tensile cracks are caused by the high local centralised contact force. The shear cracks propagate during the impact force transmission, resulting in a large delamination area. In the thin laminate, however, the same impact force will cause larger bending than in its thick counterparts, causing the tensile cracks to appear on the back face. The cracks are initiated from the back side to the front, so there is a large delamination area near the impact side. Matrix cracks have a relatively minor influence on the overall integrity and stiffness of the laminate.

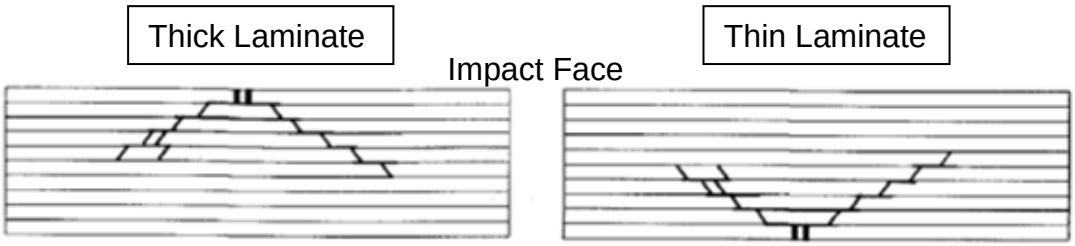

Figure 2-3 Through thickness effect on thick and thin laminate, impact surface is on the top surface (Source: Abrate 1998)

Delamination

Delamination during impact is caused by transverse normal and shear stresses in the matrix between plies of different fibre orientation. Liu (1988) states that the

bending stiffness mismatch is the major contributor to delamination as the matrix enforces the uniform deformation of two adjacent plies. As the interlaminar stress increases until it reaches the strength of the matrix, the failure of the local matrix will initiate the delamination. The delamination size is dependent on the angle difference between two adjacent plies. Liu (1988) derived curves resembling the impact-induced delamination shape in different angle mismatches (Figure 2-4).

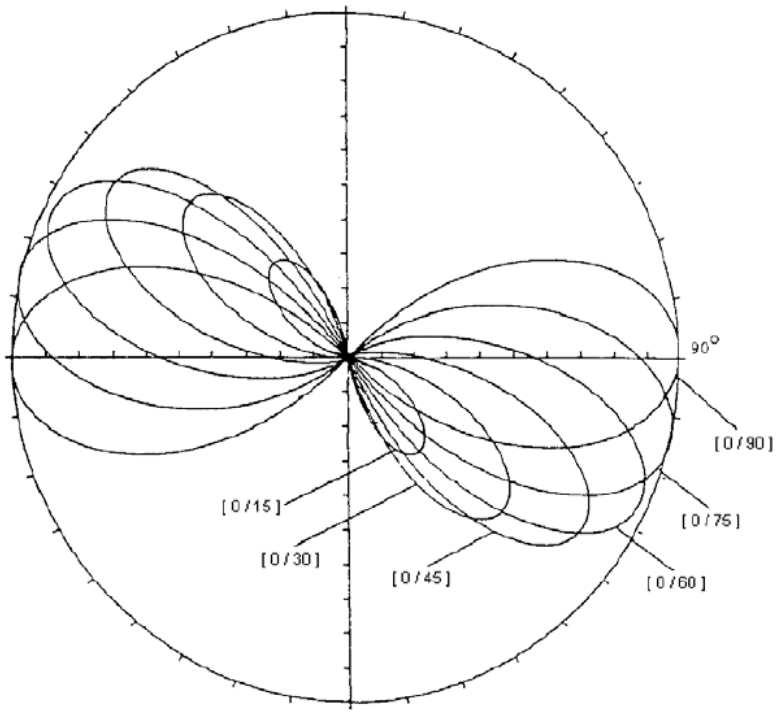

Figure 2-4 Predicted delamination size and shape based upon stiffness mismatch (Source: Liu 1988)

The accumulated “peanut” shapes in Liu’s research represent the delamination in different interfaces, outlining the projected delamination boundary. Some supporting evidence was given by other researchers (Levin, 1992; Hull and Shi, 1993; Davis and Olsson, 2004) who used fractographic approaches for delamination shape appreciation with QI layups. “Peanut” shape delamination was obtained on each ply interface (see Figure 2-5). Thud, it can be said that delamination is propagated in the fibre of the lower ply after an impact strike. Suemasu and Majima (1998) explained the effect that remaining delamination barrel-shaped in thick laminate and expanding to non-impacted surface in thin

laminate using the influence of membrane stresses on the strain energy release rate through the thickness. The projected delamination area in QI laminates is often represented using a circular or elliptical area (Katerelos et al., 2004). In laminates with a large number of 0° plies, the damage morphology can change, as Cristescu et al. (1975) found that it elongates along the 0° axis for higher impact energies.

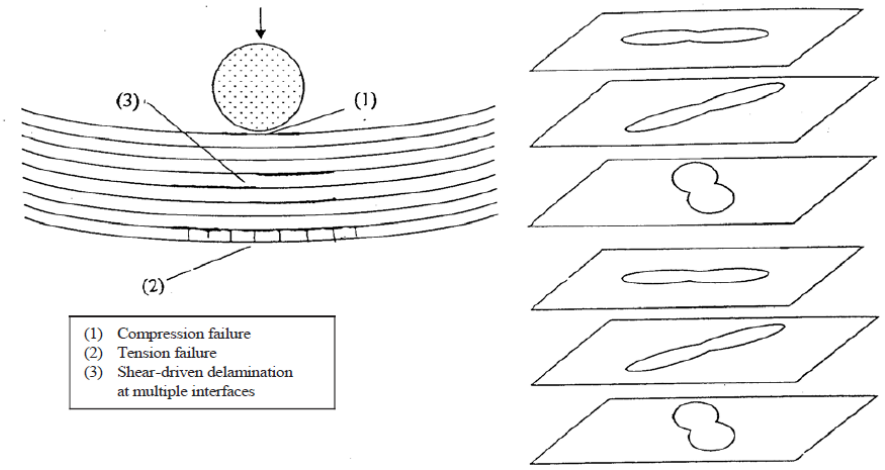

Figure 2-5 Typical distribution of delamination (Source: Davis and Olsson 2004)

Among different impact-induced damages, delamination is the major area of concern for structural integrity as it has the strongest influence on laminate strength, particularly in compression (Mitrovic et al., 1999).

Fibre breakage

Fibre breakage appears when a laminate is subjected to high-energy impact. Avery and Grande (1990) observed many instances of fibre breakage during their study on the impact of force of over 30 J on a 24-ply carbon fibre epoxy laminate.

High-level impact will cause high local centralised contact force at the contact point, and the fibre will break when the stress caused by deflection exceeds the fibre strength.

2.1.2 Damage Occurrence Threshold

Unlike HVI that results in visible damage or even penetration on the composite plate, LVI can produce interlaminar delamination, which is barely visible on the

impact surface. Some researchers proposed the delamination threadshold load during an low-velocity impact (Davis and Zhang 1995, Xu et al. 2013). Davies and Zhang (1995) proposed that damage initiated by the contact force (P) reaches a critical value (P_C), as indicated by eq. (2-1):

$$P_c^{\,2} = \frac{8\pi^2 E t^3}{9(1-v^2)} G_{IIC} \qquad \textbf{(2-1)}$$

Where P_C is the critical force for damage initiation, E is the equivalent in-plane modulus, v is the Poisson's ratio, t is the laminate thickness, and G_{IIC} is the critical SERR for mode II fracture. A typical impact force response is shown in Figure 2-6.

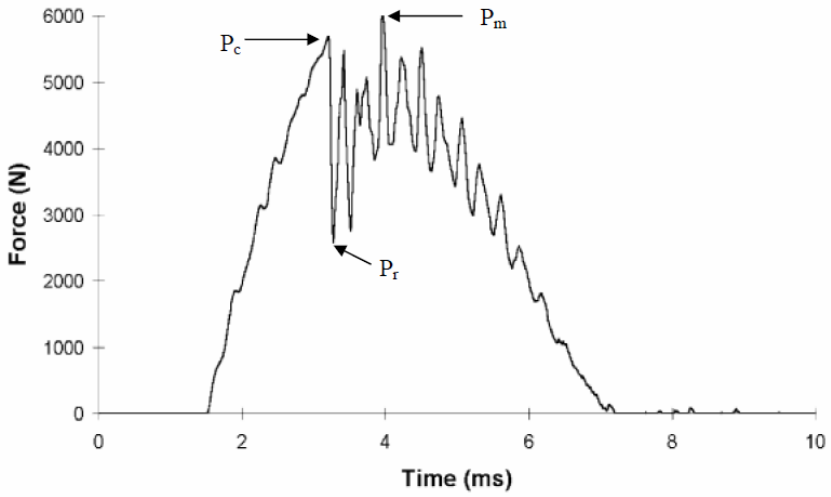

Figure 2-6 Typical impact force response (source: Davies and Zhang 1995)

The equation indicates that G_{IIC} is a key parameter for determining low energy impact damage, which agrees with later research (Bibo et al., 1994; Cartié and Irving, 2002).

Delamination will propagate when the applied SERR G exceeds the critical SERR G_C, resulting in the imbalance of the system (Hashemi et al., 1990), in which G_C indicates the energy needed to propagate the new per unit delamination surface. The three modes of fracture are illustrated in Figure 2-7, associated with the three modes of SERR G_I, G_{II}, and G_{III}. Fracture toughness testing is performed on

laminates for mode I and mode II delamination propagation using DCB and End Notch Flexure (ENF) testing, respectively (Anderson, 2005).

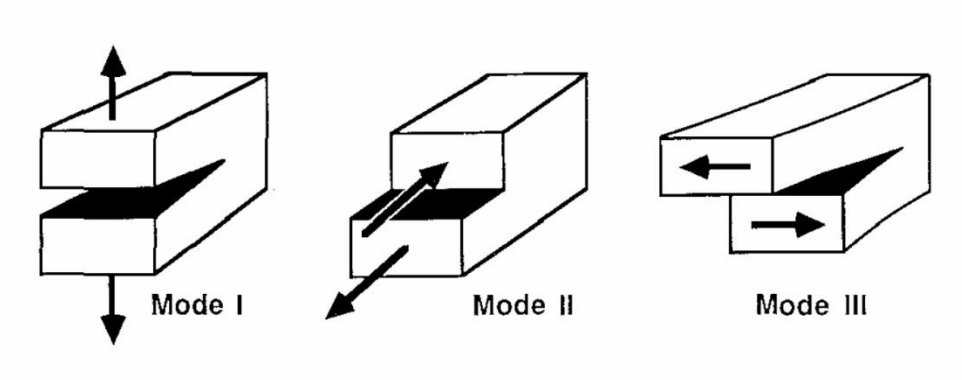

Figure 2-7 Three modes of fracture (Source: Hashemi et al., 1990)

Research has shown that the dominant mode of SERR under impact load is mode II (Bibo et al., 1995; Abrate and Schoeppner, 1999; Cartié and Irving, 2002).

2.1.3 Parameters Influencing Impact Damage

According to previous research, impact damages can be attributed to many variables during impact testing, such as impactor geometry, matrix properties, fibre properties, stacking sequence, and laminate thickness.

Impactor geometry

The shape of the impactor can lead to diverse types of damage patterns. For instance, a sharp impactor will cause more fibre breakage at the contact point near the impact surface than a blunt impactor, which may cause more internal damage, such as matrix cracks and delamination. In the currently accepted testing standards for LVI, such as Boeing Standard D888-10026, ASTM D7136, and Airbus AITM1-0010, a hemisphere with a diameter of 16-mm is used as an impactor to simulate a dropping toolbox in a maintenance scenario. The unification of impactor geometry allows a direct comparison between impact testing with other variables.

Matrix properties

The matrix is not only the major portion that transfers load in a composite laminate but also determines the through-thickness properties, which are vital parameters that affect the impact response. Cartié and Irving (2002) found that the toughness of resin, both G_I and G_{II}, affects the impact-induced delamination area when they compared samples using the same fibre but resins with different fracture toughness. An increase in the G value leads to a decrease in the delamination area, representing better impact resistance ability. They attribute the observation to the impact damage threshold force, as proposed by Davies and Zhang (1995). Composites with higher fracture toughness require higher critical force to initiate the damage, but once the critical value is exceeded, the increase in impact energy becomes proportional to the increase in delamination area.

Fibre properties

Fibre is the main portion of the composite that directs the tension and compression in the fibre's direction. As the impact force is usually perpendicular to the fibre, none or only a small portion of fibre properties can be used. FAA (1998) found that fibre properties have a small influence on a composite's impact resistance ability. However, Abrate (1998) proposed that the ratio of Young's modulus in the longitudinal and transversal directions (E_1/E_2) of a single lamina is relative to the bending stiffness mismatch, which is regarded by Liu (1988) as the important driving force for delamination in ply interfaces. Resins with a high modulus usually have a high value of E_2, which amplifies the effect of bending stiffness mismatch, resulting in a larger delamination area. Some research also showed that apart from fibre strength, fibre failure strain also affects the delamination. Cantewell and Morton (1991) found that fibres with high failure strain have enhanced impact damage resistance to high-energy impact. Cartié and Irving (2002) found that fibres with low failure strain can also reduce LVI-induced damage by absorbing the energy in the form of fibre breakage instead of progression of internal delamination.

Stacking sequence

Liu (1988) proposed attributed delamination to the bending stiffness mismatch between two adjacent layers. As shown in Figure 2-4, the larger angle difference

between two adjacent ply interfaces leads to a larger delamination area. Although the stacking sequence affects the impact damage area, the critical force required to initiate delamination is independent of ply orientation and was shown to be a function of the matrix properties (Strait et al., 1992). In the research by Reis and Freitas (1998), although the laminate equivalent of Young's modulus was different owing to the stacking sequence, the failure strain when the specimen came under uniaxial compression turned out to be close values to each other.

Laminate thickness

As stated in the previous paragraph, thin and thick laminates exhibit different delamination patterns under impact strike, mainly owing to the stiffness difference. Thin laminate has a delamination pattern that grows from the back face to the central ply due to larger bending deformation, resulting from lower stiffness. Thick laminate has a "pine tree" delamination distribution pattern. Some studies showed that laminate thickness has an effect on the critical delamination initiation threshold value (Davies and Zhang, 1995; Hounslow, 2000).

2.2 Compression after Impact

Mechanical properties of composites can be reduced considerably after a certain level of impact that can cause delamination in the composite. Delamination-induced performance degradation could be severe. Usually, the compressive strength may reduce to 40–60% of that of an undamaged composite (Cantwell et al., 1984; Abrate, 1998; Cartié and Irving, 2002). The reduction in strength and stiffness is a major issue in the damage tolerance structure design.

2.2.1 Compressive Failure Mechanism

Fleck (1997) identified six failure mechanisms for pristine composites under compression, as shown in Figure 2-8. These modes have all been observed during experimental testing.

Failure mode may alter an impacted composite owing to the changes in the composite form. Abrate (1998) proposed that buckling and subsequent mode II delamination growth is reason behind compression failure of an impact-damaged

composite with a thin laminate. For a thick laminate, mode I-type local buckling can be observed clearly. Buckling modes have been classified into three types: local buckling, global buckling, and mixed-mode buckling.

Pavier and Chester (1990) conclude that the failure induced by delamination results from both compressive and bending stresses due to the out-of-plane buckled plies.

CAI test standards such as ASTM D7137 impose the use of anti-buckling guides to confine failure induced by local buckling to a certain area and to prevent premature failure induced by global or mixed-mode buckling.

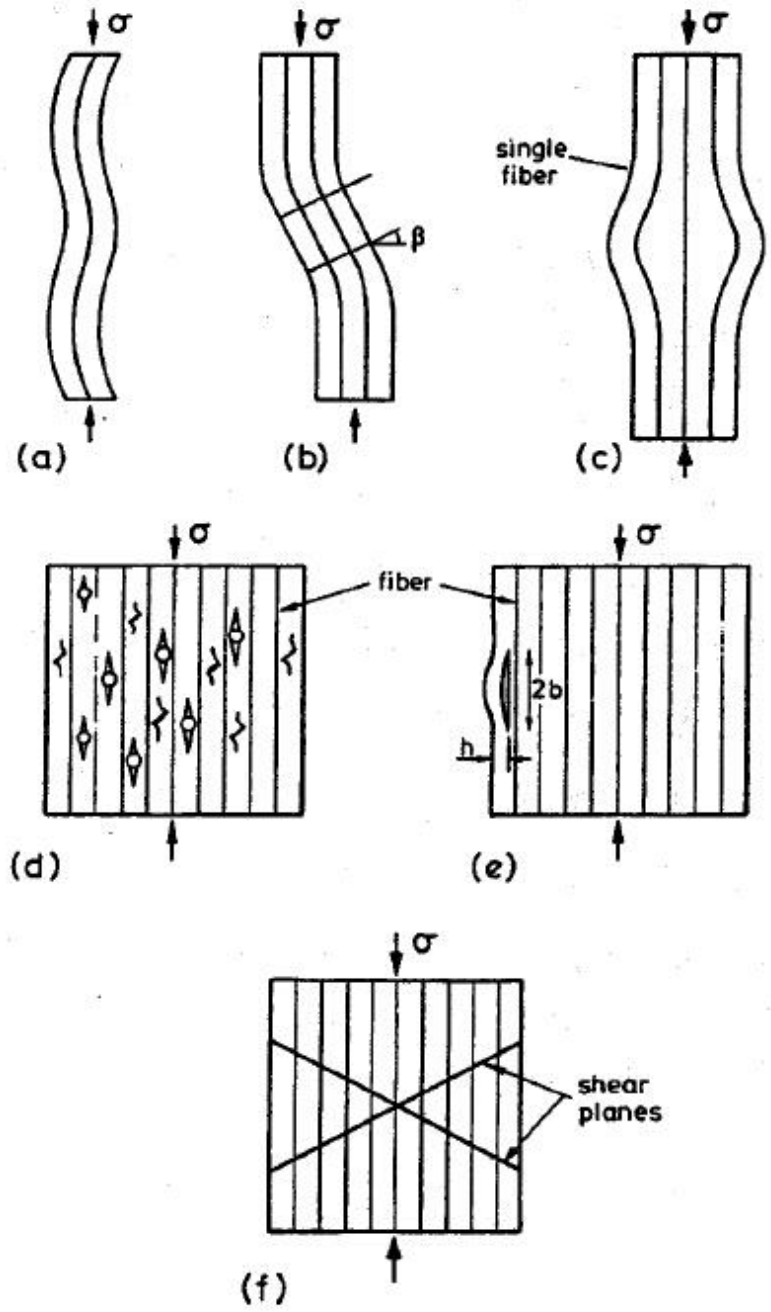

Figure 2-8 Compression failure mechanism in pristine laminates (Source: Fleck, 1997): (a) Elastic microbuckling of the fibres, (b) plastics microbuckling of the fibres, (c) fibre crushing, (d) splitting of the matrix, (e) buckle delamination, and (f) shear band deformation

2.2.2 Parameters Influencing Compression

A large body of research has explored the parameters affecting the CAI strength. Some researchers state that delamination area is the key controlling parameter for post-impact residual compression strength (Abrate 1998). However, the delamination area is a dependent variable that is correlated with the impact energy. Cartié and Irving (2002) studied several types of epoxies for CAI testing and obtained a better correlation between CAI strength and impact energy.

2.2.3 Prediction of Compressive Residual Strength

Due to the variations in the testing results and sometimes lack of testing equipment and conditions, it was highly desirable to have an accessible approach for estimating the compressive residual strength after impact. FAA had spent over 10 years and carried out numerous experimental test to obtain this estimation approach. The equation is shown in (2-2):

$$\sigma_r = \frac{\sigma_0}{1 + C_1 C_2 C_3 C_4 C_5 W_e} \quad \textbf{(2-2)}$$

Where

σ_0 is undamaged compressive strength; to obtain this value, another equation was established by Hadcock (1982):

$$\sigma_0 = \frac{X_c}{1+\alpha}\left[L + \frac{MN}{4M+N} + \alpha\right] \quad \textbf{(2-3)}$$

X_c is the ply's longitudinal compressive strength;

L is the proportion of 0° ply;

M is the proportion of 90° ply;

N is the proportion of ±45° ply;

$\alpha = \frac{E_{22}}{E_{11} - E_{22}}$

Returning to residual strength calculation,

$$C_1 = 0.547\left(\frac{E_x}{E_L}\right)^{0.524}$$

C_1 is a parameter of laminate layup;

E_x is the laminate modulus in loading direction and E_L denotes the lamina;

$\boldsymbol{C_2}$ is the parameter for full-penetration stress; the specific value can be referenced from Table 2-1;

$$C_3 = \frac{0.499}{t^{0.5056}}$$

C_3 is the thickness parameter, and t is the thickness of the laminate;

$$C_4 C_5 = A(kE)^B$$

$$A = \frac{0.749}{G_{IC}} + 0.0145$$

$$B = 0.4345 + 0.109G_{IC} - 0.0098G_{IC}^2$$

C_4 is the toughness parameter of the material;

C_5 is the impact energy parameter;

k is the support coefficient and value for centre impact equals 1;

E denotes impact energy;

G_{IC} is the mode I fracture toughness of the material;

$$W_e = \frac{2 + (1 - \frac{D}{W})^3}{1 - \frac{D}{W}} + 0.0145$$

W_e is the parameter for impactor size;

D is the diameter of the striker;

W is the distance of the fixture's support area.

The above equation was used by Krutop (2007) showed that the accuracy of undamaged compressive strength can be guaranteed by using Hadcock (1982) and Tsai-Hill and Hoffmann's (Guo, 2015) failure theories.

Table 2-1 Value of parameter C_2 affected by layup (Source: FAA)

Percent of 0º plies	0	10	20	30	40	50	60	70	80
20% of ± 45º plies	2.7677	3.1777	3.5022	3.7775	4.0215	4.2456	4.459	4.6732	4.9098
40% of ± 45º plies	2.6841	3.0081	3.2766	3.5124	3.7282	3.9335	4.1372	***	***
60% of ± 45º plies	2.6137	2.8883	3.1204	3.3251	3.5075	***	***	***	***
80% of ± 45º plies	2.5069	2.7373	2.9172	***	***	***	***	***	***

2.3 Post-impact Fatigue

2.3.1 Fatigue of Composite

CFRP is found to have superior fatigue damage performance over metal alloys. The onset and development of fatigue damage in carbon fibre laminates was described by Zhang (2013). The fatigue failure has three main sources: matrix crack, fibre breakage, and delamination (see Figure 2-9). Irving (2013) and Nettles et al. (2011) indicated that the fatigue limit for a QI laminate is approximately 60–80% of its static ultimate strength.

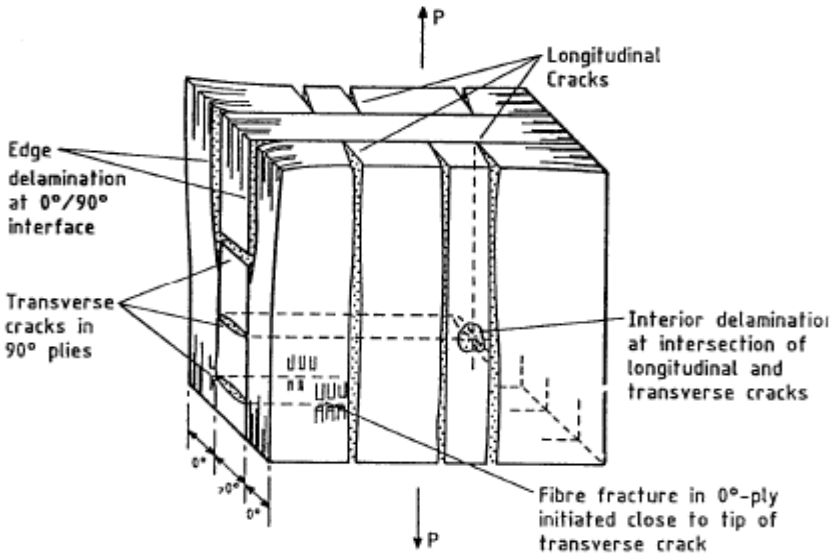

Figure 2-9 Fatigue damage mechanisms in carbon epoxy laminate (Source: Zhang, 2013)

When delamination is initiated and propagated within the composite because of defects during manufacturing or after an impact attack, the strength level could decrease, especially the compressive strength, which could decrease drastically to about 40% of the undamaged strength. This reduction also affects the fatigue performance. The fatigue failure due to delamination propagation of carbon fibre composites has also led to some design concerns in the industry. The poor understanding of post-impact fatigue performance limits the exploration of the full application potential of CFRPs.

Some studies have been conducted in this relatively new field of post-impact fatigue behaviour of composites. Some efforts have been made to understand the post-impact fatigue phenomenon during the fatigue process and the effect of the delamination propagation.

2.3.2 Fatigue of Damaged Laminates

The introduction of out-of-plane load and subsequent damage can reduce the damage tolerance and resistance capability of carbon fibre composites. It is important to understand the influence of out-of-plane load (such as impact) on a CFRP. Nettle et al. (2011) and Irving and Soutis (2014) showed the relationship between residual compression strength, damage size, and fatigue life using schematics (Figure 2-10).

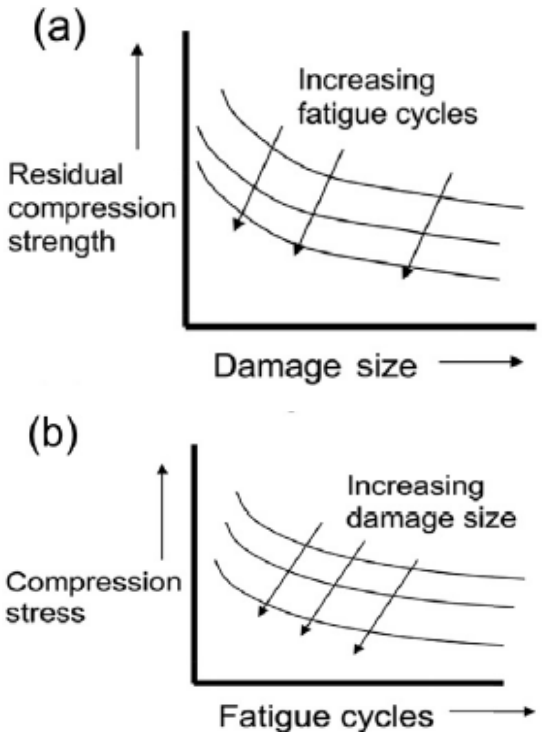

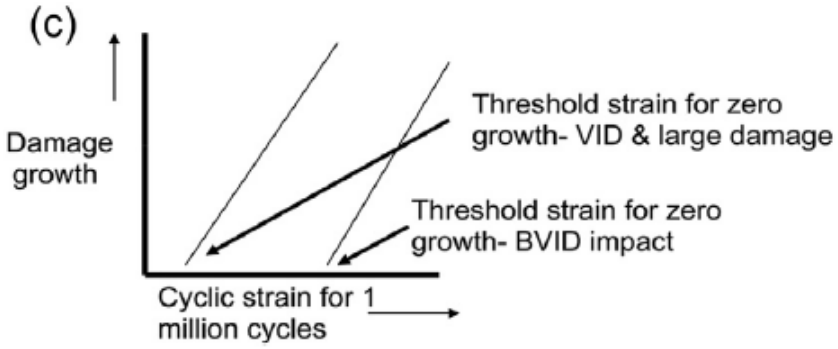

Figure 2-10 Relation between residual compression strength, damage size, and fatigue cycles (Source: Irving and Soutis 2014)

The relationship between residual compressive strength and damage size under different fatigue cycles is shown in Figure 2-10 (a). The curve represents the fatigue loading condition, and the topmost curve represents the static condition. The lower position of the curve denotes the increment in fatigue cycles. They concluded that the residual compression strength is negatively correlated with fatigue cycles and damage size. Figure 2-10 (b) shows the relationship between applied compressive stress and fatigue life under different impact damage sizes. It can be found that with larger impact damage, the maximum compressive stress required to achieve the same fatigue life is reduced. Also, for the same compressive load, with less impact damage imparted within, longer fatigue lifetime could be achieved. Figure 2-10 (c) exhibits the threshold for damage growth with different damage sizes. The diagram shows the strain threshold for the upper and the lower boundary of damage size of no growth for one million cycles. Figure 2-10 came with only the schematic trend but no actual numbers. The actual data could be filled in with some experimental input and would be effective for future design.

Many researchers have studied post-impact fatigue behaviour. Ong and Liou (1993) found that fatigue characteristics of composites do not change by impact damage; the fatigue life of a damaged specimen is obviously decreased at a specific cyclic loading. A 10-Hz tension-tension post-impact fatigue test was carried out to determine whether AS4/PEEK has a short damage fatigue growth life compared with thermosetting composites. Beheshty and Harris (1998, 1999) found that for fatigue loading at R = 10, no damage growth was detected until

rupture was approached. Specimens loaded at R = -0.3 showed damage propagation in the direction of 45° ply. Ogasawara et al. (2013) proposed a statistical model based on Weibull distribution; they reported the ratio between the endurance limit at 10^6 and 10^7 cycles, and the initial static strength was estimated to be 0.74 and 0.68, respectively. Davies and Irving (2014) compared many reports on fatigue delamination growth and found inconsistencies in the data reported. Some investigations reported zero delamination growth until just before failure and others found that delamination propagation occurred throughout life.

2.3.3 Fatigue Delamination Growth of Damaged Laminates

As known, undamaged carbon fibre-reinforced composite is superior to its metallic counterparts. The post-impact fatigue delamination growth in composite materials is still poorly understood while mature theory has been developed for crack growth in metallic structures.

Tai et al. (1998) conducted tension-tension cyclic loading tests at 3-Hz load frequency on a QI layup with CF/epoxy laminate with a thickness of 2 mm, subjected to an impact of 6.46 J. From Figure 2-11, the fatigue delamination was initiated from both free edges of the specimen, and this accelerated the fracture of the specimen during the subsequent fatigue loads.

Chen et al. (2002) used acoustography to monitor damage in composites in real-time during long-term dynamic fatigue tests on AS4/8552, using carbon composites with $[45/0/-45/90]_{2s}$ lay-up. The results shown in Figure 2-12 indicate a three-stage growth pattern of impact damage during constant amplitude load fatigue tests. The growth rate increases near 30000 cycles.

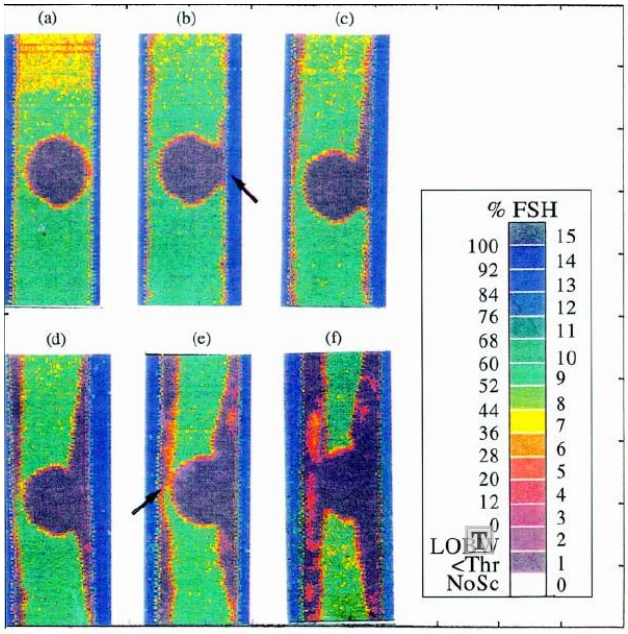

Figure 2-11 C-scan graphs of impacted specimens after various fatigue load cycles at 65% UTS: (a) 5000 cycles, (b) 10000 cycles, (c) 15000 cycles, (d) 20000 cycles, (e) 25000 cycles, (f) 30 000 cycles (Source: Tai et al. 1998).

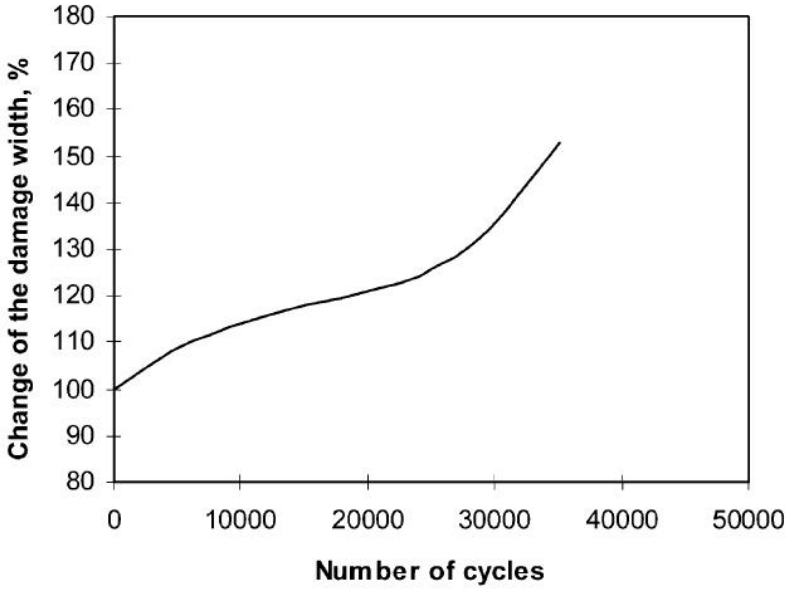

Figure 2-12 Damage growth during fatigue, measured by acoustography images; R = 10, σ_{max} = 170 MPa (Source: Chen et al., 2002)

Mitrovic et al. (1999) tested a QI 32-ply laminate with 0° outer plies under compression-compression fatigue loading and found that delamination growth from the impact site was parallel to the applied load, in the laminate 0° direction.

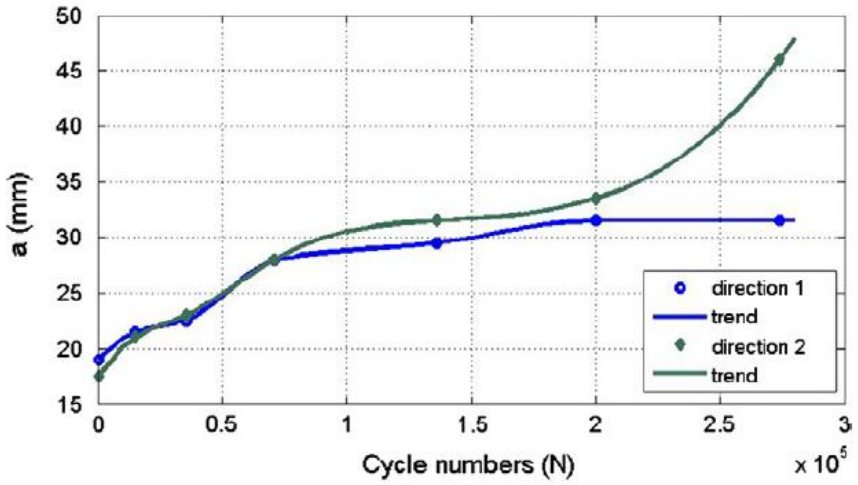

Figure 2-13 Impact defect evolution along the two directions (Source: Garnier, 2013)

Garnier et al. (2013) found that at the beginning of the tension-compression fatigue test at 0.3 Hz, the defect evolves in the two directions of the loading plane. After stabilisation, the defect propagation appears only along the direction perpendicular to the load direction (see Figure 2-13).

No delamination growth after one million cycles in an impact damaged laminate when applied with the maximum fatigue load was less than 60–70% of its static CAI strength (Nettles et al. 2011). The research proposed a threshold around 70% of its RCS for the fatigue delamination propagation.

Isa et al. (2011) and Mitrovich et al. (1999) conducted studies on fatigue delamination growth. Their results were replotted by Irving and Soutis (2014) (see Figure 2-14). Isa et al. (2011) found that during the fatigue process for an impacted laminate, the delamination area has no detectable growth until 90–95% of the fatigue life. After the start of delamination growth, the propagation was fast, resulting in failure of the composite after very few cycles (see Figure 2-14 a).

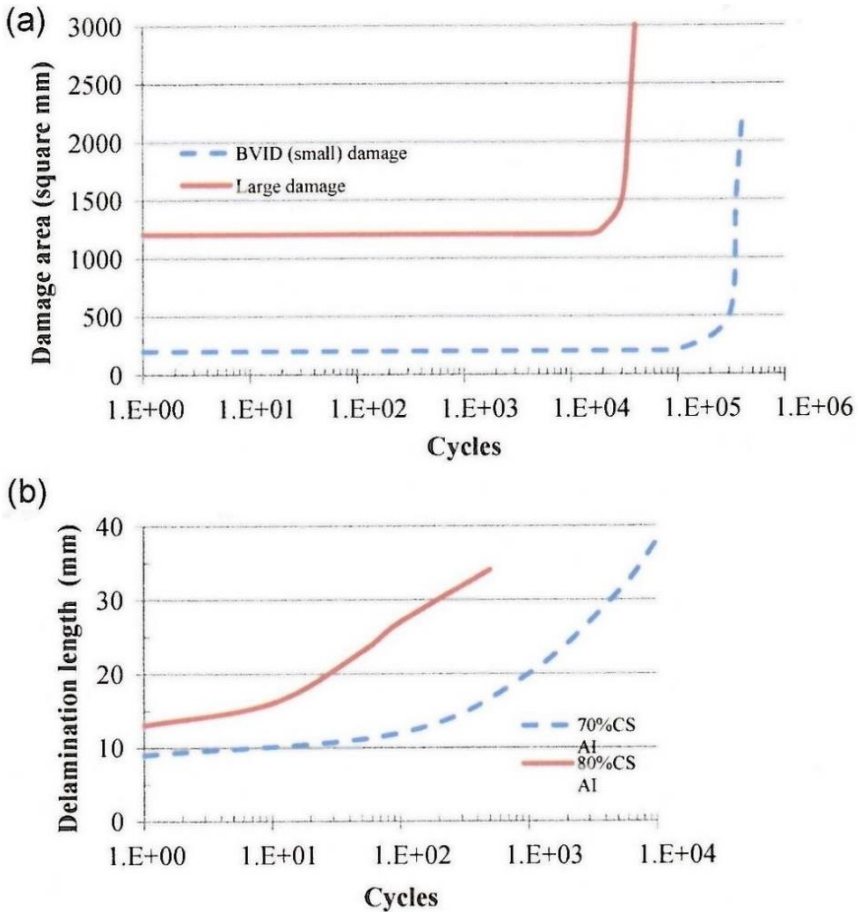

Figure 2-14 Fatigue delamination growth (Source: [a] Isa et al., 2011; [b] Mitrovich et al., 1999)

Mitrovich et al. (1999) in their investigation of fatigue delamination growth in composite materials observed that delamination propagation occurs much earlier in life and grows further (see Figure 2-14 b).

2.3.4 Buckling Progression during Post-Impact Fatigue

Most of the previous studies quantified and measured the delamination progression and the fatigue damage by internal delamination using non-destructive testing methods such as ultrasonic scan or acoustography. Besides the delamination area, the surface buckling mode is another traceable indicator of the severity of fatigue damage.

Gerharz et al. (1989) have suggested two phases during the fatigue failure. The first stage is occupied by small buckling deformation and compliance increase. There was no delamination growth observed out of the damage envelope. The

second stage, occupying the last 10% of the fatigue life exhibits rapid damage growth to failure.

Melin et al. (2001, 2002) conducted experiments in constant amplitude tension-compression fatigue and monitored the process using an optical whole field measurement technique. Delamination propagation and local buckling were found only during the compression period.

2.3.5 Propagation Criteria

Among the several methods for predicting the delamination growth within the impacted laminate, fracture mechanics-based approach is one of the most popular approaches. The approach is used for establishing the delamination propagation model to predict the remaining life of composite components. In the fracture mechanics approach, the Paris law is commonly used in predicting the crack and delamination growth in metals and composites. As it has been well established that stress intensity factor (SIF) is regarded the major driving force for crack growth in metals, the equivalent SIF for composites, acting as the driving force for declamation propagation, in composites is the SERR (Al-Khudairi et al., 2015).

Equation (2-4) and (2-5) showed below are the Paris Law for both metals and composites:

$$\frac{da}{dN} = C(\Delta K)^m \qquad \text{For metals} \qquad \textbf{(2-4)}$$

$$\frac{da}{dN} = C(\Delta G)^m \qquad \text{For composites} \qquad \textbf{(2-5)}$$

Where, da/dN is the delamination growth rate;

C and m are the crack propagation parameters;

ΔK is the stress intensity factor (SIF) of metals;

ΔG is the strain energy release rate (SERR) of composites.

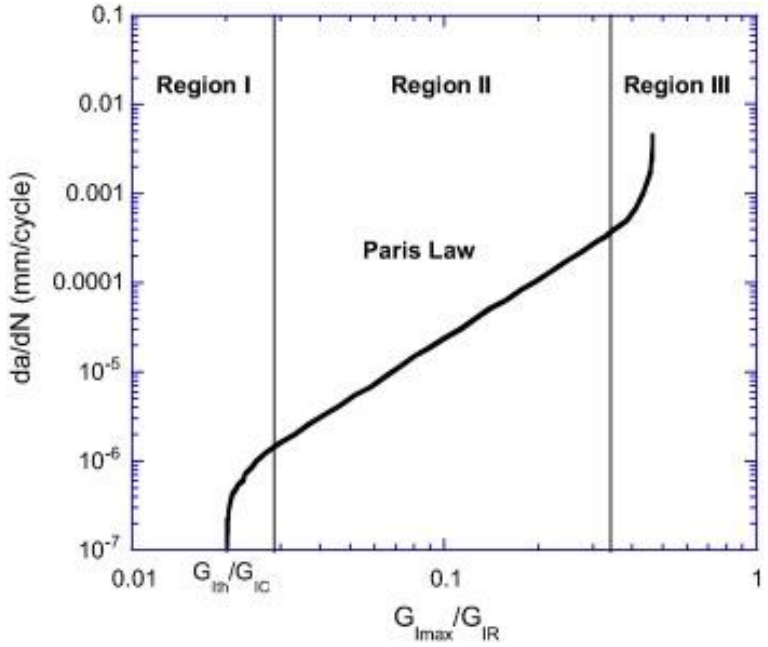

Figure 2-15: Growth curve for fatigue crack (Source: Al-Khudairi et al. 2015)

Figure 2-15 shows the growth curve for fatigue crack and the region where Paris Law applies (Al-Khudairi et al. 2015).

Although it is broadly accepted that the SERR is the driving force for delamination propagation, some researchers (Stelzer et al., 2012; Hojo et al., 2006; 2010) proposed that the current fatigue delamination growth models claim that maximum SERR G_{max} represents delamination propagation behaviour while Beghini et al. (2006) used the SERR rang $\Delta G = G_{max} - G_{min}$ to simulate the propagation. Furthermore, Rans et al. (2011) and Yao et al. (2014) used another SERR range $\Delta G = \left(\sqrt{G_{max}} - \sqrt{G_{min}}\right)^2$ as the delamination driving force. Each form of the crack driving force has been proven appropriate for certain conditions through tests and analyses but not ubiquitously applicable.

The application of the Paris law gains its agreement with tests and analysis with mostly the basic fracture tests. In other words, the adjacent ply interfaces are identical while the delamination is all through the cross-section. Only one mode exists in those scenarios. However, in actual damaged composite scenarios, delamination propagation during cyclic loading occurs in the mixed mode. Some studies were conducted to correlate the key parameters in Paris Law and the mix mode condition. Blanco et al. (2004) proposed general model for fatigue

delamination propagation in mixed mode. The expressions are given in equations (2-6) and (2-7).

$$\log C = \log C_I + \log C_m \left(\frac{G_{II}}{G}\right) + \log \frac{C_{II}}{C_I C_m} \left(\frac{G_{II}}{G}\right)^2 \quad \textbf{(2-6)}$$

$$r = r_I + r_m \left(\frac{G_{II}}{G}\right) + (r_{II} - r_I - r_m) \left(\frac{G_{II}}{G}\right)^2 \quad \textbf{(2-7)}$$

Where C_m and r_m are mixed-mode parameters obtained by curve fitting.

Much previous research proposed their criteria for delamination propagation in mixed mode. Figure 2-16 gives a summary for those research results.

The delamination propagation criteria inferred by Benzeggagh and Kenane (1996) are one of the most received ones. Their interpolation of Paris Law is given in equation (2-5). They determined the Paris Law delamination propagation parameters (C and m) from pure Mode I and Mode II fracture toughness. The BK law with the determination of C and m is given in equations (2-8) and (2-9).

$$\ln C = \ln C_{II} + (\ln C_I - \ln C_{II}) \left(1 - \frac{G_{II}}{G_T}\right)^{m_B} \quad \textbf{(2-8)}$$

$$m = m_I + (m_{II} - m_I) \left(\frac{G_{II}}{G_T}\right)^{m_d} \quad \textbf{(2-9)}$$

Where m_B and m_d are material constant values determined by tests data fitting.

The parameters obtained from the B-K law of the cracks propagation for Paris Law gave the good agreement between predicted fatigue delamination growth and the experimental data.

Some other research also reported important conclusions. Kardomateas et al. (1995) reported the fatigue delamination growth driven by the mixed mode condition but dominated by mode II. The mode II value increased with the propagation of the delamination size. Also, from their experimental study, the delamination propagation was also affected by the other declamation adjacent in the through-thickness direction. Bennati et al. (2006) reported in their study on

fatigue delamination propagation with a composite panel subjected to compression fatigue load. In their study, some small changes in crack-governing parameters for composite materials were found resulting in the completely different direction of delamination propagation. Katerelos et al. (2004) studied the shape of fatigue delamination under c-scan and assumed the contour of each delamination was elliptical. Subsequent SERR values were calculated with the orientation and aspect ratio of the ellipse to predict the fatigue delamination response.

Rhead et al. (2008) proposed an analytical model by simplifying the complicated impact BVID damage into a single circular delamination present at critical interface. The predicted compressive fatigue strains threshold achieved very good agreement with the experimental results.

Shen et al. (2001) developed numerical models with embedded delamination using VCCT to predict the delamination propagation in a composite laminate under cyclic loading. It was reported that the maximum SERR value was coincide with the delamination propagation direction and the full model could provide better agreement than the quarter model due to the boundary effect.

Reference	Expression of the propagation law
Ramkumar and Whitcomb (1985)	$\frac{da}{dN} = C_I\left(\frac{G_I}{G_{Ic}}\right)^{n_I} + C_{II}\left(\frac{G_{II}}{G_{IIc}}\right)^{n_{II}}$
Gustafson and Hojo (1987)	$\frac{da}{dN} = C_I(\Delta G_I)^{n_I} + C_{II}(\Delta G_{II})^{n_{II}}$
Russell and Street (1989)	$\frac{da}{dN} = \left(\frac{G_I}{G_I+G_{II}}C_I + \frac{G_{II}}{G_I+G_{II}}C_{II}\right)\left(\frac{\Delta G_I}{G_{Ic}} + \frac{\Delta G_{II}}{G_{IIc}}\right)^{\left(\frac{G_I}{G_I+G_{II}}n_I + \frac{G_{II}}{G_I+G_{II}}n_{II}\right)}$
Dahlem and Springer (1994)[a]	$\frac{da}{dN} = \left[g_I\frac{E_{22}G_{Ic}}{S_{22}^2} + g_{II}\frac{E_{22}G_{IIc}}{S_{12}^2}\right](C_I^{g_I} + C_{II}^{g_{II}})\left[U\left(\frac{G_I}{G_{Ic}} + \frac{G_{II}}{G_{IIc}}\right)\right]^{(g_In_I + g_{II}n_{II})}$ $g_I = \frac{\frac{G_I}{G_{Ic}}}{\frac{G_I}{G_{Ic}} + \frac{G_{II}}{G_{IIc}}}; \quad g_{II} = \frac{\frac{G_{II}}{G_{IIc}}}{\frac{G_I}{G_{Ic}} + \frac{G_{II}}{G_{IIc}}}$
Kardomateas et al. (1995)	$\frac{da}{dN} = C\frac{\left(\frac{G_{Ic}G_{IIc}}{G_c}\Delta G\right)^r}{1 - \frac{G_{Ic}G_{IIc}}{G_c}G}$ $C = C_I + (C_{II} - C_I)\sin^2\psi$ $r = r_I + (r_{II} - r_I)\sin^2\psi$ $G_c = G_{IIc} + (G_{Ic} - G_{IIc})\sin^2\psi$
Kenane and Benzeggagh (1997)[b]	$\frac{da}{dN} = \exp\left[\ln(C_{II}) + (\ln(C_I) - \ln(C_{II}))\left(1 - \frac{G_{II}}{G}\right)^b\right](\Delta G)^{\left(r_I + (r_{II} - r_I)\left(\frac{G_{II}}{G}\right)^d\right)}$
Andersons et al. (2001)	$\frac{da}{dN} = C\left[\left(\frac{K_I}{K_{Ic}}\right)^2 + \left(\frac{K_{II}}{K_{IIc}}\right)^2\right]^{\frac{r}{2}}$ $r = \frac{a_1 + a_2}{\frac{a_1}{n_I} + \frac{a_2}{n_{II}}}$ $C = \left(\frac{r}{r-2}\right)\frac{a_1 + a_2}{\left(\frac{\cos\psi}{K_{Ic}}\right)^2 + \left(\frac{\sin\psi}{K_{IIc}}\right)^2}$ $a_1 = \frac{r_I - 2}{r_I}\left(\frac{\cos\psi}{K_{Ic}}\right)^2 C_I;$ $a_2 = \frac{r_{II} - 2}{r_{II}}\left(\frac{\sin\psi}{K_{IIc}}\right)^2 C_{II}$

Figure 2-16: Mixed-mode models for delamination growth rate (Source: Blanco et al., 2004)

2.4 Summary

The review of previous studies in this chapter shed light on the impact response and CAI performance of carbon fibre composites. However, the post-impact fatigue performance, which is a critical aspect in the damage tolerance design, is not well understood. A quick and short period of propagation to failure was observed but nothing ahead. Few studies have used the buckling behaviour

during the fatigue process to detect the damage area and other important parameters. Furthermore, experimental test procedures have been established to measure the fatigue delamination propagation caused by impact damage. Specimen dimensions were chosen by the researchers. For instance, Garnier et al. (2013) combined the specimen size of impact testing standards (ASTM D 7136) and fatigue testing standards (NF EN ISO 527-4) (see Figure 2-17) while other researchers used a different configuration (Ogasawara et al., 2013). It is accepted that the damage tolerance behaviour is strongly dependent on many testing parameters such as edge effect, boundary constraints, and damage size.

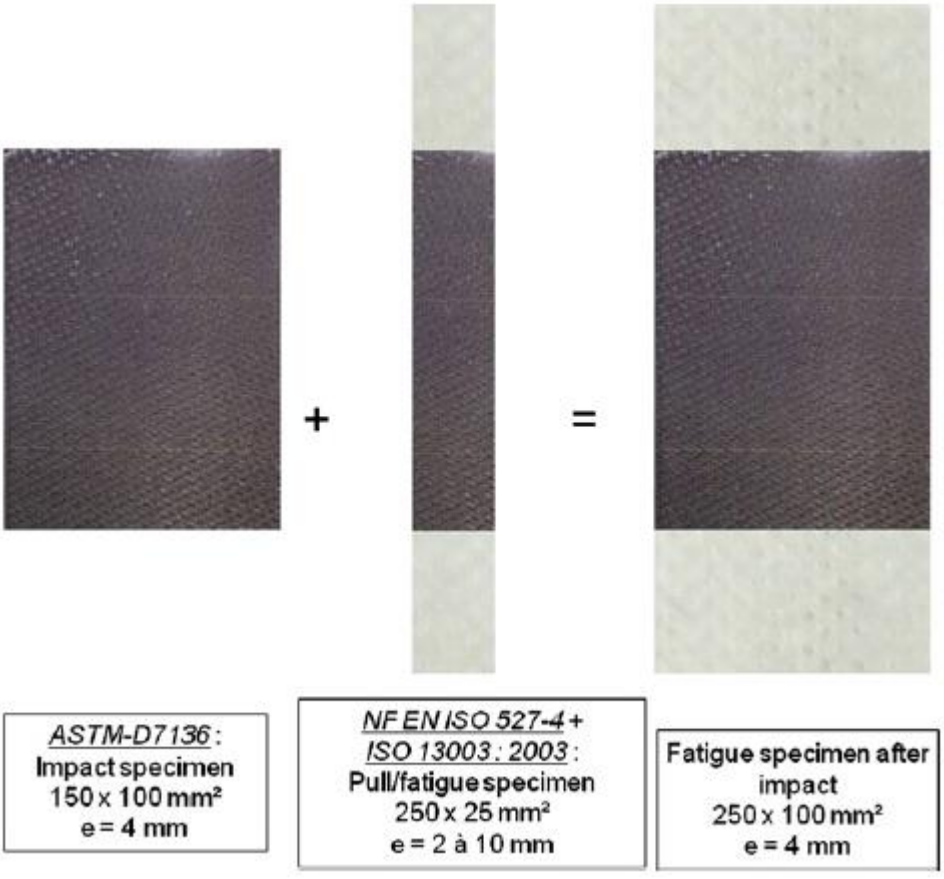

Figure 2-17 Illustration of combined FAI specimen dimensions, Garnier et al. (2013) added two aluminium gripping to the standard CAI testing sample to make it for tension-compression fatigue testing (Source: Garnier et al., 2013)

3 METHODOLOGY

3.1 Experimental Testing Methods

There were three sessions of tests in the experimental work: drop weight impact test, compression after impact, and post-impact fatigue test. The drop weight impact test was conducted within the ASTM 7136 framework to introduce the initial impact damage to the testing sample. Subsequent compression after impact test, per the ASTM 7137, would provide the residual compressive strength of the samples impacted by different energies. The resultant nominal residual strength will provide a reference to the following post-impact fatigue test. During the fatigue testing, samples impacted by the same energy were loaded with a different fraction of the residual strength obtained from the CAI test and more tests were carried out with different energy groups.

3.1.1 Drop Weight Impact Test

Low-velocity drop weight impact testing was performed to introduce the initial damage to the laminate and simulate the scenario of potential LVI damage during service life.

Impact testing is achieved by dropping an impactor with variable mass along a guided carriage to strike onto a specimen sitting below, which ensures the striking point is located at the centre of each specimen and the identical impact condition for the specimen was maintained. The immediate application of two “second strike” catchers is triggered by the optical switch once the first strike is applied to prevent the multiple strikes from rebounding on the same specimen. Impact force is collected from a force transducer placed between the mass object and the striker. Velocity prior to the impact was also recorded, triggered by the optical switch. All the collectable data are recorded and transferred to the controlling software package on the computer console.

The impact testing was performed using a Rosand Instrumented Falling Weight Impacting Tester – Type 5 in building 57 of Cranfield University (Figure 3-1).

The impact machine was controlled by the console software Rosand Precision Limited Instrumented Falling Weight (version 1.11p). The various levels of impact energy were achieved by inputting the desired energy level. The control console software worked out the appropriate height based on the mass of the impactor head and set the impactor to the height of the required impact energy.

The testing was conducted under the framework of ASTM standard D7136 - *Standard Test Method for Measuring the Damage Resistance of a Fiber-Reinforced Polymer Matrix Composite to a Drop-Weight Impact Event,* which allows a direct comparison to previous results.

A 16-mm hemispherical impactor was selected to comply with the standard's requirement of LVI. The impactor had a mass of 0.251 kg, and the mass object weighed 2.281 kg, making the total dropping weight 2.531 kg. The dropping mass allows the impact velocity to remain within the region of LVI for the impact energy level required for this test. Test samples were placed below the impactor and placed onto a wooden and steel mounting base that had a 125 mm × 75 mm window. Two rubber head clamps located at each long lateral sides of the test sample ensured the stability of the sample.

A sweep time of 10 ms was set for the whole impact response behaviour; 4000 checkpoints were mapped within the 10-ms sweep, obtaining a record of response data per 2.5 microseconds.

After the tests, the data were examined, and the samples were scanned using ultrasonic inspection.

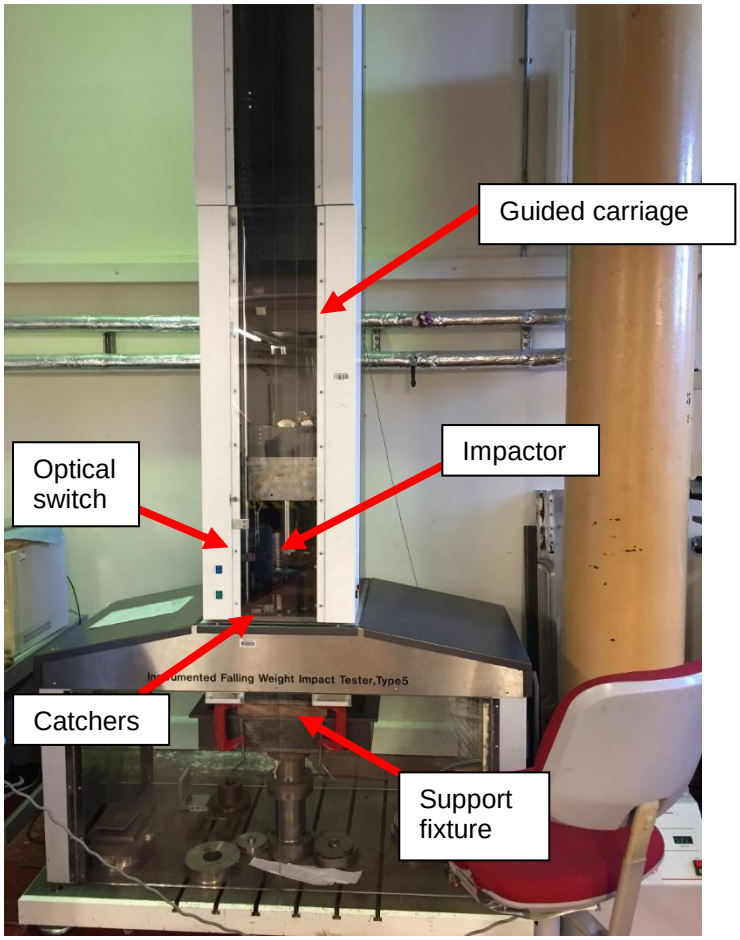

Figure 3-1 Rosand Instrumented Falling Weight Impact Tester – Type 5

3.1.2 Compression after Impact Test

The subsequent uniaxial compression test aimed to give the benchmark of the residual compressive strength of the impacted specimen. The test method used for CAI investigation was ASTM D7137 Standard - *Test Method for Compressive Residual Strength Properties of Damaged Polymer Matrix Composite Plates*. This standard applies to artificially impacted CFRP composites under uniaxial compressive load using a stable fixture.

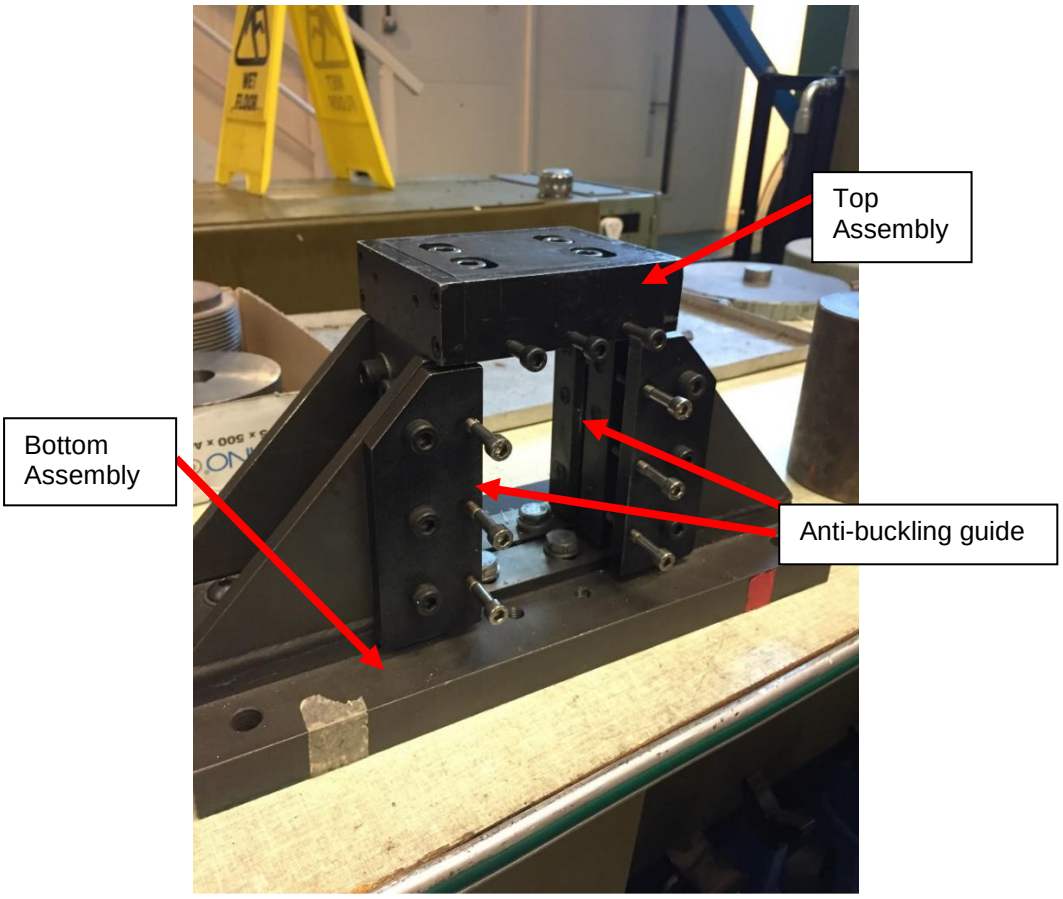

Figure 3-2 Compression after impact (CAI) fixture comply with standard

The fixture was designed to reduce the eccentric loading condition and overall bending during the test. The fixture consists two parts: top assembly and base assembly (see Figure 3-2). The top assembly restrains the displacement in directions other than the loading direction and the all clamped slot at the bottom of the jig to restrain the movement from all degree of freedom. The application of two edge slots along the long side of the specimen prevents premature failure and global buckling failure.

The testing involved an Avery 600 kN load system (Figure 3-3) provided in the mechanical testing lab in Building 83 of Cranfield University. The compressive displacement was added at a gentle pace at 0.05 mm/s. The controlling console software recorded load response and displacement.

During the compression testing, the pre-treated test panel was placed in the CAI fixture. The loading cell started from the contact point to the top assembly. The trigger value for the automatic stop was controlled by 3 mm in displacement which

is just below the gap distance. The compression started at the designated slow pace, and the session stopped when the displacement value was triggered. Load and displacement data were recorded at the same rate at which the displacement progressed. The whole process was also recorded by DIC for the displacement and strain.

Of note, the overall alignment and the clearance between the knife edge of the anti-buckling guide and the specimen should be carefully examined and maintained to ensure a valid failure rupture in the mid-section of the specimen and prevent invalid premature failure.

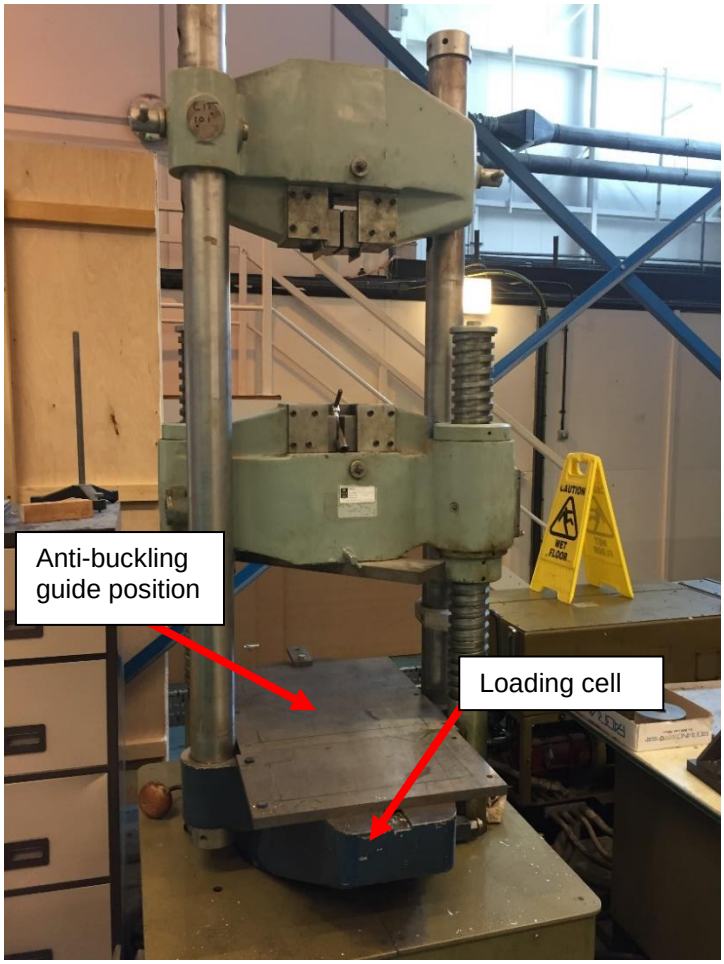

Figure 3-3 Avery 600-kN servo-hydraulic test machine

3.1.3 Post-impact Fatigue Test

Fatigue testing was performed using an Instron 8800 250-kN servo-hydraulic system. There is currently no published testing standard for post-impact fatigue

testing. It was found the current CAI fixture is useful for simulating the condition of an impacted panel in a real situation (e.g. a fuselage skin panel impacted by a dropped toolbox). The CAI jig was firstly designed for static compression testing. To apply the cyclic load to the CAI jig, two loading heads were manufactured to fit the CAI jig to the fatigue test machine.

Thus, a top and a head were designed and machined. Top loading head was designed into one piece including the gripping and the loading block to allow the smooth load transition and the bottom loading head consisted two parts: a bottom supporting plate and a grip with threads. Two parts from the bottom loading head were assembled using a threaded connection.

The diameter of both grip cylinders was 36 mm, based on the requirement of the machine-gripping mechanism. The size of the bottom-supporting plate was the same as the bottom plate of the bottom assembly of the CAI fixture, measuring 350 (L) × 150 (W) × 30 mm (D). An M20 through-drill was used with a thread placed in the middle of the plate for fitting the gripping cylinder. Four M10 through drills were placed near four corners for fastening the bottom plate to the CAI fixture. The top side loading grip had the same contact surface area as the top assembly. The outskirt of the CAI fixture top assembly measured 122 (L) × 97 (W) × 34 mm (D).

The depth of the block of the top loading head is vital since it determines the uniformity of the load distribution from the loading machine to the specimen. The effective depth should be reduced to 26 mm since there is an 8-mm clamping block inside the cap from the CAI jig. A subsequent numerical simulation was carried out in ABAQUS using the schematic work of the top side loading grip (see Figure 3-4) to determine the depth of the object.

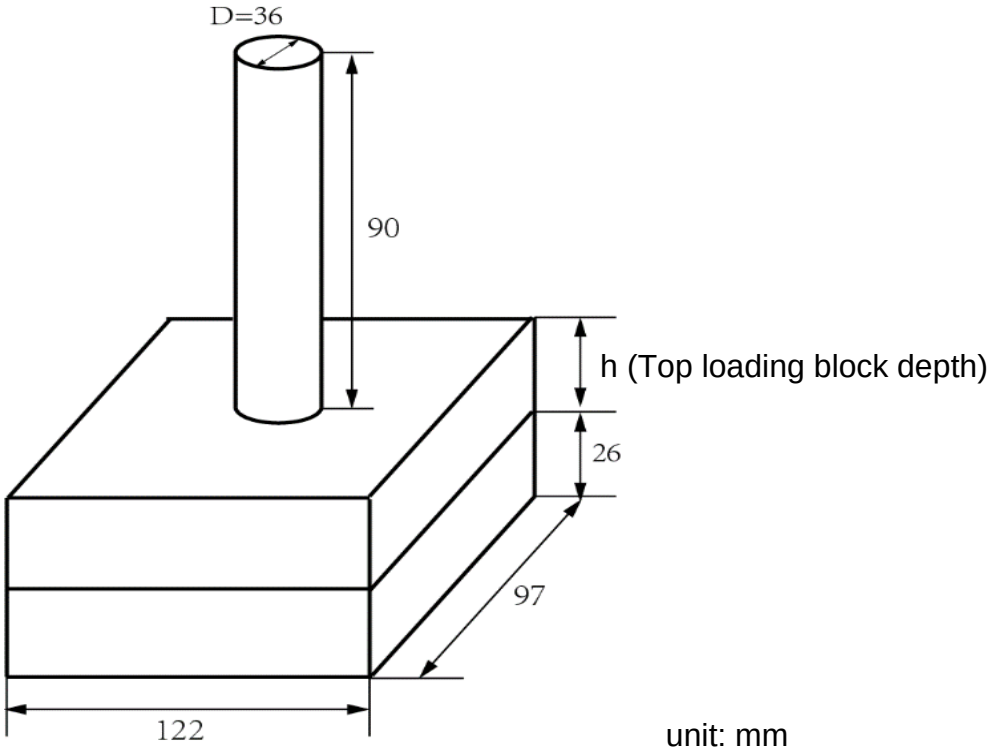

Figure 3-4 Schematic of loading grip contact of loading cell and the top assembly of CAI fixture, the dimensions were showed in the figure above while the top loading block depth *h* is the parameter to be determined

The reaction force cloud graph is shown in Figure 3-5. The evenness of the distribution of reaction force is proportional to the increase in object thickness. To avoid the distraction from the edge effect, four elements on each side of the central line were omitted in the calculation of the deviation. The results are tabulated in Table 3-1. In general, the coefficient of variation (CV) is negatively correlated with the increase in thickness but is always affected by the influence of the edge effect. The force deviation was smaller for *h* = 80 mm than for *h* = 60 mm in the central range, but with higher singular value on the side; the case of h = 80 mm achieved a higher CV. However, the *h* = 60 mm case had already obtained a low CV. With a relatively low CV and the need for using materials economically, *h* = 60 mm was chosen to be the thickness of the top loading block.

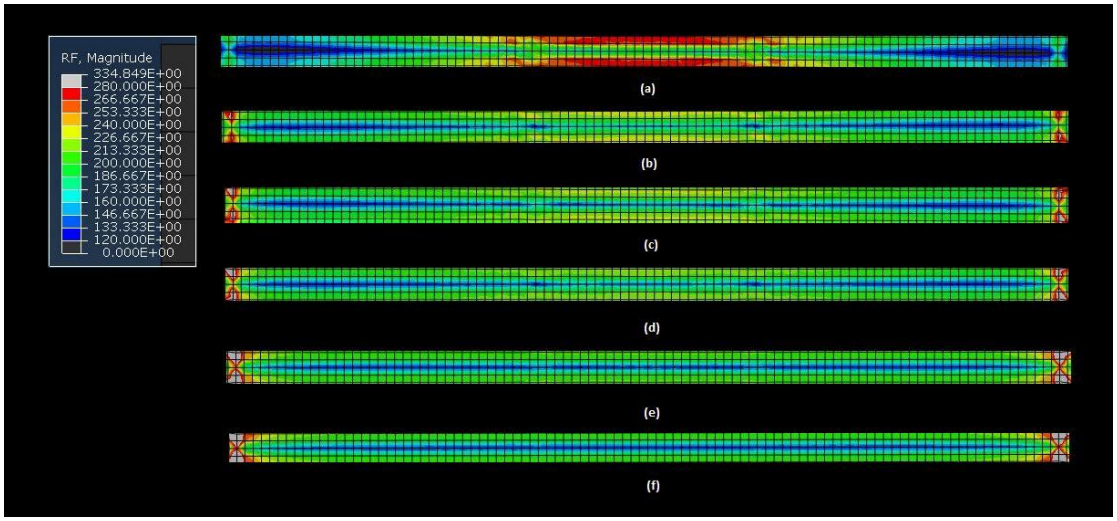

Figure 3-5 Stress distribution of reaction force on the specimen top surface when loading block depth (a) *h* = 20 mm, (b) *h* = 36 mm, (c) *h* = 40 mm, (d) *h* = 44 mm, (e) *h* = 60 mm, and (f) *h* = 80 mm

Table 3-1 Compairson of average stress, standard deviation and coefficient of variation with different block depth

Loading Block Depth *h* (mm)	Average Stress (MPa)	Standard Deviation	Coefficient of Variation
20	138.9	24.8	17.82%
36	138.1	13.5	9.74%
40	134.2	7.6	5.64%
44	136.4	8.2	6.01%
60	133.0	3.8	2.86%
80	132.8	4.8	3.62%

Before fatigue testing, the samples were impacted at the same energy levels as used previously and then subjected to in-plane compression-compression fatigue loading. The ratio of maximum compressive stress to initial static CAI strength ranged between 0.7 and 0.8. Test frequency was limited to 5 Hz to avoid thermal heating, and the R ratio was 10 for all fatigue tests. The test was interrupted at intervals for ultrasonic and DIC measurements. The experimental setting is shown in Figure 3-6.

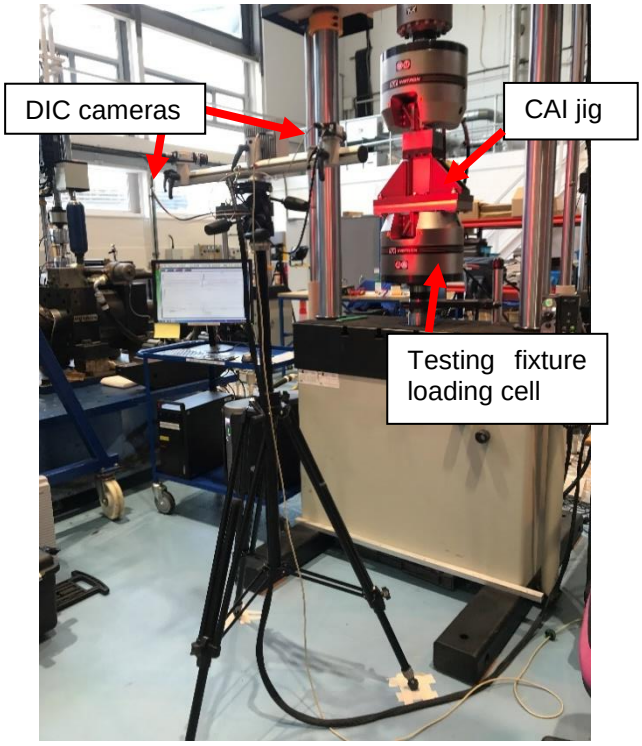

Figure 3-6 Specimen, fixture, testing rig, and DIC equipment used for fatigue testing

3.2 Non-destructive Test Method

During and after the test, a few non-destructive test methods were employed to collect the data. A coordinate measuring machine was used to measure the dent depth after the drop weight impact test. Phased array ultrasonics equipment provided the overall internal delamination size of the sample, before and during the fatigue session. The DIC equipment could collect important information about on-surface displacement and strain during both static and fatigue test.

3.2.1 Coordinate Measuring Machine (CMM) surface measurement

A Renishaw Cyclone Series 2, touch-trigger probe CMM machine, was used to evaluate the hemispherical dent depth introduced by the LVI. The probe comes in contact with the object surface and transfers the x-, y- and z-coordinate data points to the controlling software. Each collection point was 1 mm ×1 mm in the x- and y-axis and the probe could achieve a ±1-μm accuracy in the z-direction.

The scanning area for each specimen was 90 × 140 mm, which was sufficient to contain the central deformation introduced by the impact. The result was saved as IGES data, consisting of the X, Y, and Z coordinates of each scan point. The data file was then imported to CATIA to extract the data on dent depth.

3.2.2 Phased Array Ultrasonics

Ultrasound is commonly used for non-destructive testing (NDT); the principal is based on comparing the received sound signal with the emitted one to detect the discontinuity inside the material. Traditional ultrasonic detectors usually use one active element which both emits and receives high-frequency sound signals or sometimes uses a pair of elements, which will take the outgoing and ingoing work separately.

Phased array probes, however, are made up of a large transducer assembly, usually varying from 16 to 256 small individual elements that can each be pulsed separately. The arrangement of elements can be found in various shapes such as strip (linear array), ring (annular array), circular matrix (circular array), or sometimes a more complex shape. Figure 3-7 shows a strip element layout. Just like conventional transducers, frequencies usually range between 2 to 10 MHz. Since the multiphase array system needs more elements, a computer-like equipment is a necessary to help deal with the echo. Unlike conventional flaw detectors, phased array systems can sweep a sound beam through a range of refracted angles, along a linear path, or dynamically focus at different depths, thus increasing both the flexibility and capability of inspection setups.

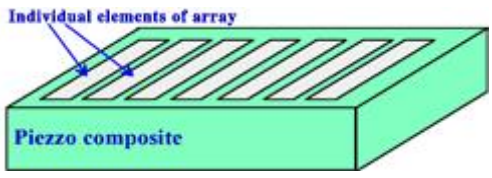

Figure 3-7 Typical multi-element construction

NDT of the testing samples involved the use of a multiphase ultrasonic system Sonatest Veo 16:64 (see Figure 3-8). The 5-MHz probe consists of 64 groups of

transducers, which enable the system to inspect the sample in various scans. C-scan data were processed to show the delamination inside the panel. A 15-db gain was set to obtain an optimal scan result. Three washers were placed under the sample for support as well as for reference points to ensure the sound signal travelled through the sample.

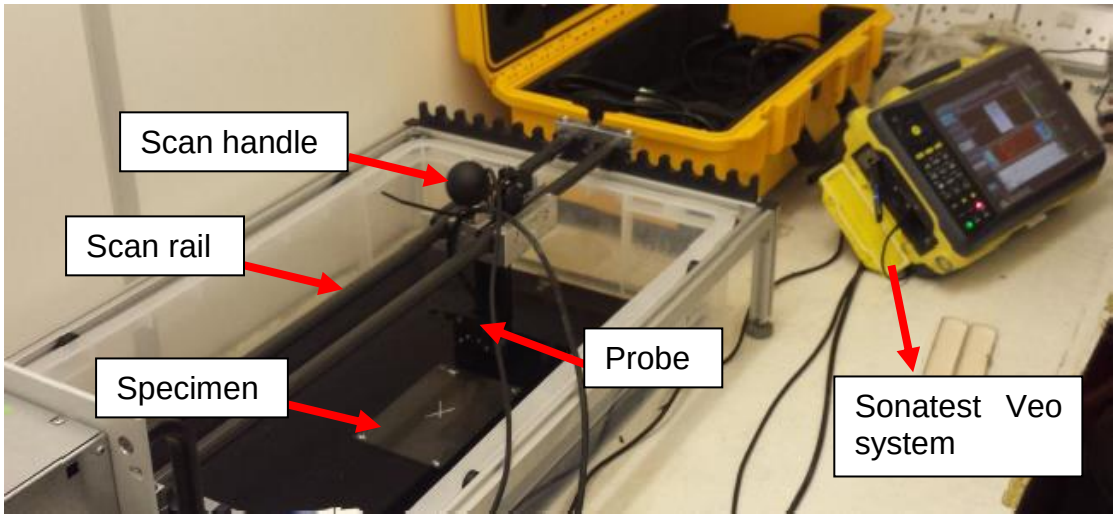

Figure 3-8 Multi-phased ultrasonics system of Sonatest Veo 16:64

A typical scan image is shown in Figure 3-9. With the multiphase array, several types of scans can be obtained and plotted in one scan process. In this stage of data processing, only A-scan and C-scan were used to obtain the projected delamination area of each sample. The signal gate indicates the threshold for the signal to be plotted. A higher gate will result in less information, and a lower gate will cramp the screen with all the signals, making the damage inaccurate and indistinguishable. The gate chosen for each sample was based on the clear contour of three washers that were set as reference points.

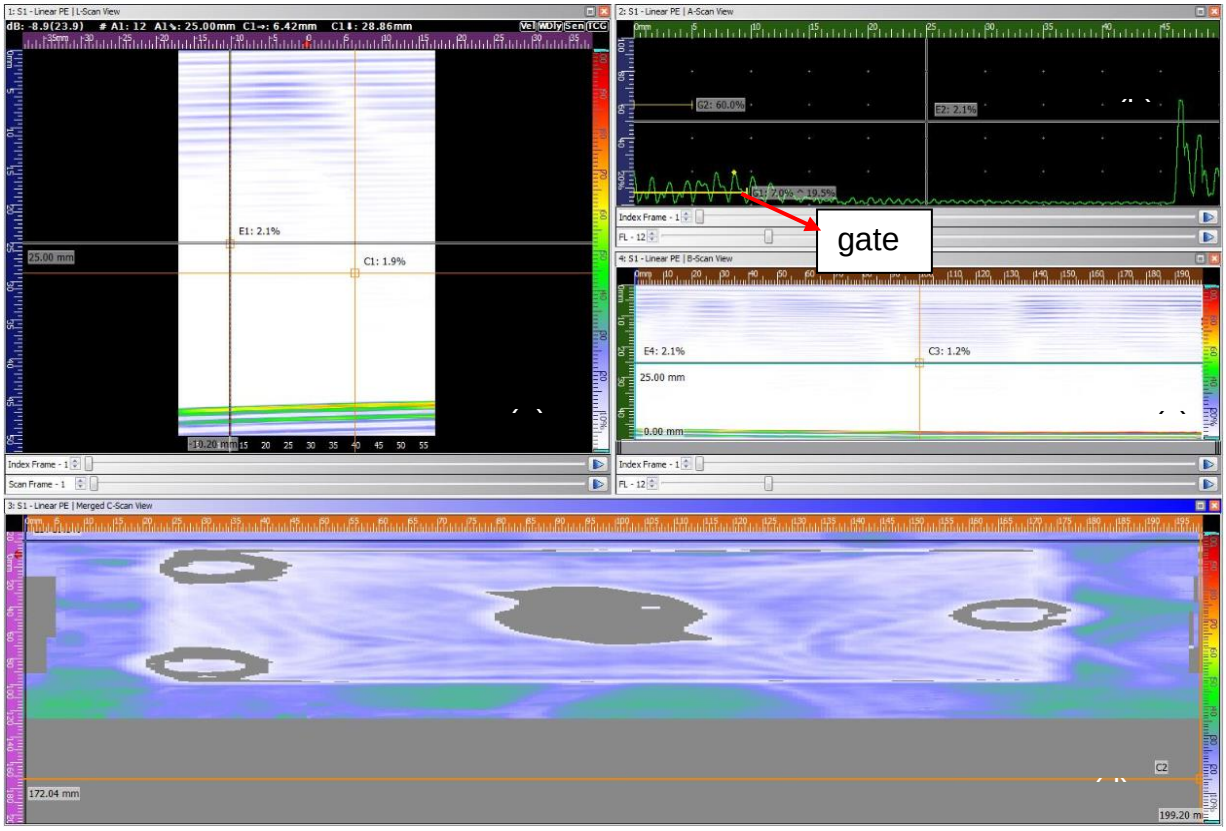

Figure 3-9 Scan result for sample Q5 (20 J) using Veo 16:64 (a) L-scan, (b) A-scan, (c) B-scan, (d) merged C-scan

3.2.3 Delamination Size Measurement

Each specimen was scanned under phased array ultrasonics after impact and at the fatigue checkpoint. The merged C-scan images were imported to ImageJ (by Wayne Rashand, National Institute of Health, USA) for the pixel level measurement of the detected delamination area. ImageJ is a software that can measure the pixel number of a designated area. The panel size was measured with a rectangular shape based on the ruler in both vertical and horizontal directions provided in the Sonatest Viewer package to ensure accuracy. The detected delamination area can be selected by the polygon option of ImageJ. The polygon catches the boundary of the central delaminated area. The pixel number was exported from the software. The delamination area was calculated using the ratio of delamination pixels to whole panel pixels and multiplying by the surface area of the specimen (15000 mm^2). An example of the delamination measurement is illustrated below (see Figure 3-10).

Delamination length in vertical and horizontal directions can be directly measured using the built-in “free head” ruler in the Sonatest Viewer software.

Of note, certain criteria were applied to maintain the quality of delamination detection: (a) the filter gate is set to 20% of the highest response signal intensity and (b) the outline of the washer underneath should be recognisable.

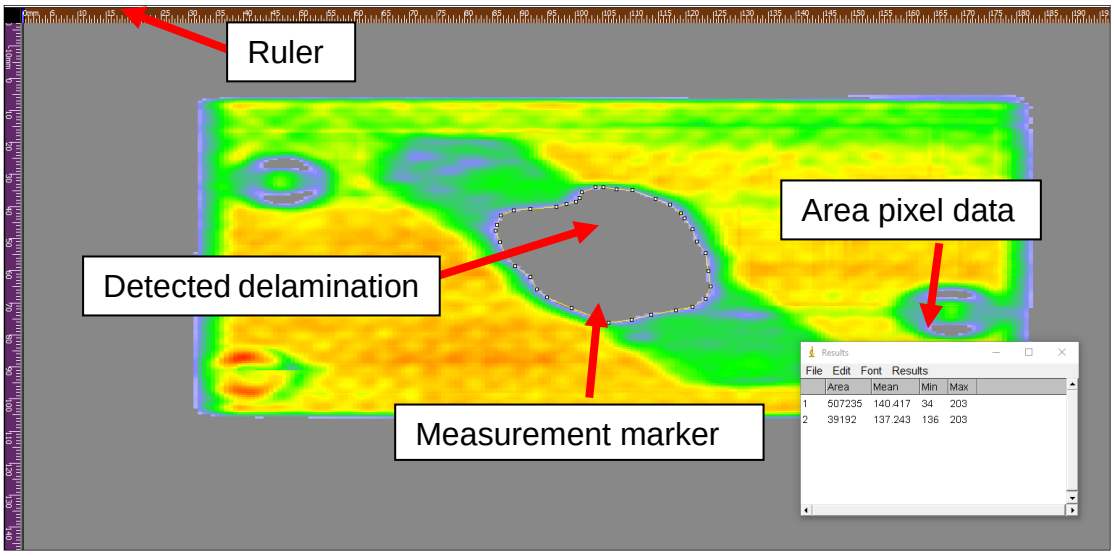

Figure 3-10 Example of C-scan image of Q15-3 at 3000 cycles and delamination area measurement

3.2.4 Digital Image Correlation

DIC techniques are attracting more interest given their relative simplicity on micro- and nano-scale mechanical testing applications. The rapid development of the camera industry is also boosting its popularity. DIC and tracking is an optical method that employs tracking and image registration techniques for accurate 2D and 3D measurements of changes in images to obtain parameters like displacement and strain.

Concisely, in a DIC system, an image taken at a load step (acting as a reference step) is compared with an image captured subsequently. The visual features (certain greyscale patterns) are recognised and found in the new deformed target image using advanced pixel recognition and interpolation software (see Figure 3-11). This enables translational and rotational displacement to be calculated so that a full field map of strain and displacement data can be generated. Exact pixel

recognition and interpolation algorithms are typically derived from displacement mapping methods and can vary between DIC systems.

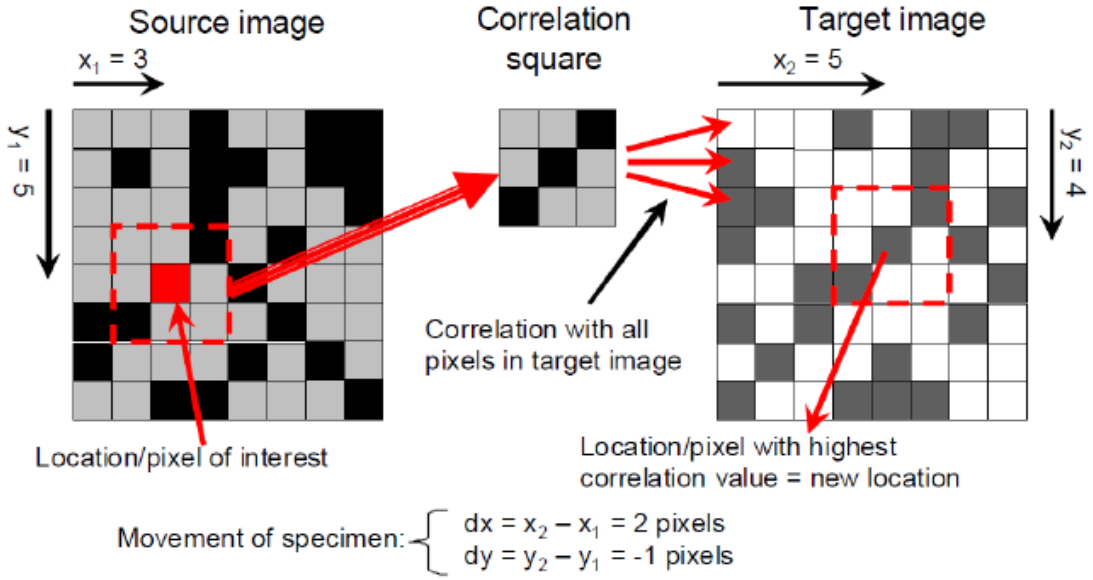

Figure 3-11 Illustration of DIC mechanism

The principle that DIC is based on is the maximisation of a correlation coefficient that is determined by examining pixel intensity array subsets on two or more corresponding images and extracting the deformation mapping function that correlates the images (see Figure 3-12) (Reu, 2012).

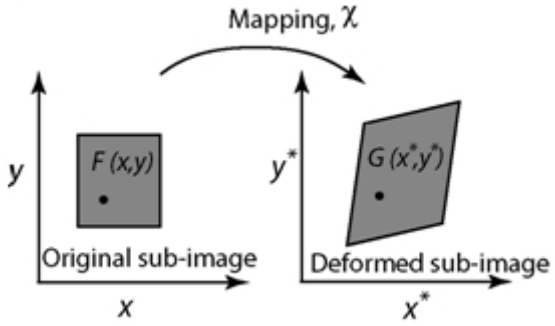

Figure 3-12 Basic concept of digital image correlation

The cross-correlation coefficient r_{ij} is defined as

$$r_{ij}\left(u, v, \frac{\partial u}{\partial x}, \frac{\partial u}{\partial y}, \frac{\partial v}{\partial x}, \frac{\partial v}{\partial y}\right) = 1 - \frac{\sum_i \sum_j [F(x_i, y_i) - \bar{F}][G(x_i^*, y_i^*) - \bar{G}]}{\sqrt{\sum_i \sum_j [F(x_i, y_i) - \bar{F}]^2 \sum_i \sum_j [G(x_i^*, y_i^*) - \bar{G}]^2}} \quad \textbf{(3-1)}$$

Where $F(x_i, y_j)$ is the pixel intensity or the grey scale value at a point (x_i, y_j) in the undeformed image; $G(x_{i*}, y_{j*})$ is the grey scale value at a point (x_{i*}, y_{j*}) in the deformed image; and $\bar{F}$ and $\bar{G}$ are mean values of the intensity matrices F and G, respectively. The coordinates or grid points (x_i, y_j) and (x_i^*, y_j^*) are related by the deformation that occurs between the two images. If the motion is perpendicular to the optical axis of the camera, then the relation between (x_i, y_j) and (x_i^*, y_j^*) can be estimated by a 2D affine transformation such as in equation (3-2) and (3-3):

$$x^* = x + u + \frac{\partial u}{\partial x}\Delta x + \frac{\partial u}{\partial y}\Delta y \quad \textbf{(3-2)}$$

$$y^* = y + v + \frac{\partial v}{\partial x}\Delta x + \frac{\partial v}{\partial y}\Delta y \quad \textbf{(3-3)}$$

Here, u and v are translations of the centre of the sub-image in the x- and y-directions, respectively. The distances from the centre of the sub-image to the point (x, y) are denoted by Δx and Δy.

The Dantec Q400 DIC system was used during static and fatigue tests. The DIC system is capable of 2D and 3D image data analysis. The whole DIC system consists of following major parts: two charged-coupled devices (CCD) digital cameras, monochromatic direct current light, light control box, buffering and data collection box, and control software Istra4D. Two CCD cameras were mounted on the crossbar of a tripod with the DC light placed in the middle. The light was cabled to the lightbox which enabled the tuning of the brightness of the light. Cameras were connected to the buffering and data collection box, which was connected to the controlling laptop. Two analogue input cables were connected between the testing machine and the buffering and data collection box for the load and displacement input. The DIC system control and data processing were carried out using the Istra4D software.

Q400 DIC system was positioned in front of the test machine. The view of specimen and lenses needs to be obstacle free. Some adjustments were made to rotate the two cameras facing angle towards the specimen and to change the height of the cameras. When the specimen was captured inside the region of interest (ROI), it had to ideally be positioned at the centre area of the ROI, and

the lighting condition needed to be tuned to achieve a non-reflection, focused image by changing the aperture and focus of the two lenses. These requirements were important as the surface within the ROI was recognised and differentiated into a subset of pixels. High reflection can cause inability of recognition, resulting a loss of information in certain areas. Calibration was done using the calibration target provide by Dantec and auto-calibration facility in the Istra4D software using a minimum of 12 images of the calibration target in different orientations. The purpose of calibration is the input of different deformation shapes of sub-images and to set guidelines of deformation using the built-in algorithms under the current lighting and focus conditions. The speed of image capturing was set to 100 ms (10 Hz) to ensure a through capture of the static progression and at least 10 images within 1 fatigue cycle to capture the peak and trough load.

3.2.5 Stiffness reduction measurement during fatigue

Stiffness degradation is another index to unveil the fatigue progression. The stiffness degradation of a sample at certain cycle under fatigue loading is determined by calculating the ratio of load range to displacement range within a loading half cycle.

Mathematically,

$$K = \frac{\Delta F}{\Delta D} \quad \textbf{(3-4)}$$

where $\Delta D = D_{max} - D_{min}$ and $\Delta F = F_{max} - F_{min}$

K is the global stiffness of the specimen at a certain cycle; ΔF is the load range and is equal to the difference between maximum load (F_{max}) and minimum load (F_{min}) in a half fatigue cycle. ΔD is the difference between the maximum displacement (D_{max}) corresponding to maximum compressive load and minimum displacement (D_{min}) corresponding to minimum compressive load in a half fatigue cycle. The D_{max} and D_{min} are calculated from the difference in the values from two 80-mm gauges marked at the top and bottom edge of the DIC capture.

A schematic drawing for the stiffness calculation during a fatigue cycle is presented in Figure 3-13.

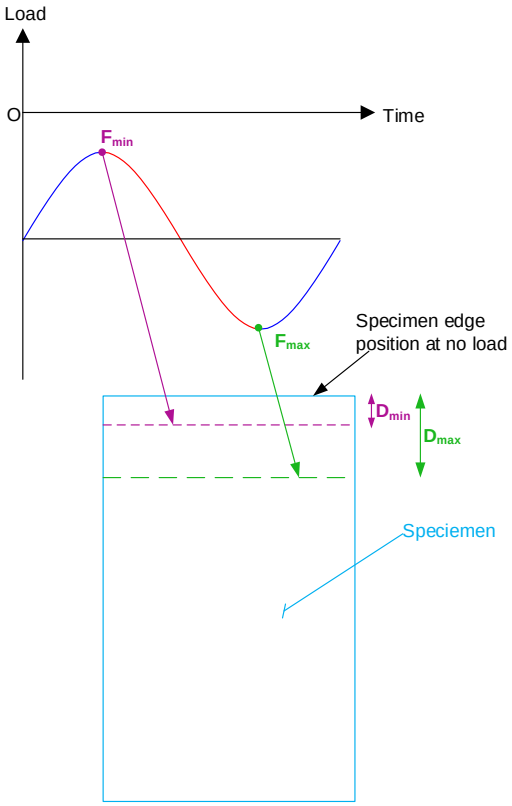

Figure 3-13 Schematic of global stiffness calculation during a fatigue cycle

3.3 Destructive Metallographic Sectioning Technique

Owing to the inability to distinguish the delamination discretely at every single interface, destructive sectioning work was carried out to observe the delamination morphology of fatigued samples to compare with the unfatigued and impacted samples in order to identify the fatigue delamination propagation.

The tested specimen was sectioned and examined under 10x zoom Nikon microscope and photographed with a JVC 3CCD integrated digital camera. The panel was sectioned horizontally and vertically into four 5 mm× 3 mm pieces. The sectioning method facilitated longitudinal and transversal observation of delamination and other flaws appeared on the section surface. The cut-off pieces were potted with resin. The potted specimen was then mounted on the grinder plate and ground several rounds with coarse grind paper and a fine one. The purpose of the polishing was to eliminate the coarse cutting marks and avoid

confusion from those marks during microspore observation. Figure 3-14 shows the setting for specimen polishing.

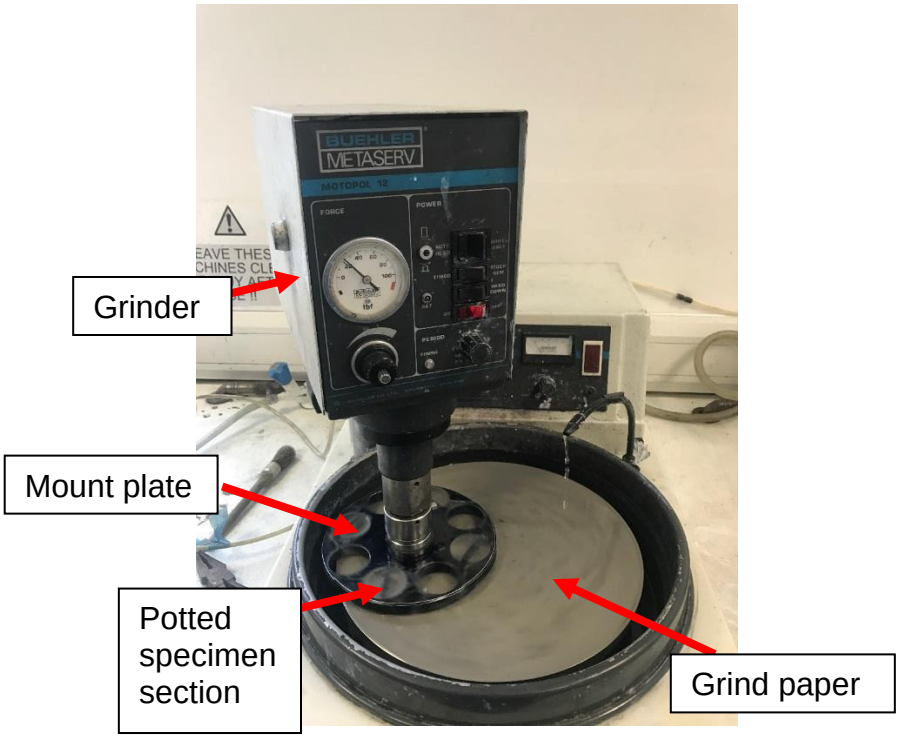

Figure 3-14 Illustration of specimen polish

A microscope fitted with a digital camera was used to produce multiple, small digital images of the finished sections. The 3 x 3 mm images were then stitched together and arranged in the correct sequence to produce a composite image (see Figure 3-15), providing a high-resolution photographic view through the section of the damaged laminate. The final results allowed identification of individual delaminations and evaluation of which interface delaminated the most and what happens when the buckling mode changes during fatigue cycles.

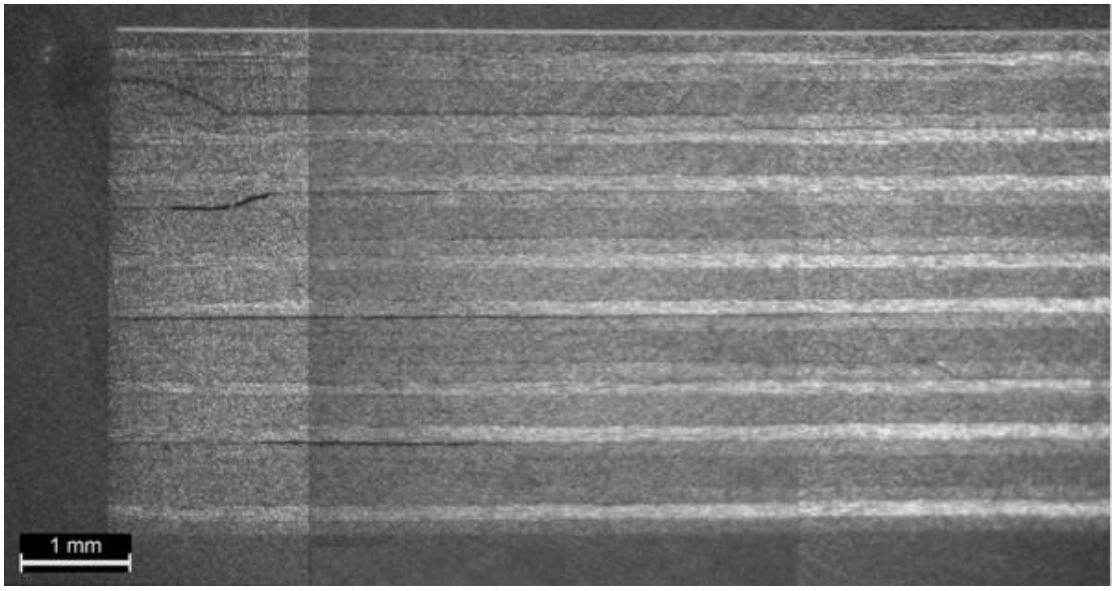

Figure 3-15 Example of metallographic sectioning observation of a sample under 10-J impact

3.4 Virtual Crack Closure Technique

As mentioned in chapter 2, the SERR played an important role in the delamination propagation in composites; it is necessary to conduct some numerical analysis to check the SERR values at the delamination front at different scenarios.

Two methods are widely used for delamination propagation: virtual crack closure technique (VCCT) and cohesive zone method. The former was selected for application in this project owing to its high efficiency in computational time and direct output of SERR values.

VCCT is a method used to calculate the SERR. The VCCT assumes that the energy required for crack extension is the same as the energy used to close the same crack extension and, the growth of the crack does not change the state at the crack tip considerably (Kruger, 2004). Figure 3-16 illustrates the technique.

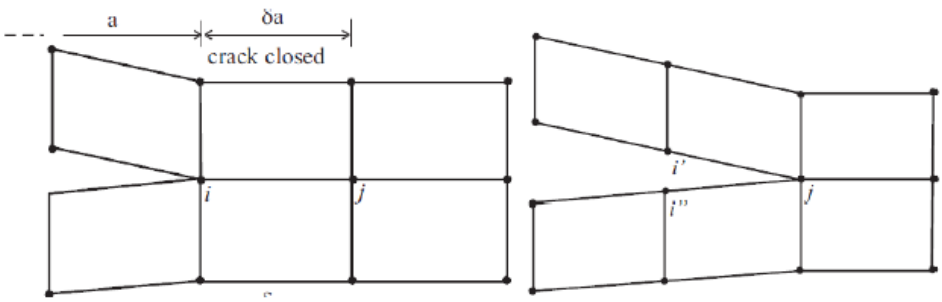

Figure 3-16 Principle of VCCT (Source: Kruger, 2004)

Linear elastic fracture mechanics (LEFM) is often applied to model the delamination growth in a composite. The delamination can be treated as a crack and the growth of the crack can be treated as delamination propagation (Kruger, 2004).

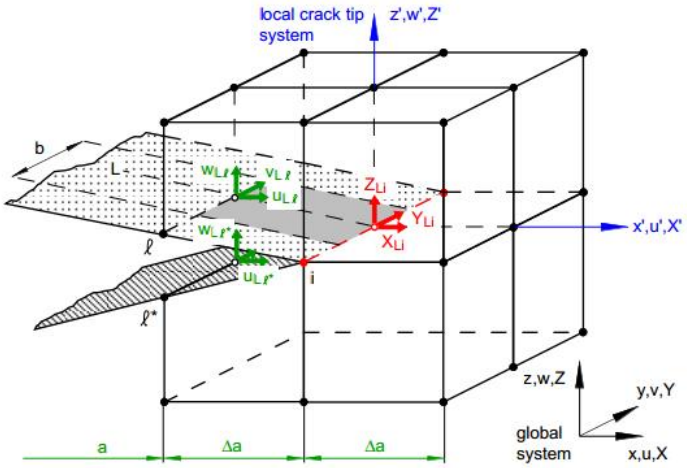

Figure 3-17 Virtual crack closure technique for four-node plate/shell and eight-node solid elements (Source: Krueger, 2004)

The calculation of SERR with VCCT uses the force of the crack tip times the displacement of previous nodes. Krueger (2004) gives the calculation of three modes of SERR by equations (3-5) to (3-7):

$$G_I = -\frac{1}{2\Delta A} Z_{Li}(w_{Ll} - w_{Ll*}) \tag{3-5}$$

$$G_{II} = -\frac{1}{2\Delta A} X_{Li}(u_{Ll} - u_{Ll*}) \tag{3-6}$$

$$G_{III} = -\frac{1}{2\Delta A} Y_{Li}(v_{Ll} - v_{Ll*}) \quad \textbf{(3-7)}$$

with $\Delta A = \Delta a b$ as shown in Figure 3.17. Δa is the length of the elements at the delamination front, and b is the width of the elements., X_{Li}, Y_{Li}, and Z_{Li} detonate the force in x, y, and z directions; w, u, and v represent the displacement shown in Figure 3-17.

It is accepted when *G* is larger than the total critical threshold value G_{TC}, the crack will propagate. G_{TC} is the mixed mode derived from three modes of *G*. The three mixed-mode criteria available in ABAQUS are the Power law (Wu and Reuter Jr, 1965), the BK law (Benzeggagh and Kenane, 1996), and the Reeder law (Reeder et al., 2002). For instance, Benzeggagh and Kenane (1996) established the criterion for two dimensional analysis, which is popularly known as BK law. The fracture criterion as per the BK law is given in equation (3-8).

$$G_{IC} + (G_{IIC} - G_{IC}) \left(\frac{G_{II}}{G_I + G_{II}} \right)^{\eta} = G_{TC} \quad \textbf{(3-8)}$$

To determine the SERR of the crack front, VCCT is essential in this project.

4 EXPERIMENTAL TESTING SETUP

4.1 Material and Specimen Fabrication

4.1.1 Material Type and Properties

The specimen was made from HexPly AS7/8552 prepreg provided by Hexcel. The pre-impregnated unidirectional carbon made of 12K AS7 fibre has a nominal thickness of 0.135 mm. The impregnated resin is 8552, indicating good toughness. This material has been used in modern aircraft structures such as the A350 XWB engine nacelles 54, Tupolev TU-204 SM Longerons, and other primary structures. The material properties are listed in Table 4-1

Table 4-1 Lamina Properties of AS7/8552 (source: Hexply 8552 datasheet)

Properties	Value
Longitudinal Modulus E_1	145 GPa
Transverse Modulus E_2	10 GPa
Poisson's Ratio v_{12}	0.3
Shear Strength G_{12}	5.8 GPa
Ply Thickness t_{ply}	0.135 mm
Longitudinal Tensile Strength 0°	2550 MPa
Transverse Tensile Strength 90°	90 MPa
Longitudinal Compression Strength 0°	1862 MPa
Transverse Compression Strength	180 MPa
In-Plane Shear Strength	115 MPa

4.1.2 Stacking Sequence

The specimens are manufactured with two different layups: QI and CP. The QI layup specimen consists of 32 plies with a stacking sequence of $[(45/0/-45/90)_s]_4$. The QI layup has an equal portion of fibre direction, providing a balanced performance in both vertical and transversal directions. The CP specimen only consisted of 0° and 90° fibres, which may have resulted in a higher compressive strength in both vertical and transversal directions. The stacking sequence was $[0/90]_{8s}$.

4.1.3 Layup

The raw material roll was measured and cut into a large square measuring 600 × 600 mm, based on the original width of the roll. The squares were cut for 0° and 90° layups. For 45° and - 45° layers, a parallelogram of the bottom angle of 45° was adapted to achieve the best use of the material. The layup should be mirrored to the central line to avoid generating a B matrix causing in-plane bending. For every four layers, a de-bulked step lasting for 15 minutes was applied to get rid of the void between the layers. Continuous debulking was carried out for 8-ply, 16-ply laminates, and the final 32-ply laminate.

4.1.4 Curing

Curing was carried out in the autoclave in the composite laboratory at Cranfield. The laminate was cured upon an aluminium base plate and pre-treated with mould release. A vacuum bag was applied to the base plate to provide negative pressure to the laminate before the autoclave pressure could reach the required level. The laminate was cured as per the instructions from the Hexcel 8552 resin datasheet. Some key stages were as follows:

- Inside ambient temperature was raised at the rate of 2°C/minute to 107°C.
- The temperature was kept steady at 107°C for 30–60 mins to maintain the resin viscosity prior to application of the autoclave pressure, minimising the void content of the final laminate.
- The pressure was then raised to about 6 bars.
- The autoclave temperature was raised to 170°C while holding the pressure.
- The laminate was cured at the above temperature and pressure for two hours.
- The ambient temperature was reduced at a rate of 2°C/minute to 65°C and keep ventilation. The finished laminate was taken out from the vacuum bag.

The de-bulked panel was placed in an autoclave for curing. The panel was placed and a metal plate of the same dimension was placed on it for application of uniform load during curing. The curing temperature was controlled as per the

prepreg manufacturer instructions to ensure optimum strength of the composite panel. The autoclave setup and curing temperature and pressure control are presented in Figure 4-1(a) and (b), respectively.

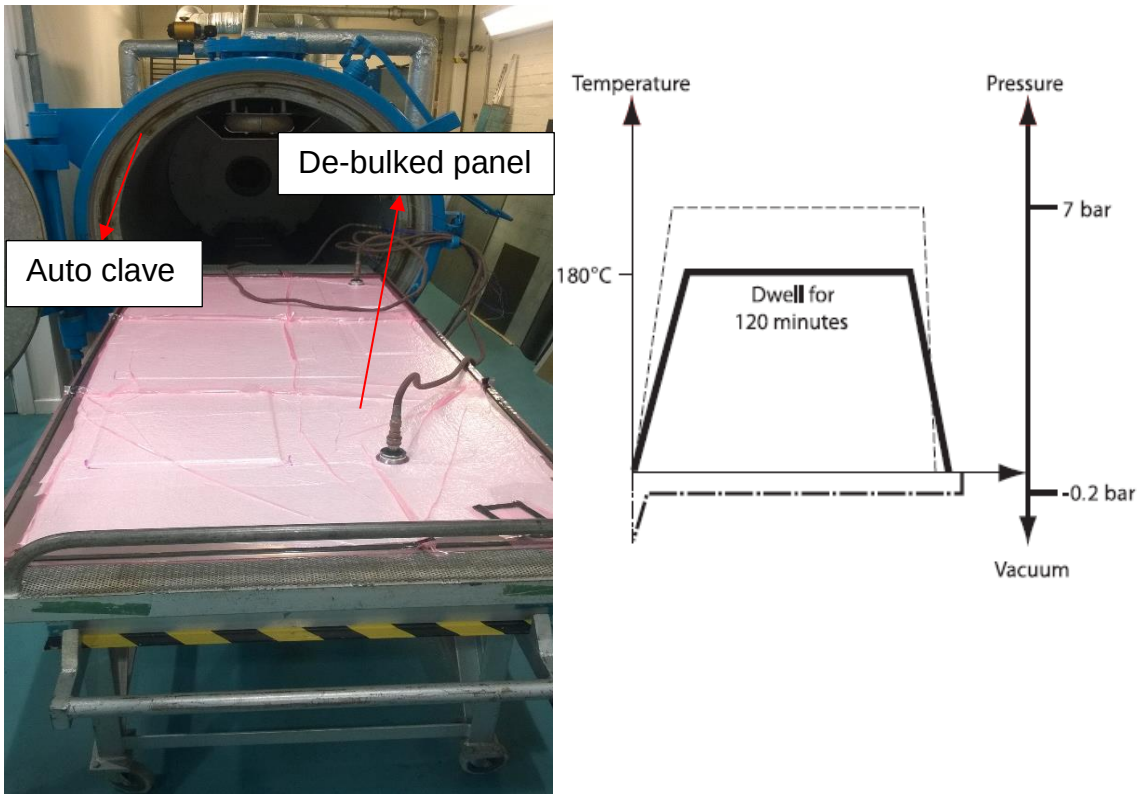

(a) **(b)**

Figure 4-1 (a) Illustration of autoclave and debulked panel; (b) Curing temperature and press control graph

4.1.5 Quality Check for Specimen Dimensions and Properties

Samples were cut from the cured laminate plate. The size of each specimen was precisely 150 (L) × 100 mm (W). The nominal thickness of each specimen should be 4.32 mm. However, owing to the resin flow during curing, the thickness varied. The average thickness of CP specimens was 4.322 mm and 4.34mm for QI plates. After NDT scanning using the Sonatest Veo 16:64, no obvious defects were observed. The quality control of the curing was satisfactory.

The laminate properties for each layup are calculated using the classic laminate theory. The results are tabulated in Table 4-2.

Table 4-2 Laminate properties

Layup		QI	CP
Longitudinal Modulus	E_x	56.4 GPa	77.9 GPa
Transverse Modulus	E_y	56.4 GPa	77.9 GPa
Shear Modulus	G_{xy}	21.6 GPa	5.8 GPa
Poisson's Ratio	v_{xy}	0.305	0.04

4.2 Phased Array Ultrasonics

4.2.1 Settings for C-scan

The C-scan was conducted using the Sonatest® Veo 16_64 system. This device is powered by the Sonatest® UTStudio 3.2.5 software. After the placement of the specimen, the first scan was carried out to find the proper signal filter gate. The criterion is a clear definition of the outline of the aluminium washer beneath to ensure the sound signal has travelled through the whole plate as the accumulated delamination area is desired. After some trails and adjustments, it finally found a gate of 20% level, and a sound intensity of 15 dB gave the best result.

4.2.2 Verification of C-scan Accuracy

Verification was conducted to ensure the accuracy of the C-scan. The three pre-embedded PTFE films with a diameter of 50 mm were fabricated for a student's work (Pramond, 2016). The three films can be detected under the C-scan.

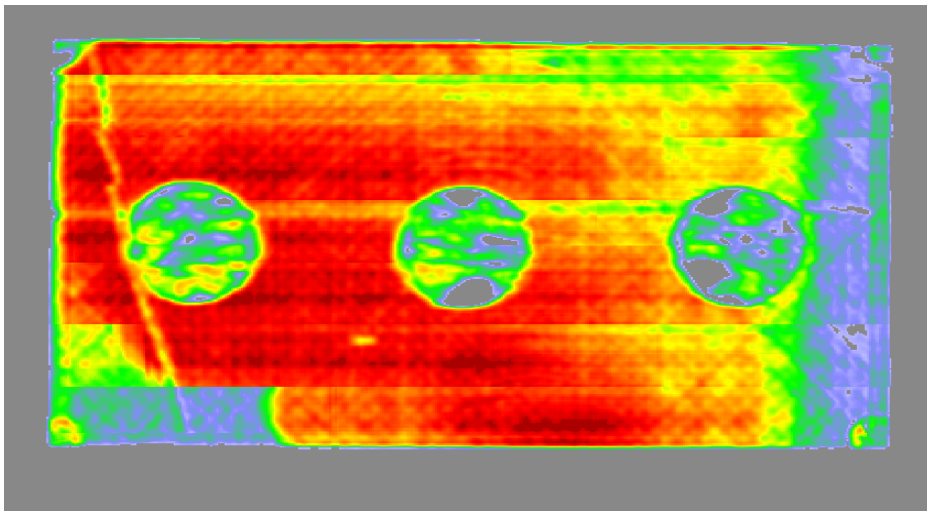

Figure 4-2 Detection of pre-embedded PTFE film

The measurement of the diameter of each circular film using the internal ruler tool provided by the software is shown in Figure 4-2. Two measurements were taken horizontally and vertically for each film. The obtained results are listed in Table 4-3. The results showed good detection with relatively high accuracy.

Table 4-3 Size measurement of pre-embedded PTFE film

Measurements (mm)						Average	Std. Dev.
50.96	51.53	48.44	49.26	52.25	52.75	50.87	1.55

4.3 Digital Image Correlation Calibration

Some key aspects of DIC experimentation needed to be calibrated to achieve results with high accuracy.

Calibration

Calibration is the approach to correlate DIC software and orient and scale camera images to the physical world (Reu 2012, 2014). To calibrate a typical DIC device for 3D imaging, certain parameters need to be determined:

a. Intrinsic (single camera) parameters:

i. Focal length (f_x, f_y)

ii. Image plane centre (C_x, C_y)

iii. Image skew angle (θ)

iv. Lens distortions $(K_{1\ldots n})$

b. Extrinsic (stereo rig) parameters:

i. Translation vectors (T_x, T_y, T_z)

ii. Rotational matrix (R_x, R_y, R_z)

These parameters are shown in Figure 4-3.

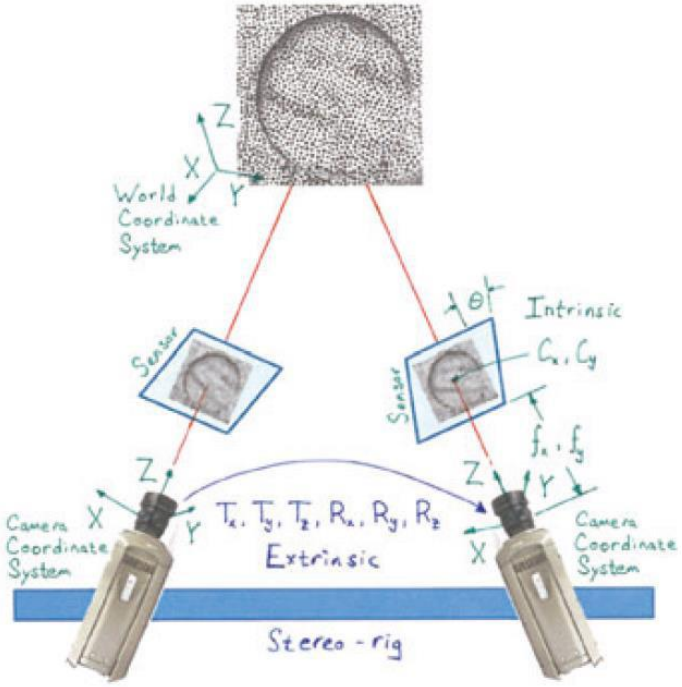

Figure 4-3 Illustration of calibration parameters in DIC

Speckle Pattern

Given the small scale of image subsets in DIC, it is important to minimise noise levels so that the translation and deformation of pixels can be tracked smoothly. To do this, the information contained in an image subset needs to be maximised with high-contrast speckle patterns. The subset size, speckle size, contrast, density, and edge sharpness all contribute to the effectiveness of the DIC image subset displacement calculations (Reu 2014, 2015). It is recommended to apply the speckle pattern manually for trial and error. Figure 4-4 gives some accepted shape of the speckle pattern, which can achieve a relatively good correlation.

Figure 4-4 Examples of accepted speckle patterns (Source: Herbst et al., 2012)

Lighting

The DIC output quality is affected by the interaction of lighting and surface speckle patterns. Reu (2012, 2015) suggested that to get the best output quality, DIC lighting should be both homogeneous and cool. Concentrated light sources or highlights on an image can distort the integrity of the speckle pattern, resulting in inaccurate displacement outputs. Furthermore, the speckle coating applied to the surface should have a matte finish and the light source should not radiate any excessive heat onto the test article as such low radiation levels can cause residual stress and reduce the quality of displacement outputs.

5 LOW-VELOCITY IMPACT

To start the experimental testing session, LVI was the first step. Drop weight impact test was carried out under the guidelines of ASTM 7136 to produce the initial impact damage to the test samples. Different impact energies were applied to both CP and QI stacked samples. The impact response was recorded and presented. Further data presented the difference in the responses of the CP and QI layup and the relation between the three key index forces of the impact response. The measured delamination morphology was compared between two different layups and different impact energies. An illustration of computed tomography was presented for the whole field delamination distribution after impact.

5.1 Impact Testing Parameters

The LVI testing was carried out within the framework of ASTM 7136. All impact testing sessions were conducted using the same mass and impactor. The total mass for the testing was 2.532 kg including the 0.281 kg of the impactor. The impactor used in the testing was a hemispherical steel impactor with a 16-mm diameter. The apparatus and operation aligned with the ASTM 7136.

Three energy levels (15 J, 20 J, and 25 J) were used for CP specimens, and 6 energy levels (5 J, 10 J, 12 J, 15 J, 20 J, and 25 J) were used for QI ones. The selection of energy aimed to maintain the energy range in the region of LVI. The measured average thickness of all the specimens was 4.34 mm, so the largest energy per unit thickness was 5.76 J/mm, included within the LVI standard (6.5 J/mm).

5.2 Impact Response Data Collection

The control and operation of the test were achieved via the console software Rosand Precision Limited Instrumented Falling Weight (version 1.11p). Several impact response data were recorded automatically during every impact session. The collectable data included contact force, impactor acceleration, impactor speed, and impact energy. A sweep time of 10 ms was set to record the whole

impact response behaviour. In all, 4000 checkpoints were mapped within the 10-ms sweep, obtaining a record of response data per 2.5 microseconds. The number of inspections can depict the overall behaviour of the impact response while not omitting any important point during the session. At the completion of each testing session, a plot of force-time response was automatically plotted on the controlling console monitor (see Figure 5-1).

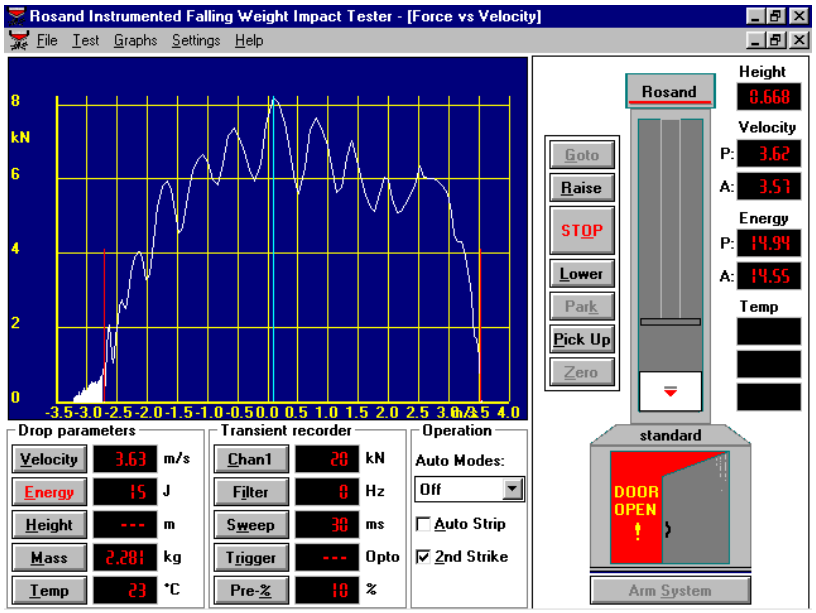

Figure 5-1 Illustration of on-site force-time impact response

5.3 Impact Test Results

Four CP samples and 12 QI samples were tested in the LVI session. The impact testing machine recorded the impact response (i.e. response impact force, total energy, etc.) for each test case. Impact response data were exported from the controlling software.

5.3.1 Contact Force Response

Impact contact force response is the most critical result of an impact test as it depicts the impact response from a testing session directly. By plotting the obtained data from the controlling console, the contact force vs. time was plotted for each testing sample. The impact damage would only initiate the damage when the P_c exceeded the critical value. Since no low energy was applied to the CP

sample, three typical responses from the damaged CP layup panel, damaged QI panel, and QI panel are exhibited from Figure 5-2 to Figure 5-4.

Cross-ply layup response

For the impact curve, usually, three points need to be observed. When the force reaches P_c, it can be considered the onset of delamination (Davies and Zhang, 1995). The delamination initiation results in a rapid reduction in force which sits at P_r. P_m is maximum response force that can be achieved if enough energy is stored in the impactor (Cartié and Irving, 2002).

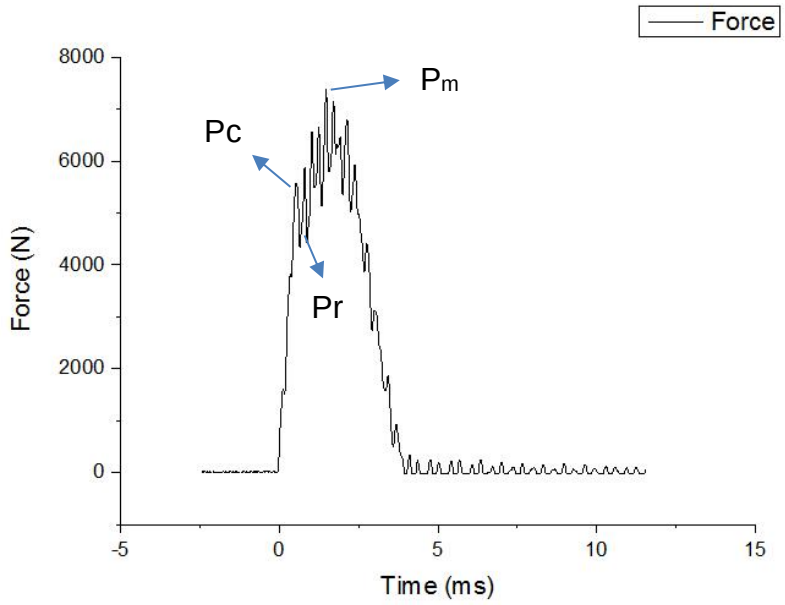

Figure 5-2 Impact response (force-time) for C3 (20J)

The contact force response of a CP sample subjected to 20-J impact energy is shown in Figure 5-2. During the sweep time of 10 ms, the full contact and break session was satisfactorily captured as the first contact force increased in 1 ms to 5442 N (P_c) and sat on the first reduction point at 4337 N (P_r) as the delamination initiated. With the downward travel of the impactor, the contact force fluctuated to climb to the peak force (P_m). After the peak load, the acceleration of the impactor decreased, but with the momentum it held, further delamination/matrix breakage was produced by the fluctuation passing the peak contact.

Quasi-isotropic layup response exceeding critical force

A similar contact force response of a QI sample impacted at 20 J is shown in Figure 5-3. Like the response from the last plot, critical force, first rest force, and maximum contact force can be determined using the same approach. The sample Q5 achieved those three values at 5763 N, 3992 N, and 9496 N.

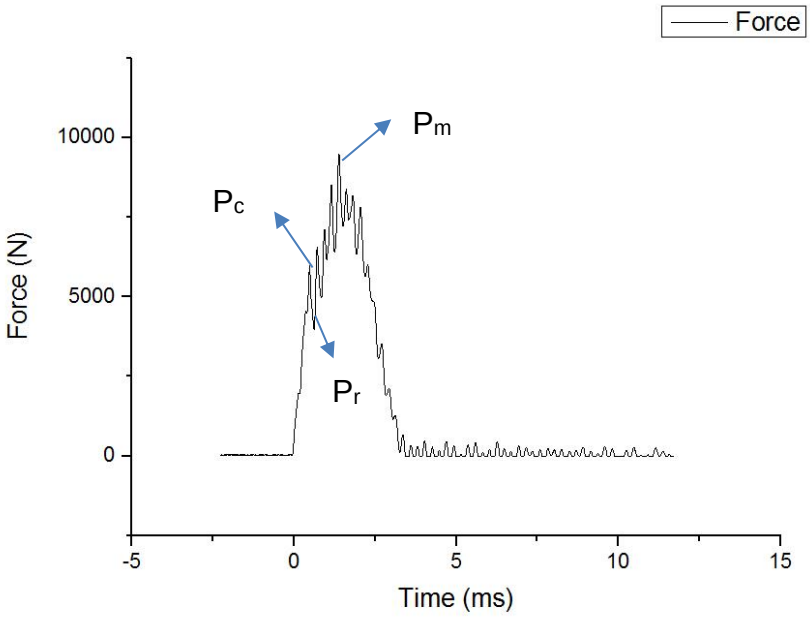

Figure 5-3 Impact response (force-time) for Q5 (20 J)

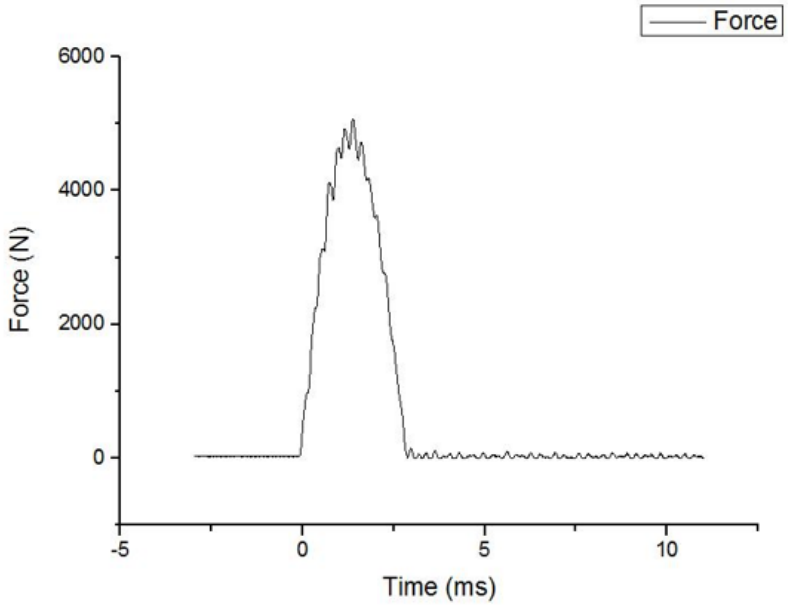

Figure 5-4 Impact response (force-time) for Q7 (5J)

Quasi-isotropic layup response not exceeding critical force

In another scenario, the specimen was impacted by a low energy level which may not cause internal delamination. Samples Q7 and Q8 were impacted by 5 J energy level. The plot for Q7 (see Figure 5-4) shows a smooth increase and decrease of the force, indicating no damage. The maximum force was retained at 5052 N and 5075 N for Q7 and Q8, respectively. The P_c, P_r, and P_m could not be found in this response figure. While comparing the P_c values from other specimens, the maximum contact force value of Q7 was at least 10% lower, which may not reach the threshold for delamination onset. The state of no delamination initiation needed to be confirmed by C-scan inspection.

5.3.2 Critical and Maximum Contact Force

The previous section showed the importance of the three major components of contact force during an impact session. Table 5-1 and Table 5-2 illustrate all those three contact forces for all the impact results.

Table 5-1 Important force components during impact response of cross-ply samples

	Thickness (mm)	Actual Energy (J)	Pc (N)	Pr (N)	Pm (N)
C2	4.32	19.86	5428	4424	7314
C3	4.29	20.36	5442	4337	7389
C4	4.33	24.5	6249	3958	8813
C5	4.36	25.6	6562	3946	7638

Table 5-2 Important force components during impact response of quasi-isotropic samples

	Thickness (mm)	Actual Energy (J)	Pc (N)	Pr (N)	Pm (N)
Q1	4.31	14.86	5480	4091	7575
Q2	4.31	19.86	5509	4097	9085
Q3	4.29	24.84	5185	4837	8732
Q5	4.35	19.37	5763	3992	9496
Q6	4.37	24.16	5613	4479	9536
Q7	4.38	4.74	N/A	N/A	5075 (peak)
Q8	4.37	4.71	N/A	N/A	5071 (peak)
Q9	4.36	9.72	5925	4311	6313
Q10	4.36	9.72	6029	4513	6226
Q11	4.37	11.55	6244	3917	7158
Q12	4.36	11.53	5948	3975	7072
Q13	4.35	14.55	5509	4664	7500

From the two tables, it can be found the critical force varies. To explore the relationship and understand the data, the following three plots were produced. Figure 5-5 to Figure 5-7 exhibit the critical force, rest force, and maximum force vs. the impact energy collected from the impact sessions.

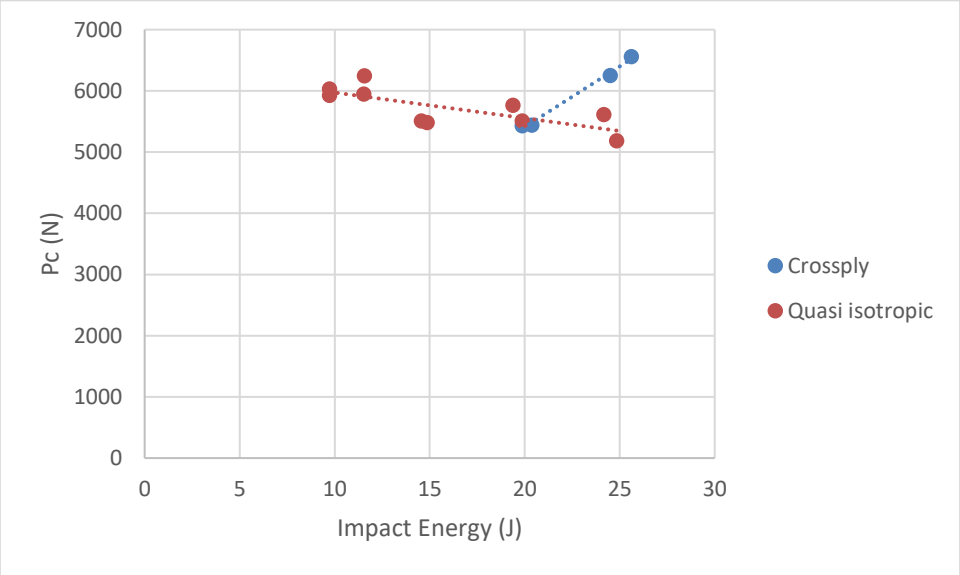

Figure 5-5 Critical force versus impact energy for both layup groups

The relationship between critical force and impact energy is negatively correlated for the QI layup. With the increased impact energy, the critical force, in other words, the threshold for delamination onset, is higher for the QI sample. The opposite observation can be found for the CP group.

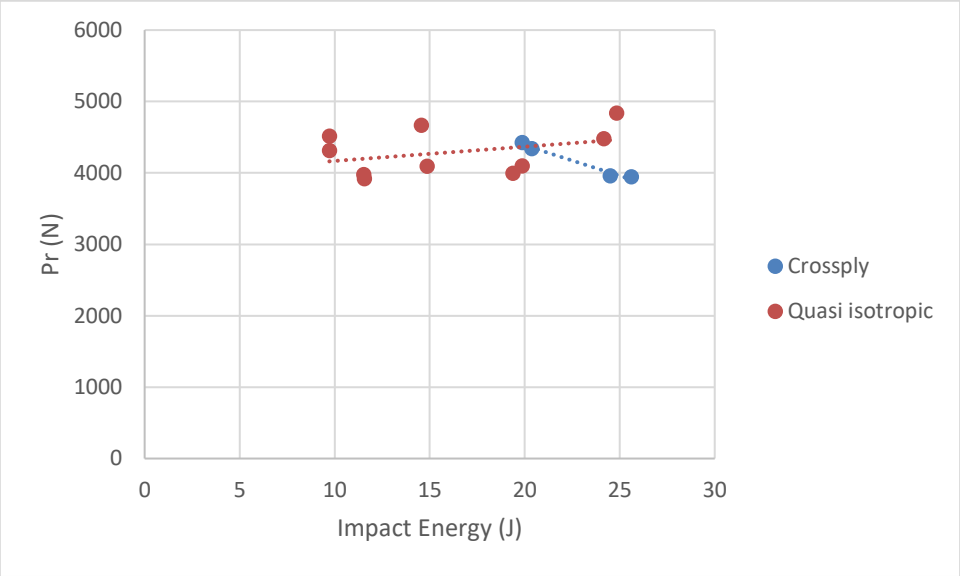

Figure 5-6 Rest force versus impact energy for both layup groups

In Figure 5-6, it can be found the behaviour of P_r is opposite to that of the critical contact force. QI samples impacted by higher energy achieved higher P_r while CP samples had a lower value after first delamination onset.

The difference between P_c and P_r indicates the first energy absorption for the initial delamination appearance. When higher impact energy is applied to the QI samples, the larger initial momentum of the impactor will cause greater deflection of the panel. With a gradual orientation change within the QI samples, the delamination would occur at a lower threshold at the introduction of a 45° fibre, resulting in a lower overall stiffness that would finally contribute to the impact-induced damage.

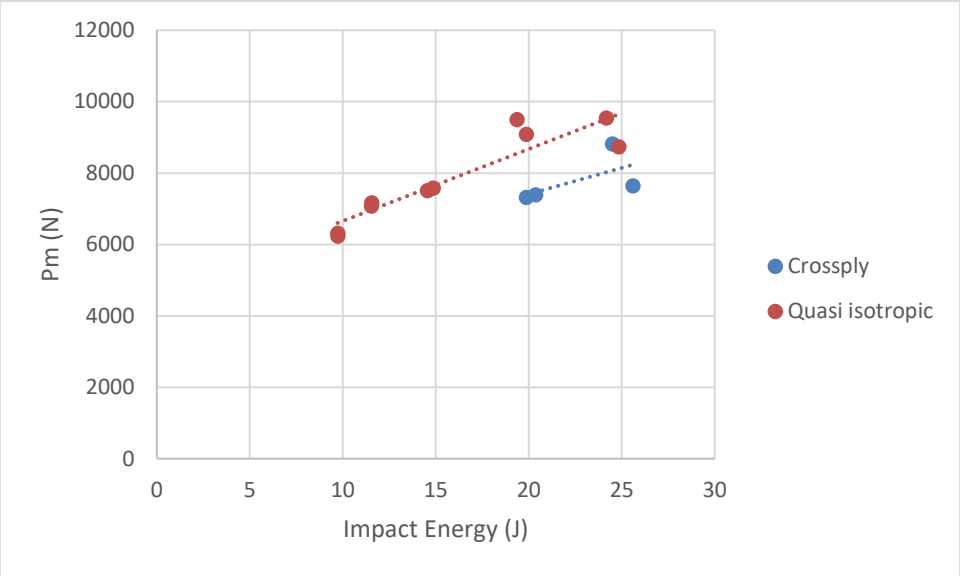

Figure 5-7 Maximum force versus impact energy for both layup groups

Figure 5-7 shows the maximum force response for both layup groups. The maximum force is proportional to impact energy. The observation is obvious to understand as the P_m indicates the maximum response force that can be achieved if enough energy is stored in the impactor (Cartié and Irving, 2002). Although both groups show similar behaviour, the gap between the two layups is worth mentioning. For the same impact energy, the maximum response force of a QI sample is higher than that of a CP one. Given the same initial energy, the difference between the two layup groups indicates the gap between energy absorption ability.

5.3.3 Critical Force and Strain Energy Release Rate

Davies and Zhang (1995) proposed that damage is initiated when the contact force (P) reaches a critical value (P_C) for a QI layup panel, as indicated by equation (5-1):

$$P_c^{\,2} = \frac{8\pi^2 E t^3}{9(1-v^2)} G_{IIC} \qquad \textbf{(5-1)}$$

Where P_C is the critical force for damage initiation, E is the equivalent in-plane modulus, v is the Poisson's ratio, t is the laminate thickness, and G_{IIC} is the critical SERR for mode II fracture.

The inversed Eq. 5.1 can be used to estimate the G_{IIC} value. The average of P_c values for QI panels is also calculated. The result seems to be in good agreement with the results of the experiment conducted by Chen (2015) (see Table 5-3).

Table 5-3 Comparison of G_{IIC} value between impact data and test results by Chen (2015)

	P_c average (N)	Calculated G_{IIC} (J/m^2)	Test result (Chen, 2015) G_{IIC} (J/m^2)	Difference
QI Sample	5784.5	763	837.6	8.9%

5.4 Inspection Results for Impact Testing

Besides LVI, the appreciation of the internal damage is also important. Two non-destructive testing approaches were used for this purpose. Ultrasonic C-scan can be performed in a satisfactory detection time, and computed tomography can provide a full-field three-dimensional description of internal delamination and other damage.

5.4.1 Ultrasonic C-scan Results

NDT was conducted using a multiphase ultrasonic system Sonatest Veo 16:64. The 5-MHz probe consists 64 groups of transducers, which allow the system to inspect the sample in various scan methods. The C-scan data were processed to show the delamination inside the panel. A 15-db gain was set to obtain an optimal scan result. Three washers were placed under the sample for support and to be taken as reference points to ensure the sound signal travels through the sample.

Details of ultrasonic C-scan are stated in section 3.2.1. Although several types of scans can be acquired in the Sonatest Veo system, only the A-scan and C-scan were used to obtain the projected delamination area of each sample. The signal gate indicates the threshold for the signal to present itself. A higher gate will result in less information, and a lower gate will cramp the screen with all the signals, making the damage inaccurate and indistinguishable.

Delamination Area

The delamination area was measured by the method stated in Section 3.2.3. The detected delamination area for the samples is tabulated in Table 5-4 and Table 5-5 for the CP layup and QI layup, respectively. The measurement approach used is stated in 3.2.3. The inspection proves that the impact force for samples Q7 and Q8 is lower than the P_c threshold to initiate the delamination for AS7/8552. Hence, no damage was found using more gains, lower than the signal gate.

Table 5-4 Delamination area of cross-ply layup under different energy levels

Specimen	Thickness (mm)	Impact Energy (J)	Actual Energy (J)	Delamination Area (mm^2)
C1	4.31	15	14.87	717.2
C2	4.32	20	19.86	963.1
C3	4.29	20	20.36	966.2
C4	4.33	25	24.5	1354.3
C5	4.36	25	25.6	1366

Table 5-5 Delamination area of quasi-isotropic layup under different energy levels

Specimen	Thickness (mm)	Impact Energy (J)	Actual Energy (J)	Delamination Area (mm^2)
Q1	4.31	15	14.86	1013.4
Q2	4.31	20	19.86	1482.2
Q3	4.29	25	24.84	1633.3
Q5	4.35	20	19.37	1464.9
Q6	4.37	25	24.16	1636.1
Q7	4.38	5	4.74	No delamination found
Q8	4.37	5	4.71	No delamination found
Q9	4.36	10	9.72	640.6
Q10	4.36	10	9.72	609.9
Q11	4.37	12	11.55	787.6
Q12	4.36	12	11.53	740.8
Q13	4.35	15	14.55	996.2

The delamination area versus impact energy is plotted in Figure 5-8 to show the relation between delamination area and impact energy. It can be observed for both layups that the delamination area increases as the impact energy goes up. Higher impact damage brought more energy and momentum to the sample, resulting in higher energy absorption. A composite panel absorbs the energy by certain forms of damage including delamination, matrix crack, and fibre breakage. The energy unable to dissipate will result in those damage patterns. Under the same impact energy level, the CP samples had a lower damage area than the QI specimens. In other words, the CP samples exhibited better impact resistance than the QI samples. The result is different from the well-accepted conclusion that delamination is severe if a larger fibre mismatch exists. The reason being is the area acquired is the projected area because according to previous publications, the total delamination area of QI is less than CP. CP sample has exhibited greater deformation than the QI samples since the CP sample has a greater mismatch (90°) than the QI sample (45°).

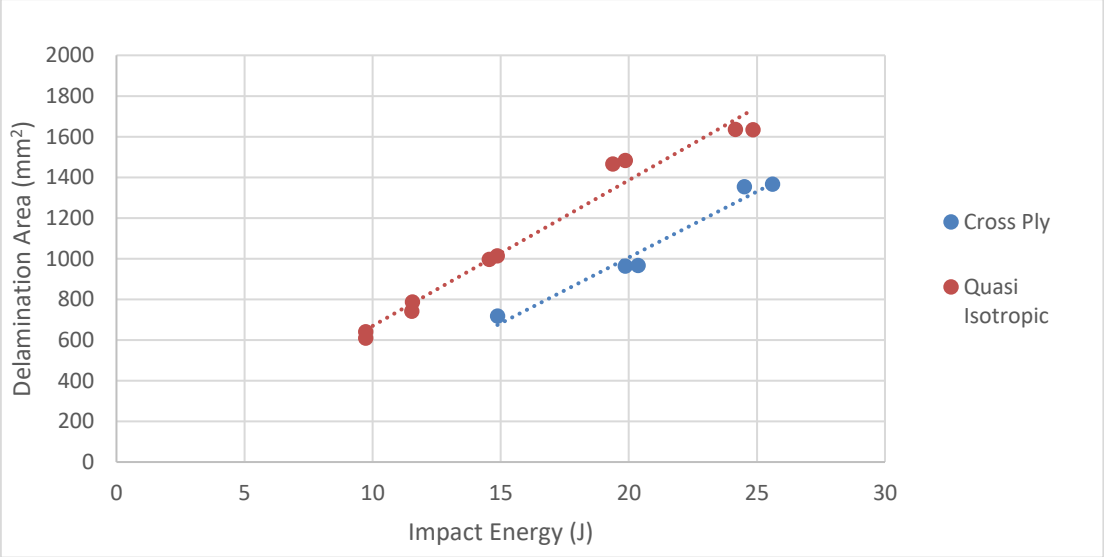

Figure 5-8 Delamination area versus impact energy for cross-ply and quasi-isotropic samples

Delamination Morphology

The delamination morphology detected from the C-scan shows the accumulated delamination area through the thickness. QI delamination shows a round shape

while the CP damage presents a more elongated shape. Figure 5-9 shows the typical delamination morphology for a QI and CP panel.

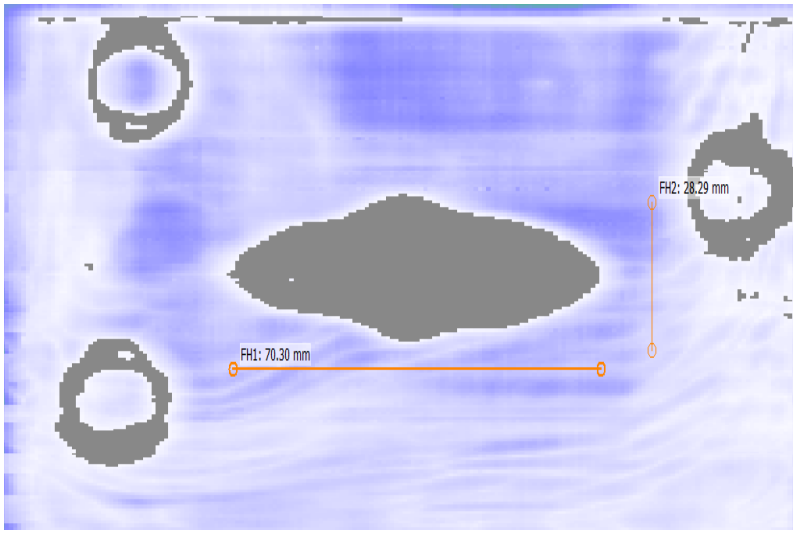

(a)

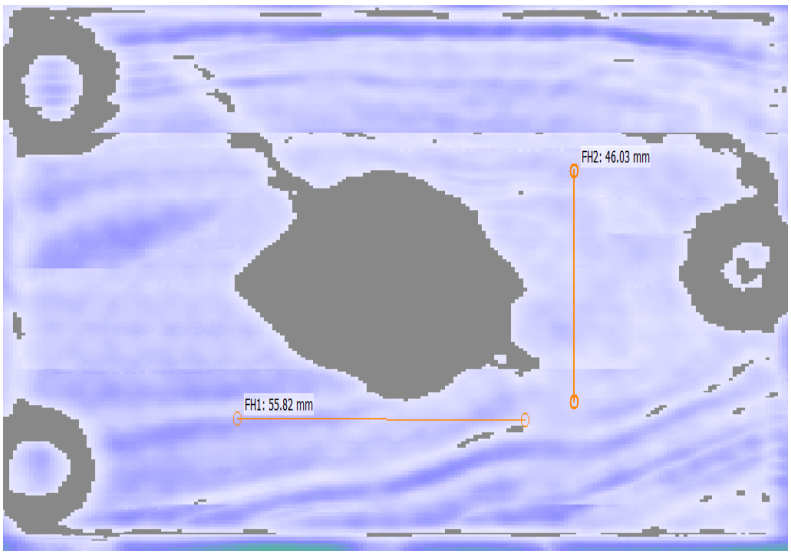

(b)

Figure 5-9 Delamination morphology and size measurement under C-scan of (a) C5 (impacted at 25 J) and (b) Q3 (impacted at 25 J)

The delamination for a CP sample is an elongated shape in the long size direction. For the specific example of C5, the measured size is 70.30 × 28.29 mm. The elongated shape is symmetrical in both longitudinal and transversal directions owing to the symmetricity of the layup. In contrast, the delamination shape from the QI layup ended up in a rounder shape, measuring 55.82 × 46.03

mm. The rounder size came from the accumulation of “peanut” shaped delaminations within the interfaces throughout the thickness.

5.4.2 Impact Dent Depth

Through the visual inspection of the impact and back surface, more evidence can be found. For impact, the dent depth of the QI sample was examined and exported by the CMM machine. The results of the impact dent depth are plotted in Figure 5-10.

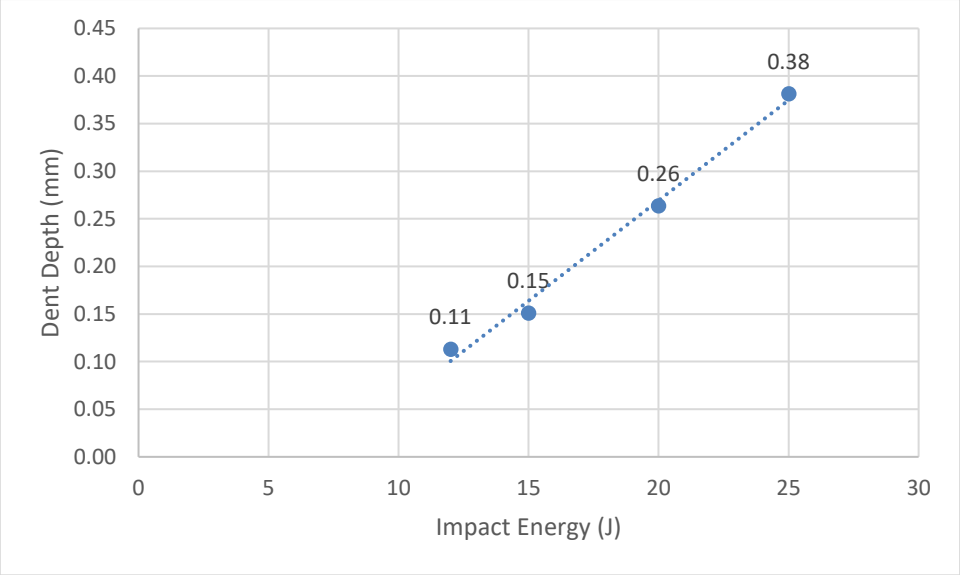

Figure 5-10 Impact dent depth of QI layup at different impact energy levels

The relationship between dent depth and impact energy follows a clear linear trend. With the increased impact energy, the dent depth increased. Dent depth examination can also be used to categorise the depth.

The depth of the residual indentation caused by BVID varies in the literature. For instance, the National Physical Laboratory in the UK defines BVID as damage causing 0.5 mm indentation (Gower, Shaw and Sims 2005), while a depth of 1.27 mm – 2.54 mm (0.05 inch – 0.10 inch) is reported in the NASA publication (McGowan and Ambur 1997). Various aspects of BVID have been studied, but in this study, the BVID criteria is selected as 0.5mm. The largest depth obtained was 0.38 mm which is also within the current BVID criteria (<0.5 mm).

5.4.3 Visual Check on the Back Face

Back face is always the most severely damaged face in the impact scenario. As the only output position, the back face usually shows obvious matrix cracks, delamination, and even fibre breakage. With the delamination area under C-scan, the rough damage area can be distinguished from visual surface inspection. Figure 5-11 shows the typical back face damage. The contour of the damage is identical to the delamination contour on the C-scan results.

Although a smaller delaminated area was detected by the C-scan on a CP layup than a QI one at same impact energy level (see Figure 5-8), a more extensive extrusion of back face deformation was observed in CP samples (see Figure 5-11). Unlike the response of a CP specimen, the QI sample absorbed the impact energy by further modes of fibre breakage. The thin and extended delamination observed from the C-scan detection is the broken fibre near the impacting point delaminated to the further side edge. The breakage and small back face delamination are marked in the elongated elliptical dashed line in Figure 5-11.

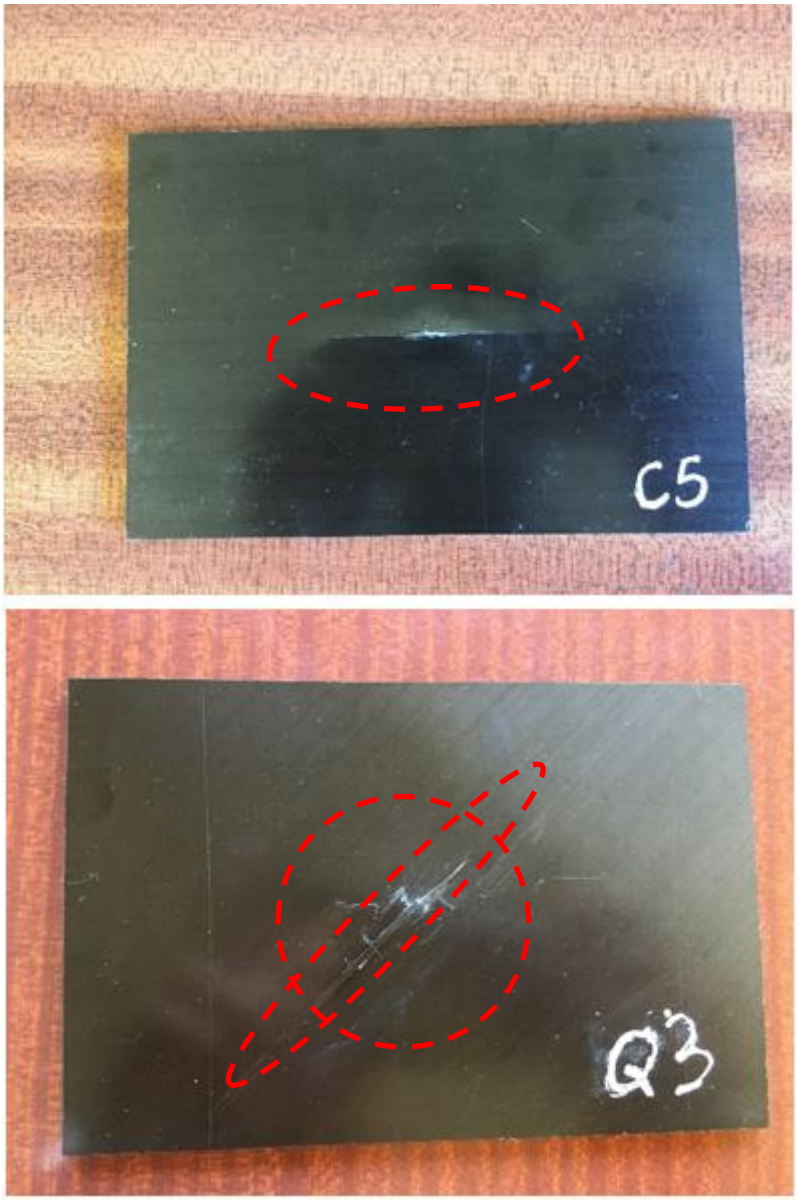

Figure 5-11 Back face of C5 (25 J) and Q3 (25 J) samples

5.4.4 Computed Tomography results

Computed tomography (CT) was also used to examine and assess the damage induced by the LVI on a CFRP. Micro CT is used for non-destructive high-resolution imaging of the internal structure of 3D objects. The test equipment used in the session was a Nikon Metris X-Tek XTH 225 provided in Cranfield University (Shrivenham Campus). The maximum voltage for the inspection was set at 60 kV after a series of trials and errors. An inspection area of 60 × 60 mm was taken in the session, which covered the delamination area fully.

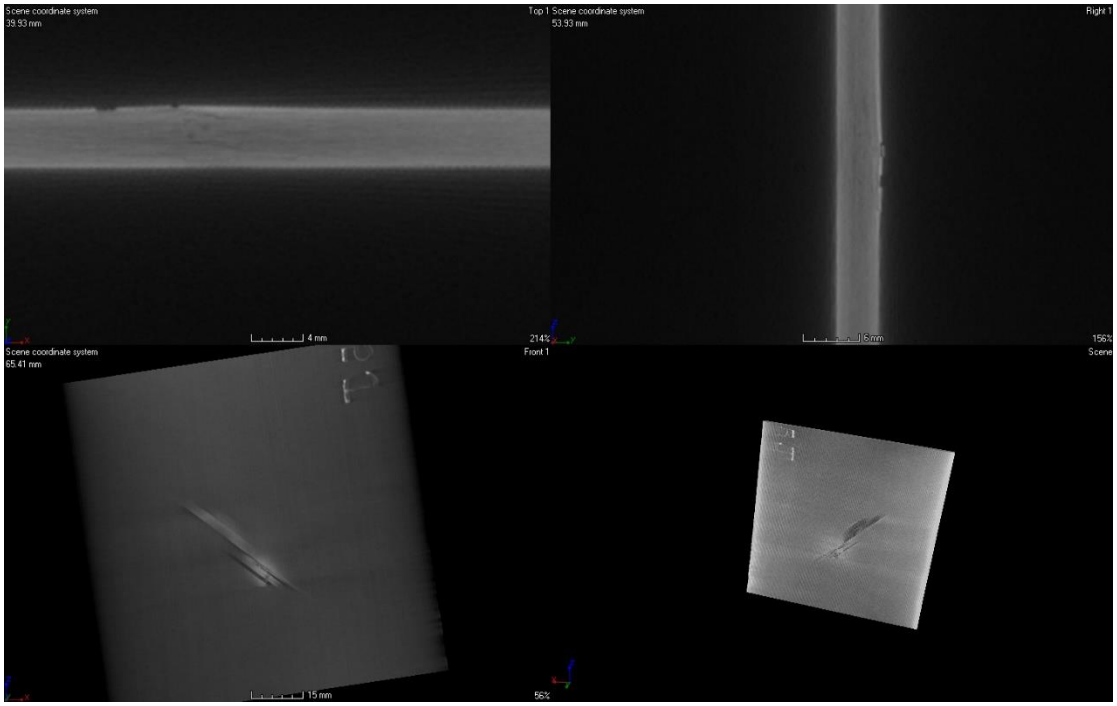

Figure 5-12 Assorted micro CT results

Since 3D remapping is available for the inspected results, the interpretation of the damage pattern is shown in the three directions. Sample Q1 under 15-J impact energy was examined using the micro CT.

Images acquired from micro CT at the sample's front face were exported for every single-layer interface. Some selected results are shown in Figure 5-12 and **Error! Reference source not found.**. The damage situation between the 1st and 2nd layer interface is illustrated in Figure 5-13(a). Being the direct contact point of the impact session, the local damage only appeared to be a local dent. The deeper interface, such as 3rd and 4th layer interface (see **Error! Reference source not found.**), shows a matrix crack in the same direction of local fibre alignment. The cracks originated from the shear force of the out-of-plane impact force and when the force exceeded the maximum shear strength of the matrix, the crack initiated. At this shallow (relative to the impact face) interface, the crack length is relatively small compared to the detected delamination size under C-scan. The distinguishable length is around 9 mm in the 90° direction.

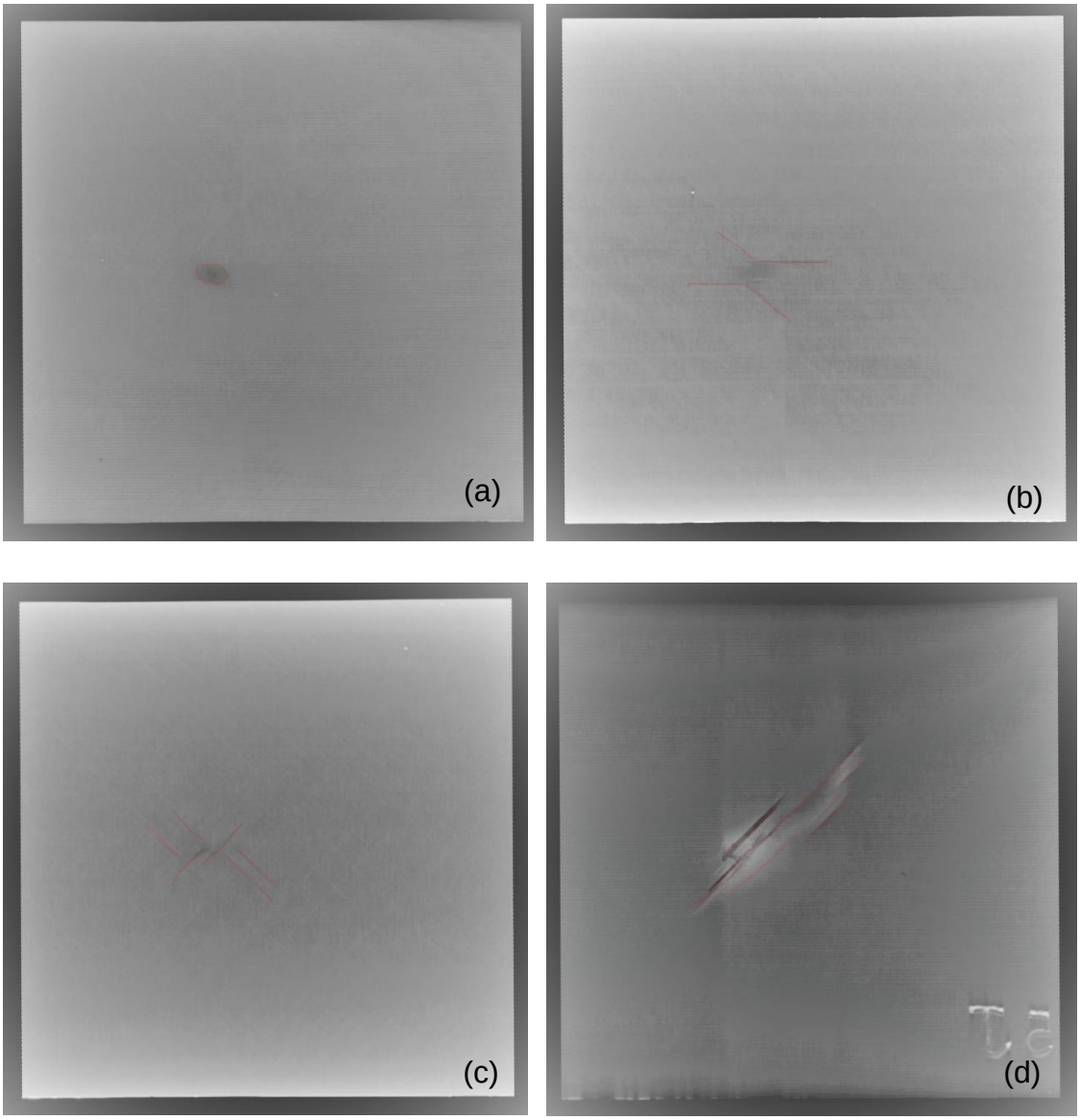

Figure 5-13 Front face micro CT result of internal damage at (a) 1st and 2nd interface, (b) 3rd and 4th interface (c) 25th and 26th interface (d) 31st and 32nd interface

Further damage pattern in a deeper interface, i.e. the 25th and 26th interface, is shown in **Error! Reference source not found.**. Even though the interface is a 45/0° interface, apart from the matrix crack at 45°, further cracks at -45° can also be observed. The finding of -45° traces back to the larger deformation of those cracks brought by the impact load. The length of those cracks was not different from that at a much shallower interface (e.g. 3rd and 4th interface). The back-surface image is shown in **Error! Reference source not found.**. The severe

cracks are depicted in the figure. Extensive cracks can be found in the same direction of the local fibre. Of note, the obvious matrix cracks were measured around 30 mm, which is 50% less than the measurement from the same C-scan result (see Figure 5-14).

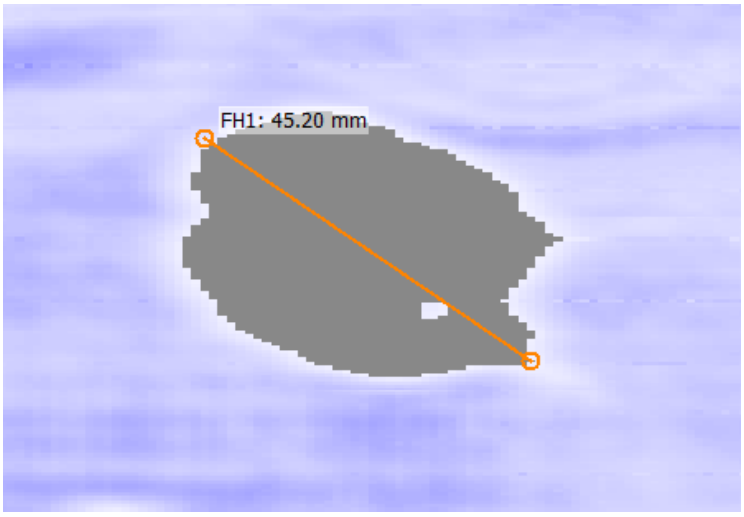

Figure 5-14 Maximum delamination length of sample Q1 (15J)

The difference comes from the low resolution of the micro CT result and the indistinguishable delamination under visual inspection.

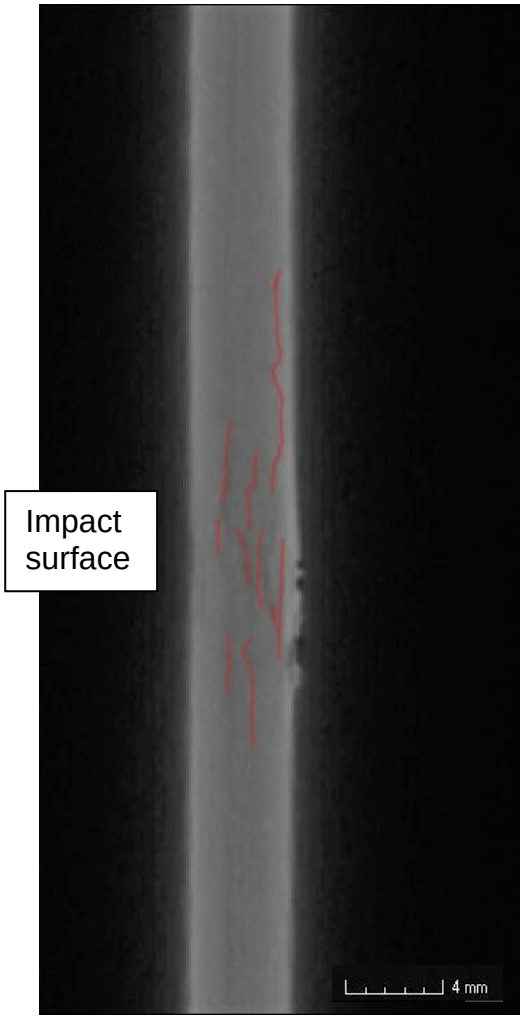

Figure 5-15 Side view of internal delamination of Q1 (15J)

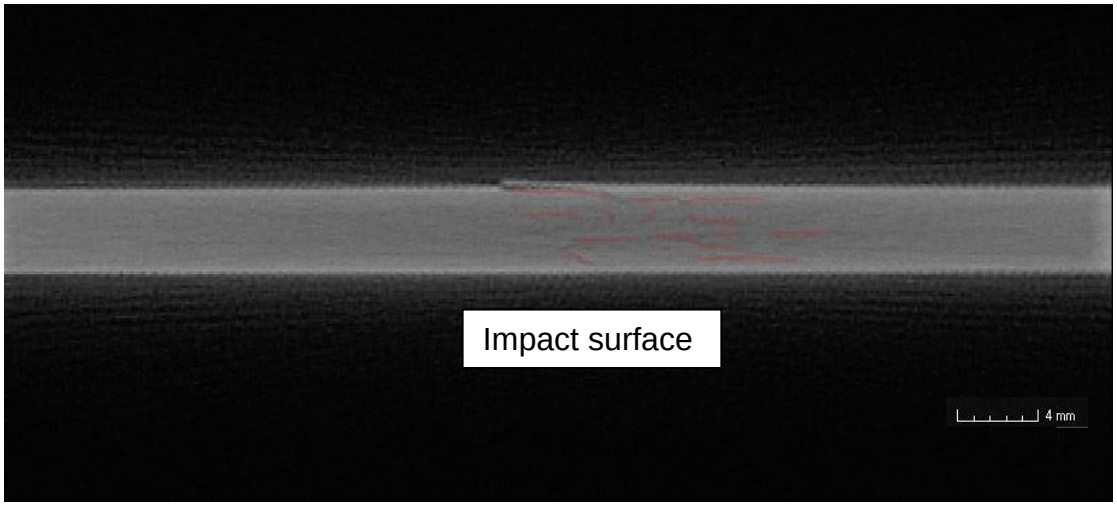

Figure 5-16 Top view of internal delamination of sample Q1 (15J)

Interlaminar delamination in cross-section view is shown in Figure 5-15 and Figure 5-16 from the side view and top view, respectively. Extensive delamination is apparent near the back surface while the delamination near the impact surface is less evident. Another phenomenon is that when a delamination encounters a matrix crack, a declamation jump will take place.

6 COMPRESSION AFTER IMPACT TESTING

Susceptibility to damage from concentrated out-of-plane forces is one of the major design concerns for many structures made of advanced composite laminates. Knowledge of the damage resistance and damage tolerance properties of a laminated composite plate is useful for product development and material selection. The residual strength data obtained using ASTM 7137D can be used in material specifications and further fatigue test benchmarks. The properties obtained in this session can provide guidance regarding the anticipated damage tolerance capability of composite structures of similar material.

6.1 Undamaged Compressive Strength

Being known for superior mechanical properties, a pristine composite can achieve high compressive strength. Testing with an undamaged composite panel will commonly result in a relatively high possibility of the occurrence of undesirable failure modes such as end crushing. In order to determine the reduction brought about by the impact damage, determining the ultimate compressive strength was a necessity. Instead of acquiring the compressive failure strength experimentally, the classical laminate theory was used to calculate the undamaged compressive strength before the test analytically. Laminate properties can be predicted using the mature laminate theory. The lamina properties are given in Table 4-1. Four failure criteria were used to identify the failure value. The calculated results of undamaged compressive strength for the QI sample are presented in Table 6-1.

Table 6-1 Calculated undamaged compressive strength for QI sample using different failure criteria

Compressive Failure Strength (MPa)	Failure Criteria
628	Tsai-Hill
683.3	Max Strain, Max Stress
883.6	Max Fibre Strain

6.2 CAI Testing Procedure

All the tests were conducted in compliance with the ASTM 7137 for CAI testing. Six specimens impacted under different energies were tested in this session to obtain their residual compressive strength under quasi-static compression load. The testing involved an Avery 600 kN load system (see Figure 3-3) provided in the structural integrity lab of SATM at Cranfield University. An anti-buckling guide (see Figure 3-2) was used in the tests. The guide was equipped with clamped edge restraints and simply supported the testing object in the x direction and y direction in the laminate local coordinate system so that there was proper displacement in the x direction (vertical in the figure) and enough space for the sample to break in the y direction (through-thickness direction in the figure). The cap was simply put on the specimen rather than fastened, as in other approaches. The sample alignment and the clearance between the knife edge of an anti-buckling guide and the specimen should be carefully examined and maintained to ensure a valid failure rupture in the mid-section of the specimen rather than invalid premature failure.

The compressive displacement was 0.05 mm/s. The controlling console software recorded the load response and displacement.

During the compression testing, the pre-treated test panel was placed in the CAI fixture. The loading cell started from the contact point with the top assembly. The trigger value for an automatic stop was 3 mm in displacement, which is just below the gap distance. The compression loading started at the designated rate and stopped when the displacement value was triggered.

During the testing process, the DIC equipment was arranged to measure the displacement and strain distribution on the specimen from the initial stage to failure. The Dantec Dynamics Q-400 DIC system was used in the test. All the samples were sprayed with a speckle pattern in accordance with the DIC measurement requirement.

6.3 Compression after Impact

Six samples were tested in compliance with the testing standard. The data of load and displacement were exported from the analogue output. All samples failed during the testing session.

Result Validation

The residual compressive strength value for each specimen is shown in Table 6-2. The results for all samples, except sample Q8, showed valid failure. Five commonly observed acceptable compressive residual strength failure modes are listed in Figure 6-1. All the samples except Q8 ended up in the ideal “LDM” failure mode. Q8 experienced premature end crushing between the fixture and the cap. The invalid failure occurred because of the pristine or near-pristine nature of the sample as stated in the previous chapter, so no delamination was observed for sample Q8. Thus, the RCS value for Q8 is invalid and unusable.

Table 6-2 Residual compressive strength of the testing specimen

Specimen	Impact Energy (J)	CAI (MPa)
Q5	20	211.8
Q6	25	192.2
Q8	5	282.3
Q9	10	297.9
Q12	12	253.9
Q13	15	243.7

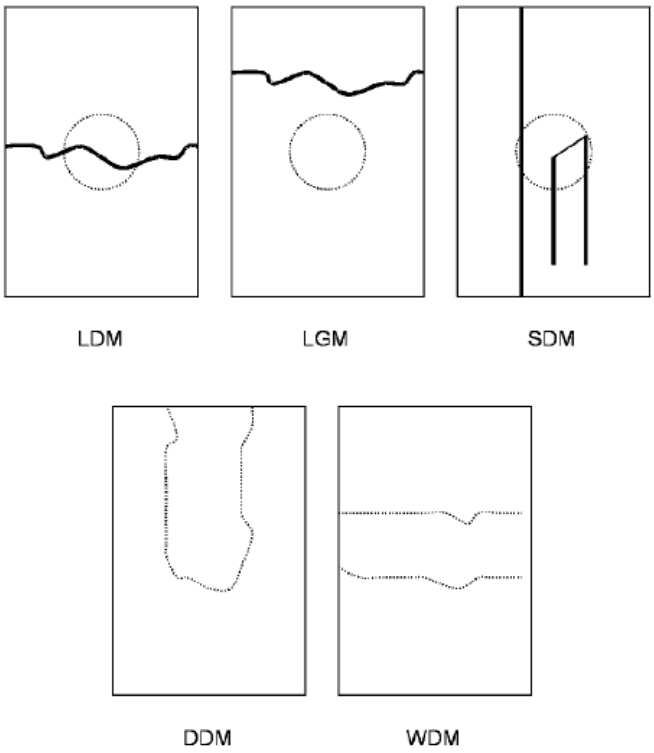

Figure 6-1 Commonly observed acceptable compressive residual strength failure modes (Source: ASTM 7137)

Failure Mode

All other five specimens with detectable delamination failed at a valid pattern, as shown in Figure 6-2. This type of failure is caused by the local buckling and shear band deformation initiated from the delamination (Fleck, 1997). The stress concentration around the delamination is the driving force for the delamination propagation.

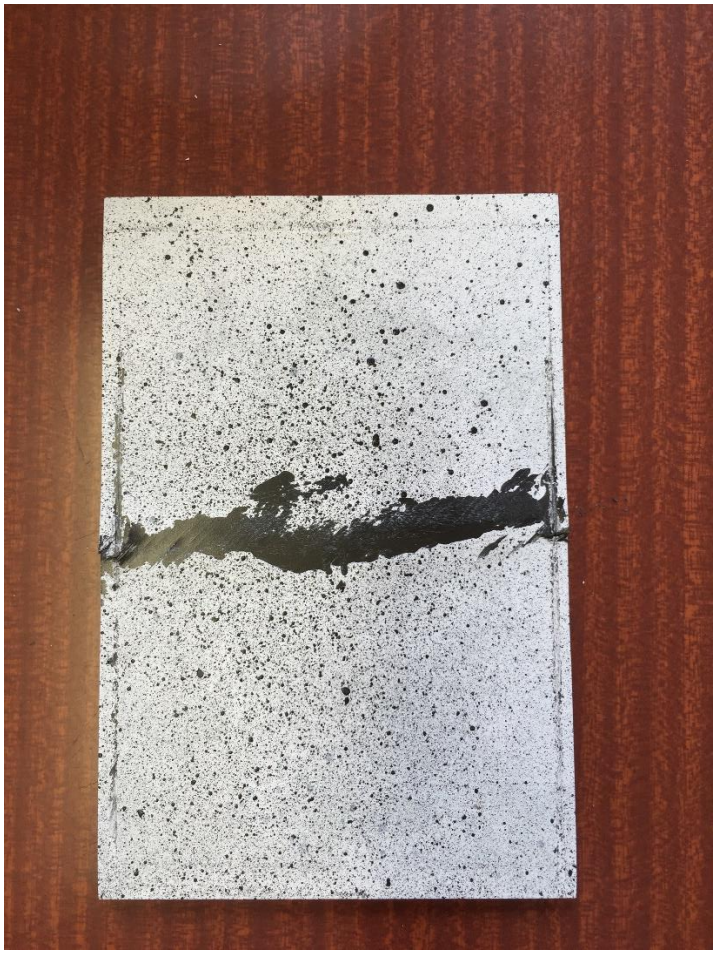

Figure 6-2 Damaged Q13 specimen (15 J) shows valid failure in the compression test

Figure 6-3 shows the side view of the damaged panel. The damage pattern was provided as evidence of local buckling and shear band deformation.

Figure 6-3 Side view of damaged specimen Q13 (15J) showing the local buckling and shear band deformation of the specimen

Residual Compressive Strength

The results from Table 6-2 are plotted in Figure 6-4. Compared with the calculated pristine compressive strength, the reduction is at least 60% even at the 10-J energy level. The reduction shows that the impact, even at low energy, can cause a severe decrease in composite performance.

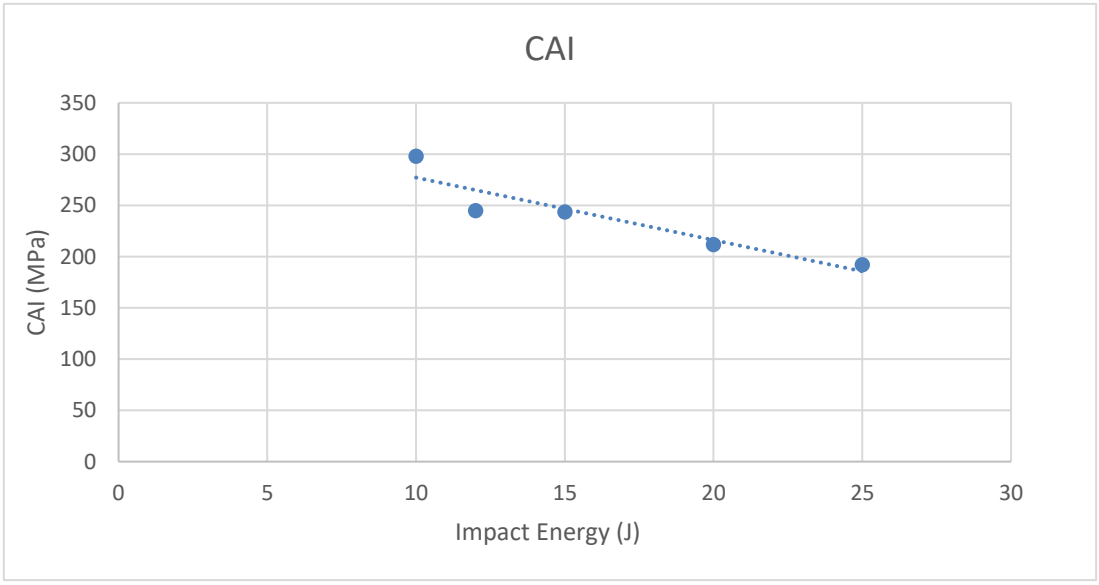

Figure 6-4 Residual compressive strength versus impact energy for QI specimen

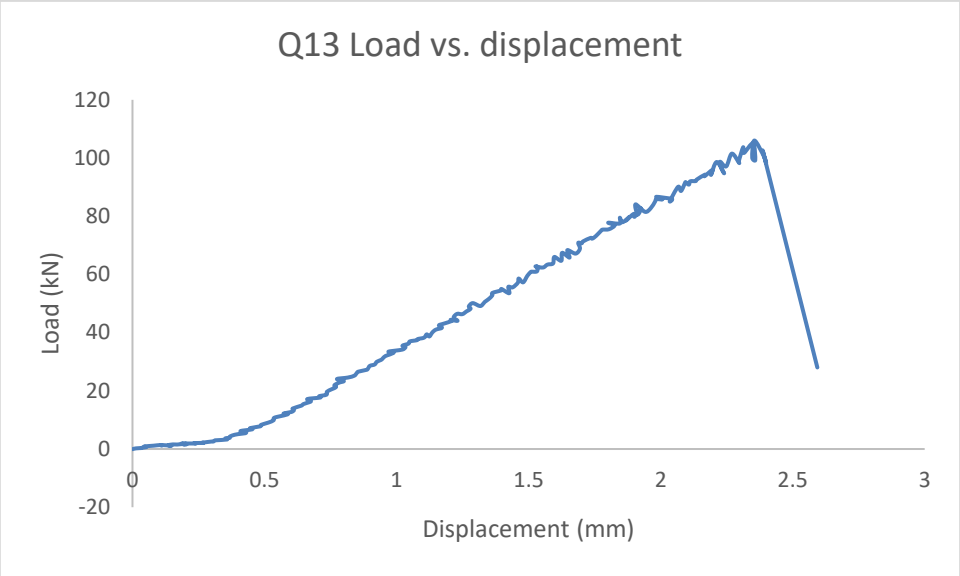

Figure 6-5 Load vs. displacement response of sample Q13 (15J)

Figure 6-5 shows a typical load and displacement response during a CAI test. Owing to the linear behaviour of composites, the sample showed a linear response with the increased load. The failure happened suddenly when the RCS point was reached. The common failure mode is impact-induced delamination propagated when the strain energy release rate exceeds the critical value and the rest of structure ruptures when no further load can be taken. During the experimental test, this session progressed almost instantly. To explore the failure mode and behaviour of impacted CFRP samples, DIC was used to capture the state before failure.

6.4 DIC Results for Compression after Impact

The Dantec Q-400 DIC system was adopted during the CAI tests to determine the displacement and surface strain changes during the whole testing duration. The loading rate of Avery 600kN was taken as low as 0.05 mm/s, and the interval for DIC to take pictures was 0.25 s/shot. The DIC cameras recorded the whole compression testing. After post-processing, the surface displacement and strain were obtained for all the testing samples.

Figure 6-6 shows a typical result after post-processing. The correlated area could not cover the entire sample size (150 mm × 100 mm) owing to the covering of the

testing jig: the top cap, bottom clamped area, and two knife edges were attributed to the reduction in correlated area. Commonly, an area of 132 mm (or 120 mm, if the area between 2 bolts is omitted when selecting the ROI) × 72 mm would be achieved after the processing.

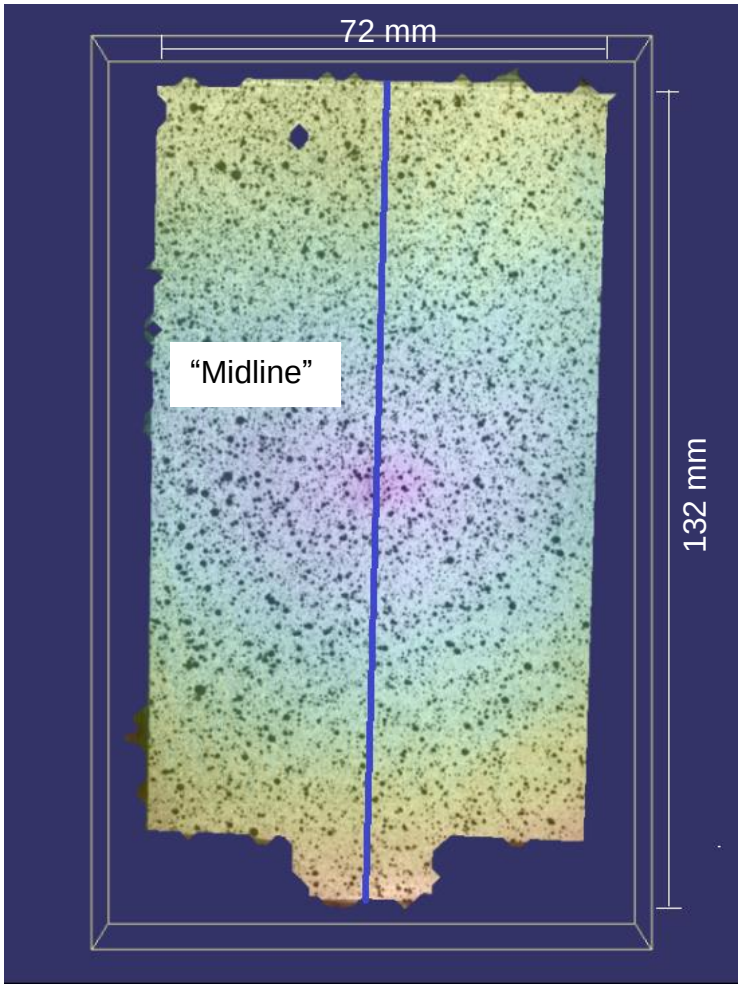

Figure 6-6 Typical DIC results illustration and the location of “midline”

In Figure 6-5, the sample shows a linear response to the instant rupture when the load reached its ultimate value. The DIC equipment captured the whole process by a series of pictures. Among those, the moment approaching failure would be most intriguing to the compressive failure mode test.

For the sample Q6, the camera caught the moment before rupture. The displacement in the z direction and the shear strain distribution are shown in Figure 6-7. The image captured the local buckling behaviour in the real scenario. The linear lump parallel to the bottom edge indicates the local buckling.

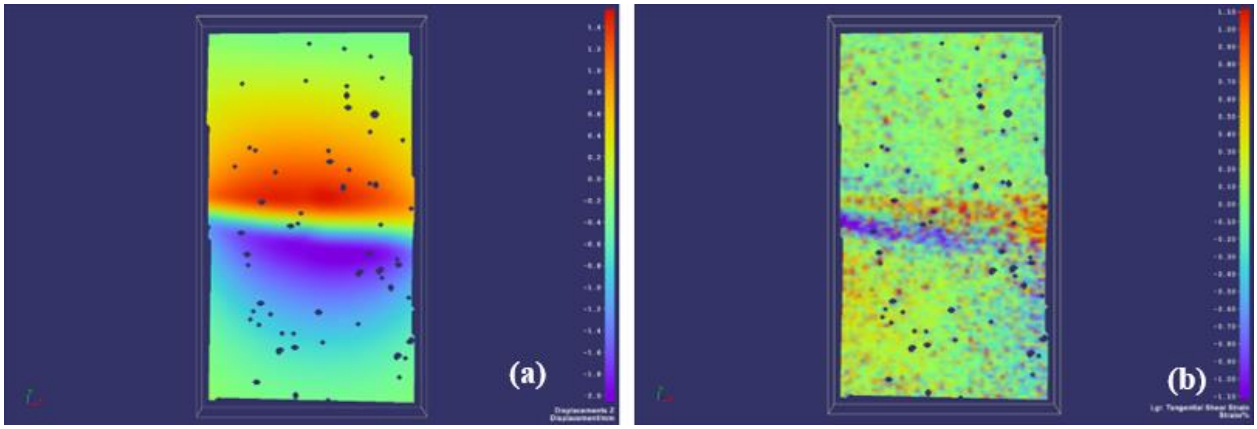

Figure 6-7 (a) Displacement in z direction and (b) shear strain of Q6 (25 J) before rupture

A different pattern can be found in another sample. Figure 6-8 shows the z displacement and shear strain of Q5 before failure. The failure happened so quickly that the point just before rupture could not be recorded. However, the interesting fact is that the shear strain will firstly form a cross shape which indicates the concentration of shear stress on the surface before rupture. The concentration may be the reason behind shear band deformation on the surface. Another observation from the testing was that before the local buckling just before the final rupture (see Figure 6-7a), there existed a smaller local buckling area (see Figure 6-8a).

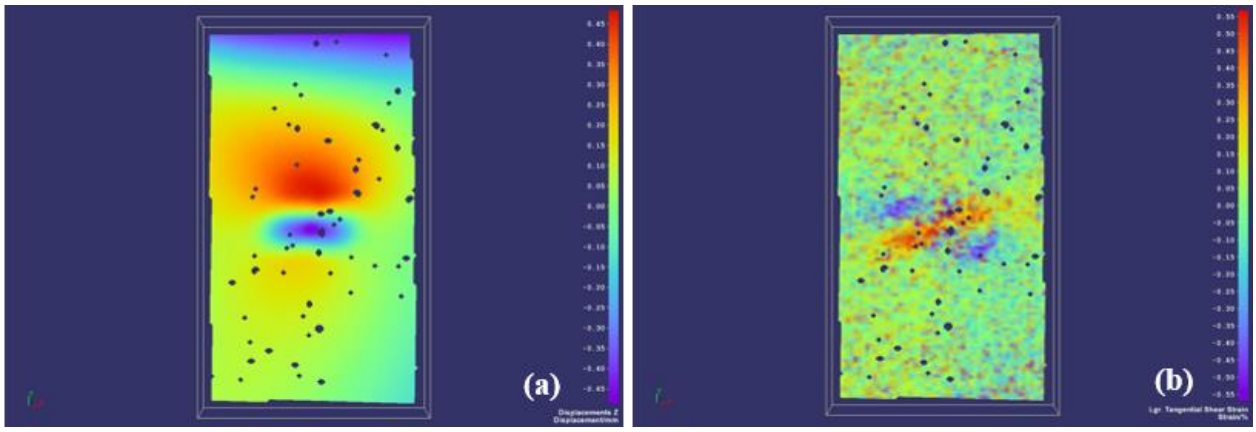

Figure 6-8 (a) Displacement in z direction and (b) shear strain of Q5 (20 J) before rupture

To present the out-of-plane displacement more clearly, a sectioned view of displacement along the “midline” (see Figure 6-6) is presented. The mean

displacement in the z direction during the recording process is plotted in Figure 6-9. The drastic increase before failure can be seen in the figure. The positive and negative values of the mean z displacement come from the difference in the compressive status of each specimen. The main trend is that for a larger damaged specimen, the damage comes earlier. The slight difference may come from the slight deviation in the time of recording.

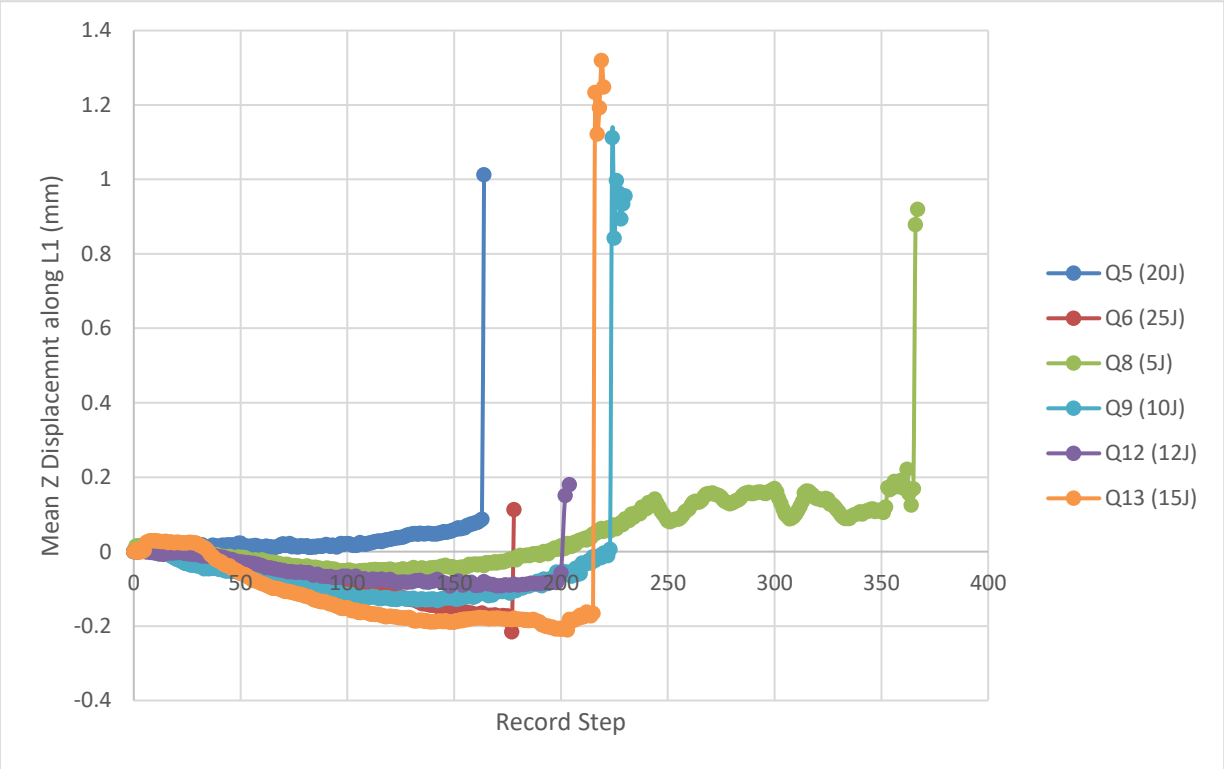

Figure 6-9 Mean displacement in z direction through the testing process

The spatial z displacement shown in Figure 6-10 to Figure 6-15 illustrate the out-of-plane displacement along the midline of the specimen in the loading direction for each specimen. For lower impact energy (5–12 J), the samples exhibited “outward” bending besides the two half-wavelength local buckling when approaching failure for those more severely impacted samples (15–25 J). The difference is regarded to its severity of internal damage. The less impacted sample (5-12J), has a less internal damage area which means less internal delamination exists. The panel can exhibit a response similar to a pristine panel while the structure is not losing too much of the structural integrity by the delamination. So, a delamination buckling mode with one half-wavelength is more

likely to happen while for the more severe impacted cases, with the interaction between more delaminated interfaces, a delamination buckling mode with two half-wavelengths seems to be the lowest energy requirement.

It can also be observed from Figure 6-10 to Figure 6-15 that the displacement changes usually occurred during the last quarter of the loading session.

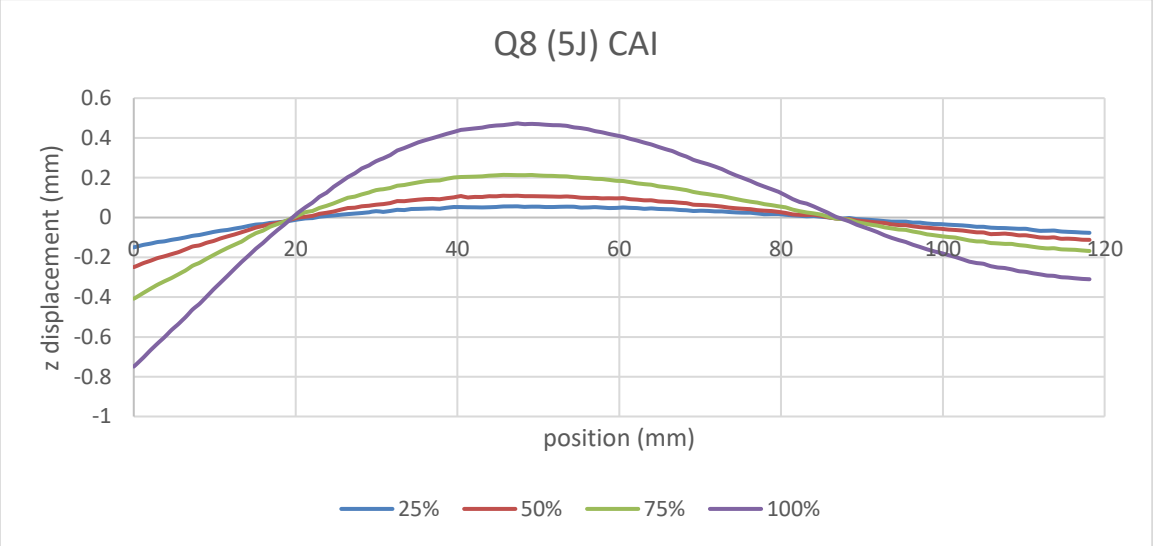

Figure 6-10 Out-of-plane displacement response at a noted fraction of ultimate load during CAI testing of sample Q8

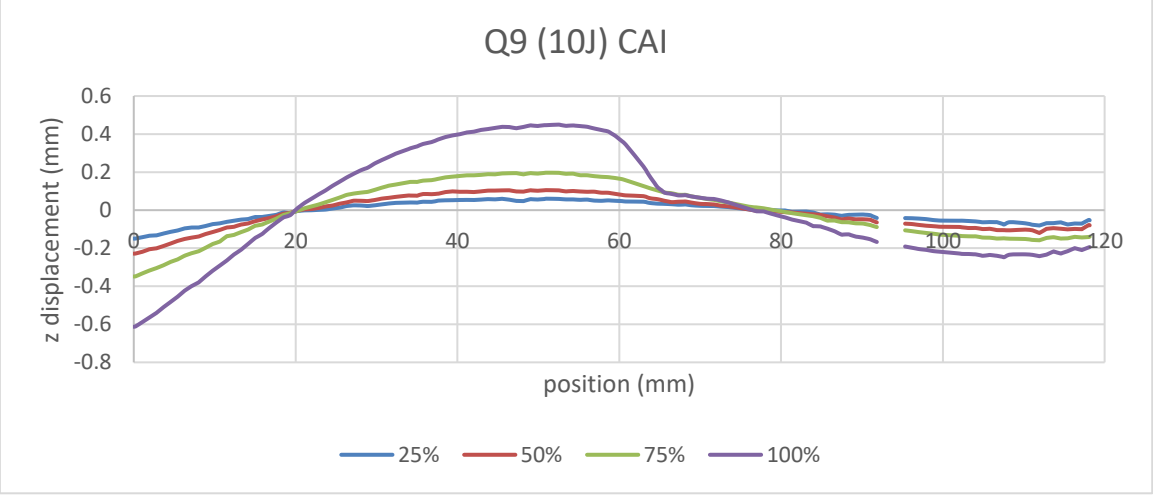

Figure 6-11 Out-of-plane displacement response at a noted fraction of ultimate load during CAI testing of sample Q9

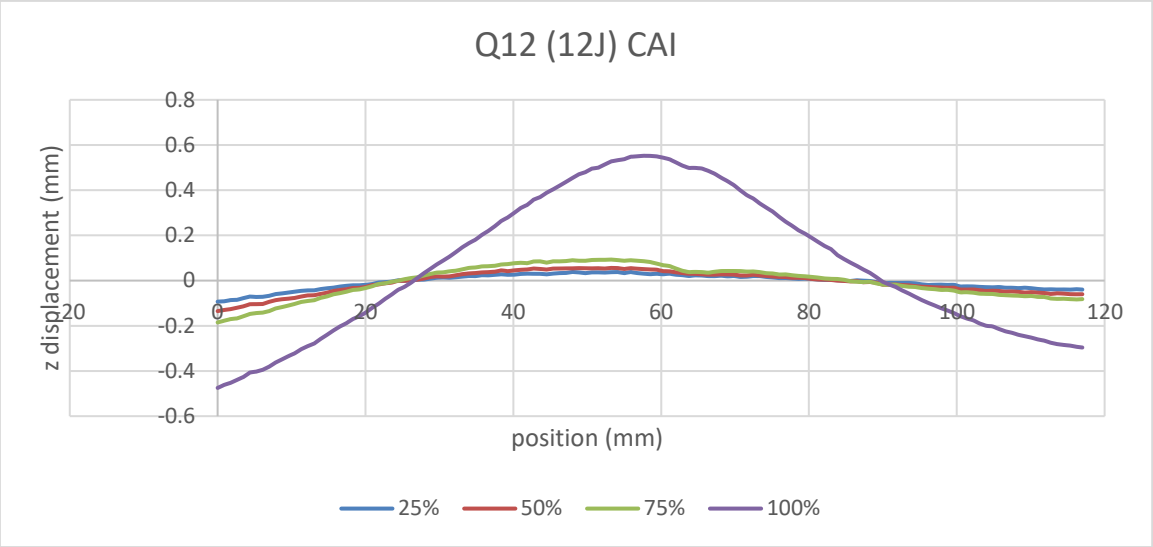

Figure 6-12 Out-of-plane displacement response at a noted fraction of ultimate load during CAI testing of sample Q12

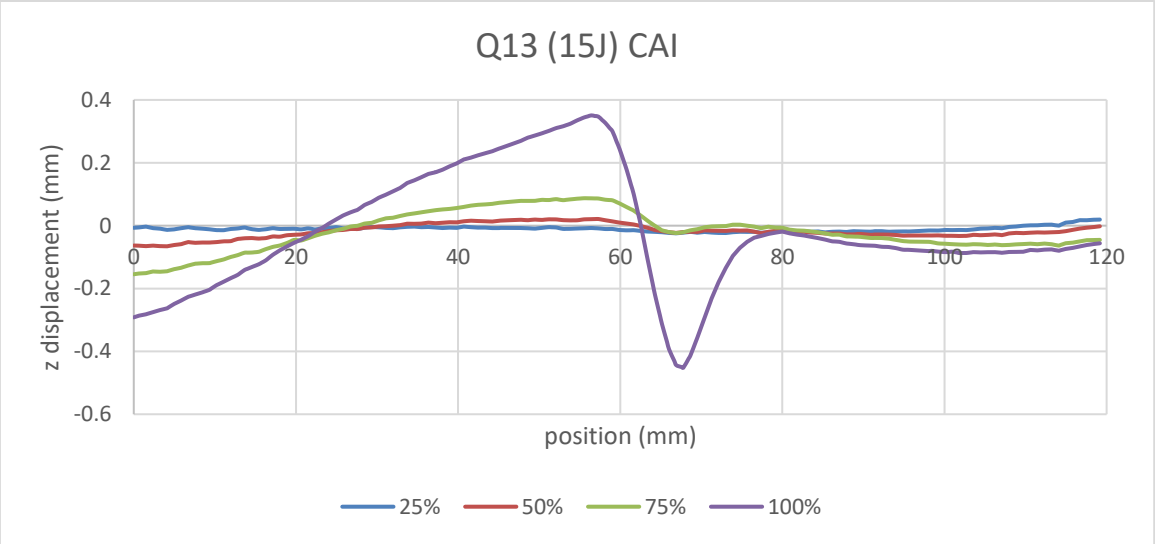

Figure 6-13 Out-of-plane displacement response at a noted fraction of ultimate load during CAI testing of sample Q13

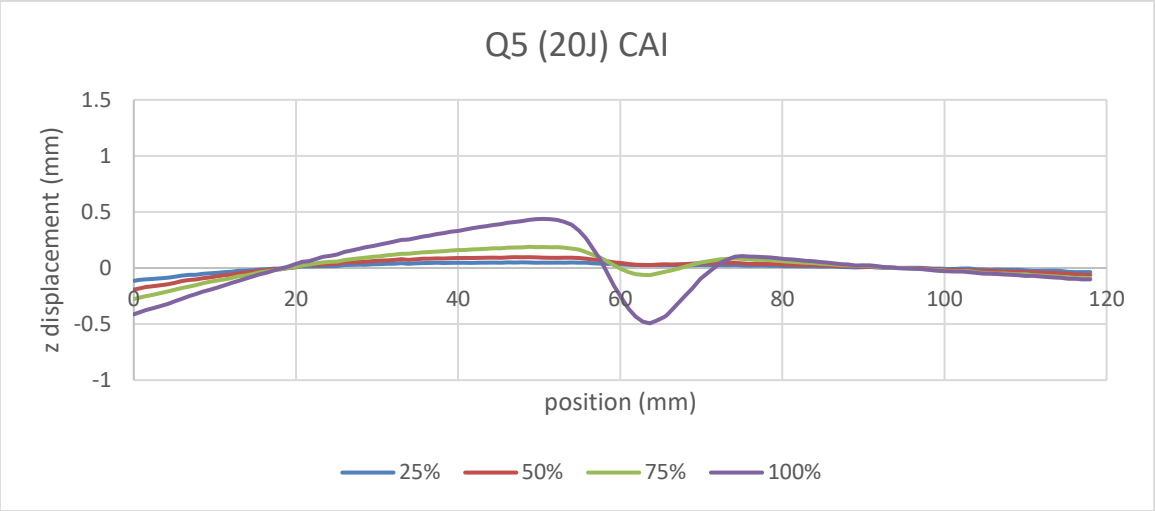

Figure 6-14 Out-of-plane displacement response at a noted fraction of ultimate load during CAI testing of sample Q5

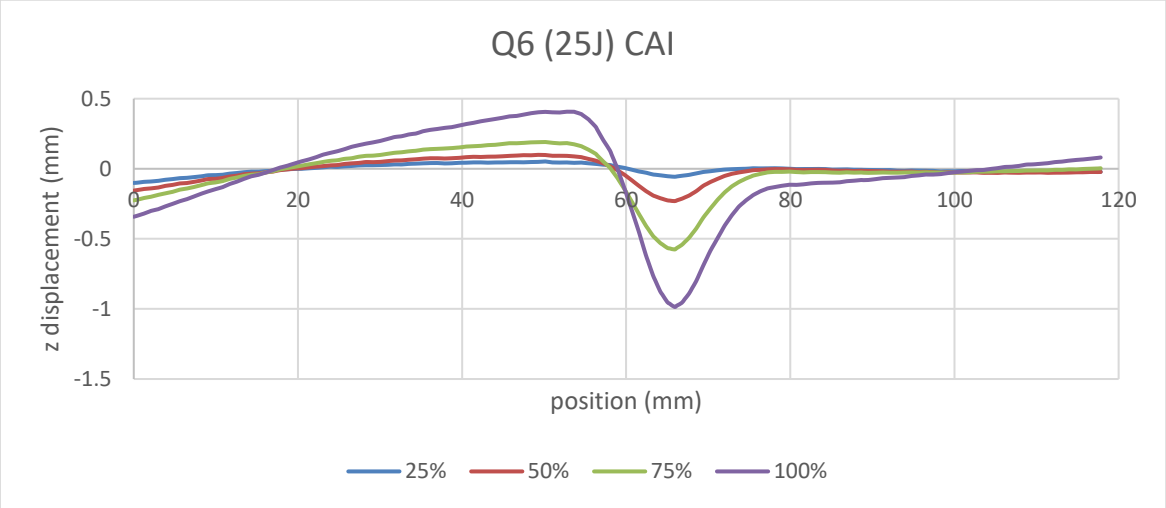

Figure 6-15 Out-of-plane displacement response at a noted fraction of ultimate load during CAI testing of sample Q6

7 POST IMPACT FATIGUE

Post-impact fatigue was observed after the impact tests. Apart from the compression after the impact test to determine the damage tolerance capability of the CFRP under impact damage, fatigue after impact is another presentation of the damage tolerance behaviour of carbon fibre composites. Moreover, the knowledge for fatigue behaviour of the impacted structure during service is more important to just design by the static residual strength. Among fatigue situations, the compression-compression fatigue is the most critical and common scenario as the most frequent loading case for top wing skins. Therefore, compressive fatigue tests were performed to explore fatigue life, delamination initiation, and subsequent propagation.

7.1 Experimental Testing Introduction

Although it is important to acquire the post-impact fatigue performance for CFRP, there is no currently agreed or published testing standard for post-impact fatigue testing so far. Thus, the static CAI jig was adapted for use in the subsequent cyclic period after impact testing. Fatigue testing was performed by using either a 250-kN Instron 8800 servo-hydraulic system or a 100-kN Instron system owing to load range and availability. The samples to be tested were impacted by the same energy levels in one group, and four different energy groups were used. The impact session was similar to that stated in Chapter 5.

The ratio between the maximum compressive stress and the nominal initial static residual compressive strength (RCS) was between 0.7 and 0.8 initially. The RCS used for each specimen was taken the result from the static compression test with the same impact energy. It is assumed with similar input (impact energy, specimen thickness), similar RCS would be expected among the samples impacted at same impact energy. Test frequency was limited to 5 Hz to avoid thermal heating, and the R ratio was 10 for all fatigue tests.

For all the samples, the testing was stopped when the sample was subjected to a total compressive failure or the cycle number hit 5×10^5. The common stop cycle for fatigue life is set from 1×10^6 to 1×10^7 cycles. But in this test, stop time is shortened due to following reasons: 1) failed samples had a fatigue life

significantly shorter than 5×10^5 cycles and the longest among which is still less than 1/3 of that.2) The non-failure samples, apart from one, exhibit a constant response behaviour without any change. During a test, loading was interrupted at intervals for ultrasonic and DIC measurements. The final fatigue life, C-scan detection for delamination size, displacement, and strain on the impacted surface were recorded for each specimen tested using the equipment provided.

A test matrix is presented in Table 7-1. In all, 19 samples were tested for 4 different impact levels. Four 12-J impacted samples were tested from 77% to 85% of their nominal RCS owing to the high threshold of delamination propagation. For other 3 higher energy levels at 15 J, 20 J, and 25 J, 5 samples underwent fatigue tests from 70% to 80% of their nominal RCS. The increment was set at 2% or 3% aiming to cover the range more evenly. Owing to the load control accuracy, the samples with a maximum load below 80 kN were tested using the 100-kN servo-hydraulic system. For the rest of the cases, a 250-kN machine was used.

The post-impact fatigue behaviour of composites in this test is presented in the following outputs: fatigue life, delamination area behaviour, and surface displacement and strain. The results were examined in terms of both general fatigue behaviour such as the fatigue life and detailed damage progression and surface monitoring of each specimen.

In general, the fatigue tests were straightforward as a consistent loading spectrum was applied. The sample was loaded initially at the set point load i.e. mean load calculated using the average of the maximum and minimum load value. The range of amplitudes was then added on to proceed with the cycles. All the samples resulted in either failure or were manually cut when 5×10^5 was reached. All eventually failed samples presented perfect compression failure with the through-width crushing. The observation under C-scan showed the progression of the delamination in the direction perpendicular to the loading direction, and the DIC revealed the subtle on-surface displacement change during the fatigue session. Even though most of the failed cases were monitored and recorded under both C-scan and DIC equipment, the sudden outbreak of compressive fatigue failure prevented successful capture using two

NDT techniques for two samples. In the later paragraphs of the chapter, fatigue life and on surface monitoring would be introduced.

Table 7-1 Fatigue testing matrix

Sample ID	Imp. Erg. (J)	RCS (MPa)	Level %	Max. Load (kN)	Min. Load (kN)	R ratio	Freq. (Hz)	Load Amp. (kN)	Mean Load (kN)
Q12-1	12	254	77%	-85.0	-8.50	10	5	38.2	-46.7
Q12-3	12	254	80%	-88.3	-8.83	10	5	39.7	-48.6
Q12-4	12	254	82%	-90.5	-9.05	10	5	40.7	-49.8
Q12-7	12	254	85%	-93.8	-9.38	10	5	42.2	-51.6
Q15-2	15	244	80%	-84.8	-8.48	10	5	38.2	-46.6
Q15-4	15	244	77%	-81.6	-8.16	10	5	36.7	-44.9
Q15-5	15	244	75%	-79.5	-7.95	10	5	35.8	-43.7
Q15-8	15	244	73%	-77.4	-7.74	10	5	34.8	-42.6
Q15-7	15	244	70%	-74.2	-7.42	10	5	33.4	-40.8
Q20-2	20	212	80%	-73.7	-7.37	10	5	33.2	-40.5
Q20-3	20	212	77%	-70.9	-7.09	10	5	31.9	-39.0
Q20-4	20	212	75%	-69.1	-6.91	10	5	31.1	-38.0
Q20-5	20	212	73%	-67.3	-6.73	10	5	30.3	-37.0
Q20-7	20	212	70%	-64.5	-6.45	10	5	29.0	-35.5
Q25-1	25	192	80%	-66.9	-6.69	10	5	30.1	-36.8

Q25-2	25	192	77%	-64.4	-6.44	10	5	29.0	-35.4
Q25-3	25	192	75%	-62.7	-6.27	10	5	28.2	-34.5
Q25-4	25	192	73%	-61.0	-6.10	10	5	27.5	-33.6
Q25-6	25	192	70%	-55.8	-5.58	10	5	25.1	-30.7

7.2 Fatigue Life

The fatigue life presents the general response to the damage tolerance performance of carbon fibre composites. The impacted panel exhibits different resistance to different fatigue loads and initial damage condition. A comparison of samples under different initial damage or similarly impacted samples under different maximum compressive cyclic load would give a clearer picture of the damage tolerance performance of the carbon fibre composites.

Table 7-2 Experimental results of fatigue after impact tests

Sample ID	Initial Damage Area (mm^2)	Nominal RCS Percentage	Max. Compressive Stress (MPa)	Total Cycles
Q12-1	810	77%	197	>500000
Q12-3	810	80%	204	>500000
Q12-4	890	82%	210	>500000
Q12-7	757	85%	217	146785
Q15-2	1132	80%	196	3560
Q15-4	1023	77%	189	274821
Q15-5	939	75%	184	61865
Q15-8	1021	73%	179	> 500000
Q15-7	1080	70%	172	> 500000
Q20-2	1453	80%	171	6142
Q20-3	1417	77%	164	16497
Q20-4	1515	75%	160	31814
Q20-5	1484	73%	156	11300
Q20-7	1438	70%	149	>500000
Q25-1	1544	80%	155	1906
Q25-2	1598	77%	149	6501
Q25-3	1504	75%	145	8966
Q25-4	1552	73%	141	45465
Q25-6	1497	70%	129	> 500000

All the testing samples with the initial damage area, the maximum compressive load applied, the ratio of the maximum load to the residual compressive strength, and the failure cycle number are shown in Table 7-2.

The tested samples were impacted in the same manner as mentioned in Chapter 5. The initial damage was examined using the C-scan. The initial damage induced by the same impact has scattered but not significantly. For each impact energy level, the damage area values are around a value that can be distinguished from others sourced from another impact energy. Of note, with the same increase of 5-J impact energy, an increase in the damage area from 20 J to 25 J (from around 1400 mm^2 to around 1500 mm^2) is significantly smaller than the increase from 15 J to 20 J (from around 1000 mm^2 to around 1400 mm^2).

Table 7-3 Mean damage area and standard deviation

Impact Energy	Mean damage area (mm^2)	Std. Dev.
12J	817	47.5
15J	1039	64.6
20J	1462	34.8
25J	1539	36.3

The mean damage area and standard deviation were calculated for all fatigue testing samples, as shown in Table 7-3. The standard deviation shows that higher impact damage will result in a more stable initiation damage area while inconsistencies would be observed for lower energy impact.

Similar to Figure 5-8, impact energy against damage area is shown in Figure 7-1 with the input of all fatigue samples. As the trend found in the previous plot, the damage area from a 20-J impact does not sit on the trendline but above it. The response was said to be a non-linear response to the damage area, and impact energy should be considered when a certain level of energy is exceeded. Besides, the scatter of data points for 12-J and 15-J impact group helps visualise the standard deviation.

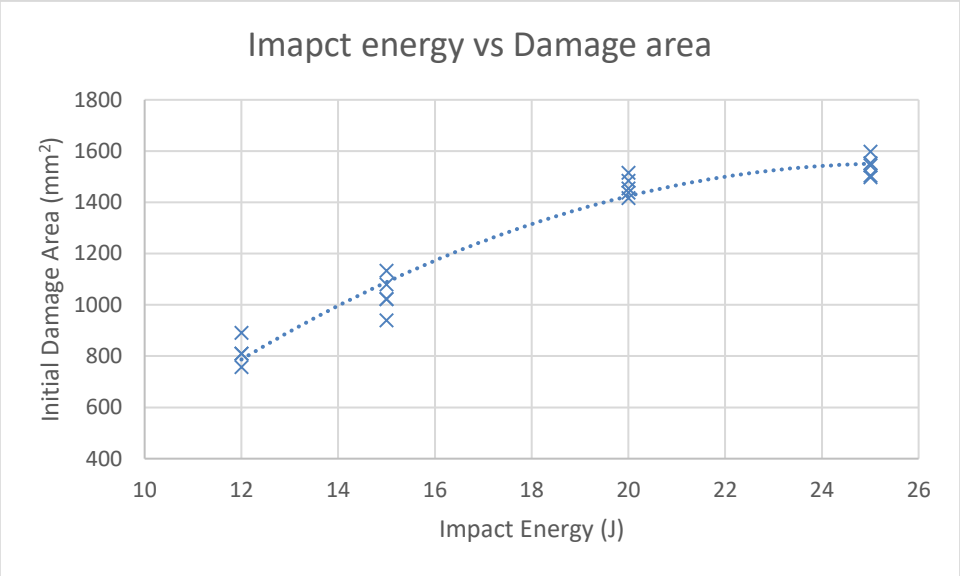

Figure 7-1 Impact energy vs. damage area plot for fatigue test samples

With similar initial impact-induced damage established internally in each sample, it was assumed that the initial condition of each sample was similar in each impact energy group. The diversity of internal damage caused by LVI still exists even though the sample dimensions and properties are controlled.

Samples with different damage areas were tested at a range of different stresses to maintain the ratio of fatigue stress to CAI stress. From Table 7-2, it is found that samples with a small impact damage area had greater fatigue strength and longer lives than samples with a large damage area, despite being tested at the same ratio of fatigue to static strength.

Three graphs were plotted to illustrate the fatigue life trend for impact-damaged composites based on the table above.

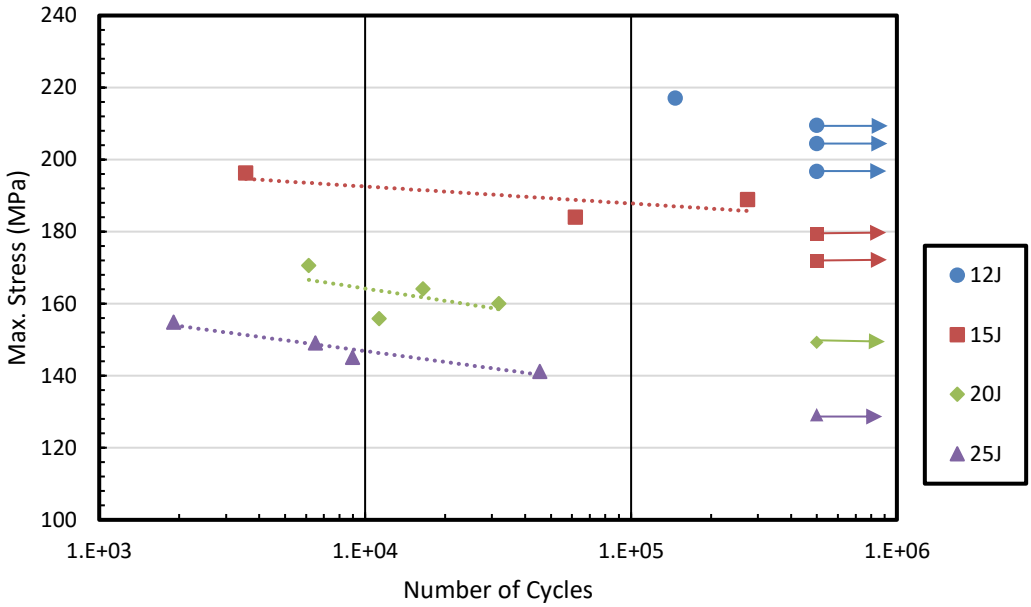

Figure 7-2 S-N curve for samples impacted at different energy levels

The S-N curve for each energy group is plotted in Figure 7-2. The arrow on the graph represents each run-out (cycle number reached 5×10^5) sample at a certain stress level. The figure reveals the number of cycles the damaged panel will sustain at a certain stress level. Unlike metal that presents a significant non-linear drop of stress level corresponding to a longer fatigue life, composites exhibit a gentle, linear slope in the stress drop.

Within each group under the same impact energy, the decrease in maximum cyclic stress level leads to an increase in the fatigue life. For instance, with a decrease of almost 6% in maximum stress level, the fatigue life expanded 3 times for the Q12 series samples. A similar general trend can also be observed in other groups but with some exceptions. In the case of samples Q15-4 (max. load 189 kN, 77% RCS) and Q20-4 (max. load 160 kN, 75% RCS), an oddly longer fatigue life than Q15-5 (max. load 184 kN, 75% RCS) and Q20-5 (max. load 156 kN, 73% RCS) can be observed with lower stress levels. The unusual case is attributed to the diversity of internal damage which cannot be simply presented from initial damage area. Different damage mechanisms of out-of-plane impact contribute differently to damage progression and failure.

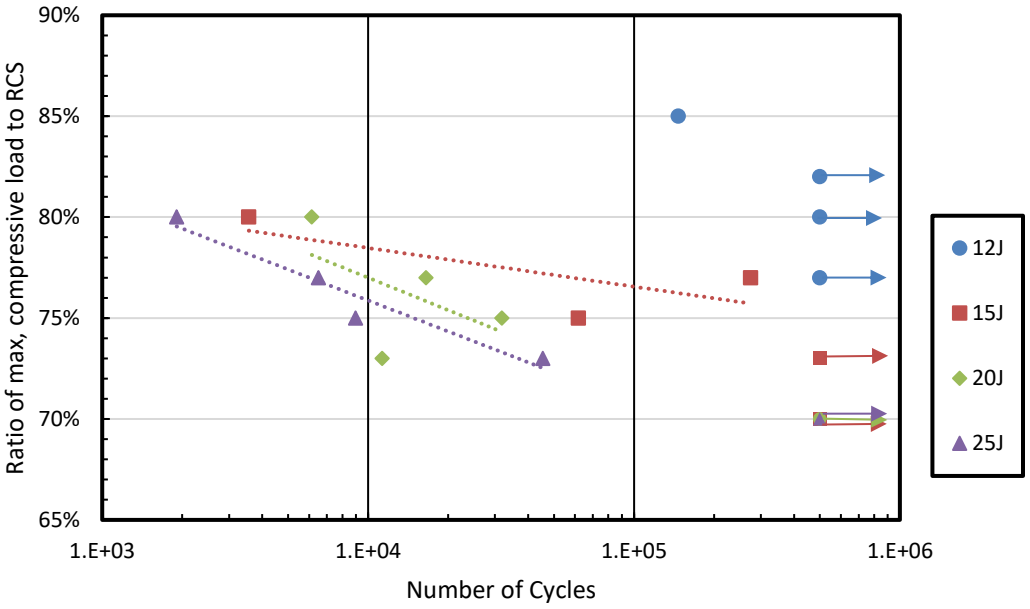

Figure 7-3 Max. stress vs. fatigue life of samples impacted by different energy levels

The ratio of maximum cyclic stress to its RCS is another important index of the damage tolerance performance of composites. Previous studies have reported that under compression-compression in-plane fatigue, the delamination propagation and final failure could happen once a threshold stress of around 70% of the static compression strength is exceeded.

In Figure 7-3, the ratio of 70% is the threshold to ensure non-failure within a certain number of cycles. In the Q25 and Q20 series, the sample under 70% of RCS hit the run-out criteria. Two samples in the Q15 series were run-out as the ratio could be lifted to 73% of the RCS. Furthermore, the Q12 series remained undamaged and achieved an astonishing 82% non-failure output. The ratio of non-failure at 70% is acceptable for most BVID samples, but the ratio can be lifted as less damage exists in composites.

Of note, the figure only classifies the samples as “non-failure”. The classification does not exclude the existence of subtle internal damage growth (i.e.

delamination propagation). Further detailed checks to explore the “non-growth” are described in the following sections.

7.3 Monitoring of Damage Changes during Fatigue Cycling

Fatigue progress was obtained by both C-scan and DIC approaches and the response behaviour was found to be different between failed and “run-out” samples. The fatigue failure progress in the impacted samples exhibits a similar pattern in most cases, despite different initial impact energy levels and maximum stress percentage of RCS. The observation of such progress enables the presentation of the differentiation of several periods during failure. Three or four different stages can be distinguished from C-scan and DIC observation. The progress is directly conducted using C-scan delamination dimension detection and out-of-plane displacement obtained from DIC. Different from some previous research choosing the back surface, the impacted surface was observed under DIC equipment in this study. Butler et al (2012) used DIC to observe the strain level change at a single artificial embedded delamination. The PTFE film was placed at the near camera interface to simulate the delamination on the back face. Experimental observation on impacted quasi-isotropic laminate showed an early popped-out area on the back surface but not effecting the delamination area under C-scan (Ogasawara et al., 2013). Therefore, observing the surface deformation on the impacted surface is selected. The selection can not only show the stages of the progression related to the surface deformation but also provide a more realistic scenario to a real-world situation.

For the results, the typical stages under C-scan detection can be divided into delamination initiation, delamination propagation, and through with failure. Meanwhile, the progress observed from DIC involved local buckling progression. The appearance of detectable delamination area propagation was late during fatigue life, averaging at 93.6% of the fatigue life from the gathered data in the test session.

It was also noticeable the initial z-displacement direction varied among the test samples. The behaviour was not identical between an initially inward bent and an initially outward bent sample even though they were all “run-out”. Figure 7-4

Sketch of outward and inward displacement shows the direction of inward and outward displacement relative to the DIC camera position.

Table 7-4 shows the initial z-displacement direction for all the noted samples. The following part will describe the response under C-scan detection and DIC measurement for the failed sample with initial inward and outward bending and “run-out” samples in the same approach.

Table 7-4 Initial z-displacement direction under load

Sample ID	Nominal CAI Percentage	Total Cycles	Initial z-displacement direction
Q12-1	77%	>500000	Inward
Q12-3	80%	>500000	Inward
Q12-4	82%	>500000	Inward
Q12-7	85%	146785	Outward
Q15-2	80%	3560	Inward
Q15-4	77%	274821	Inward
Q15-5	75%	61865	Inward
Q15-8	73%	> 500000	Outward
Q15-7	70%	> 500000	Inward
Q20-2	80%	6142	Inward
Q20-3	77%	16497	Inward
Q20-4	75%	31814	Inward
Q20-5	73%	11300	Inward
Q20-7	70%	>500000	Outward
Q25-1	80%	1906	N/A
Q25-2	77%	6501	Inward
Q25-3	75%	8966	Inward
Q25-4	73%	45465	Inward
Q25-6	70%	> 500000	Inward

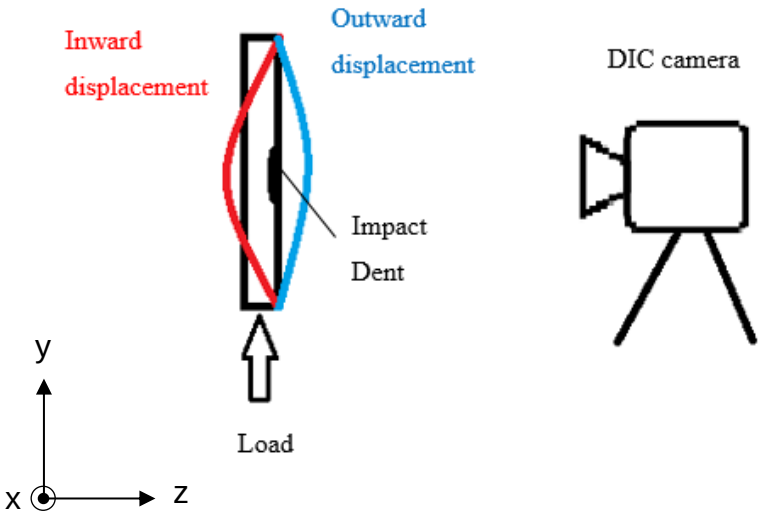

Figure 7-4 Sketch of outward and inward displacement

7.3.1 Samples under 12-J Impact

Samples under 12-J impact had the smallest impact-induced damage and exhibited very good damage tolerance behaviour. Three of four samples fulfilled the “run out” criteria, and one sample failed at 146785 cycles. The threshold to trigger the failure within 500000 cycles was lifted to 85%, substantially higher than that for the other impact group.

Sample Q12-7 sustained a maximum compressive load of 85% of its RCS and failed at 146785 cycles. As mentioned in the section 5.4.1, the central grey area was the detected delamination. Three ring-shaped grey area the supportive washer beneath rather than the delamination area. And the rectangular contour was the tape on the back face of the testing sample to prevent the interference from water. The C-scan detection firstly identified the change in damage shape at N = 50000 (see Figure 7-5). The samples were deformed during the fatigue session (see Figure 7-6). At the initial loading period, the upper part of the panel had positive deformation towards the camera and the lower part had negative deformation away from the observation point. With the cycle number added, the deformation did not change much until it reached N = 100000, and a more concentrated deformation was presented. Meanwhile, the very top edge of the panel became more deformed away from the camera which is another sign of the greater central extrusion.

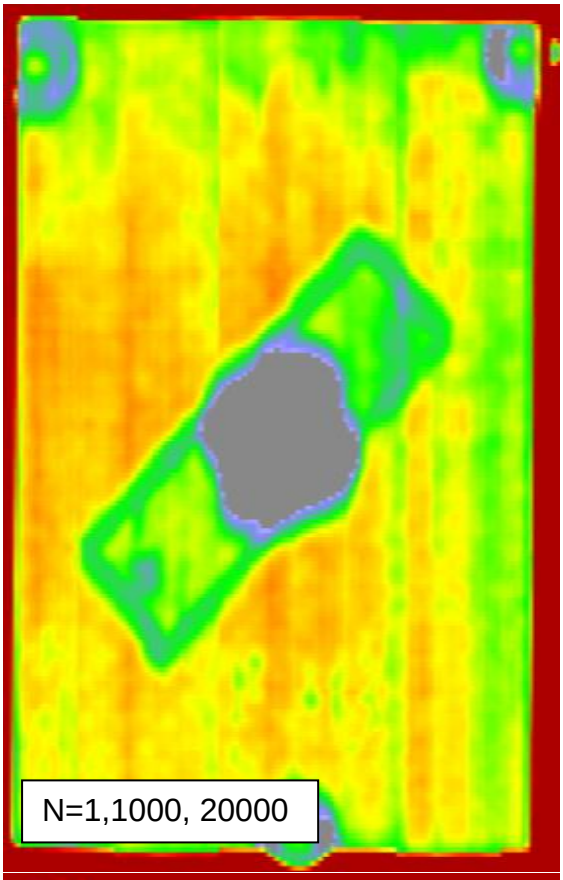
N=1,1000, 20000

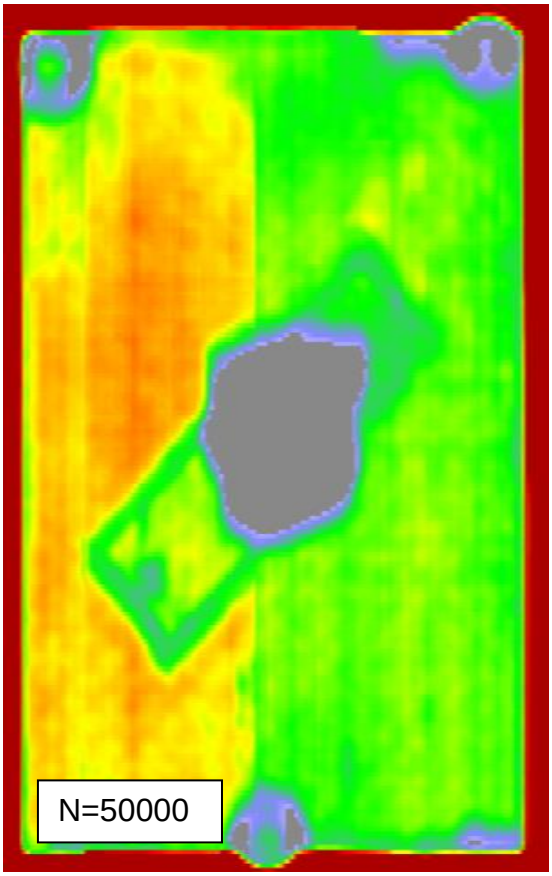
N=50000

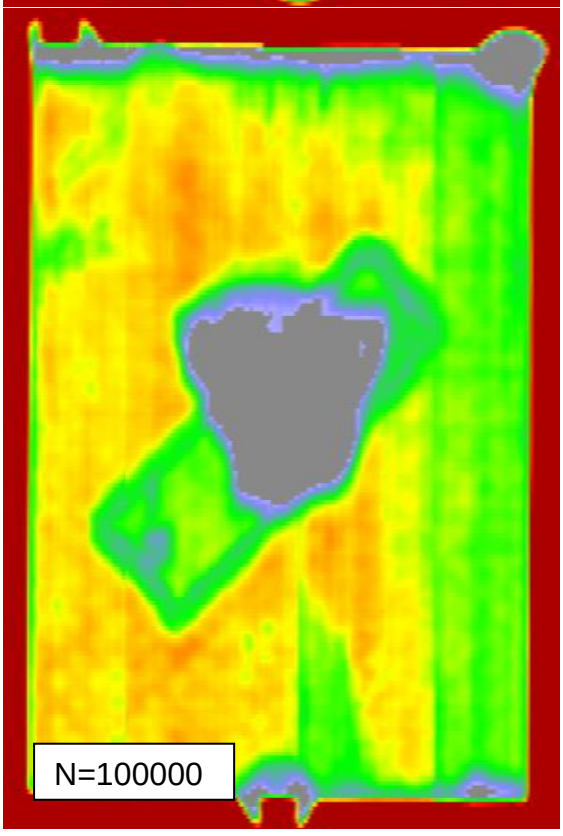
N=100000

Figure 7-5 Captured C-scan image of sample Q12-7 (max. load 217 kN, 85% RCS) at noted cycle number

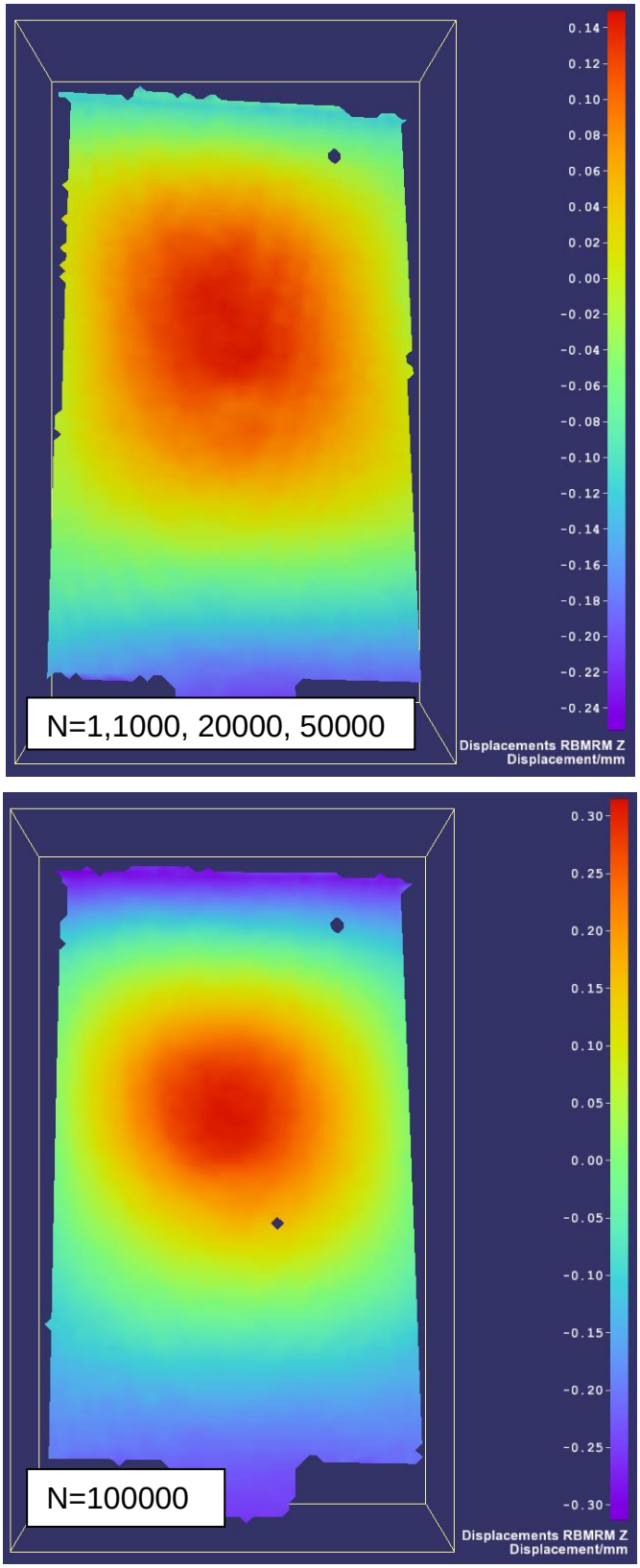

Figure 7-6 Out-of-plane displacement (removal of rigid movement) of sample Q12-7 (max. load 217 kN, 85% RCS) at noted cycle number

A clearer trend can be found in a midline z-displacement graph shown in Figure 7-7. At the beginning (N = 1), the dent area could be depicted even as the whole central area popped out. As the cycle number reached 10000 and 50000, the displacement vertex continued to increase in a relatively slow manner from 0.158 mm to 0.211 mm at 50000 cycles. In the meantime, the surface out-of-plane deformation looked similar in pattern. The obvious change in z-displacement only occurred at N = 100000 where the gathered data checkpoints showed further bending from the top to the central part of the panel. The trend started from N = 50000, but the displacement was minor at the top panel from -0.141 mm to -0.145 mm. A significant difference was observed from N = 50000 to N = 100000. Not only did the positive displacement vertex increase to 0.31 mm but the negative deformation also increased to -0.27 mm. The sample eventually failed at N = 1,46,785, but the image was unfortunately not captured during the test.

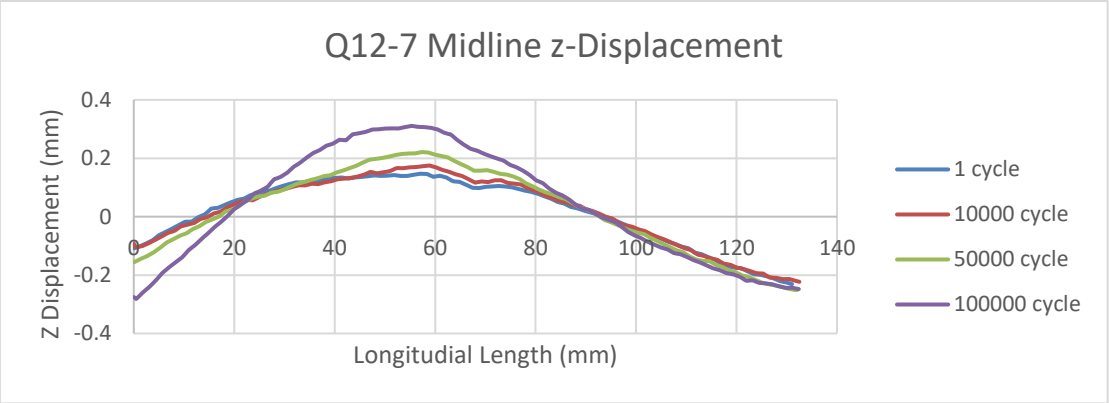

Figure 7-7 Midline z-displacement at noted cycle number of sample Q12-7 (max. load 217 kN, 85% RCS)

The “run-out” criteria, mentioned in previous chapters, were set at 500000 cycles. The number of cycles in real life can ensure the structural integrity and safety during routine service life. AS stated in the ASTM 7137D, the properties obtained using this test method can provide guidance regarding the anticipated damage tolerance capability of composite structures of similar material, thickness, stacking sequence, and so forth. However, it must be understood that the

damage tolerance of a composite structure is highly dependent upon several factors including geometry, stiffness, support conditions, and so forth. Significant differences in the relationships between the existent damage state and the residual compressive strength can result from the differences in these parameters. For example, residual strength and stiffness properties obtained using this test method are more likely to reflect the damage tolerance characteristics of an un-stiffened monolithic skin or web than of a skin attached to a substructure that resists out-of-plane deformation.

An example of “run-out” sample can be found below. Sample Q12-4 is a sample impacted by 12-J energy and the maximum compressive load applied during the fatigue session was 0.82 RCS at 210 MPa. The sample sustained the whole 500000 cycles of cyclic load, and the C-scan observation and DIC capture did not show any trace of delamination propagation.

Sequential C-scan images during the fatigue period showed no trace of delamination as the internal delamination retained the same shape at all the checkpoints (see Figure 7-8; images at more checkpoints provided in the appendix). But the no-growth was still sceptical because based on the knowledge of the previous failed case, there still existed the possibility of small delamination growth within the overall initial delamination area boundary. To ensure no-growth behaviour of the sample at such conditions, captures from DIC were used to find the traces of delamination propagation.

Out-of-plane displacement at certain checkpoints is shown in Figure 7-9. In the first cycle, the panel presented a similar inward bending like other testing samples. With the added cycles, the displacement pattern remained the same with the initial image. No obvious changes were observed from the DIC capture.

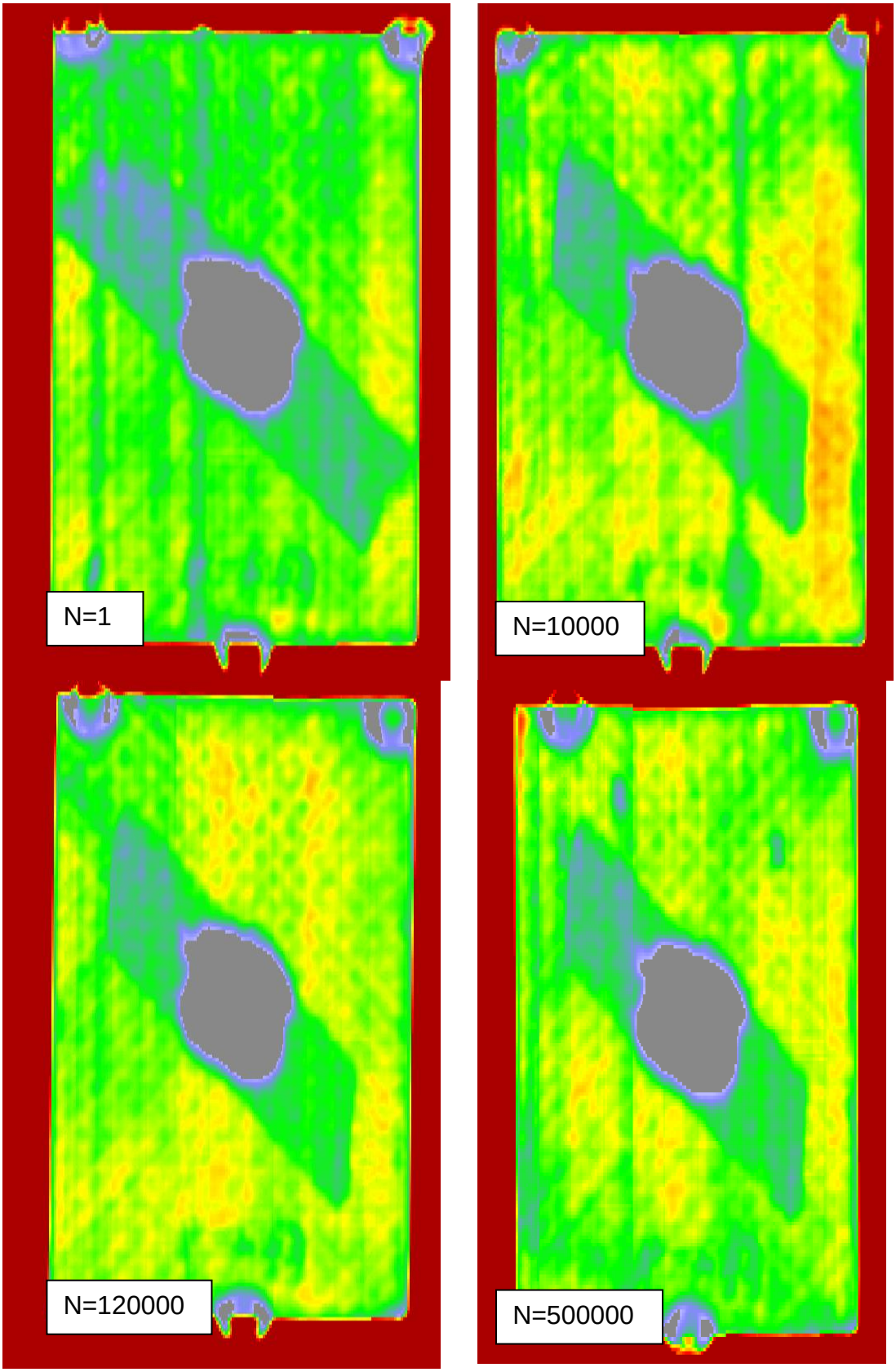

Figure 7-8 Captured C-scan image of sample Q12-4 (max. load 210 kN, 82% RCS) at noted cycle number

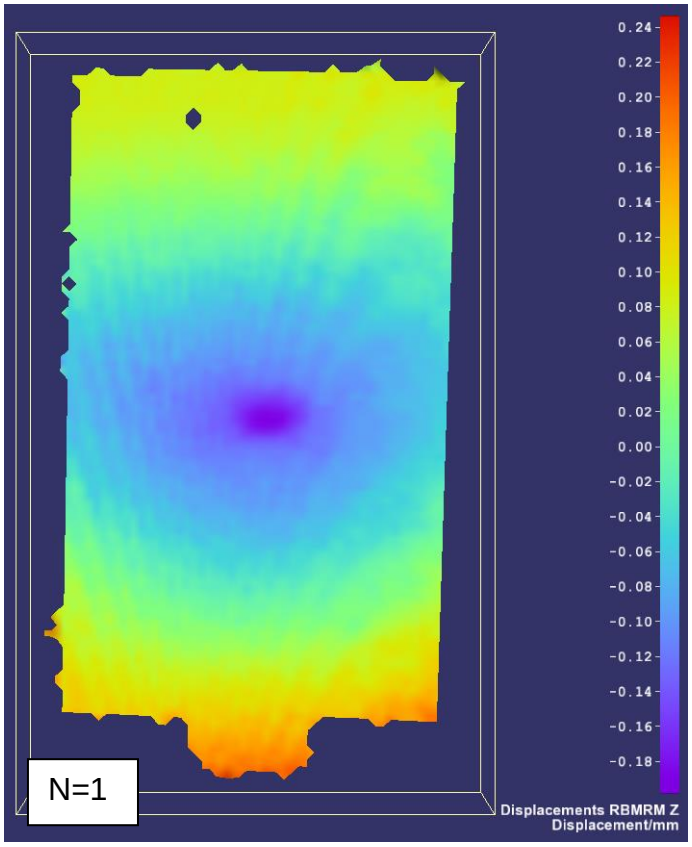
0.24
0.22
0.20
0.18
0.16
0.14
0.12
0.10
0.08
0.06
0.04
0.02
0.00
-0.02
-0.04
-0.06
-0.08
-0.10
-0.12
-0.14
-0.16
-0.18
N=1
Displacements RBMRM Z
Displacement/mm

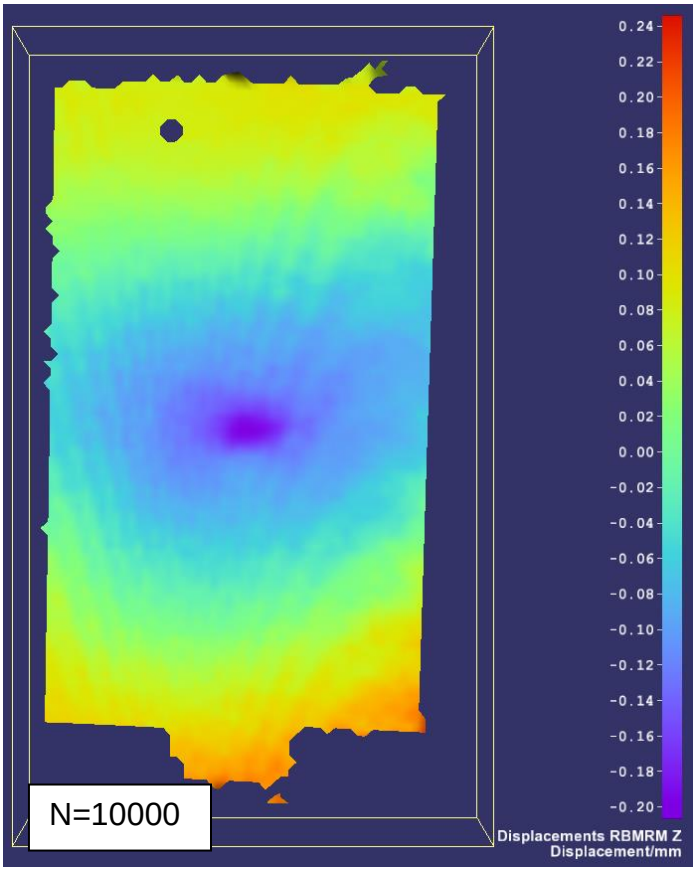
0.24
0.22
0.20
0.18
0.16
0.14
0.12
0.10
0.08
0.06
0.04
0.02
0.00
-0.02
-0.04
-0.06
-0.08
-0.10
-0.12
-0.14
-0.16
-0.18
-0.20
N=10000
Displacements RBMRM Z
Displacement/mm

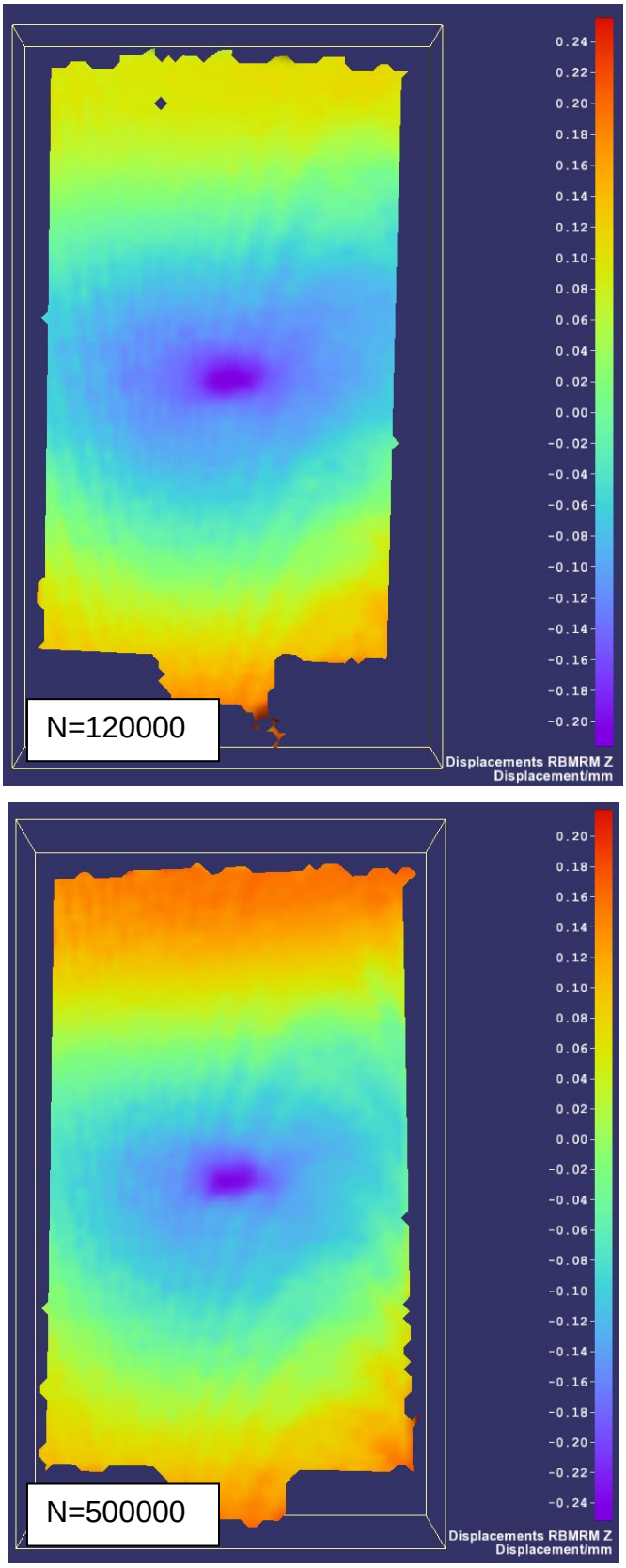

Figure 7-9 Out-of-plane displacement (removal of rigid movement) of sample Q12-4 (max. load 210 kN, 82% RCS) at noted cycle number

Similarly, the midline z displacement is plotted in Figure 7-10. The 1st cycle line shows the outline of the midline displacement in the z direction under maximum compressive load. The panel presented a similar inward bending with the most deformed position at the dent area. Initially, the deformed dent area reached -0.18 mm. The deformation remained almost identical and even passed some substantial cycles. A mere increase of 0.04 mm in the maximum deformation was obtained after another 250000 cycles. This state was observed for at least another 200000 cycles afterwards. Even though the progression was unnoticeable in the C-scan detection, the traits of slow propagation were captured using the DIC equipment.

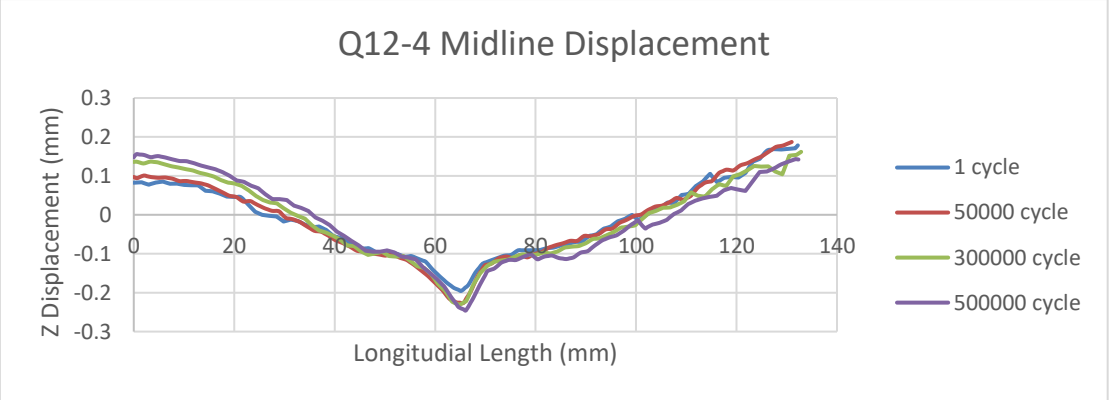

Figure 7-10 Midline z displacement at a noted cycle number in sample Q12-4 (max. load 210 kN, 82% RCS)

Similar behaviour like Q12-4 was also observed for samples Q12-1 and Q12-3, as shown in Figure 7-11 and Figure 7-12, respectively.

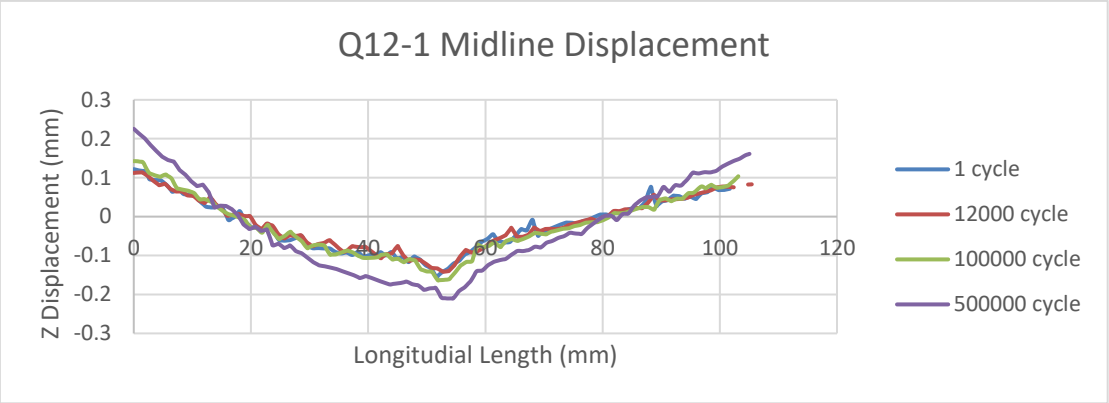

Figure 7-11 Midline z displacement at a noted cycle number in sample Q12-1 (max. load 197 kN, 77% RCS)

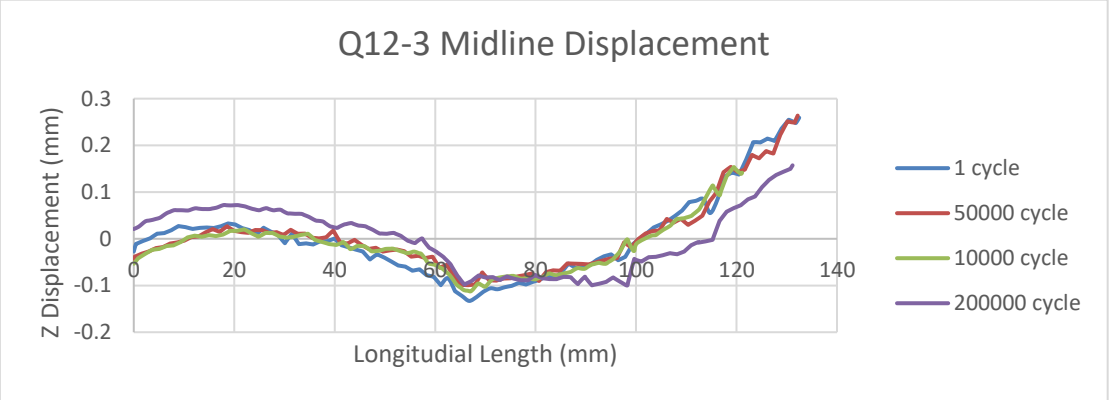

Figure 7-12 Midline z displacement at a noted cycle number in sample Q12-3 (max. load 204 kN, 80% RCS)

7.3.2 Samples under 15-J Impact

Samples under 15-J impact behaved differently compared to the less impacted 12-J group. The run-out criterion for the group was over 73%. Two samples tested at 70% and 73% reached the run-out criterion, and the remaining 3 (80%, 77%, and 75%) failed at N=3560, 274821 and 61865 respectively.

An example of a failed sample is Q15-5. The panel failed after 61865 cycles at 0.75 RCS (see Figure 7-13 and Figure 7-14). The impact-induced delamination is presented at 0 cycles. The delaminated area was detected at N = 56650 when the delamination initiation at the transversal direction was observed. The delamination propagation accelerated after the initiation. The final developed through-width delamination caused the eventual failure as the through-width

delamination degrades the stiffness of the panel drastically. The delamination grew along the transversal direction (perpendicular to loading direction) and grew wider in the longitudinal direction to form an elliptical area at the delamination front. Another sudden change can be found at N = 61850, 15 cycles before the eventual failure. An area from the impact centre directed to the lower right corner was observed. The progression showed the delamination area propagated in more than one direction under the fatigue cycling.

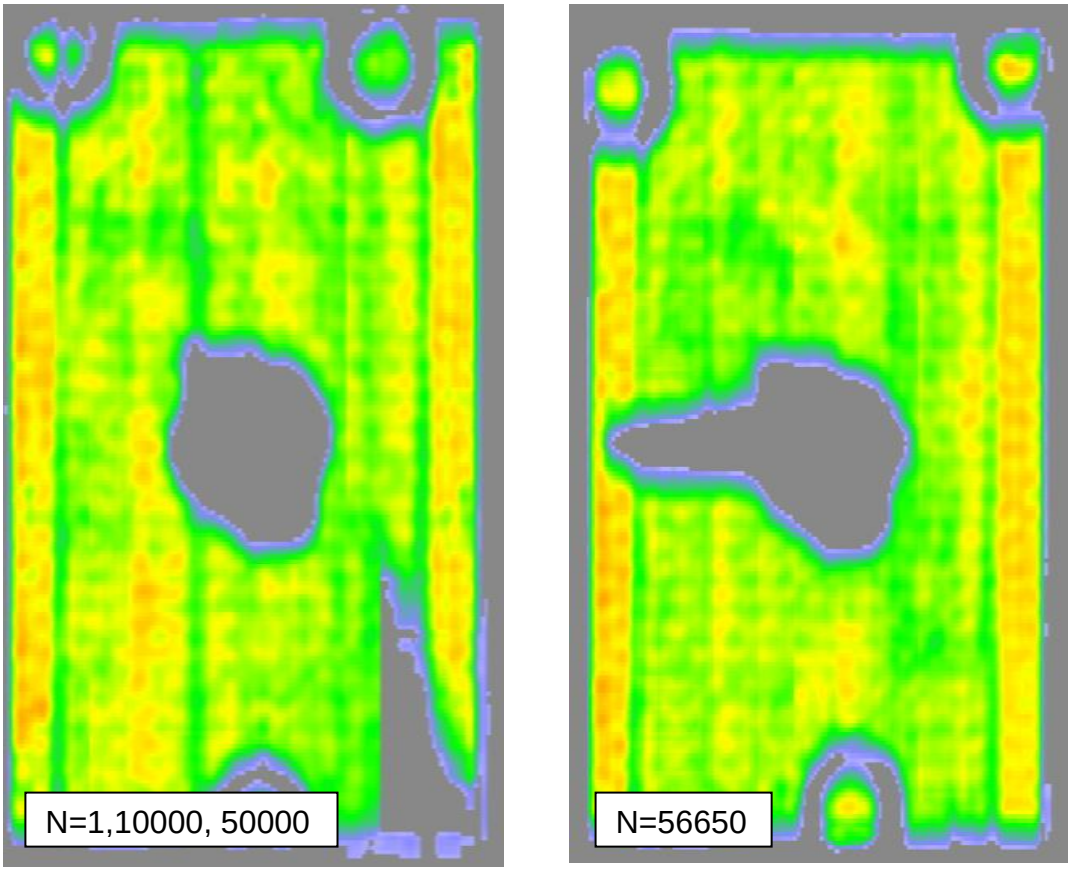

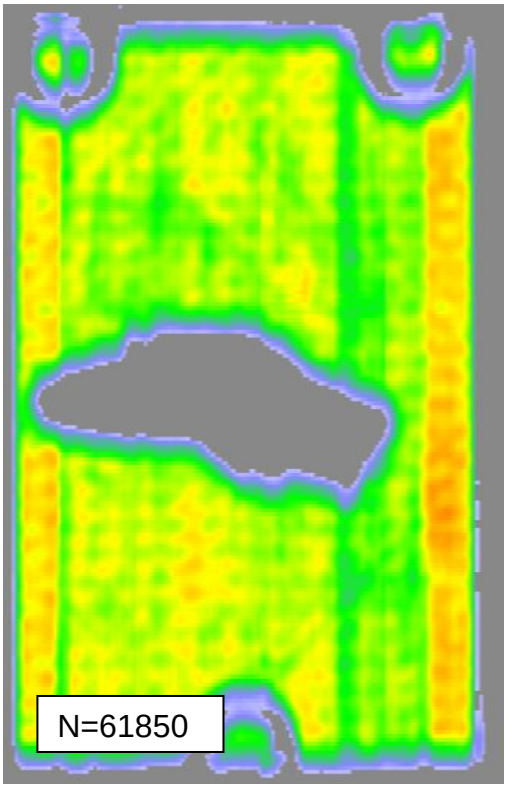

Figure 7-13 C-scan image of sample Q15-5 (max. load 184 kN, 75% RCS) at a noted cycle

Out-of-plane displacement of sample Q15-5 is shown in Figure 7-14. The displacement presented is the one in which rigid movement was removed to obtain higher accuracy and minimise system error. As shown in the figure, at the beginning of fatigue life (N = 1), delamination buckling had one half-wavelength bending inward with a displacement of -0.3 mm. When the cycle number increased to 50000, the delamination buckling mode was changed to two half-wavelengths, one positive and one negative. The displacement soon increased as the buckled area grew to the left margin, and the maximum z displacement had also increased to 0.45 mm. When approaching failure, a further buckled area was observed from the impact centre to the lower right corner.

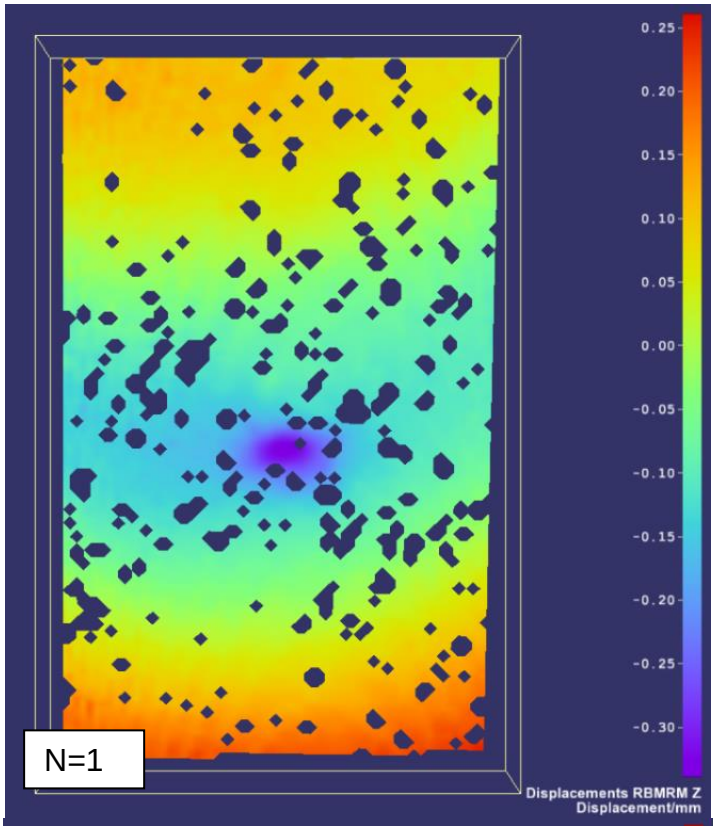
0.25
0.20
0.15
0.10
0.05
0.00
-0.05
-0.10
-0.15
-0.20
-0.25
-0.30
N=1
Displacements RBMRM Z
Displacement/mm

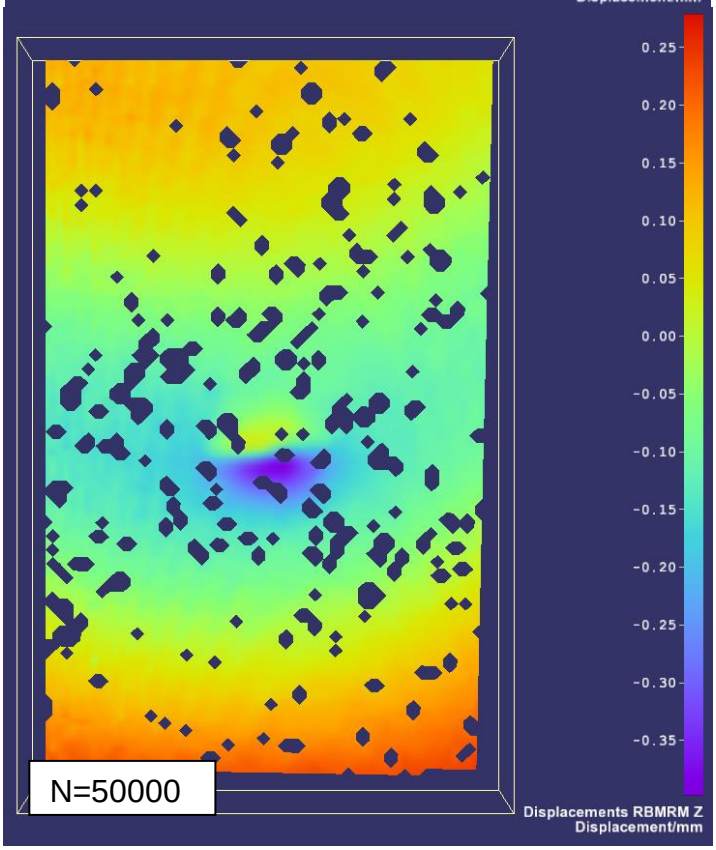
0.25
0.20
0.15
0.10
0.05
0.00
-0.05
-0.10
-0.15
-0.20
-0.25
-0.30
-0.35
N=50000
Displacements RBMRM Z
Displacement/mm

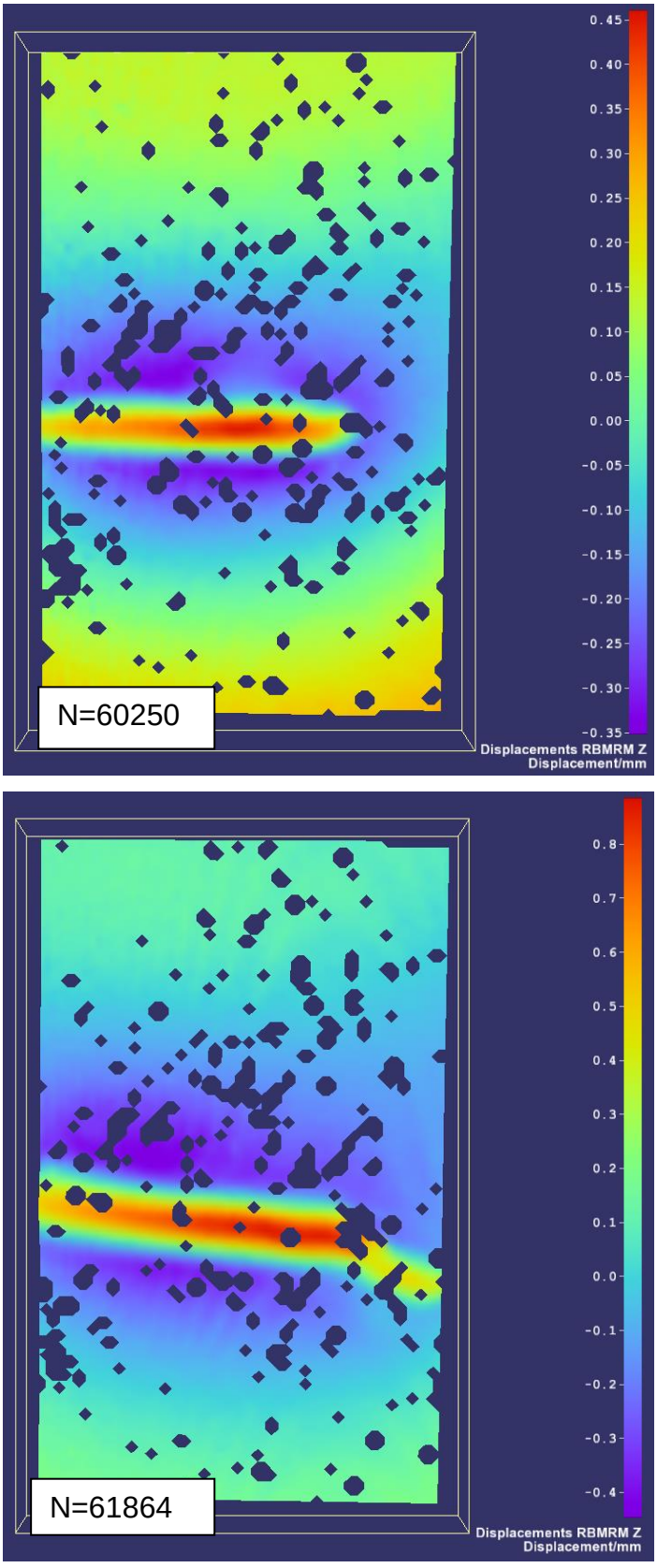

Figure 7-14 Out-of-plane displacement (removal of rigid movement) in sample Q15-5 (max. load 184 kN, 75% RCS) at a noted cycle number

Normal displacement data were extracted from the DIC data on the midline of the sample surface and plotted as a function of longitudinal position in Figure 7-15. At the beginning of fatigue, the impact-damaged area underwent a simple inwards bending displacement. The most deformed area was the area adjacent to the dent, with an initial deformation of -0.37 mm. As the cycle number increased, the top surface of the damaged area generated the local buckling towards the outer side of the panel at N = 50000 while the upper side of the dent area popped out. With the extension of this buckled area to the side of the sample, the displacement also increased at the same time. The extensive extrusion measured 0.43 mm. The peak continued to increase to 0.79 mm when approaching the rupture.

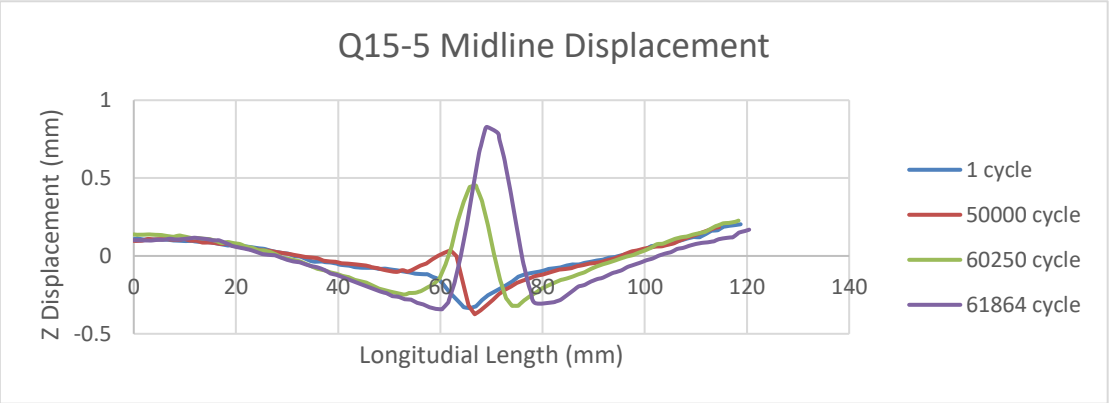

Figure 7-15 Midline z displacement at a noted cycle number in sample Q15-5 (max. load 184 kN, 75% RCS)

A similar progression from inward bending to eventual failure was observed from samples Q15-2 and Q15-4, as shown in Figure 7-16 and Figure 7-17, respectively.

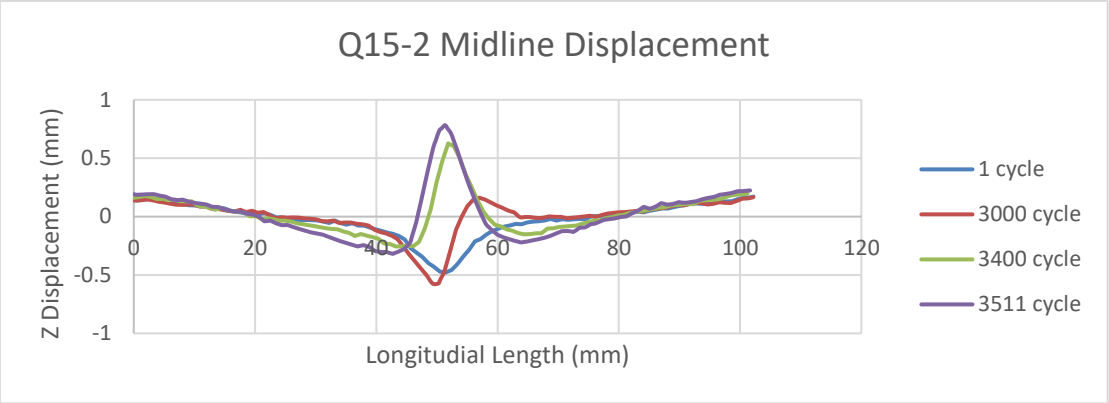

Figure 7-16 Midline z displacement at a noted cycle number in sample Q15-2 (max. load 196 kN, 80% RCS)

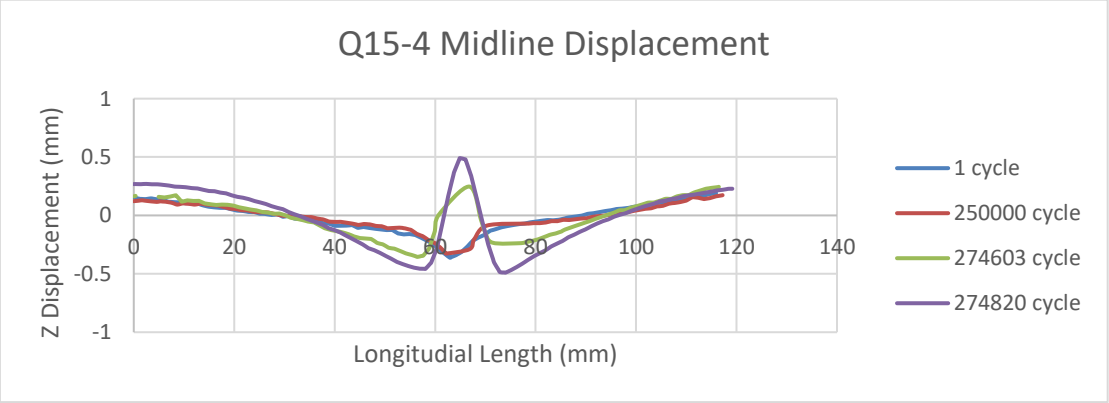

Figure 7-17 Midline z displacement at a noted cycle number in sample Q15-4 (max. load 189 kN, 77% RCS)

As some failed samples had outward initial bending, some “run-out” samples showed that trait as well. Sample Q15-8 is one case tested at 73% of its nominal compressive strength after an impact testing at 15-J energy. The sample remained intact during all 500000 cycles of loading. The C-scan of the sample showed a similar trend along the cycles as its “run-out” peers (see Figure 7-18). The detected delamination shows an identical shape at various checkpoints in the fatigue session.

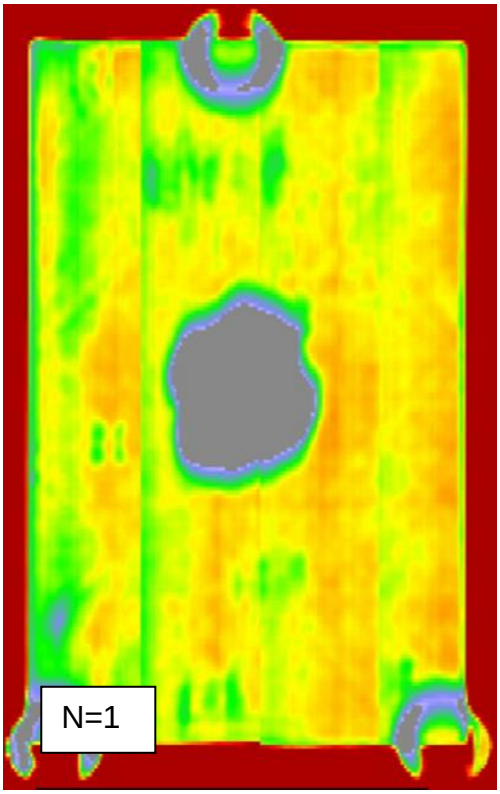
N=1

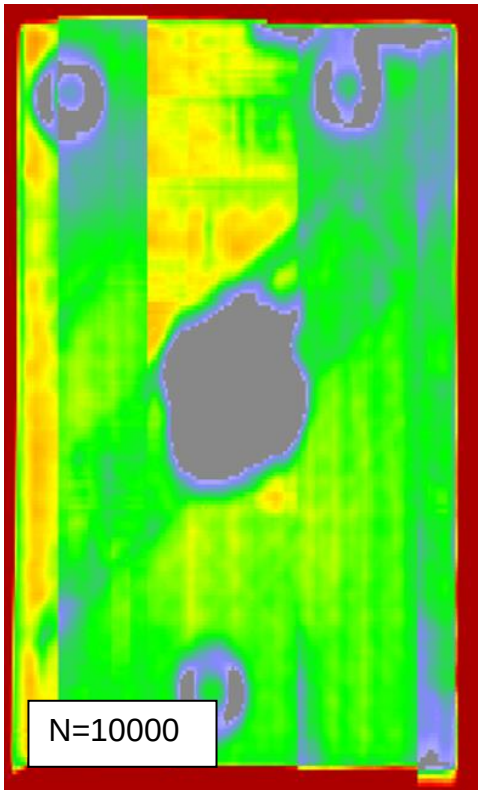
N=10000

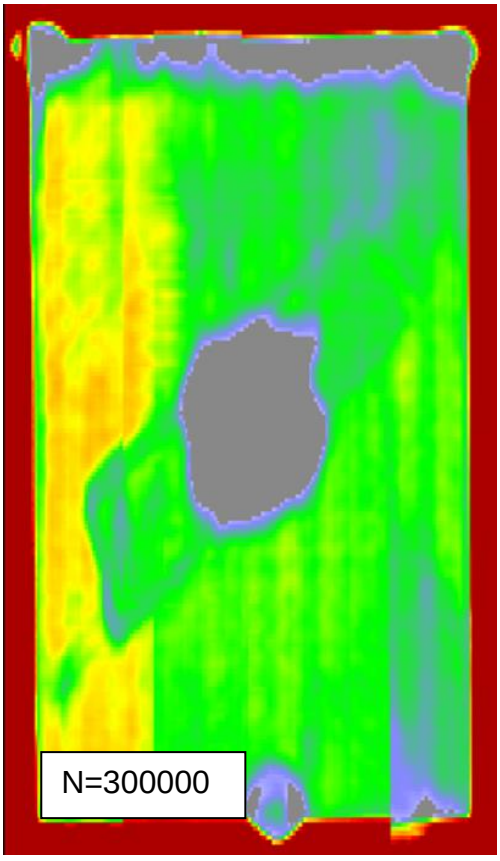
N=300000

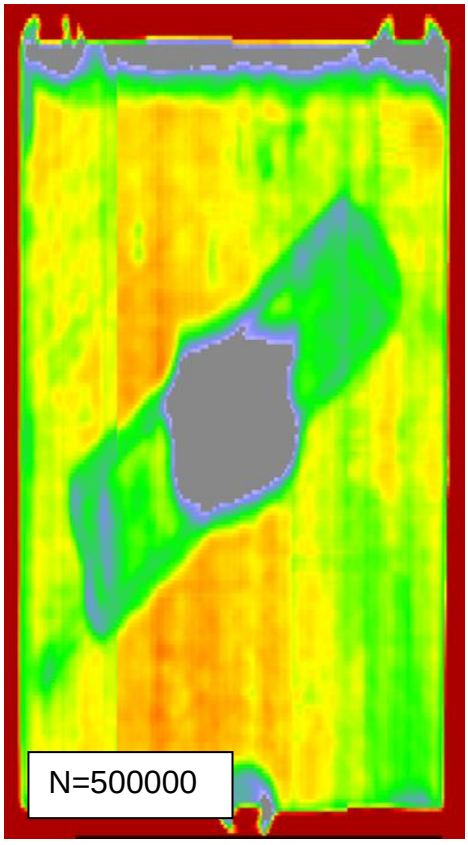
N=500000

Figure 7-18 Captured C-scan image of sample Q15-8 (max. load 179 kN, 73% RCS) at a noted cycle number

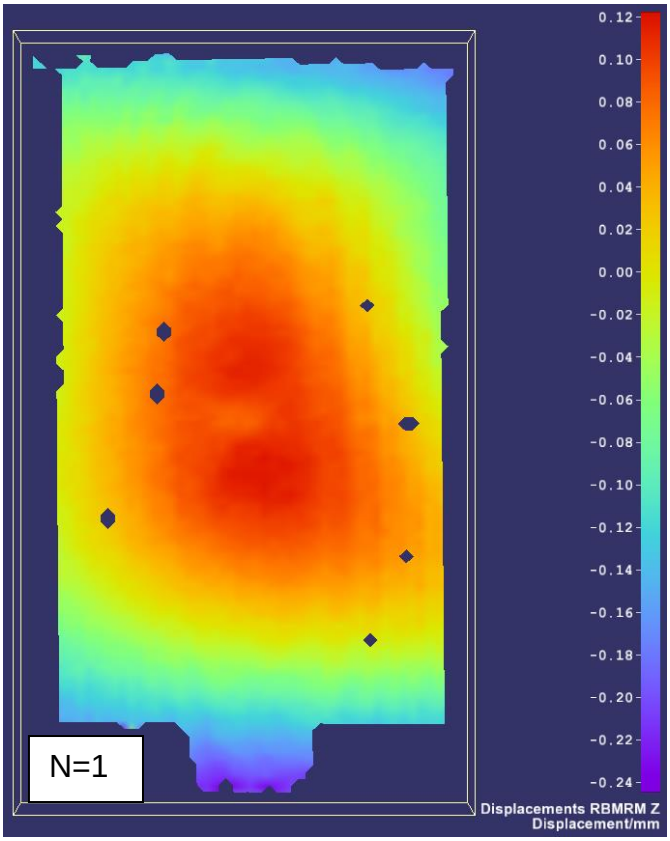

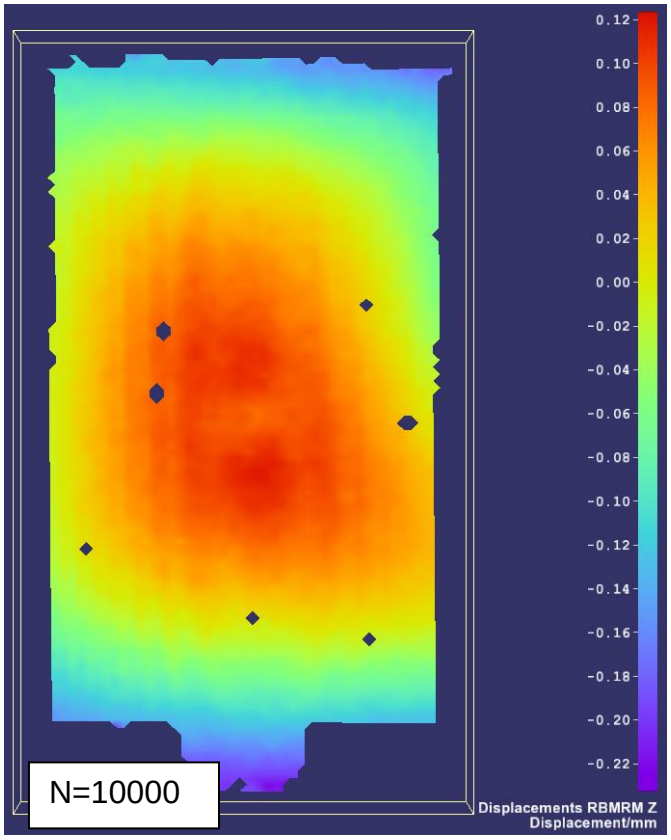
0.12
0.10
0.08
0.06
0.04
0.02
0.00
-0.02
-0.04
-0.06
-0.08
-0.10
-0.12
-0.14
-0.16
-0.18
-0.20
-0.22
N=10000
Displacements RBMRM Z
Displacement/mm

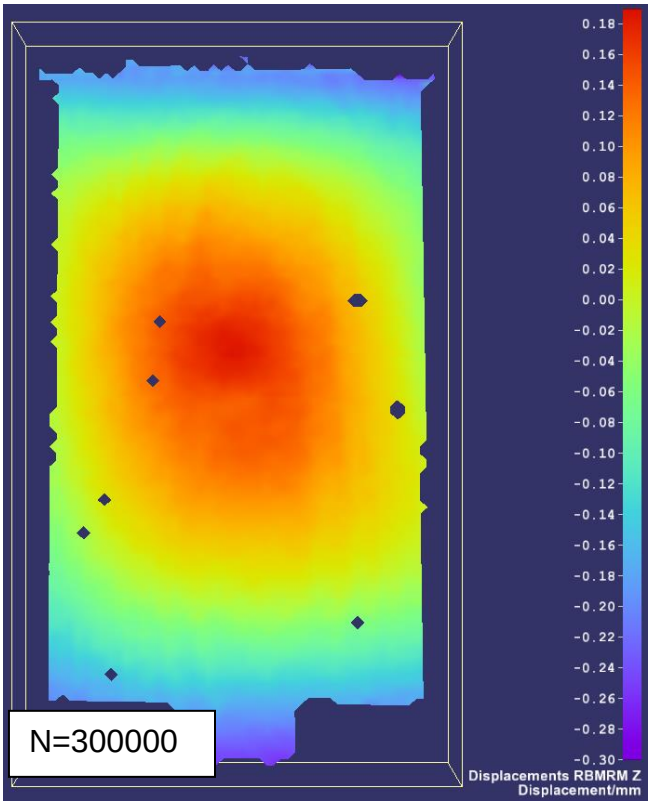
0.18
0.16
0.14
0.12
0.10
0.08
0.06
0.04
0.02
0.00
-0.02
-0.04
-0.06
-0.08
-0.10
-0.12
-0.14
-0.16
-0.18
-0.20
-0.22
-0.24
-0.26
-0.28
-0.30
N=300000
Displacements RBMRM Z
Displacement/mm

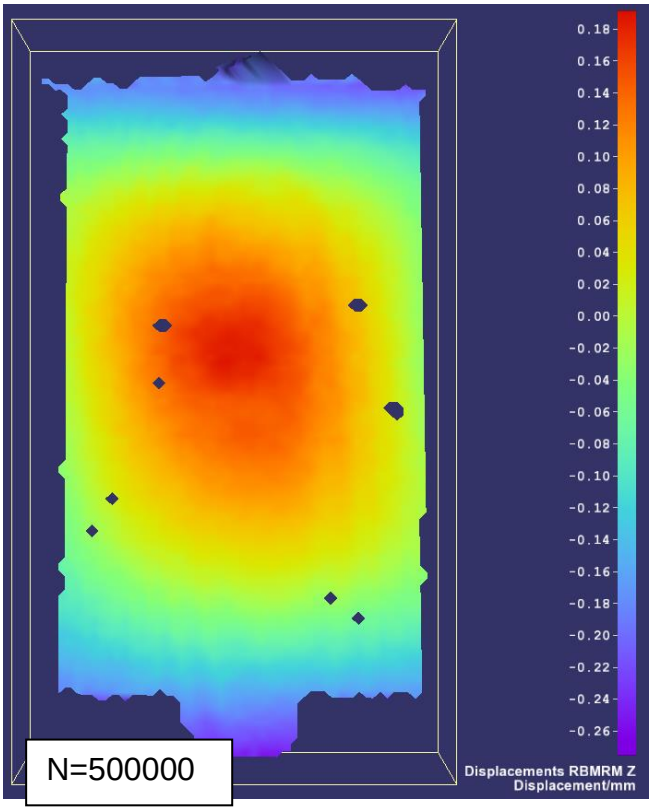

Figure 7-19 Out-of-plane displacement (removal of rigid movement) in sample Q15-8 (max. load 179 kN, 73% RCS) at a noted cycle number

At the initial loading period, the upper part of the panel had a positive deformation towards the camera and the lower part had a negative deformation away from the observation point. With the cycle number added, the deformation did not change hugely at N = 100000. When cycle number reached N = 300000, a more concentrated extrusive deformation was observed (see Figure 7-19).

A clearer trend can be found in a midline z displacement graph, as shown in Figure 7-20. At the beginning (N = 1), the dent area can be depicted even though the whole central area popped out with a displacement value of 0.08 mm. Then, 10000 cycles later, the shape almost remained the same with the initial response. After a relatively long period, when the number reached N = 300000, similar to the samples in the “run-out” group, there was a greater extrusion area just above the dent area position. The deformation did not change obviously even with a further 200000 cycles, and the vertex of the displacement remained at 0.18 mm.

All the c-scan and DIC captures at the checkpoint cycle number for all the samples are presented in the appendix.

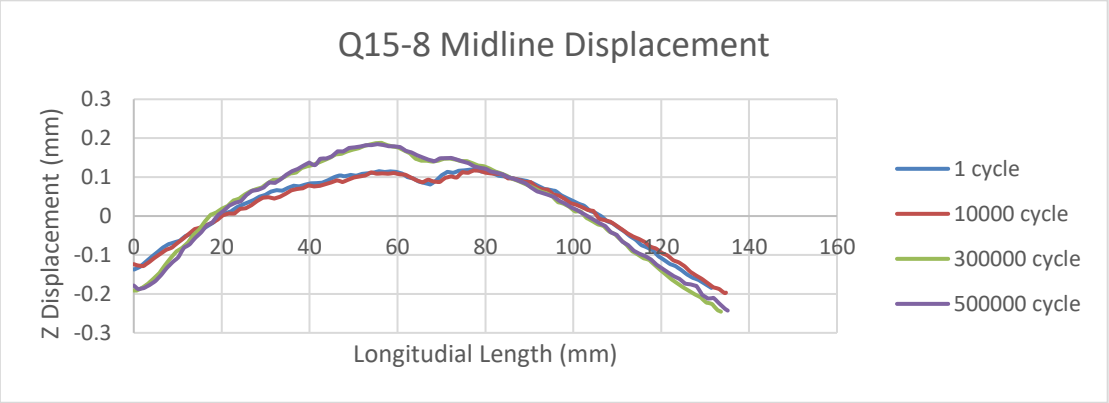

Figure 7-20 Midline z displacement at a noted cycle number in sample Q15-8 (max. load 179 kN, 73% RCS)

Unlike sample Q15-8, sample Q15-7 tested at a lower stress level presented an inward bending throughout the full fatigue cycling session and behaved similar to sample Q12-7 (see Figure 7-21).

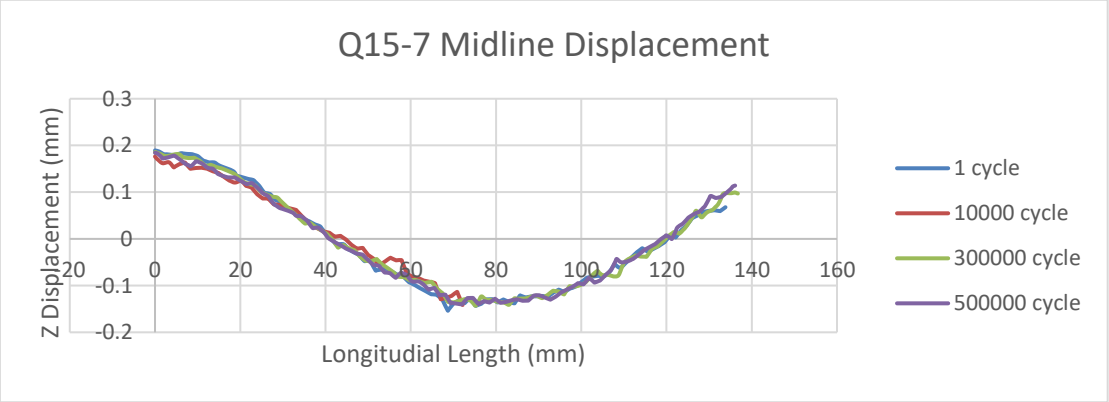

Figure 7-21 Midline z displacement at a noted cycle number in sample Q15-7 (max. load 172 kN, 70% RCS)

Samples included in the “run-out” group indicated that the structural integrity was assured during the 500000-cycle period. However, “no growth” of any internal delaminations was not guaranteed. The two previous examples showed no matter the initial bending morphology, traces of slow and minor degradation can be observed with DIC measurements but not sufficiently with C-scan detection.

7.3.3 Samples under 20-J impact

Further impact severity at 20J lowered the threshold of non-growth to 70%. Only one sample sustained the half million cycles.

An example that underwent eventual failure is Q20-3. The panel failed after 16497 cycles at 0.77 RCS. The C-scan and DIC captures are shown in Figure 7-22 and Figure 7-23, respectively. The delaminated area was firstly detected at N = 15000 when the delamination initiation at the transversal direction was observed. In this case, an interesting two-way propagation was observed. The left propagation had a more extensive length compared to the right-hand side one. The delamination propagation accelerated after the initiation but only the longer one propagated to the left edge when further cycles were added. The right-side delamination propagation grew at a much slower pace. Like other failed samples in other impact groups, the final failure was obtained when the delamination drastically reduced the residual stiffness by growing to one edge.

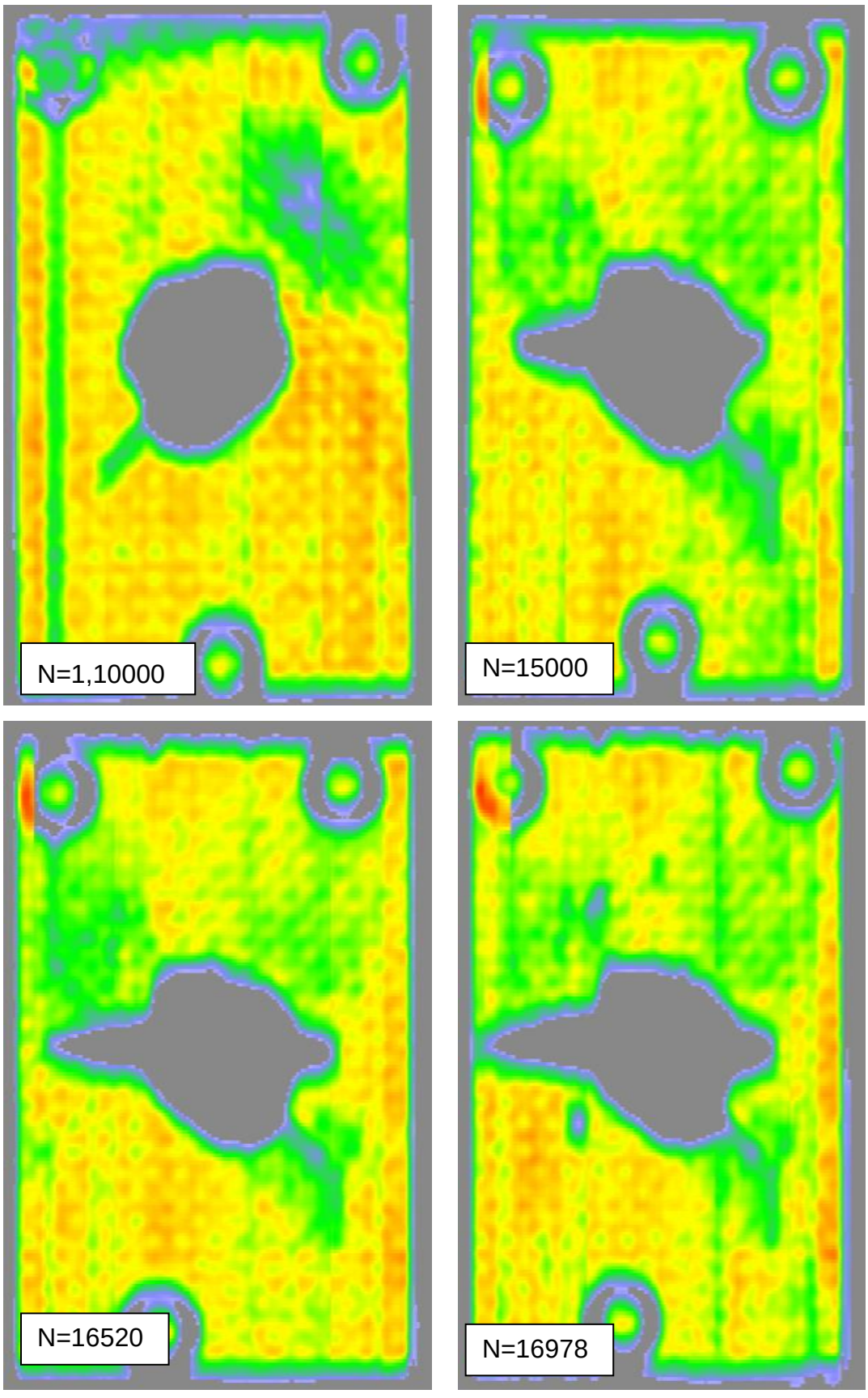
N=1,10000
N=15000
N=16520
N=16978

Figure 7-22 C-scan image of sample Q20-3 (max. load 164 kN, 77% RCS) at a noted cycle

Out-of-plane displacement of sample Q20-3 is shown in Figure 7-23. The displacement presented is the one in which rigid movement has been removed to obtain higher accuracy and minimise the system error. Just like other inward bending samples, at the beginning of fatigue life (N = 1), delamination buckling had one half wavelength bending inwards with a displacement of -0.59 mm. The local buckling mode change can be found as early as N = 10000 when the familiar two half-wavelengths appeared. The buckled area grew to both sides of the sample, but with the left propagation leading.

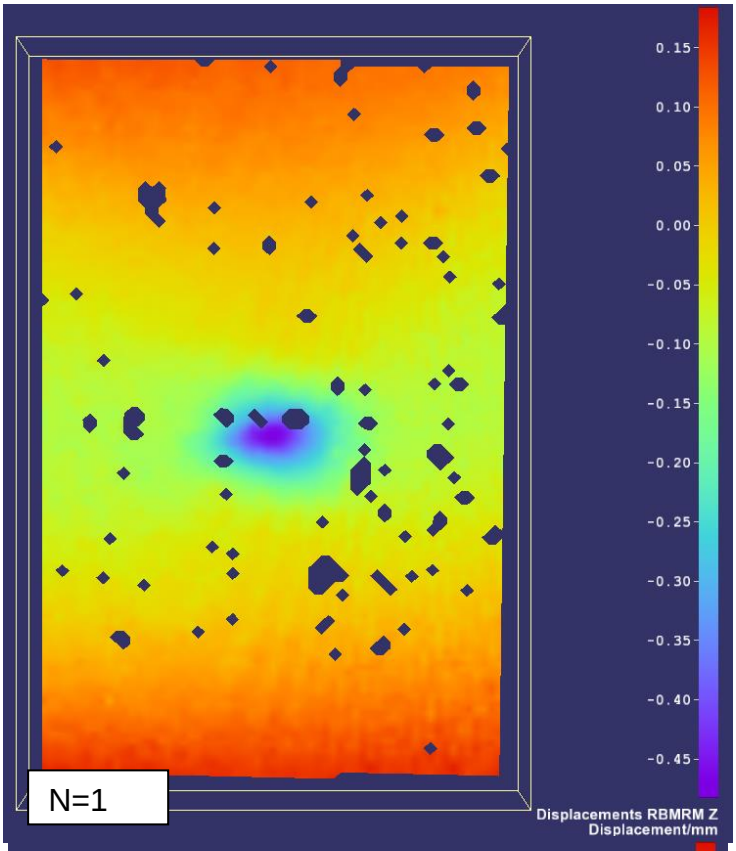
0.15
0.10
0.05
0.00
-0.05
-0.10
-0.15
-0.20
-0.25
-0.30
-0.35
-0.40
-0.45
N=1
Displacements RBMRM Z
Displacement/mm

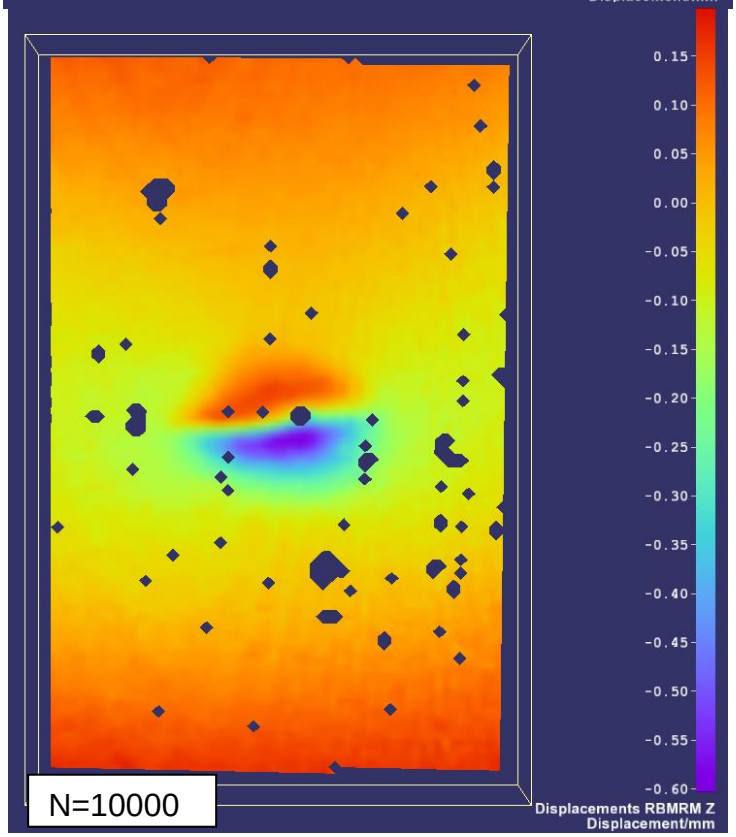
0.15
0.10
0.05
0.00
-0.05
-0.10
-0.15
-0.20
-0.25
-0.30
-0.35
-0.40
-0.45
-0.50
-0.55
-0.60
N=10000
Displacements RBMRM Z
Displacement/mm

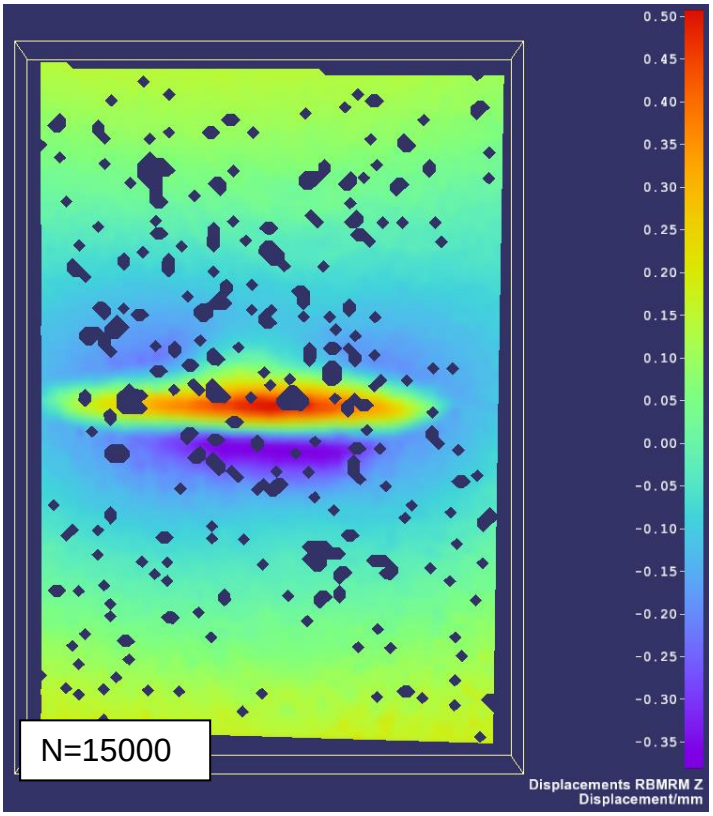

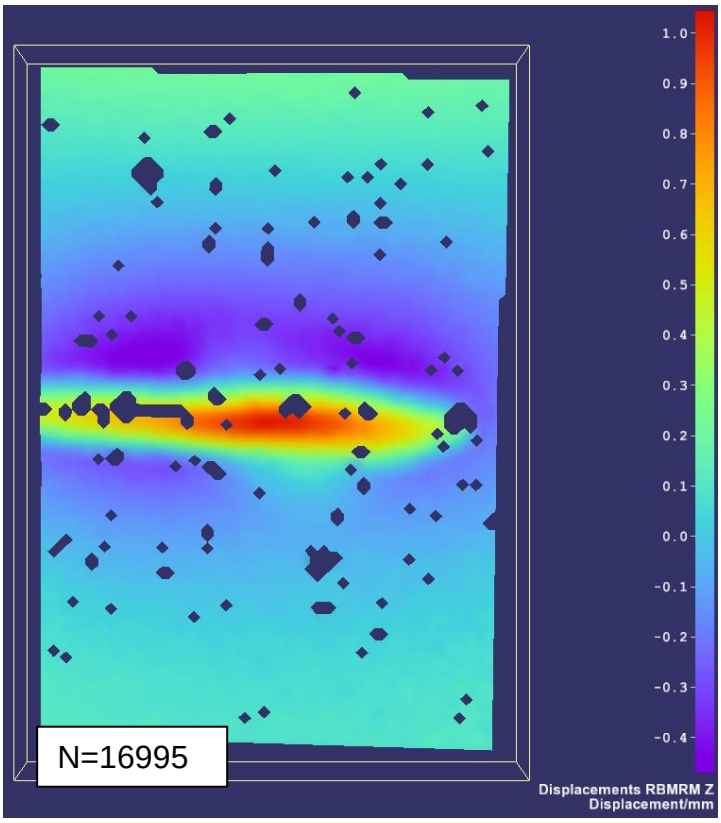

Figure 7-23 Out-of-plane displacement (removal of rigid movement) in sample Q20-3 (max. load 164 kN, 77% RCS) at a noted cycle number

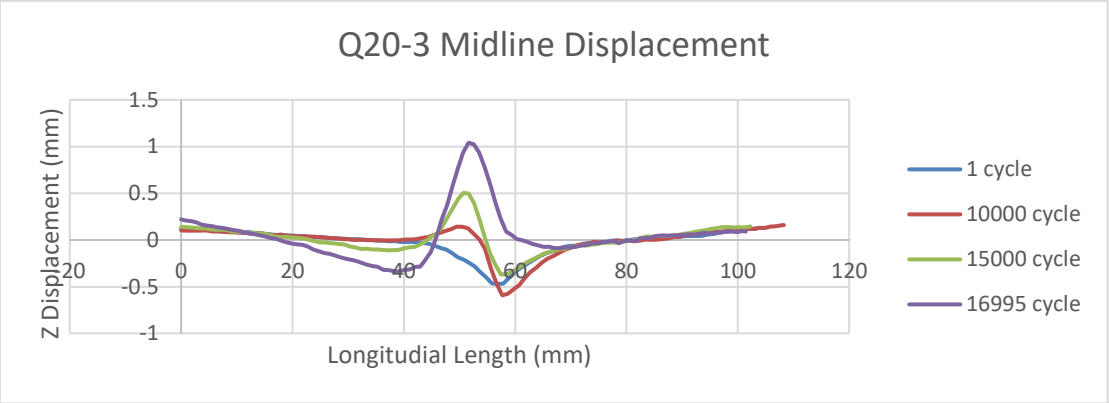

Figure 7-24 Midline z displacement at a noted cycle number in sample Q20-3 (max. load 164 kN, 77% RCS)

Normal displacement data were extracted from DIC data on the midline of the sample surface and plotted as a function of longitudinal position in Figure 7-24. At the beginning of fatigue, the impact damage area underwent simple bending displacement inwards as the displacement of the damage adjacent area value is all negative while there were some positive values near the top and bottom side of the sample. The most deformed area was the area adjacent to the dent area with an initial deformation of -0.57 mm. As the cycle number increased, the top surface of the damage area generated local buckling towards the outer side of the panel at N = 15000 while the upper side of the dent area popped out. With the extension of this buckled area to the side of the sample, the displacement also increased at the same time. Extensive extrusion can be measured at 0.47 mm. The peak continued to increase to 1.09 mm when approaching eventual failure.

Similar behaviour and progression can also be found from cases Q20-2, Q20-4, and Q20-5 (see Figure 7-25 to Figure 7-27).

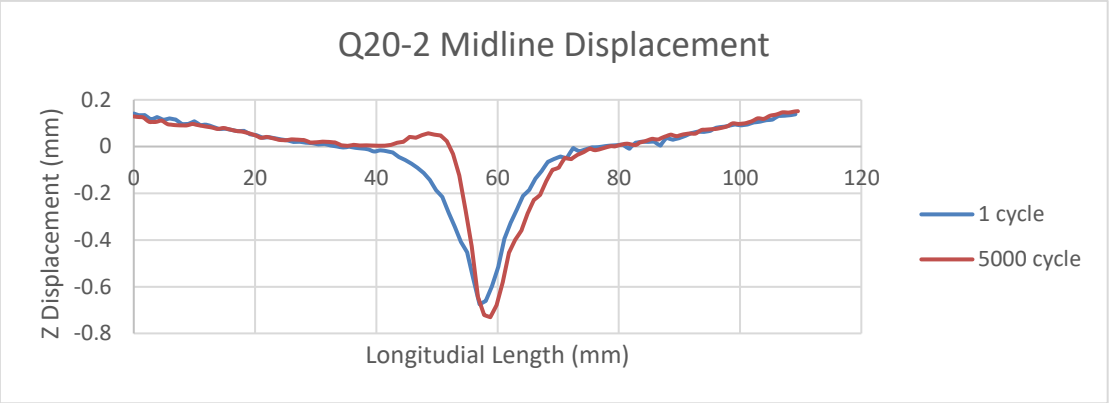

Figure 7-25 Midline z displacement at a noted cycle number in sample Q20-2 (max. load 171 kN, 80% RCS)

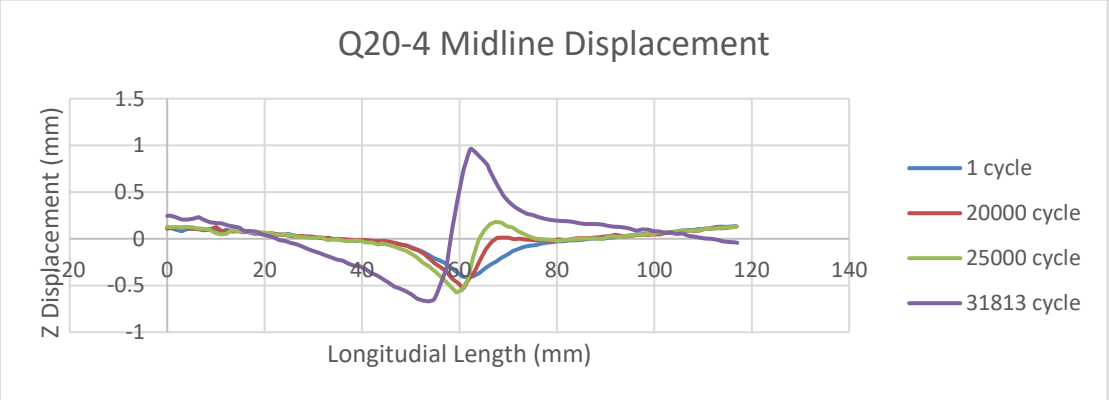

Figure 7-26 Midline z displacement at a noted cycle number in sample Q20-4 (max. load 160 kN, 75% RCS)

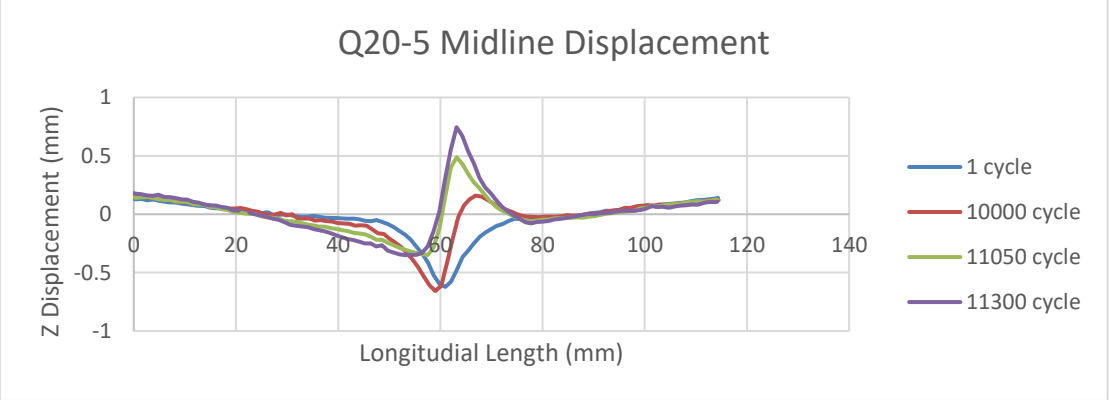

Figure 7-27 Midline z displacement at a noted cycle number in sample Q20-5 (max. load 156 kN, 73% RCS)

Q20-7 is a run out sample loaded at 70% of the RCS. The outward bending exhibited a similar behaviour (see Figure 7-28) as observed for sample Q15-8.

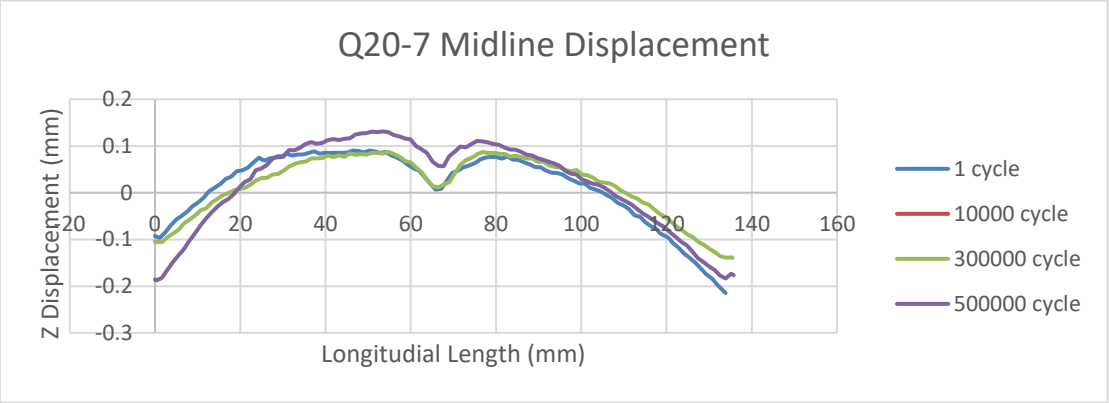

Figure 7-28 Midline z displacement at a noted cycle number in sample Q20-7 (max. load 149 kN, 70% RCS)

7.3.4 Samples under 25-J Impact

In the group under the most severe impact damage, the Q25 series samples not only had the lowest scatter of damage area but also presented a good pattern of increasing fatigue life with a decreasing load. One sample in this group was a run-out.

An example of sample Q25-2 shows 3 stages of failure progression. The panel failed after 6501 cycles at 0.77 RCS with an initial 25-J impact on it (see Figure 7-29 and Figure 7-30). The impact-induced delamination was presented at 0 cycles. The delaminated area remained unchanged until N = 5000 when the delamination initiation at the transversal direction was observed. The delamination propagation accelerated after the initiation and the through width delamination caused eventual failure as it degraded the stiffness of the panel drastically. The pointed-out delamination along the transversal direction (perpendicular to loading direction) was captured during cycles between N = 5000 and N = 6500. The final failure due to cyclic loading is similar to the one resulting from a static test of through-width crushing.

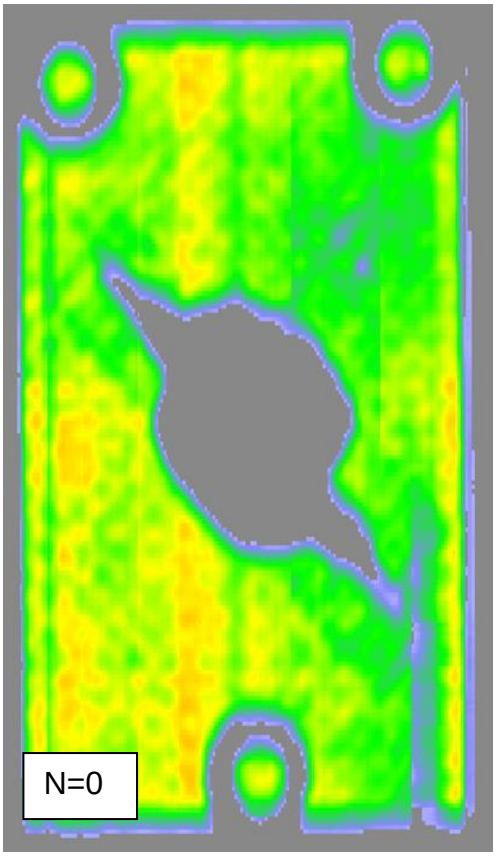
N=0

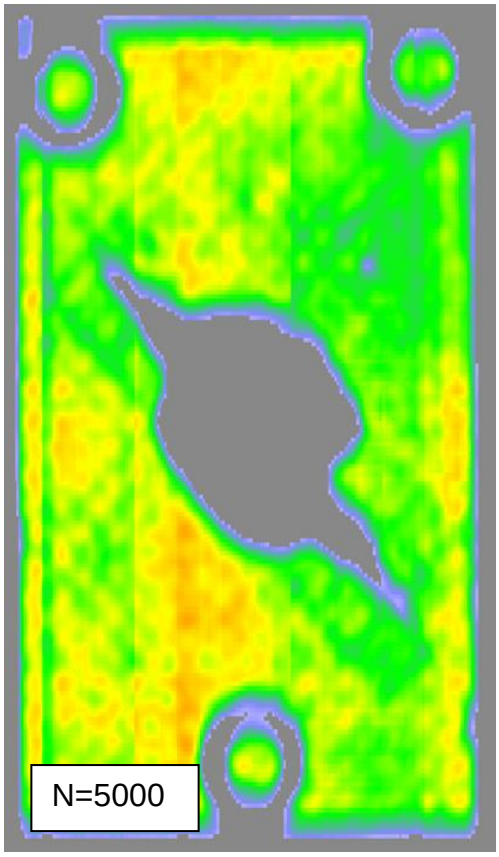
N=5000

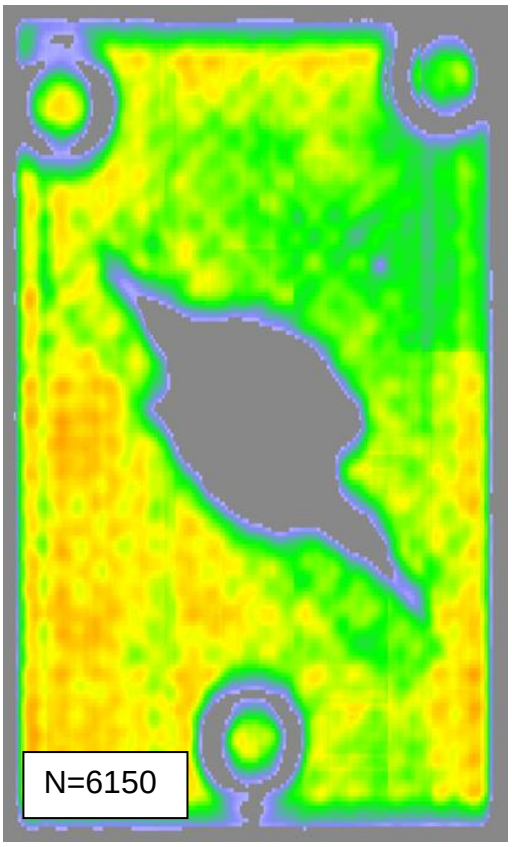
N=6150

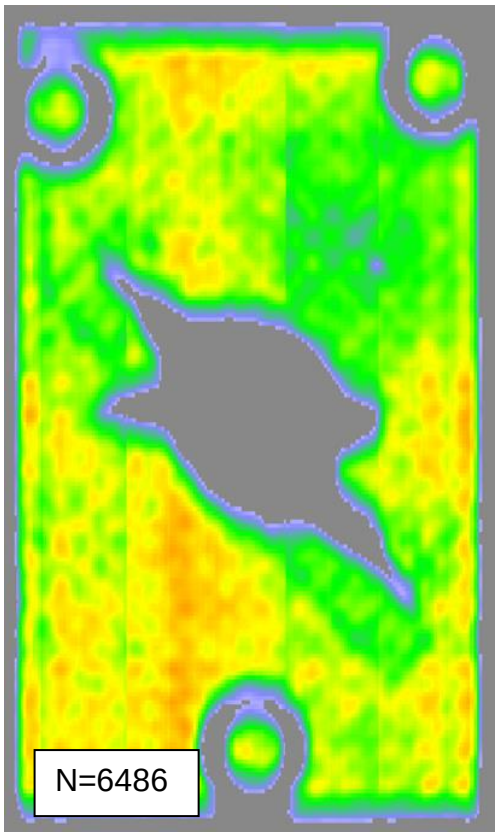
N=6486

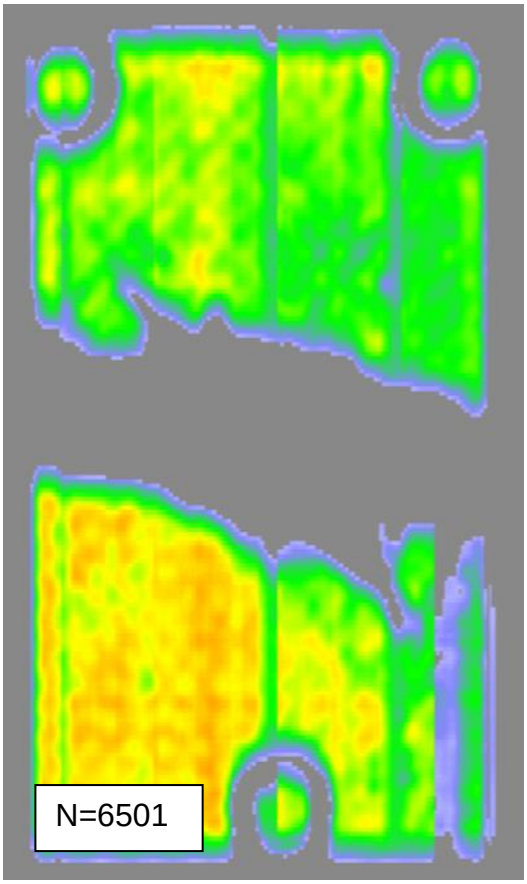

Figure 7-29 C-scan image of sample Q25-2 (max. load 149 kN, 77% RCS) at a noted cycle

Out-of-plane displacement of sample Q25-2 is shown in Figure 7-30. The displacement presented is the one for which rigid movement has been removed to obtain higher accuracy and minimise the system error. As shown in the figure, at the beginning of fatigue life (N = 1), delamination buckling had one half-wavelength bending inwards with a displacement of -0.6 mm. The local area was severely deformed. As the cycle number increased to 5000, the delamination buckling mode changed to two half-wavelengths, one positive and one negative. Between cycle 1 to cycle 5000, no obvious change at the checkpoint (N = 2000) was observed, with a gradual extrusion of the positive wavelength from N = 3000. During the third stage at 6150 cycles, the local buckling propagated to one side of the edge along the direction shown in the C-scan images, indicating the propagation of detectable delamination.

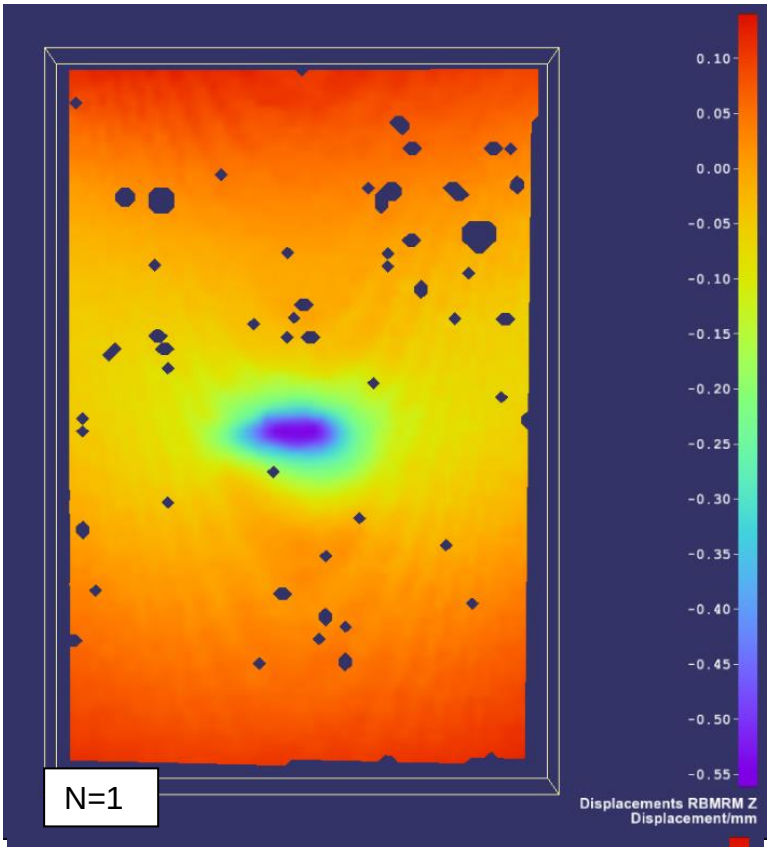
0.10
0.05
0.00
-0.05
-0.10
-0.15
-0.20
-0.25
-0.30
-0.35
-0.40
-0.45
-0.50
-0.55
Displacements RBMRM Z
Displacement/mm
N=1

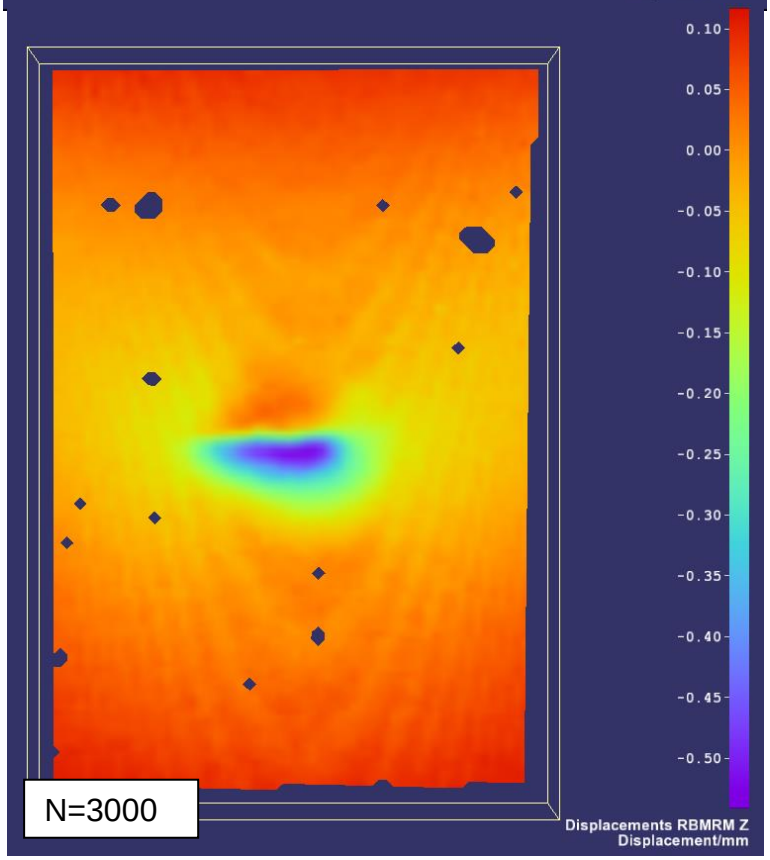
0.10
0.05
0.00
-0.05
-0.10
-0.15
-0.20
-0.25
-0.30
-0.35
-0.40
-0.45
-0.50
Displacements RBMRM Z
Displacement/mm
N=3000

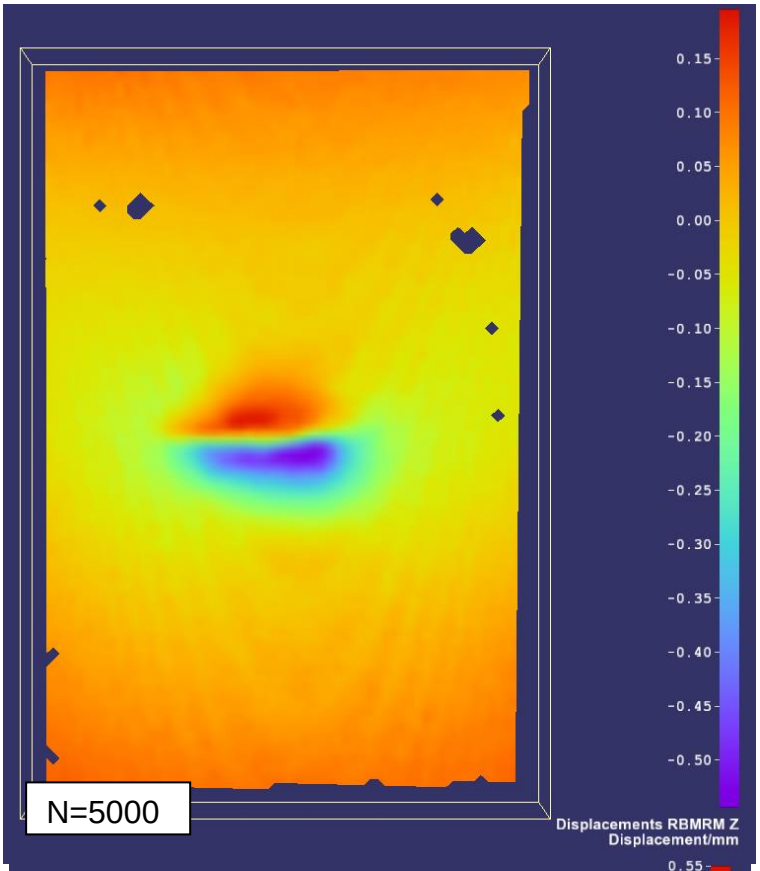
0.15
0.10
0.05
0.00
-0.05
-0.10
-0.15
-0.20
-0.25
-0.30
-0.35
-0.40
-0.45
-0.50
Displacements RBMRM Z
Displacement/mm
N=5000

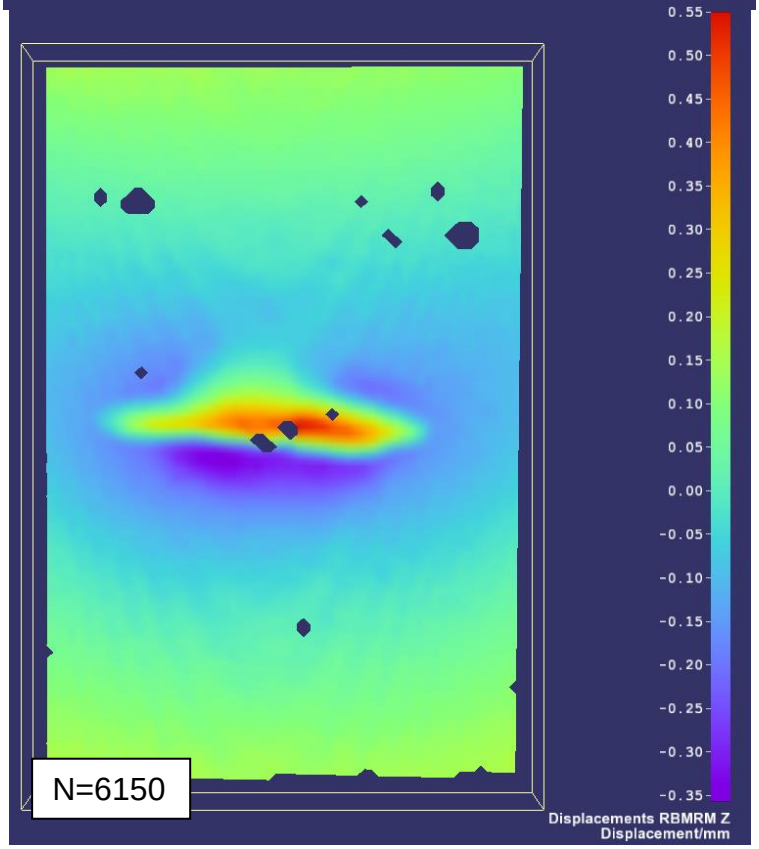
0.55
0.50
0.45
0.40
0.35
0.30
0.25
0.20
0.15
0.10
0.05
0.00
-0.05
-0.10
-0.15
-0.20
-0.25
-0.30
-0.35
Displacements RBMRM Z
Displacement/mm
N=6150

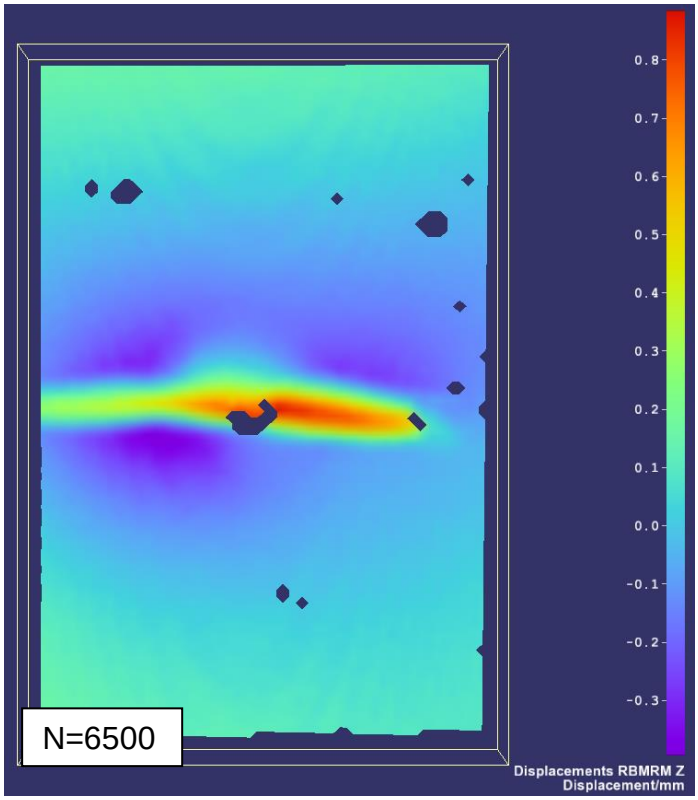

Figure 7-30 Out-of-plane displacement (removal of rigid movement) in sample Q25-2 (max. load 149 kN, 77% RCS) at a noted cycle number

Normal displacement data were extracted from DIC data on the midline of the sample surface and plotted as a function of longitudinal position in Figure 7-31. At the beginning of fatigue, the impact damage area underwent a simple bending displacement inward as the displacement value was negative. The most deformed area was the area adjacent to the dent area, with an initial deformation of -0.54 mm. As the cycle number increased, the top surface of the damage area generated local buckling towards the outer side of the panel. The top part of the central area showed a “popped up” area. As more fatigue cycles were added, the two half-wavelengths buckling extended to the edge and resulted in fatal failure. When approaching failure, not only the buckled area width was extended but also the vertex of out-of-plane displacement had increased to a relatively high value of 0.58 mm.

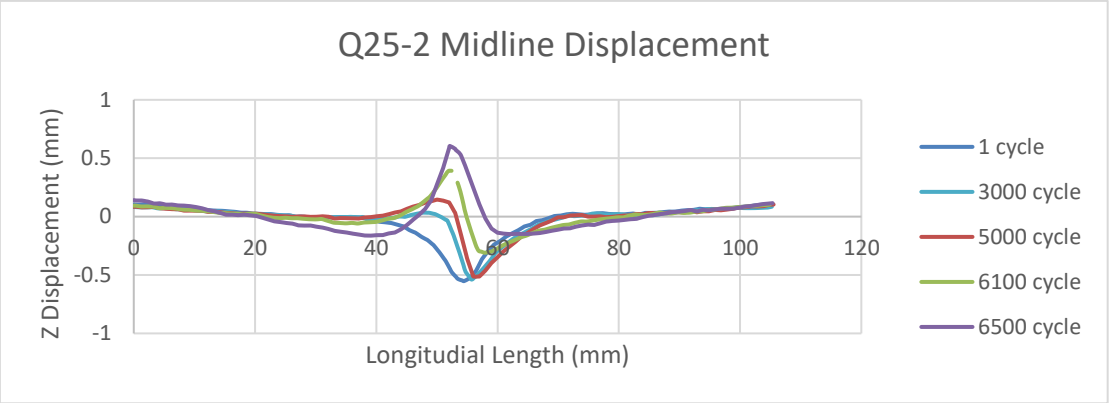

Figure 7-31 Midline z displacement at a noted cycle number in sample Q25-2 (max. load 149 kN, 77% RCS)

The samples that underwent eventual failure exhibited the same pattern under c-scan detection: from initial damage to delamination initiation and propagation to final failure. Similar behaviour was observed for samples Q25-3 and Q25-4 (see Figure 7-32 and Figure 7-33). All the C-scan and DIC captures at the checkpoint cycle number for all the samples are presented in the appendix. However, the out-of-plane response may vary among different cases.

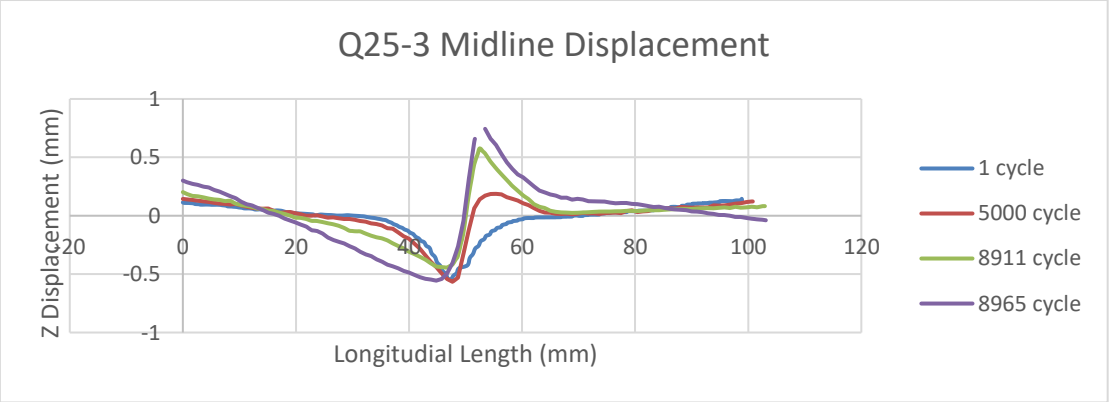

Figure 7-32 Midline z displacement at a noted cycle number in sample Q25-3 (max. load 145 kN, 75% RCS)

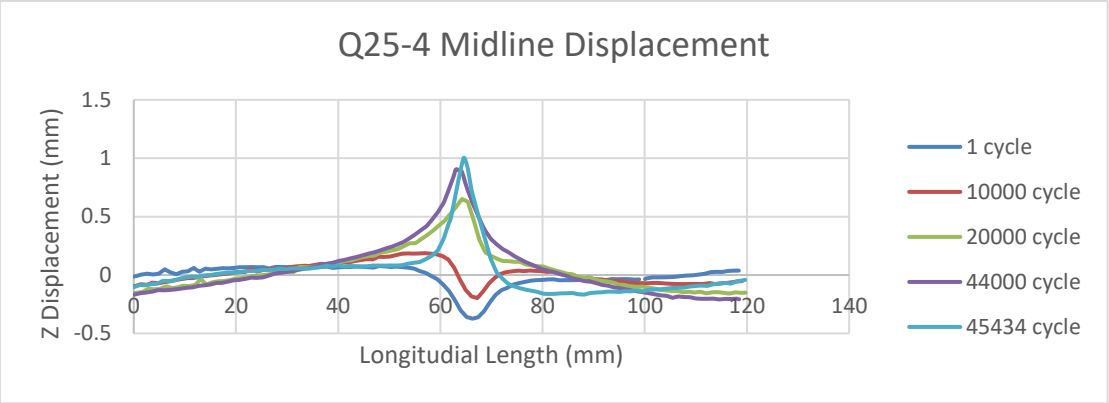

Figure 7-33 Midline z displacement at a noted cycle number in sample Q25-4 (max. load 141 kN, 73% RCS)

Among all the “run-out” samples, one sample behaved obviously different from other samples – Q25-6, which is fatigued under 70% of its nominal RCS at 129.2 MPa. Unlike other “run-out” samples, the progression pattern was already shown within the 500000 cycles.

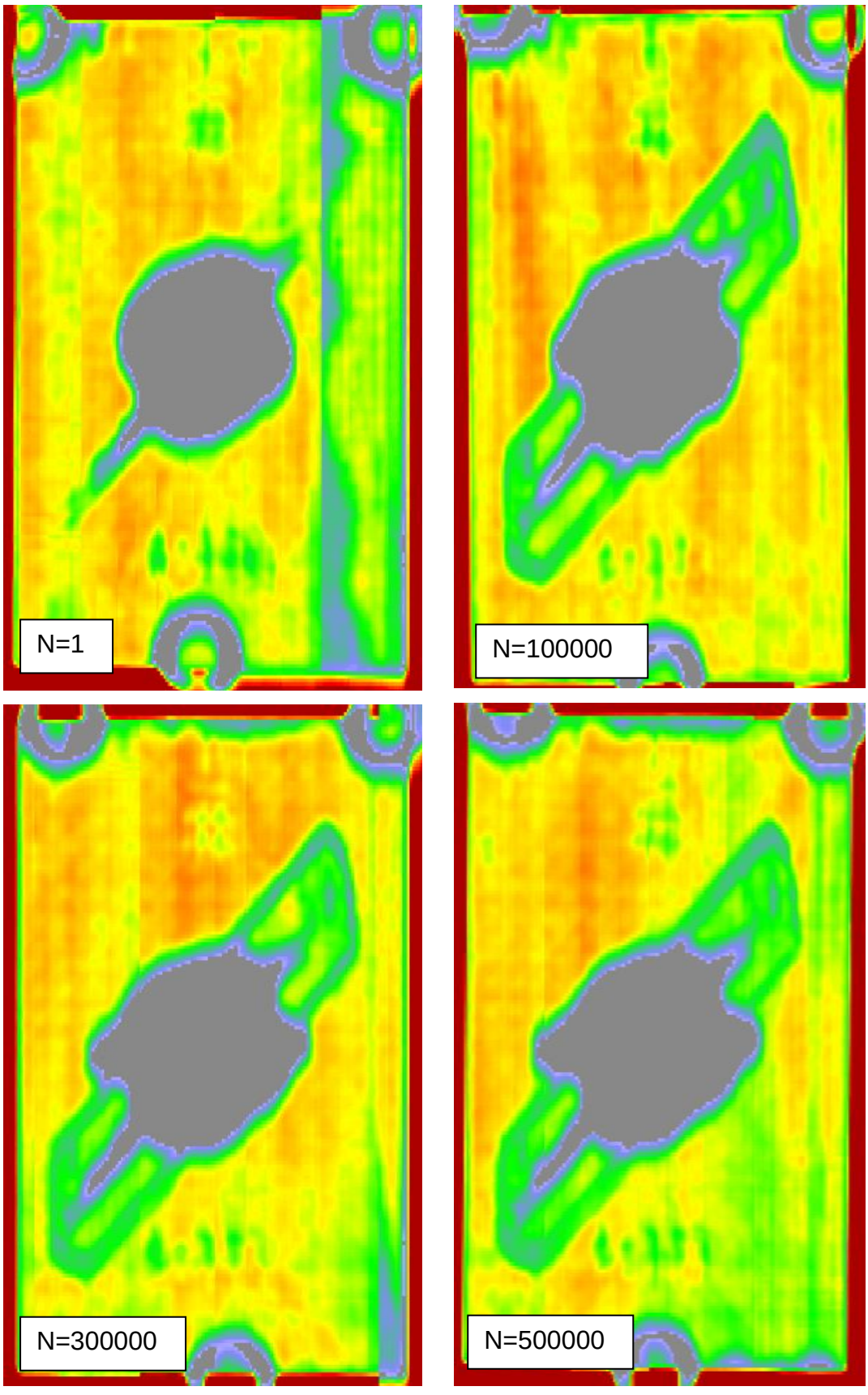
N=1
N=100000
N=300000
N=500000

Figure 7-34 Captured C-scan image of sample Q25-6 (max. load 129 kN, 70% RCS) at a noted cycle number

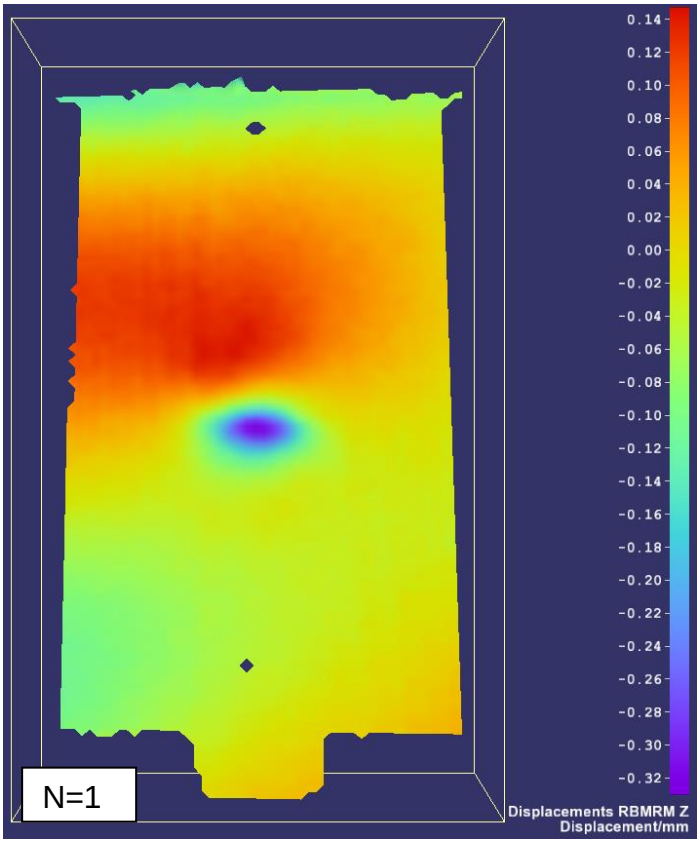

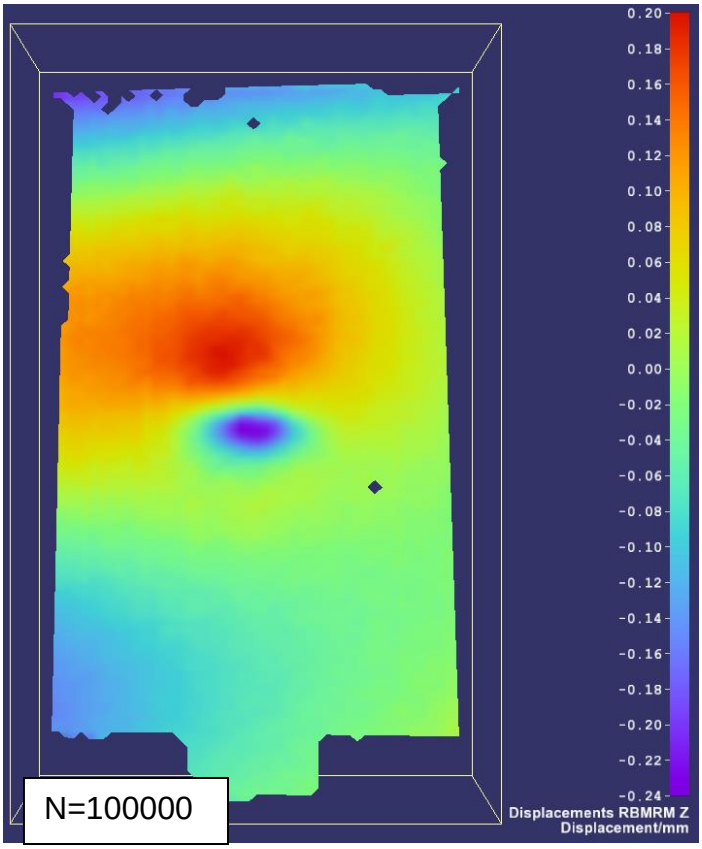
0.20
0.18
0.16
0.14
0.12
0.10
0.08
0.06
0.04
0.02
0.00
-0.02
-0.04
-0.06
-0.08
-0.10
-0.12
-0.14
-0.16
-0.18
-0.20
-0.22
-0.24
Displacements RBMRM Z
Displacement/mm
N=100000

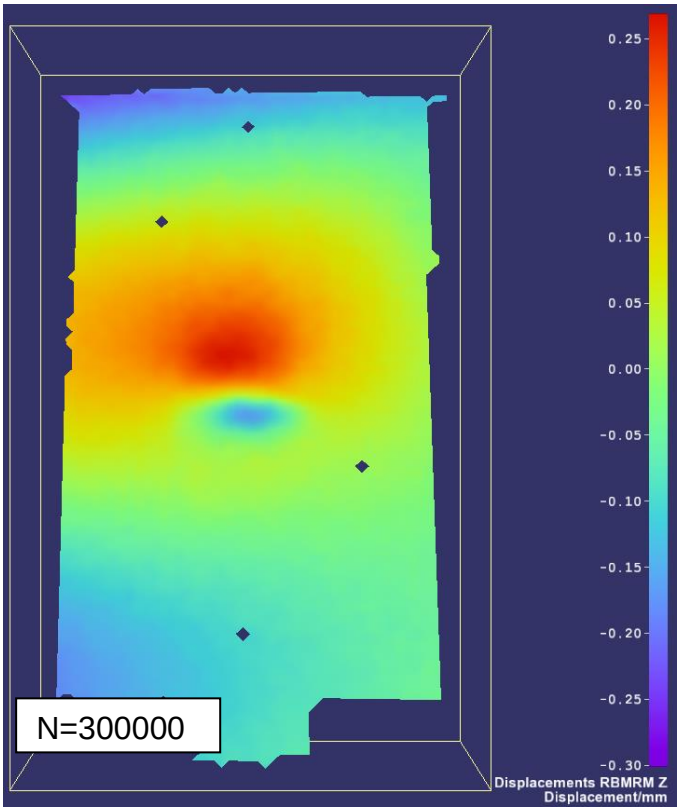
0.25
0.20
0.15
0.10
0.05
0.00
-0.05
-0.10
-0.15
-0.20
-0.25
-0.30
Displacements RBMRM Z
Displacement/mm
N=300000

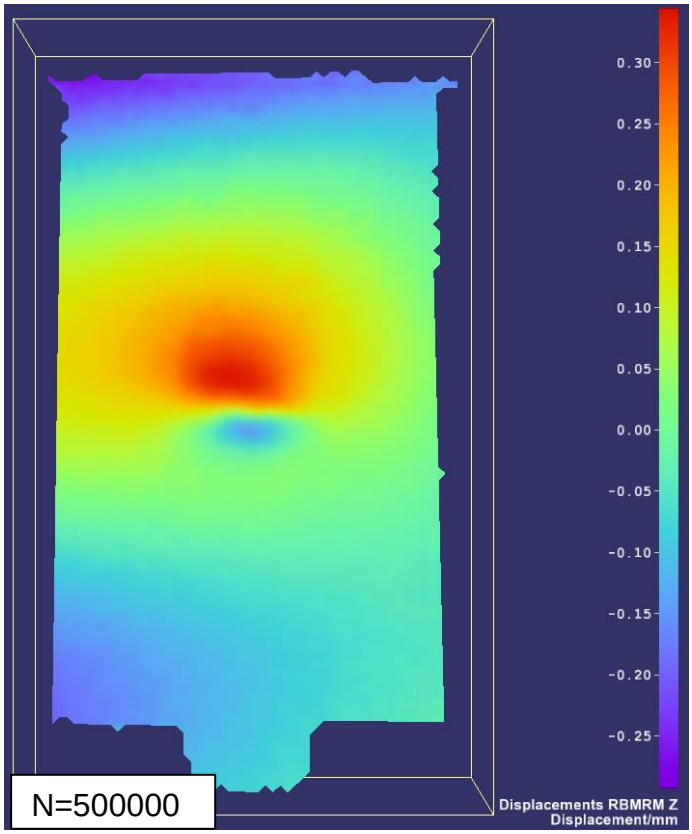

Figure 7-35 Out-of-plane displacement (removal of rigid movement) in sample Q25-6 (max. load 129 kN, 70% RCS) at a noted cycle number

The sample showed a progression of the delaminated area transversely at N = 100000 (see Figure 7-34). The propagation extended at a gradual pace from N = 100000 to N = 300,000 and then to N = 500000. From the DIC captures, the initial inward bending was observed (see Figure 7-35). Unlike the other cases with initial inward bending, sample Q25-6 exhibited a concentrated positive deformation above the impact dent area at an early stage of the fatigue cycles. When the cycle numbers were added, the positive deformation area seemed to extrude further with a noticeable decrease in the negative deformation.

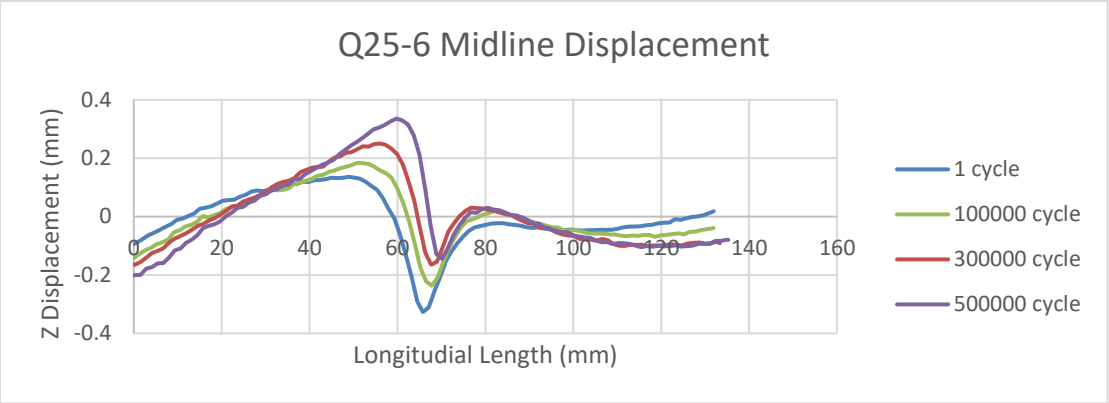

Figure 7-36 Midline z displacement at a noted cycle number in the sample Q25-6 (max. load 129 kN, 70% RCS)

A clearer trend can be found in the midline z displacement plot in Figure 7-36. With the cycles added on, the buckled area extruded further out from 0.159 mm to 0.329 mm while the negative extremum dropped from -0.33 mm to -0.15 mm. Unlike the failed samples exhibited an increase in the positive displacement only while the negative displacement maintained.

With the data gathered from the C-scan and DIC, it can be found the failed samples underwent similar fatigue failure no matter the initial z displacement direction. From the DIC results, the progress includes simple bending (inward/outward), local buckling initiation, buckled area propagation, and eventual failure. Delamination propagation usually appeared along the buckled area. The extension of the on-surface buckling area was due to the detectable delamination growth.

7.4 Buckling on Back Surface

Back surface was not observed in this study. Previous study shows a progression in transversal direction but no influence on the ultrasonic delamination area (Ogasawara et al., 2013). In addition to the observed results in Section 7.3 showing the progression of three stages from overall bending to the appearance of buckling mode change and finally move on to the buckling progression to both sides.

Different from the behaviour to the impact surface, buckling on the back surface is more straightforward. A single half-wavelength buckling appeared right after the load was applied due to the existing large delamination near back surface. With fatigue cycle increases, the buckled area does not change either mode or longitudinal length but only progresses in the transversal direction. Figure 7-37 shows this behaviour at noted cycle number. All the tested samples were behaved similar on the back surfaces.

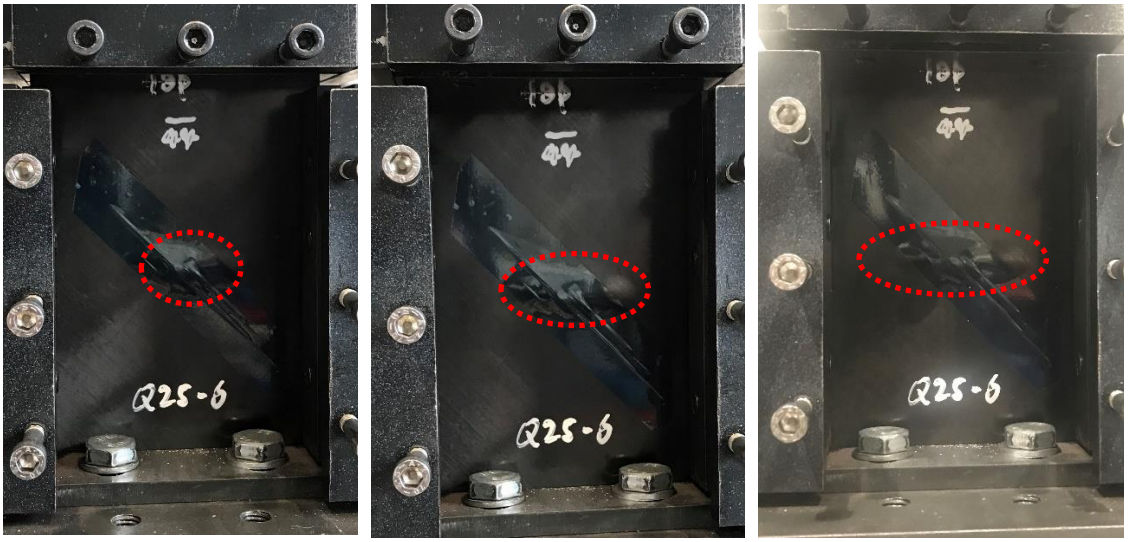

(a) (b) (c)

Figure 7-37 Buckling Progression on Back Surface of Sample Q25-6 at (a) 100 cycle (b) 30000 cycle (b) 200000 cycle

In order to give a clear image of the changing during fatigue session, a combined schematic drawing is shown in Figure 7-38 showing both impact surface and back surface buckling and internal delamination.

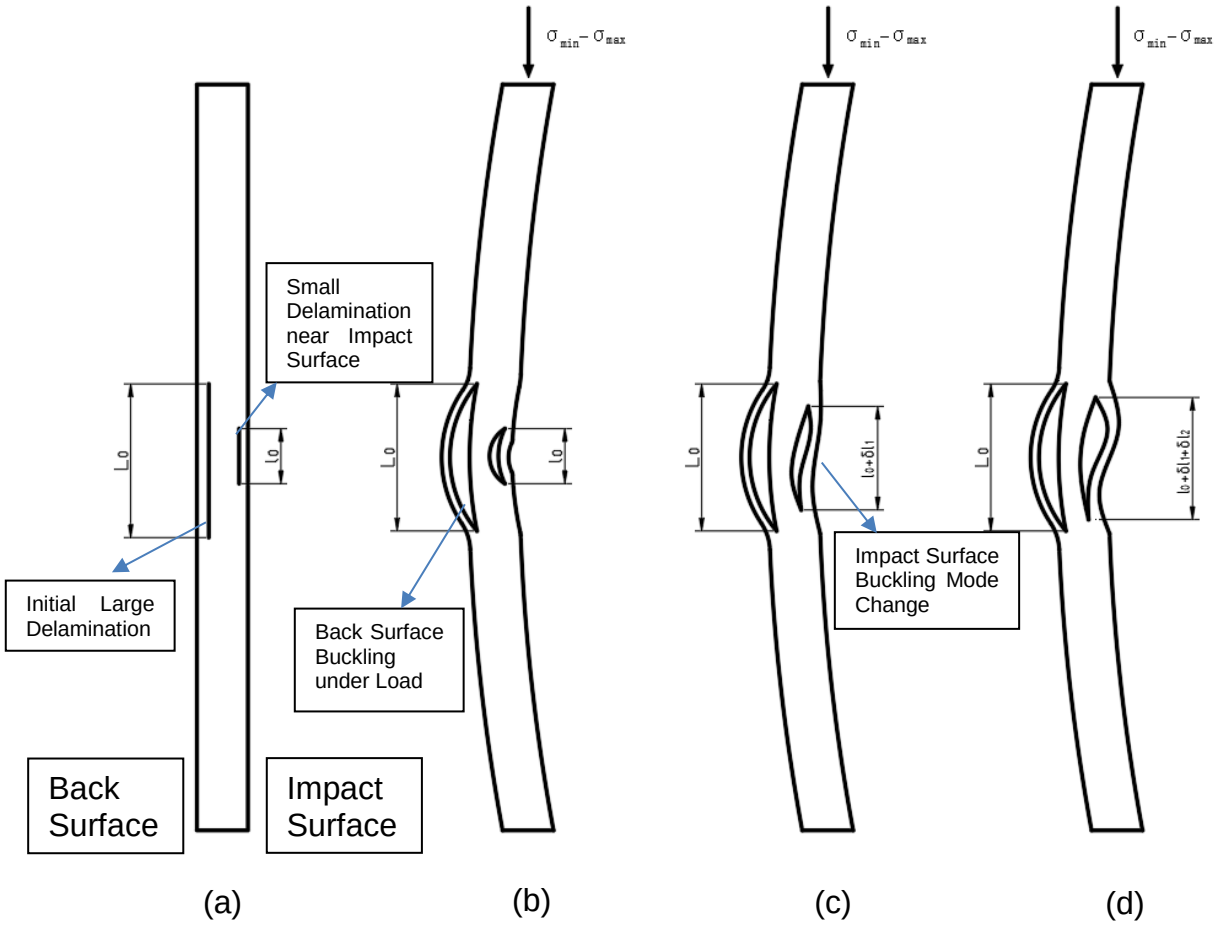

Figure 7-38 Schematic drawing of cross section of test samples showing impact surface and back surface buckling progression during fatigue session at (a) without loading (b) Initial stage of loading with an overall sample bending (c) Initiation of impact surface buckling mode change (d) buckling area on impact surface transversal progression

7.5 Delamination Growth

Delamination size was measured using the image taken under the C-scan. Three components of each sample at certain checkpoints were acquired to explore the delamination size changes in the longitudinal direction (loading direction), transversal direction, and overall delamination area. The same five samples mentioned in the last section are presented in this section for easy comparison with the C-scan image and DIC data. The delamination lengths and areas for the rest of the samples can be found in the appendix.

Fatigue-Failed Samples

Figure 7-39 shows the delamination growth of sample Q25-2 (max. load 149 kN, 77% RCS) in both longitudinal and transversal directions. Overall, the graph shows the delamination propagated in the transversal direction only to the loading direction, conforming to the cross-width failure obtained from static compression testing. As stated in Chapter 7.3, the delamination detection under C-scan is not noticeable until cycle 6150 (the propagation initiation happened at some cycle between N = 5000 to N = 6150). When the propagation started, it grew rapidly, growing from 45.22 mm to an all through width of 100 mm in just 351 cycles. The propagation initiation cycle was already 94.6% of the total fatigue lifetime.

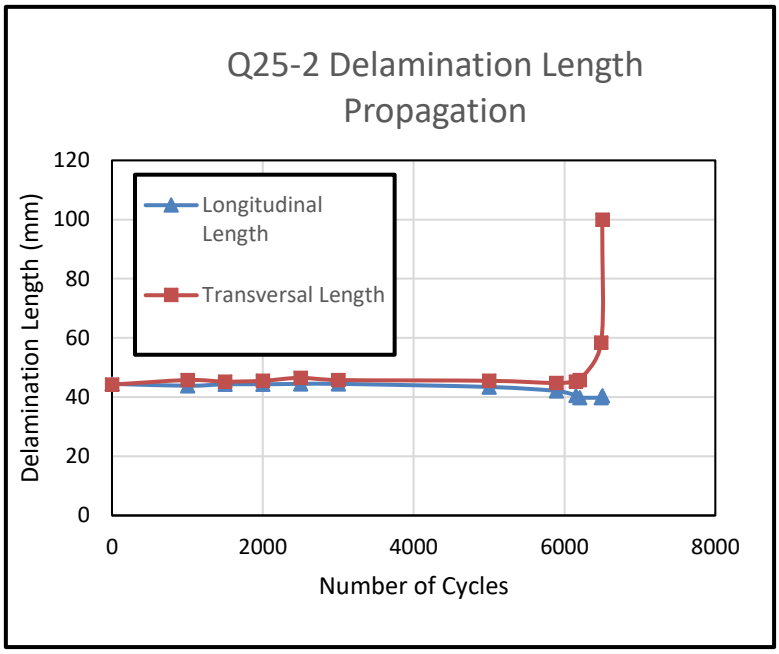

Figure 7-39 Delamination length in two directions in sample Q25-2 (max. load 149 kN, 77% RCS)

For delamination area progression during the fatigue session (see Figure 7-40), the trend was similar. The growth only happened at almost the very late stage of the fatigue lifetime, which is presented as a sudden increase as shown in the graph. Therefore, the fatigue of the composites has always been described as an unpredictable and sudden process in previous studies.

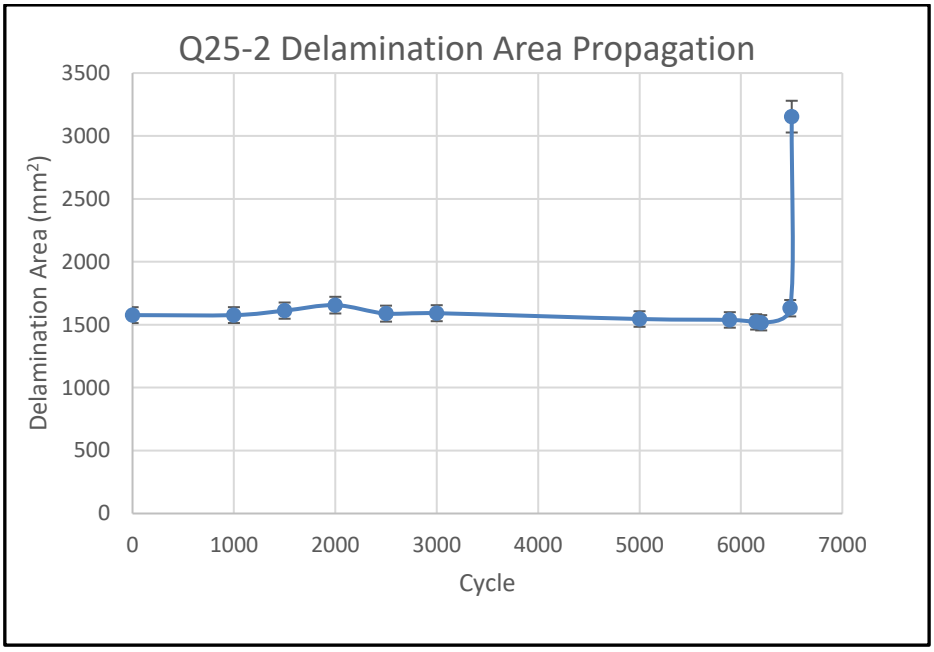

Figure 7-40 Delamination area in sample Q25-2 (max. load 149 kN, 77% RCS)

Sample Q12-7 is also listed here as its initial outward bending behaviour was unique in the failed sample group. Unlike the sudden increase in the previous case Q25-2, sample Q12-7 exhibited a gentler behaviour (see Figure 7-41). Along with the observed z displacement increase at N = 100000, a noticeable increase was found in both directions. An accelerated propagation but not as sudden as the one in Q25-2 was captured.

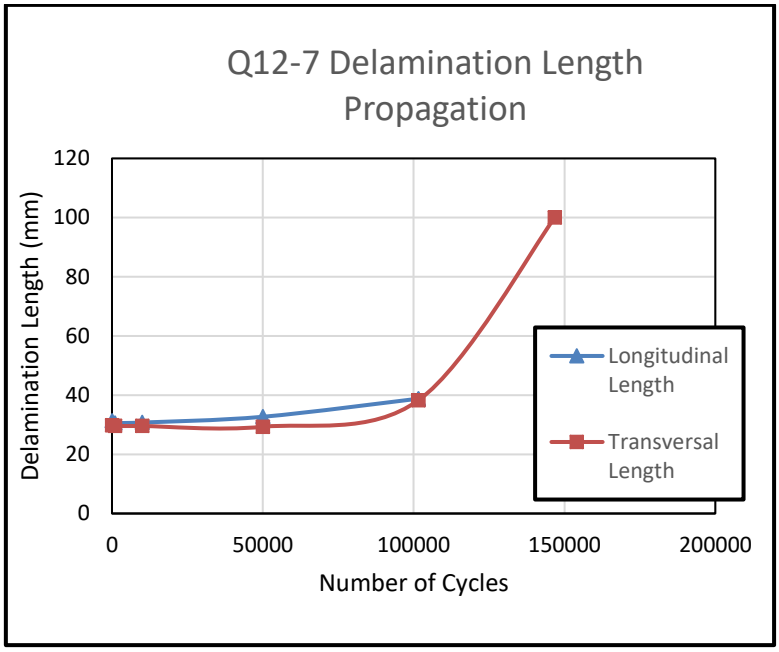

Figure 7-41 Delamination length in two directions in sample Q12-7 (max. load 217 kN, 85% RCS)

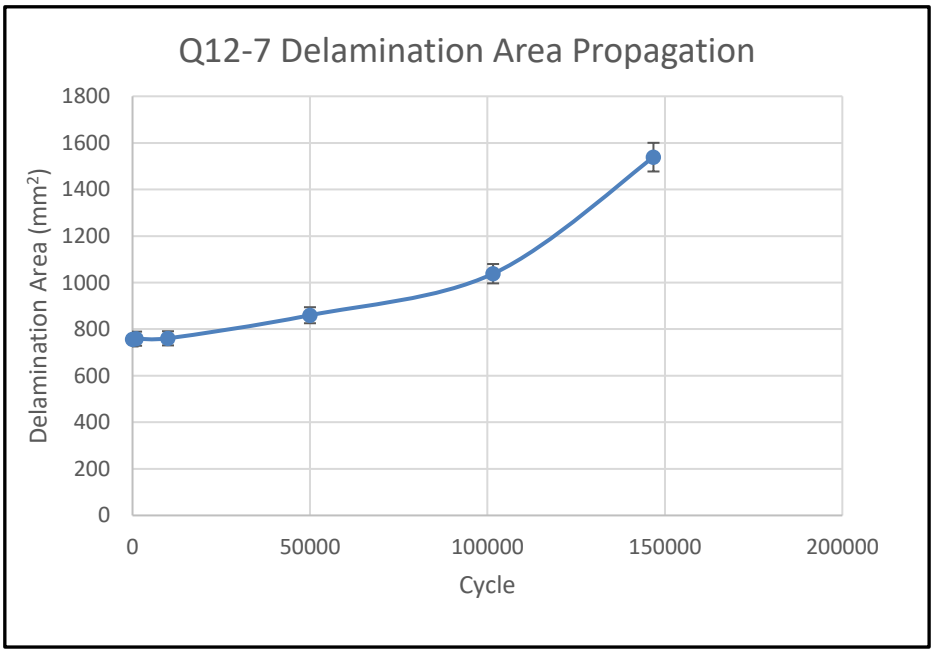

Figure 7-42 Delamination area in sample Q12-7 (max. load 217 kN, 85% RCS)

A gradual increase in the delamination area was also observed for the sample (see Figure 7-42). The delamination area showed a noticeable enhancement as early at the 50000th cycle owing to the delamination length increment in both longitudinal and transversal directions.

"Run-out" samples

Two cases from the "run-out" group are presented in this part. Q12-4 is a typical run-out sample with initial inward bending while Q15-8 is a representative for ones with initial overall outward displacement. From Figure 7-43 and Figure 7-44, it can be seen that the delamination within sample Q12-4 remained throughout the whole fatigue period. From the beginning of the fatigue session, the length of delamination was 31 mm in both directions, and the area was maintained at around 890 mm^2 despite some tolerable errors. Even though the sample Q15-8 responded with a different manner of deformation, when the load is not high enough to trigger overall delamination propagation, the delamination size and area are maintained (see Figure 7-45 and Figure 7-46).

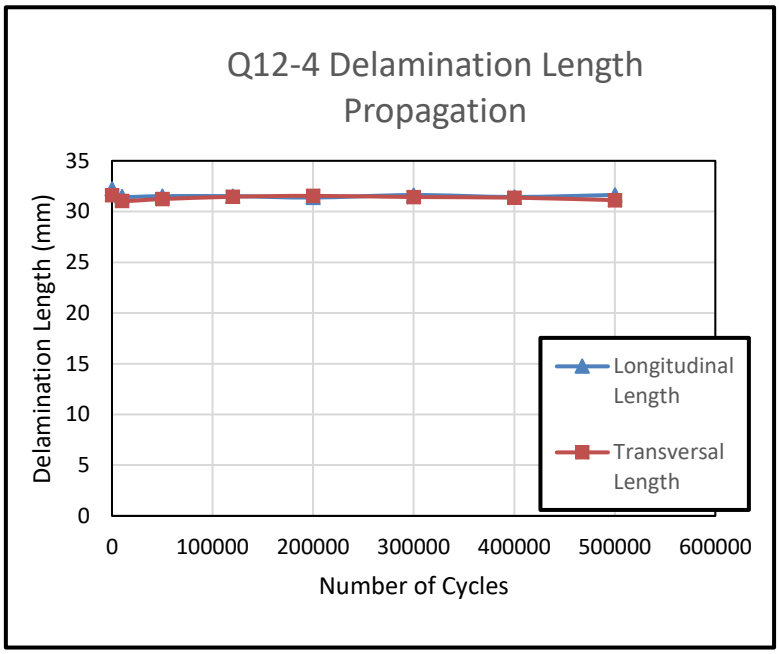

Figure 7-43 Delamination length in two directions in sample Q12-4 (max. load 210 kN, 82% RCS)

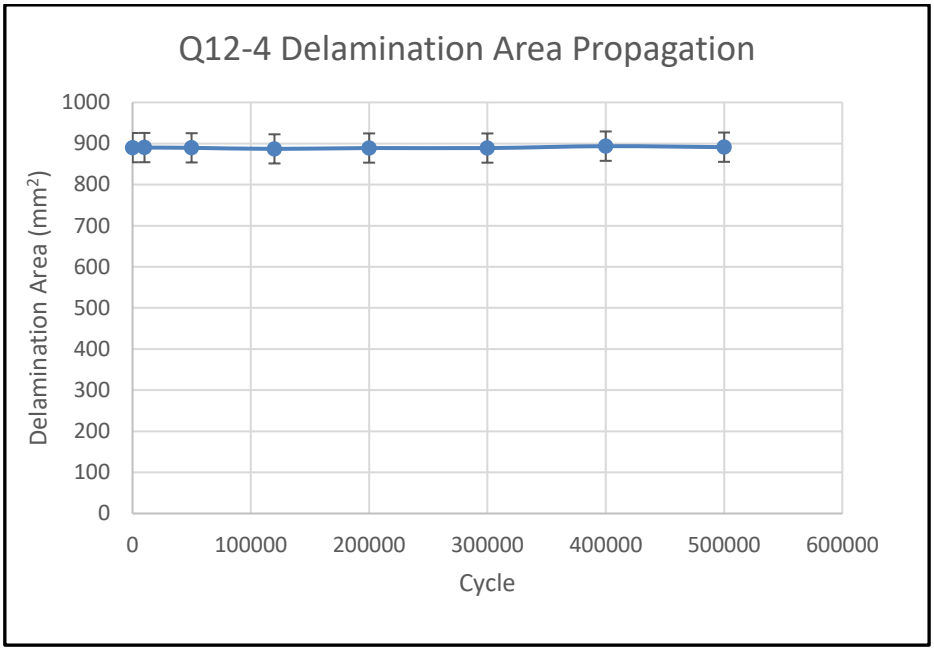

Figure 7-44 Delamination area in sample Q12-4 (max. load 210 kN, 82% RCS)

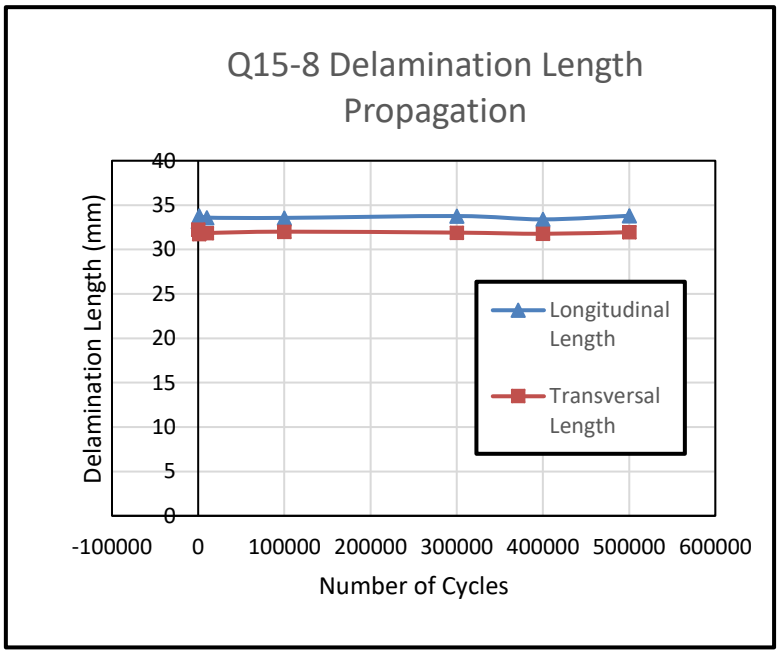

Figure 7-45 Delamination length in two directions in sample Q15-8 (max. load 179 kN, 73% RCS)

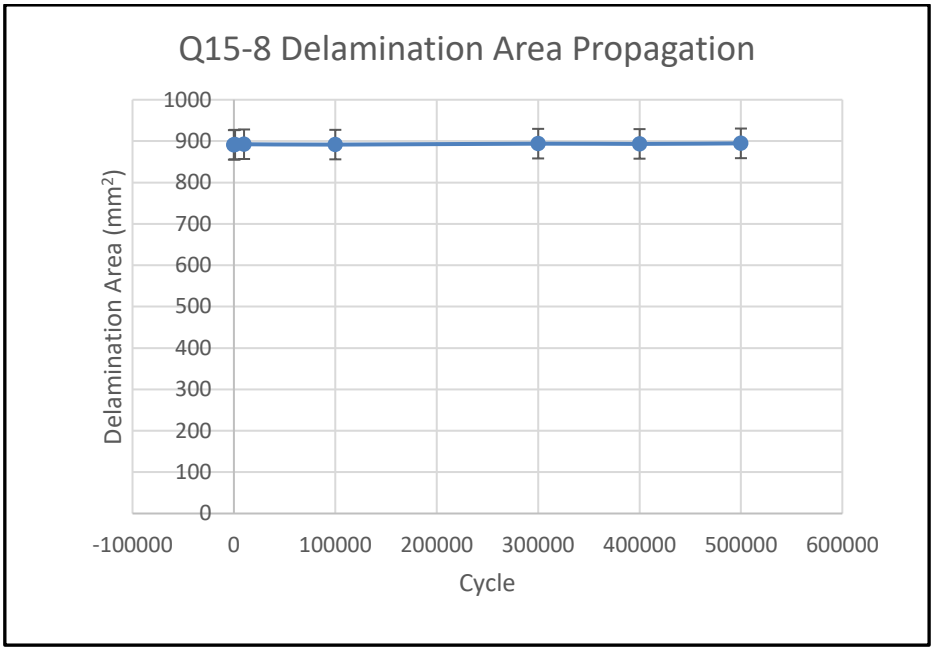

Figure 7-46 Delamination area in sample Q15-8 (max. load 179 kN, 73% RCS)

The exceptional case of Q25-6 within the “run-out” group was also examined. Although sample Q25-6 reached the ‘run-out’ criteria at 500000 cycle, slow delamination growth was discovered. The longitudinal delamination length remained while the one in transversal direction grew in a gradual manner. The increase in the length almost resulted in a linear behaviour (see Figure 7-47). Also, a gradual increase was observed in delamination area (see Figure 7-48). Interestingly, the noticeable increase was observed at the beginning of fatigue session due to the z displacement. Figure 7-45 shows the “offset” deformation shape along the cycles. The appearance of local buckling shape can be linked to the internal overall delamination growth initiation.

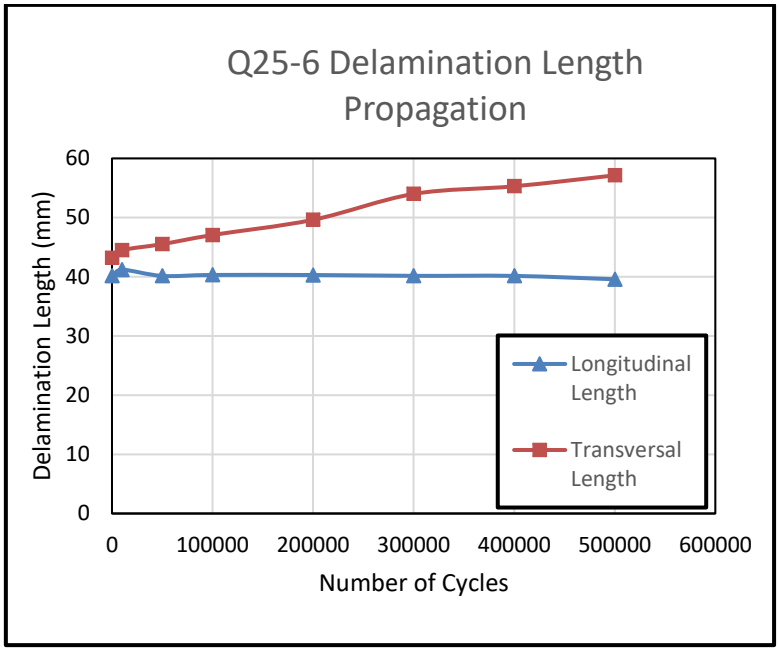

Figure 7-47 Delamination length in two directions in sample Q25-6 (max. load 129 kN, 70% RCS) showing slow delamination growth

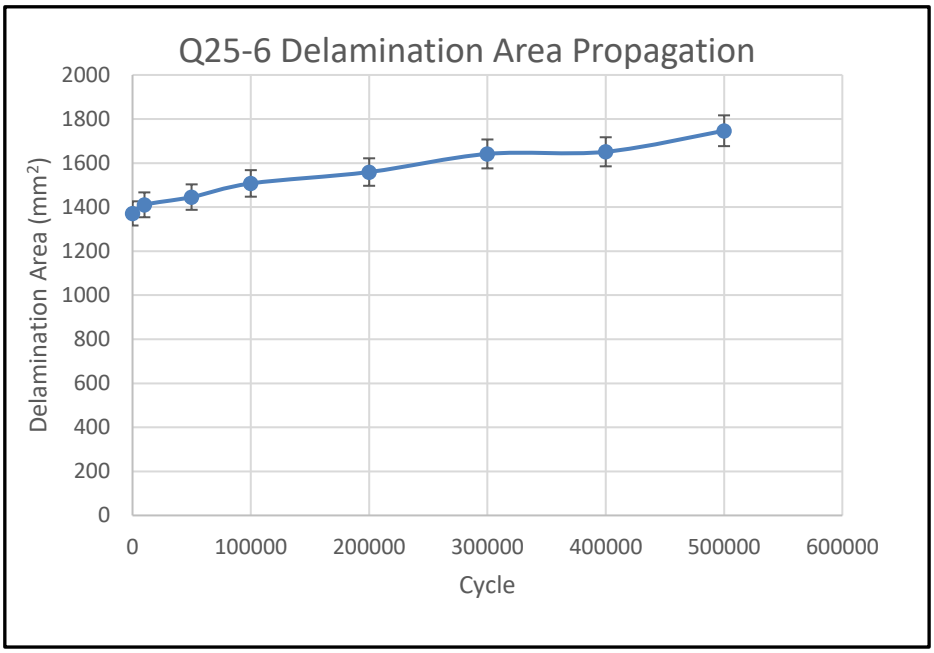

Figure 7-48 Delamination area in sample Q25-6 (max. load 129 kN, 70% RCS) showing slow delamination growth

7.6 Stiffness Degradation

The stiffness of the panel is a direct index of structural integrity. Calculated "stiffness" was obtained through the fatigue life for each sample. One thing worth

mentioning is that the calculated “stiffness” is not the actual stiffness, as specified in Chapter 3. The deformation in the loading direction is sometimes limited to the FOV of the picture taken from the DIC camera. Thus, the stiffness calculated is suitable for comparison of same samples at different fatigue cycled rather than the comparison between different samples. Observation of global stiffness of sample Q25-2 (see Figure 7-49) shows a detectable reduction at 3000 cycles (46.1% of the fatigue lifetime) whereas the C-scan image showed delamination growth at 6150 cycles (94.6% of the fatigue lifetime). The stiffness degradation appeared with the appearance of local buckling mode change on the surface, suggesting a strong linkage between them. Also, the degradation in global stiffness implied delamination propagation in the sample.

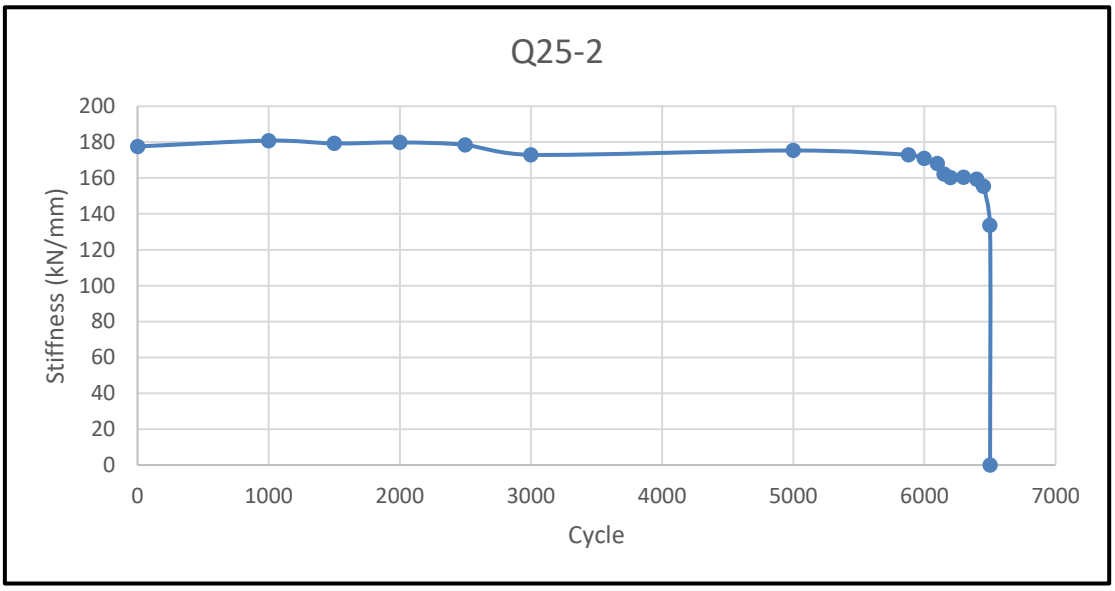

Figure 7-49 Calculated stiffness of sample Q25-2 (max. load 149 kN, 77% RCS) during fatigue session

For “run-out” samples, the calculated stiffness also showed no obvious degradation. An example of sample Q15-8 is shown in Figure 7-50. The value of global stiffness was kept steady at around 188 kN/mm during the fatigue loading period for the sample. The result only proves there is no obvious degradation within the sample. But if take its z-displacement into consideration, it can still deduct that some subtle changes happened within the laminate.

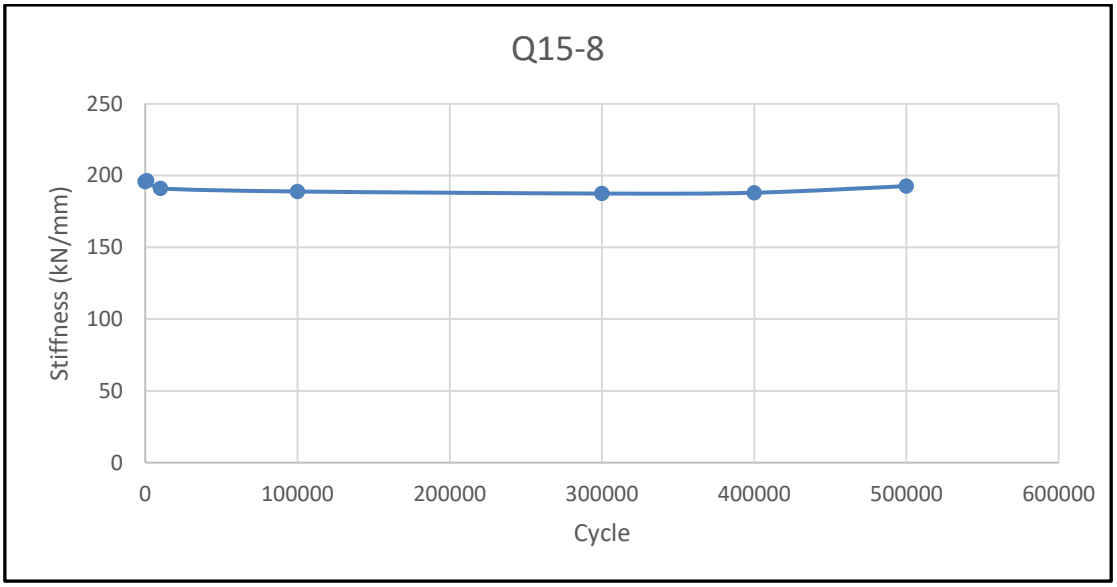

Figure 7-50 Calculated stiffness of sample Q15-8 (max. load 179 kN, 73% RCS) during fatigue session

7.7 Sectioned Delamination Observation

From the experimental observation of late growth detection in the projected area under C-scan and the earlier appearance of local buckling mode change, it can be assumed that when impacted composites are under cyclic loading, the delamination propagation first occurs at the interfaces with smaller delaminations located deeper within the laminate. When delaminations in those interfaces propagate to a similar size of the overall projected damage area, the delamination grows to enlarge the previous envelope boundary. When most of the delaminations grow to the initial overall size, the composite panel becomes too vulnerable to sustain the previous load, thus causing fatal failure after a small cycle increment.

To explore the real delamination propagation morphology during fatigue, an experimental test with sample sectioning was carried out. The test involved two similar un-impacted samples that were impacted with an identical 20-J impact. The first sample was cut right after the impact testing using the layout in the given graph (see Figure 7-51) and marked as “UF” (unfatigued). Each sectioned sample was 30 (W) × 20 mm (H) in planar size. This size was selected to fit the resin pot. The cutting plan was chosen to ensure the inclusion of the internal delamination

in both longitudinal and transversal directions. Sectioned sample marked as “T” showed multiple delaminations in the transversal direction and the sectioned sample marked as “L” represented the delaminations in the longitudinal direction. The arrow indicated the sectioning surface for acquisition. The second sample, labelled as “F” (fatigued) was cut after 100,000 cycles of fatigue load at a maximum compressive load of 0.75 RCS. The out-of-plane on-surface displacement was evaluated using the DIC equipment (see Figure 7-52). The fatigued sample presented inward bending which could also be found in the early stage of fatigue progress. The C-scan showed no detectable delamination.

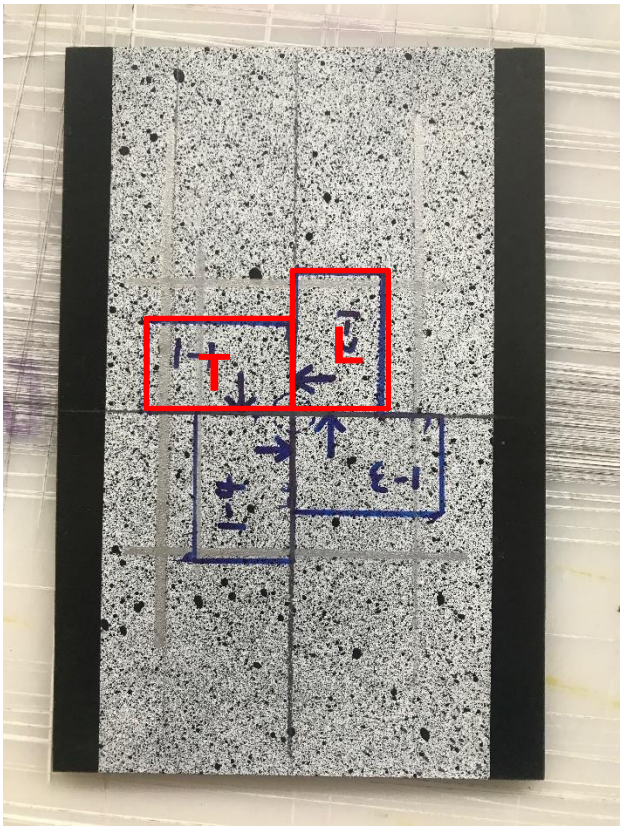

Figure 7-51 Delamination sectioning layout

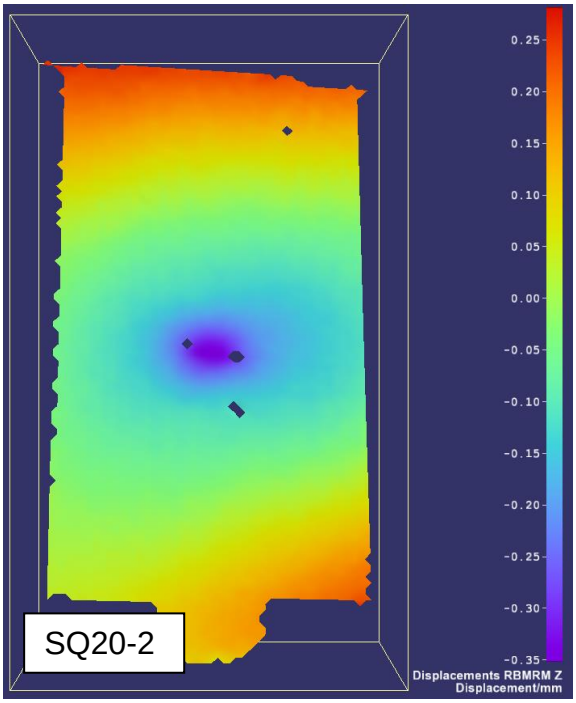

Figure 7-52 Z displacement in sample SQ20-2 under DIC evaluation

The section view was taken by the Leica microscope system in Met-Lab at Cranfield University. The results were presented for a direct comparison qualitatively between the fatigued and unfatigued sample under identical impact energy. One thing worth mentioning is that owing to the nature of different samples, the morphology could only be compared qualitatively rather than quantitatively.

The section view of section UF-T is shown in Figure 7-53. Section UF-T came from the unfatigued sample UF showing delamination distribution in the transversal direction. The cross-section view indicated the typical ‘pine tree’ distribution. The major delamination is depicted in the graph at a 0°/-45° interface that migrated to the 45°/90° interface later.

Impact surface

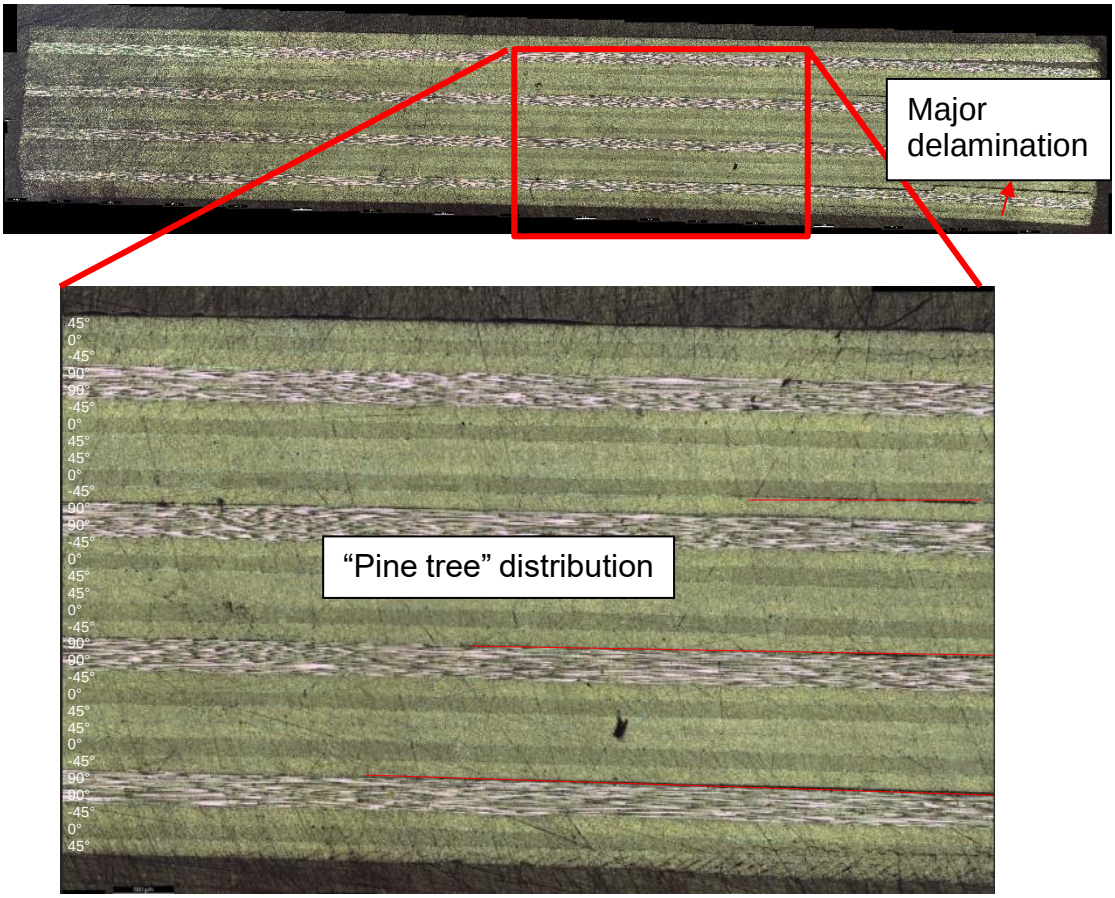

Figure 7-53 Section view of sample ‘UF-T’

The sectioned sample “F-T” showed the cross-section at the same position with “UF-T” but from a sample which had been fatigued for 100000 cycles. Even though the overall distinguishable delamination seemed shorter than that from section ‘‘UF-T’’, the samples exhibited a delamination distribution with more equal length rather than the traditional “pine tree” distribution (see Figure 7-54). The evidence proved that shorter delaminations grew earlier than the major delaminations.

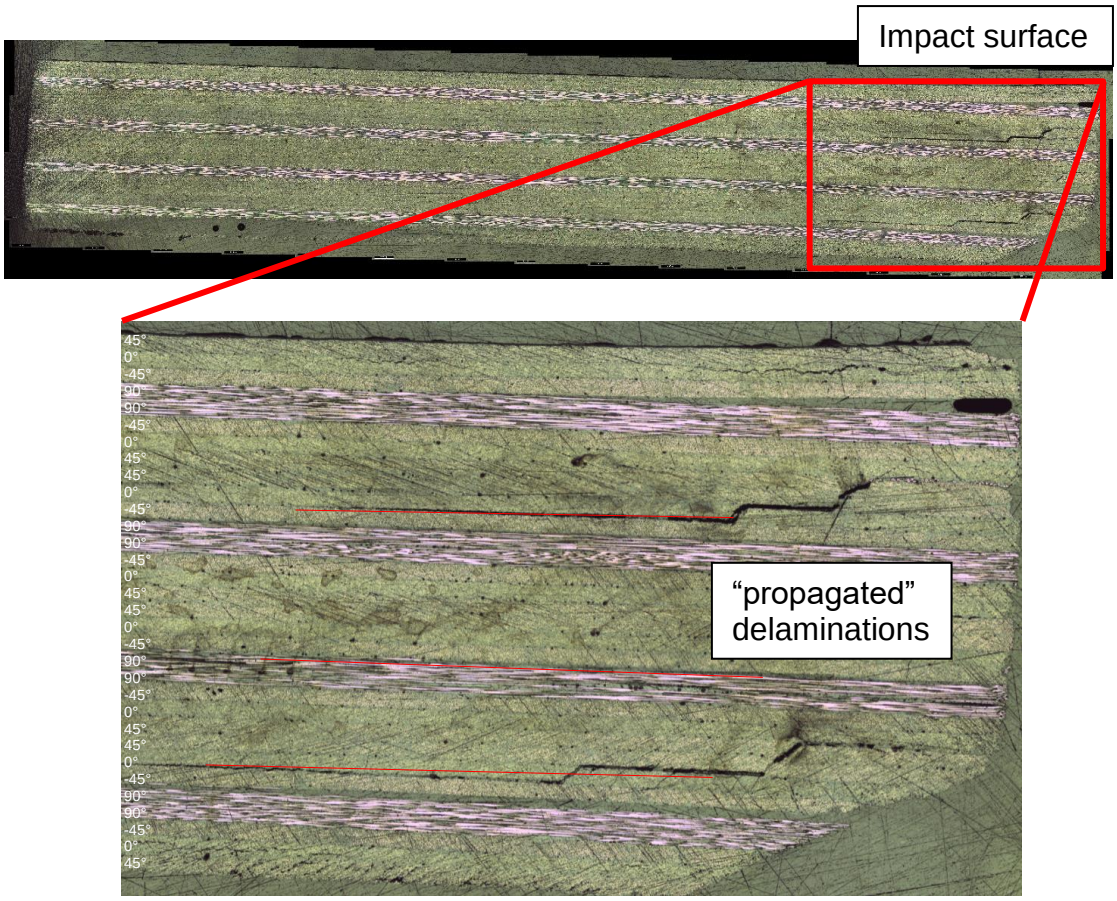

Figure 7-54 Section view of section ‘F-T’

An assorted schematic drawing for internal delamination is plotted in Figure 7-55.

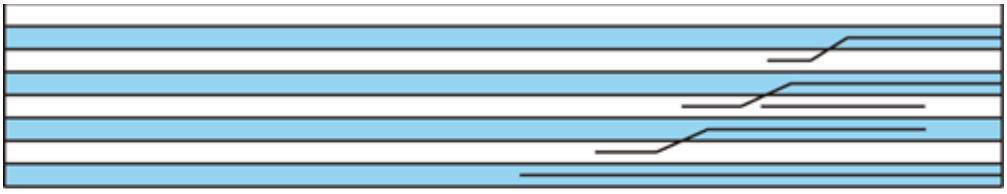

UF-T

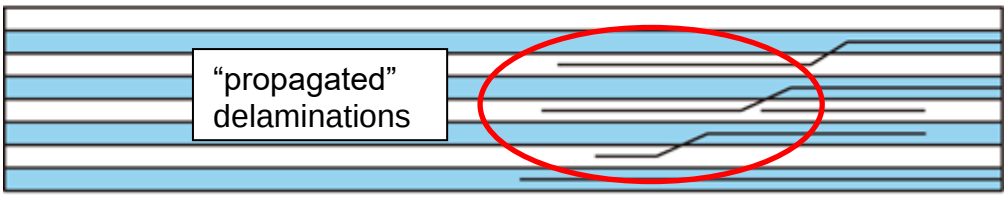

F-T

Figure 7-55 Schematic drawing of delamination distribution of section ‘UF-T’ and ‘F-T’ (each colour block represents 4 layers)

Three images at position “L” showing the delamination in longitudinal direction are presented in Figure 7-57. The impact side was at the bottom right of the cross-section view. The sectioned sample “F-L” showed “equal” distribution of delamination.

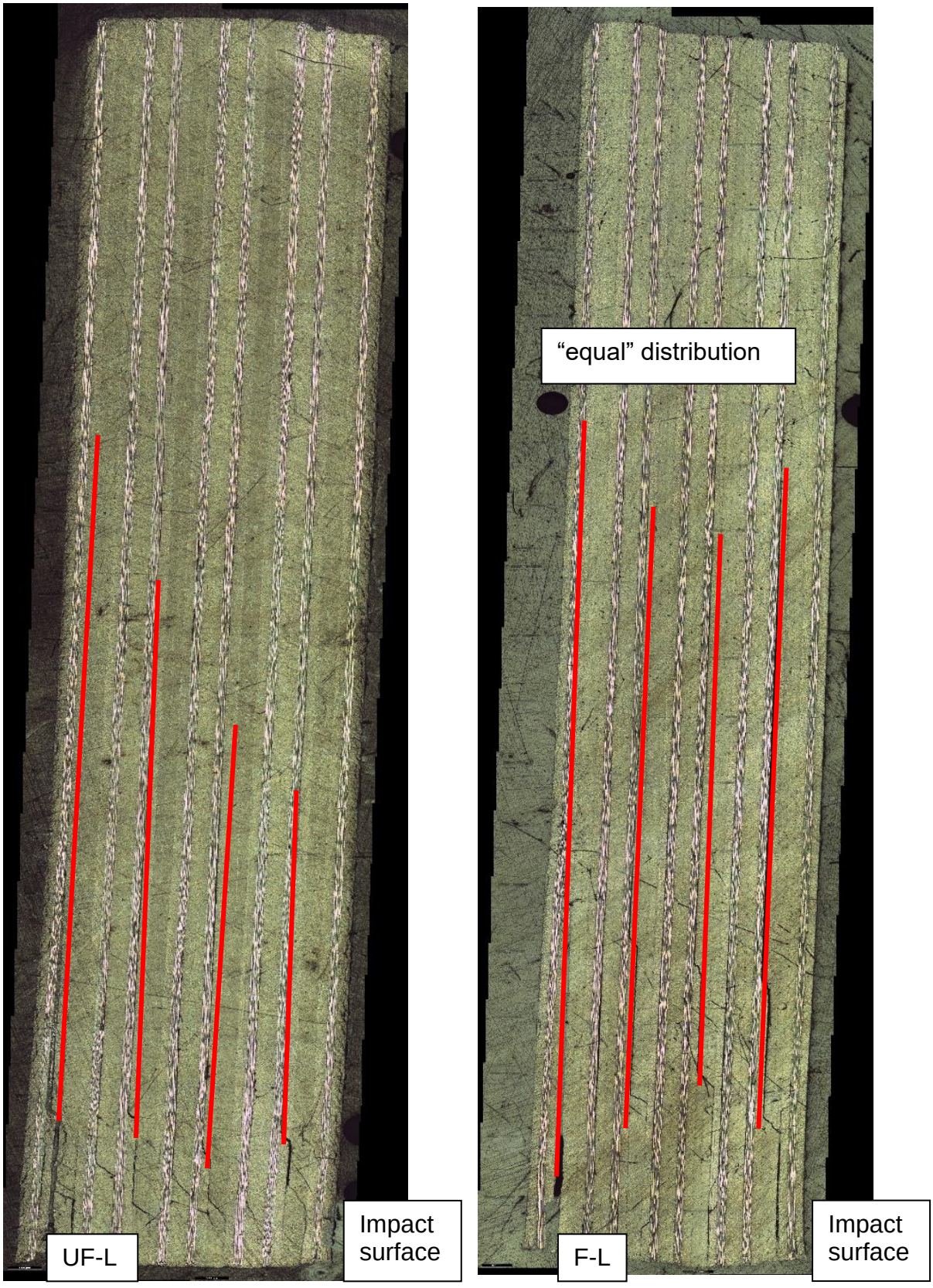

Figure 7-56 Cross-section view of sectioned sample ‘UF-L’ and ‘F-L’ (stacking sequence $[(45/0/-45/90)_s]_4$)

7.8 Summary

In this chapter, the findings of the post-impact fatigue test were presented. The fatigue life was discussed with delamination area, impact energy, and maximum compressive stress applied. Also, fatigue behaviour during cyclic loading for all the testing samples was outlined, and five typical cases were extensively presented. Three discrete stages could be identified for the compressive fatigue damage progression. Combine with the processed data of delamination growth and stiffness degradation, one can assume the shorter delaminations at the interface closer to the impact side tend to propagate earlier rather than the long and extensive delaminations, as the observation from the DIC showed that the appearance of local buckling mode changed near the impact site prior to the delamination propagation initiation detectable on C-scan. Further sectioning observations under a microscope gave some supportive evidence of some smaller delaminations grew prior to the largest one.

8 FINITE ELEMENT MODELLING OF DELAMINATION AND BUCKLING

Finite element modelling work was performed to develop a further understanding in the influence of SERR to delamination propagation.

As mentioned previously in Section 2.3.3, the SERR is widely regarded a governing factor for the delamination growth in carbon-epoxy composites. The growth is initiated when the SERR reaches the critical threshold. Although there are three components of SERR in the fracture mechanism corresponding to the three modes, Mode III is usually neglected while Mode I, Mode II, and mixed-mode I/II are considered. Some research indicated noticeable variation in the critical SERR: the critical SERR of Mode III is much higher than that of Mode I and Mode II (Reeder 2002, Robinson and Hodgkinson 2000, Juntti et al. 1999). Further research showed that during delamination growth, the influence of Mode III is too small to be considered in the case of adjacent plies in a laminated structure (Glaessgen et al., 2002). Aircraft structures normally present delaminations in either Mode I or Mode II, but they are loaded in the mixed-mode state in realistic situations owing to the curved shapes, multi-directional plies, and compression after impact (Nilsson et al. 2001).

In this chapter, the validation on pure mode I and mixed mode I and mode II numerical models were performed by comparing a double cantilever beam (DCB) experimental testing and a published mixed mode bending (MMB) numerical model. Furthermore, a validation on global buckling was carried out comparing the numerical model and the analytical results. Followed with a single embedded delamination model, the local buckling load and the SERR values of mode I/II were presented. A further two embedded delamination model was developed to unveil the SERR values in such scenario.

8.1 Mode I and Mixed Mode I/II Validation

Before the modelling for the multiple delaminations in the test sample-sized panel, some validation work was necessary. Two common testing methods, double cantilever beam (DCB) and mixed-mode bending (MMB), were modelled

in ABAQUS 6.14 to validate the responsive output and to correct some parameters for future modelling.

8.1.1 Double Cantilever Beam

The double cantilever beam (DCB) test is the most frequently used testing method to measure Mode I fracture toughness for delamination of fibre-reinforced plastic laminates. In this section, the load-displacement response is compared between the numerical results and an experimental testing to validate the critical mode I value.

In a DCB test, the initial crack is inserted into the mid-plane by using a non-adhesive film such as PEFE. The specimen is then mounted onto a jig with either hinges or loading blocks. The load is applied to open the beam from the initial film area by quasi-static loading at a very slow and constant speed, usually at 1–5 mm/min. When the mode I SERR value reaches the critical mode I value on the delamination interface, the propagation begins. So the initial propagation point is the key for validation.

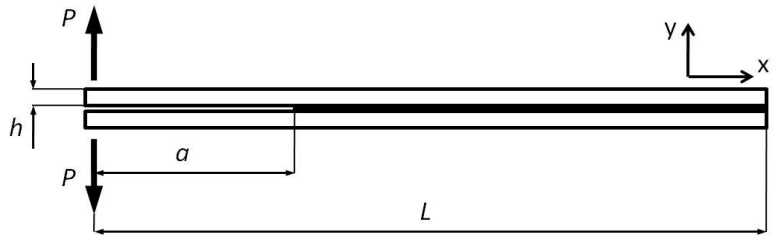

Figure 8-1 Illustration of a DCB testing

The DCB test used a stack of thirty-two 0° plies (stacking sequence $[0°]_{32}$). The lamina properties used in the modelling were collected from the real-world datasheet provided by the manufacturer. The material properties are listed in Table 8-1.

Table 8-1 Lamina properties of AS7/8552 prepreg used in testing and numerical modelling

Longitudinal Modulus E_1	145000 MPa
Transverse Modulus E_2	10000 MPa

Poisson's Ratio v_{12}	0.3	
Shear Modulus G_{12}	5800	MPa
Ply Thickness t_{ply}	0.135	mm
Longitudinal Tensile Strength 0°	2550	MPa
Transverse Tensile Strength 90°	90	MPa
Longitudinal Compression Strength 0°	1862	MPa
Transverse Compression Strength 90°	180	MPa
In-Plane Shear Strength	115	MPa

The ply thickness was 0.135 mm, so the half-thickness (h) of the beam was 2.16 mm. Other dimensional parameters including the initial crack length are listed in Table 8-2.

Table 8-2 Dimensional parameters of DCB

Total Beam Length (L)	150 mm
Total Beam Width (B)	20 mm
Half Beam Thickness (h)	2.16 mm
Initial Crack Length (a)	43 mm

The G_{IC} was obtained from the testing and subsequent processing based on the method provided by the ASTM standard. From Chen's (2015) thesis, the value was 241.3 J/m^2.

Subsequent modelling was carried out based on the experimental work carried out by the author. Continuum shell elements with eight nodes (designated as SC8 in ABAQUS) were used to model the DCB behaviour in a 3D model. Each node of the SC8 element had 3 DOFs. The SC8 elements were used to model a thick laminate. Each layup is defined as a section property, and the stresses are calculated at the integration point for each ply. The calculation of out-of-plane stress is an obvious advantage over the traditional shell elements (designated as S8 in ABAQUS 6.14) as the actual out-of-plane stress is calculated among other unknowns within the ply in the PDEs to solve. A mesh size of 1mm was applied to the model to ensure the convergence and accuracy. The parametric study was done by some previous work at Cranfield by some other students to define the optimised mesh size.

A displacement of 5 mm was applied to the top and bottom positions, as shown in Figure 8-2. The load-displacement remained linear until total displacement between the two half beams was reached. At this displacement, the crack starts with a stable propagation.

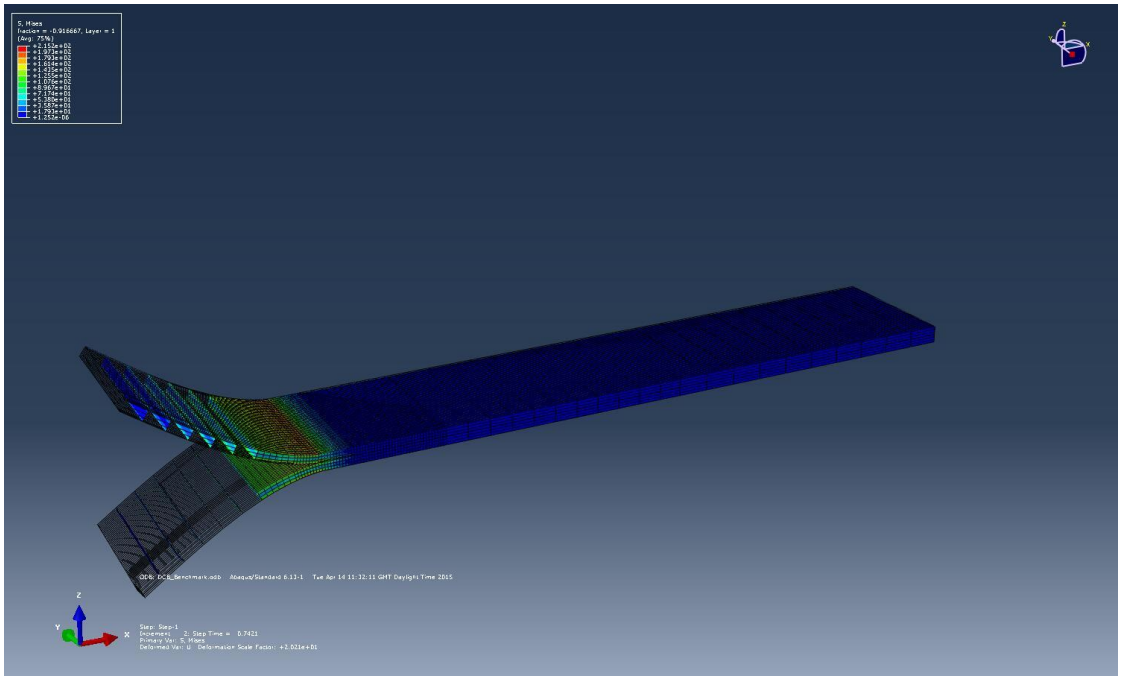

Figure 8-2 Double cantilever beam modelling in ABAQUS 6.14

The result is shown in Figure 8-3. It can be found in the figure the experimental result has a sudden drop after the crack propagation initiation. The reason is that the specimen consisted of purely 0° plies stacked during fabrication without a 5° distortion layup which was suggested by the ASTM standard, to minimise the potential effect of a sudden jump when the adhesive was released.

The validation of mode I critical value was satisfactory as the linear part fits perfectly in numerical and experimental analysis, and the propagation initiation point was well captured.

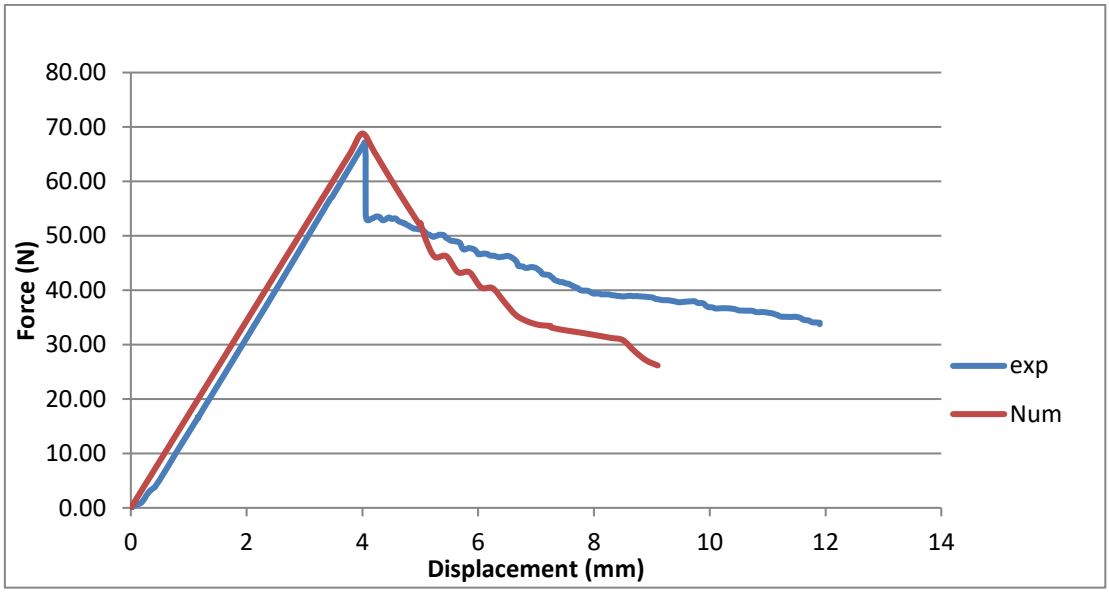

Figure 8-3 Comparison of experimental testing results and numerical results on force-displacement response for DCB

8.1.2 Mixed-Mode Bending

Mixed-mode bending (MMB) is modelled in this section to examine the critical state of delamination propagation in mixed mode I/II and obtain some key parameters for the later modelling stage. The comparison is made with a published data from Krueger (2012) in forms of load-displacement and displacement-increased delamination length for validation the delamination propagation in mixed-mode conditions.

The mixed-mode bending (MMB) test was first proposed by Crews and Reeder (1988) and has been improved immensely in the last 20 years. The MMB test can be considered a superposition of DCB and end notch flexure (ENF) tests. The highlight of this setup is that a wide mixture range is easily acquired simply by adjusting the arm distance with the same specimen geometry.

Benchmark examples for quasi-static delamination propagation prediction was adapted from Krueger (2012). The example is based on a finite element model of the MMB specimen for 50% of Mode II. The setting of the system is shown in Figure 8-4. The model used IM7/8552 unidirectional prepreg material as the sample. The property data can be found in the original literature. Similar to the

DCB model, continuum shell elements with eight nodes was used during the reproduction. The three components of SERR were used, as provided in the open data source.

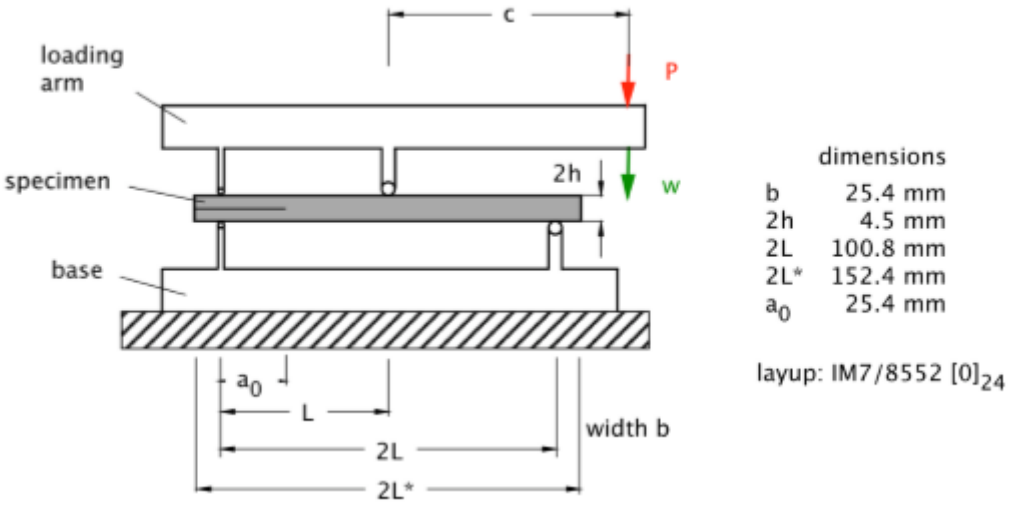

Figure 8-4 Mixed-Mode Bending specimen (Source: Kruger 2012)

The opened MMB model is shown in Figure 8-5.

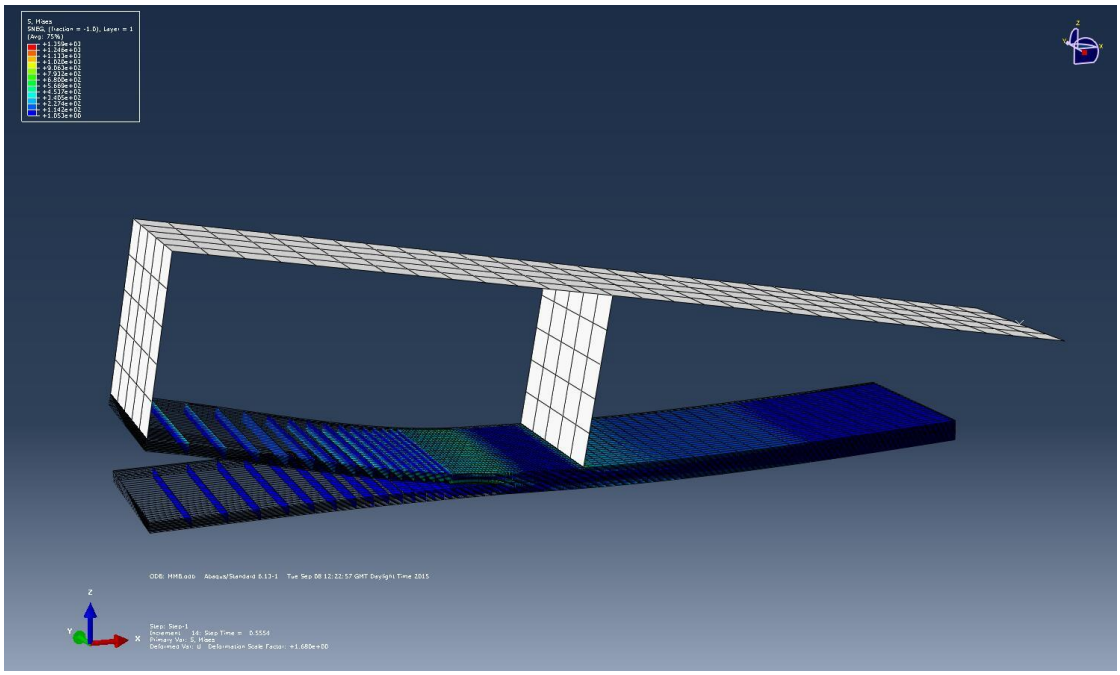

Figure 8-5 Mixed-mode bending modelling in ABAQUS 6.14

Load-displacement response and displacement-delamination response of MMB are compared in Figure 8-6 and Figure 8-7. It can be found the author's result is validated by the identical values as the benchmark specified in the literature (see Figure 8-6).

Further study has also been carried out (see Figure 8-6a) to reveal the influence of release tolerance (reltol in ABAQUS 6.14). To reduce the observed overshoot, the reltol was decreased. The lower the reltol value the earlier the crack appearance. The results show that by using the default release tolerance (reltol = 0.2) as suggested in the ABAQUS /standard handbook or increasing the value, as suggested in the user's manual, convergence problems can be addressed. However, it leads to an undesired overshoot of the computed result compared to the benchmark.

It can be found the best fit between analysis results and the benchmarks could be achieved for reltol values (reltol < 0.1) in combination with contact stabilisation (cs = 1 × 10^{-6}). These parameters are used in the next stage of numerical modelling to examine the SERR value in the delamination front.

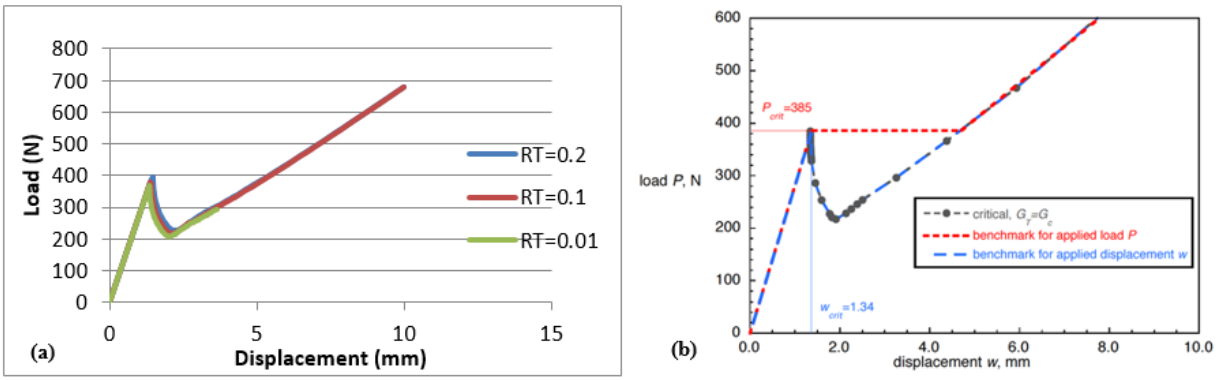

Figure 8-6 Load-displacement response of MMB model: (a) Author's result; (b) Kruger's (2012) benchmark

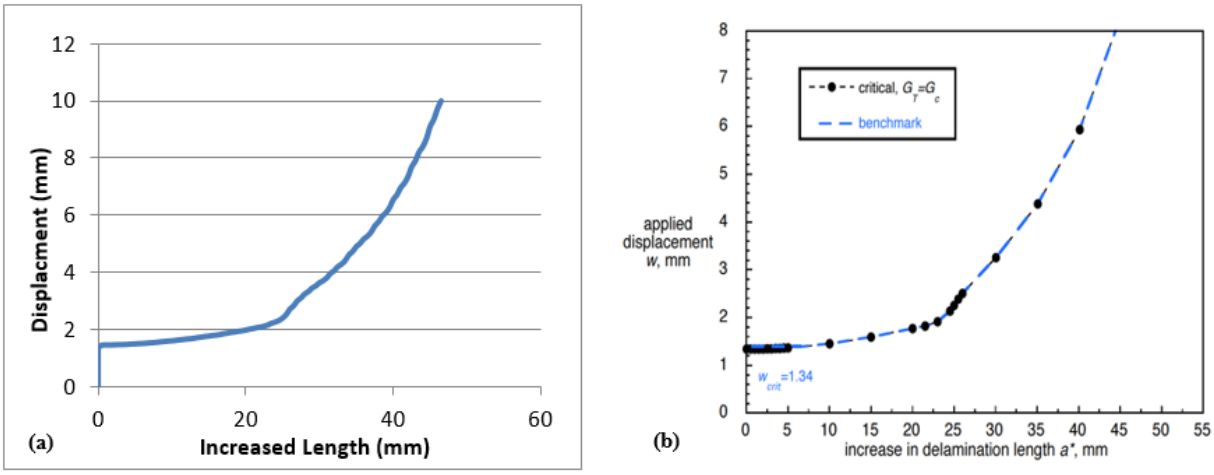

Figure 8-7 Displacement-delamination increase response of MMB model: (a) Author's result; (b) Kruger's (2012) benchmark

8.2 Buckling Model Validation

Validation of the buckling behaviour was carried out by comparing the stress causing global buckling between numerical results using ABAQUS /Standard and the analytical results obtained in previous studies (Rees, 2009).

The ply properties of AS7/8552 are shown in Table 8-1. The stacking sequence is quasi-isotropic consisting of 32 plies with a layup of $[(45/0/-45/90)_4]_S$. The dimension of the model is kept the same with experimental testing samples at 150 mm (L) × 100 mm (W) × 4.32 mm (T).

8.2.1 Analytical Calculation of Global Buckling

The axial compression of a wide, thin plate of thickness t, with similar length and width dimensions, a and b, respectively, is shown in Figure 8-8. Having simply supported (pinned) ends and unsupported sides, the strut deflects laterally with uniform curvature and surface strains in the opposite sense. The cross-section b × t remains rectangular during bending with uniaxial stresses σ in the plane of the plate.

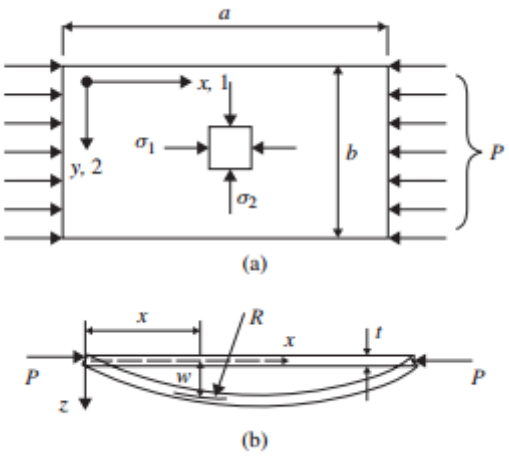

Figure 8-8 Buckling of a plate under uniaxial compression (Source: Rees, 2009)

From Figure 1, the curvature is expressed in:

$$d^2w/dx^2 = \varepsilon_1/z \tag{8-1}$$

Substituting from equation (1-1) with $M/I = \sigma_1/z$, the equation can be expressed as:

$$\frac{d^2w}{dx^2} = \frac{1-v^2}{E}\frac{\sigma_1}{z} = \frac{(1-v^2)M}{EI} \tag{8-2}$$

With a bending moment, $M = -Pw$, and substituting $P = \sigma bt$ and $I = At^2/12$, Equation 8-2 can be rewritten into:

$$\sigma_{cr} = \frac{\pi^2}{12}\left(\frac{b}{a}\right)^2\left(\frac{E}{1-v^2}\right)\left(\frac{t}{b}\right)^2 \tag{8-3}$$

Where E is Young's modulus of the laminate, which can be calculated using laminate theory. The laminate modulus, in this case, is 56.4GPa.

When substituting all the numbers into Equation 8-3, the critical stress is 42.3 MPa.

8.2.2 Numerical Modelling of Global Buckling

Similar to the analytical situation, the model was subjected to uniaxial compressive load at both ends, and there was no support in longitudinal edges. The load was applied uniformly at two end surfaces with the magnitude of 1. The

eigenvalue from Mode 1 buckling was chosen. The critical buckling stress was 44.9 MPa.

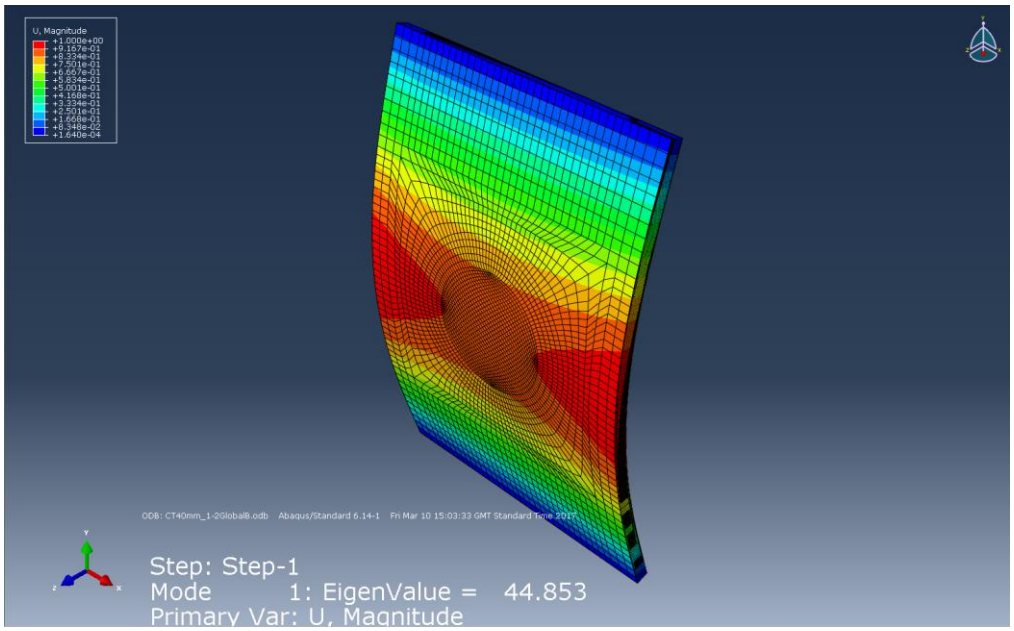

Figure 8-9 Global buckling results in ABAQUS 6.14

8.3 Single Delamination Model

Numerical models with a single embedded round delamination were developed to study the local buckling around the damage area and the SERR at the delamination front.

A single circular delamination was inserted in each layer to study the local buckling behaviour and obtain the G_I and G_{II} values at the delamination front. Laminar properties of AS7/8552 are shown in Table 8-1. The size of the model is the same as the dimension of the testing panel at the size of 150 mm × 100 mm. The QI stacking sequence, $[(45/0/-45/90)_s]_4$, was identical to that used in the real testing. The diameter of the single circular delamination size was calculated in three different dimensions: 32 mm, 40 mm, 44 mm, which the size was obtained from the approximate c-scan measured delamination size after the impact testing under 12J, 20J and 25J respectively. The damage was simplified as a single circular defect between two interfaces. The position of the single delamination was systematically changed, moving from the $1^{st}/2^{nd}$ layer interface to the mid-plane $16^{th}/17^{th}$ interface. Thus, a total of 48 cases were calculated numerically in

ABAQUS 6.14. Due to need for a clear presentation, a group of data was shown in the following section, which will be explained later.

8.3.1 Boundary Conditions and Debonding Criteria

The boundary conditions were set along with the conditions applied in the testing standard: fully clamped at the bottom and simply supported at two side edges and rotation is strictly restrained on the top edge. Detailed boundary conditions are described in Table 8-3 and illustrations of these boundary condtions are shown in Figure 8-10 Load was applied in the negative y direction using pressure locally on the top surfaces to make sure uniaxial compression is achieved. Conventional shell element with four nodes (S4) was used in this model.

Table 8-3 Boundary conditions of numerical model

Specimen edge	Edge Condition	Restrained	Free
Top edge	Clamped	U1, U2, UR1, UR2, UR3	U2
Side edges	Simply Supported	U3	U1, U2, UR1, UR2, UR3
Bottom edge	Fixed	U1, U2, U3, UR1, UR2, UR3	***

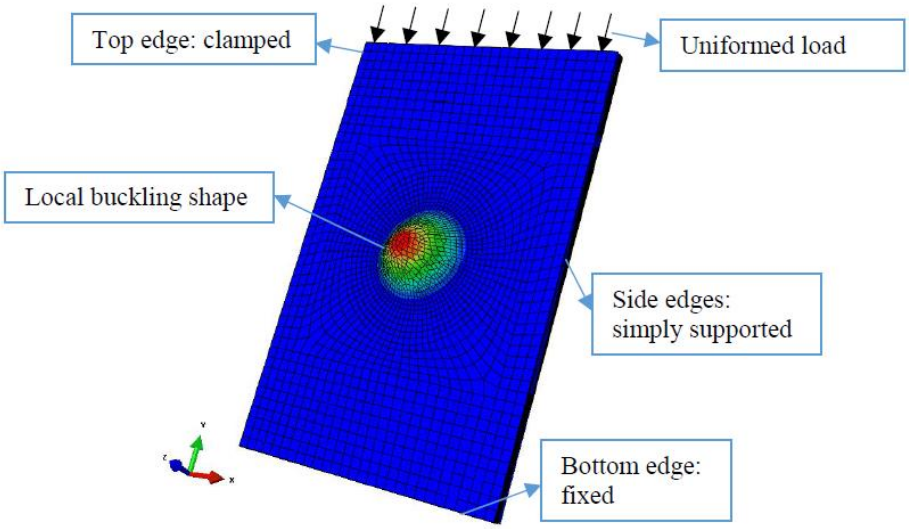

Figure 8-10 Boundary conditions and initial local buckling and at the 1st/2nd interface

The interlaminar debonding behaviour was simulated using VCCT. The B-K law was chosen to be the fracture criteria to calculate the equivalent SERR by combining the energy release rates in all three modes. The expression is given in equation 8-4.

$$G_{C\_equivalent} = G_{IC} + (G_{IIC} - G_{IC}) \left(\frac{G_{II}+G_{III}}{G_I+G_{II}+G_{III}}\right)^{\eta} \quad (8\text{-}4)$$

Where η is the B-K law exponent, and it was taken as 1.557 because this value provided a good curve fitting result for carbon/epoxy composites in the investigations conducted by Singh and Partridge (1995).

The critical SERRs taken from previous experimental tests carried out by Chen (2015) are listed in Table 8-4.

Table 8-4 SERRs used in VCCT technique

G_{IC} (J/m^2)	G_{IIC} (J/m^2)
241.3	839.93

8.3.2 Local Buckling

A local buckling model was initially calculated in ABAQUS 6.14. The purpose of the local buckling model was to obtain the local buckling load for each interface with the embedded delamination existence and to use as an essential subsequent step for the later compression session. The central circular delamination had a diameter of 40 mm. This local buckling mode obtained from the linear eigenvalue analysis was then transferred to a subsequent non-linear static analysis with less than 0.1% imperfection to guide this fracture FE model through a correct bifurcation point (see Figure 8-10).

The local buckling loads obtained from half of all the interfaces are presented in Figure 8-11. It was found that the model underwent delamination between the first and second plies, giving the lowest delamination buckling load, which is obvious due to the low stiffness of the surface sub-laminate. With the delamination location moving to the mid-plane, the buckling load increased. The increase started at a gentle pace from the 1st/2nd interface to the 5th/6th interface

after which an elevated pace was observed. The steep increase stalled from the 10th/11th interface and remained steady with a subtle decrease to the mid-plane.

Another finding is that from the 10th/11th interface, the buckling mode at the lowest eigenvalue changed from the beginning. At shallower (closer to the panel surface) interfaces, the lowest eigenvalue was obtained with a single circular pop-out area while the buckle mode for deeper interfaces was an s-shaped curvature with both positive and negative displacement.

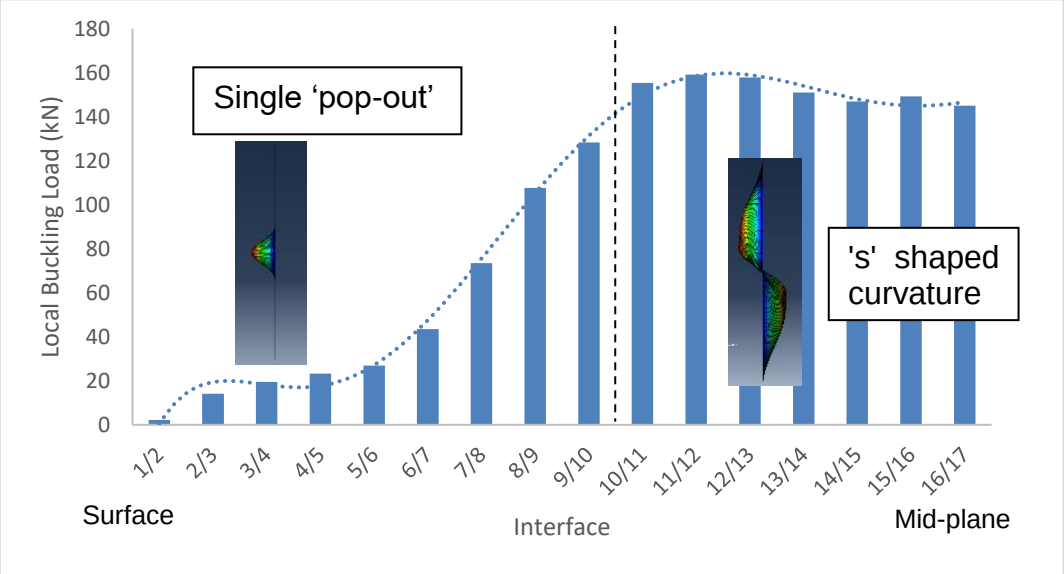

Figure 8-11 Local buckling load of 40 mm, round artificial delamination at noted interfaces

This phenomenon was observed during the fatigue testing. Although the back face of the testing samples was not measured using DIC equipment, photos were taken to report the instant local buckling at the beginning of the loading session (see Figure 8-12). The single 'pop-out' required a low load to achieve as presented in Figure 8-11.

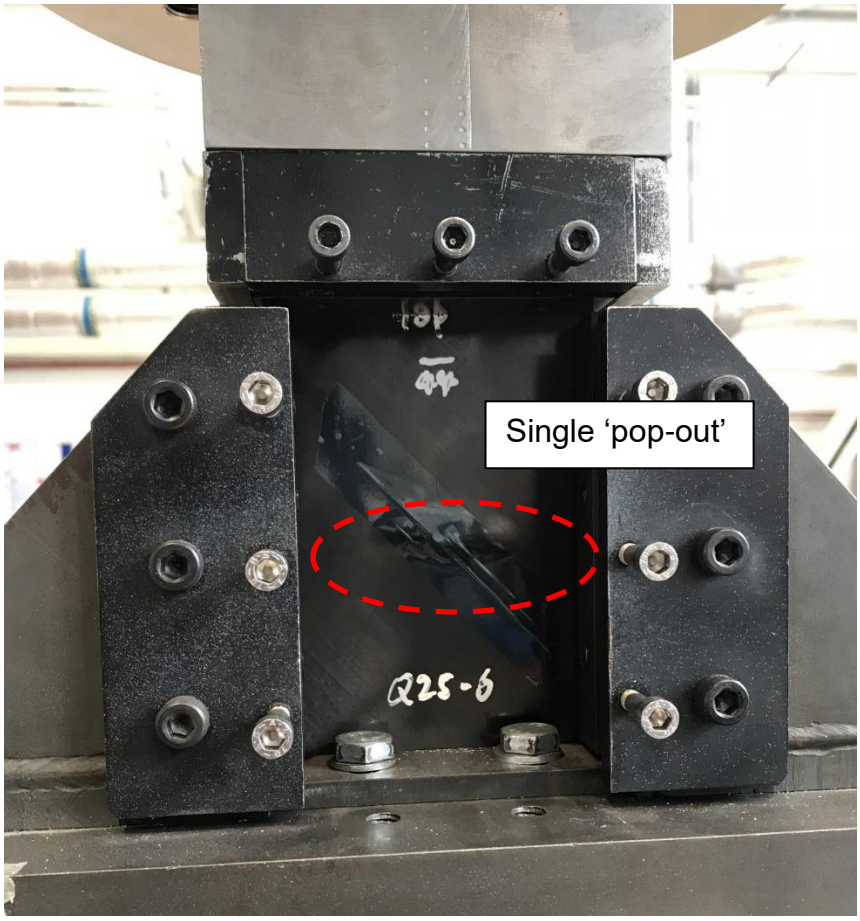

Figure 8-12 Back face local buckling (marked area) of sample Q25-6 when loaded

8.3.3 Static Compression at Same Load

The subsequent non-linear static analysis was performed after introducing the related local buckling mode obtained from the linear eigenvalue analysis at a 0.1% initial imperfection. With the introduction of the initial buckled model, additional uniformed stress was applied on the top surface of the panel. The conduction of such models is to extract the G values in mode I/II to study the relationship of G values to the delamination size.

The 3D FE model used conventional shell elements (S4) in ABAQUS 6.14. Circular shapes of delamination were inserted between ply interfaces to simulate initial impact damage based on the maximum delamination area obtained from C-scan of 12J, 15J and 25J impact energy. The Compressive load and boundary conditions were the same as those for the experimental tests. The load was 64.4 kN.

The mesh was refined near the initial circular delamination area. From the delamination front to the circumference of a concentric circle with a diameter of 50 mm, the mesh element was set as fine as 1 mm. At the far end of the model, a biased mesh was set from the 50-mm circle to the boundary, mesh element size ranged from 2 mm to 5 mm were used to save the computing consumption.

The fracture criteria were based on the same B-K law as in the MMB validation. The fracture toughness parameters are stated in the Table 8-4 adapted from Chen's (2015) experimental results.

The maximum G value of mode I and mode II are plotted in Figure 8-13 and Figure 8-14. Although it a total of 48 cases were modelled (16 interface locations by 3 different delamination size), the mode I/II SERR value was very minimal after $6^{th}/7^{th}$ interface. Thus, only the SERR values from $1^{st}/2^{nd}$ to $6^{th}/7^{th}$ interfaces are presented in the following two graphs.

Generally, it can be found the G_I value has a positive relation with the delamination size when the same load is applied. The G_I value increases in a larger delamination. The largest increase can be found in the $5^{th}/6^{th}$ interface. The mode I SERR value is not commonly increasing with a deeper delamination location. From the $6^{th}/7^{th}$ interface, the G_I value becomes very neglectable. It also can be seen the close value of G_I value from $2^{nd}/3^{rd}$ interface and $4^{th}/5^{th}$ interface.

In Figure 8-14, it can be seen the G_{II} values are less size dependent. From the $1^{st}/2^{nd}$ to the $3^{rd}/4^{th}$ interface, the G_{II} values are relatively stable regardless of the increase in delamination size. Significant increase can be found in $4^{th}/5^{th}$ and $5^{th}/6^{th}$ interface when delamination size changes from 32 mm to 40 mm. When the delamination size changes from 40 mm to 44 mm, no increase can be found in those two interfaces either, which means the GII values become being independent of size.

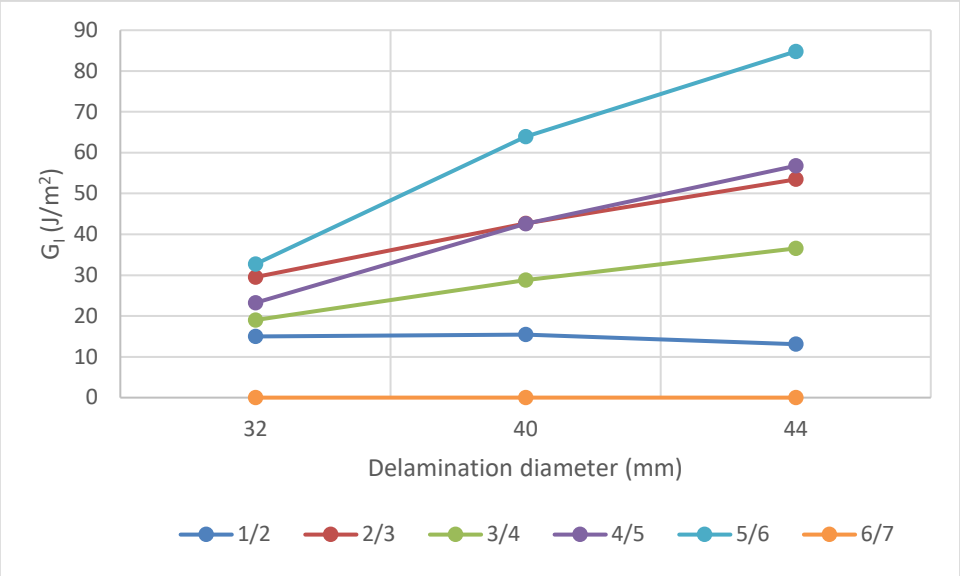

Figure 8-13 maximum G_I value of three different delamination sizes at a noted interface from 1st/2nd to 6th/7th at the load of 64.4 kN

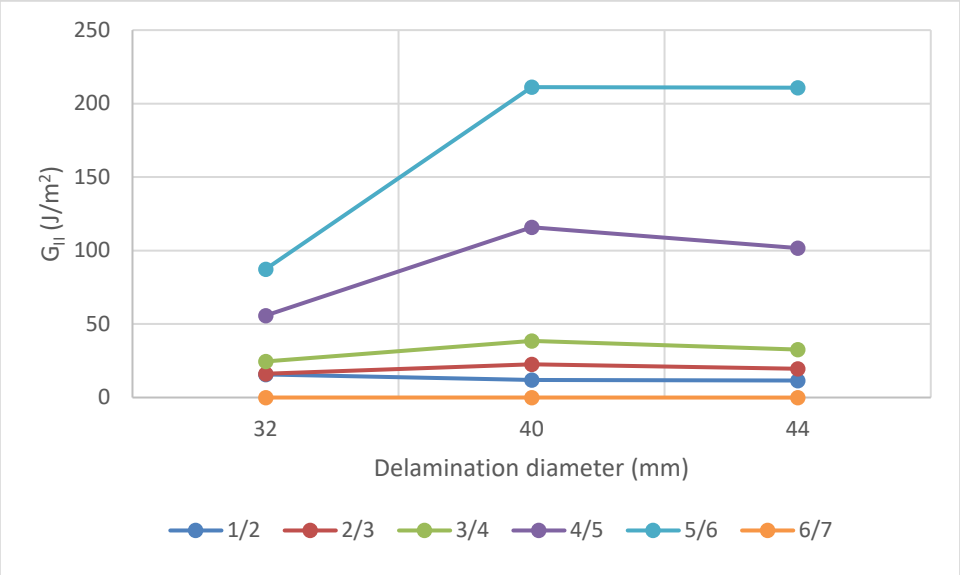

Figure 8-14 maximum G_{II} value of three different delamination sizes at a noted interface from 1st/2nd to 6th/7th at the load of 64.4 kN

This could explain the acceleration of delamination propagation in stage three of fatigue progression when the propagation was firstly found under c-scan. The slope was increasing when the delamination area and length growth started (see Figure 7-39 to Figure 7-42). The SERR value, especially the mode I value which is regarded as the delamination propagation main driving force, increases when

the size grows. This increase will accelerate the size increase in return. With this mutual effect, when the delamination starts, an accelerated growth is commonly observed.

8.3.4 Static Compression at the Same Fraction of RCS

Numerical model in static compression to study the SERR values under same fraction of its nominal RCS for different delamination size were also developed. The model changed the applied load of the model described in Section 8.3.3. The difference between this model and the model in last section was the applied load had been used the 77% RCS from the 12J, 20J and 25J level (88.3 kN, 70.9 kN, 64.4 kN). These three loads were applied to the model embedded with a delamination size of 32 mm, 40 mm and 44 mm respectively. Similar with the model in the last section, a single delamination model was submitted for processing to calculate the SERR values for each model. A total number of 48 models were performed (16 interface location alternations for each delamination size). The obtained results are introduced in the prospect of the maximum mode I and mode II SERR values and their directions.

Mode I and Mode II SERR Values

The Mode I and Mode II SERR values at the circumference of the delamination were plotted in Figure 8-15 and Figure 8-16. Only the interfaces from $1^{st}/2^{nd}$ to $6^{th}/7^{th}$ from the surface were included as the SERR value drastically dropped to an neglectable value from the $6^{th}/7^{th}$ interface. The sudden drop started at the same interface where there was a significant increase in the local buckling load. The jump in the lowest eigenvalue to achieve the local buckling made it more difficult to open the delamination.

The results showed the expected no growth in all cases. The initial static load did not trigger the fatigue delamination. In the numerical modelling, no growth was observed simply because the low SERR value at the front tip did not reach the critical value and satisfy the propagation criteria.

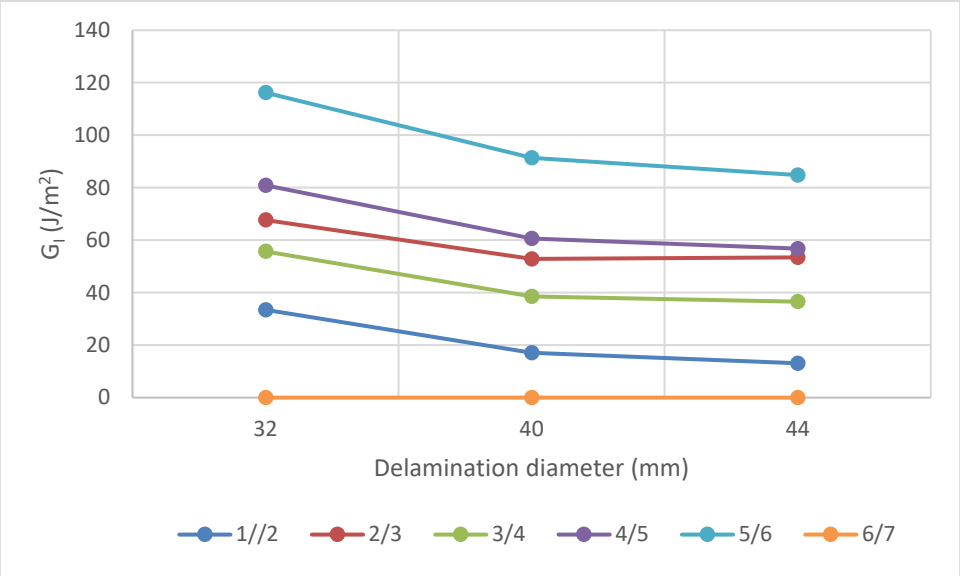

Figure 8-15 maximum G_I value of three different delamination sizes at a noted interface from 1st/2nd to 6th/7th at the load of 64.4 kN, 70. 9 kN and 88.3 kN (77% of RCS from 12/20/25J) respectively

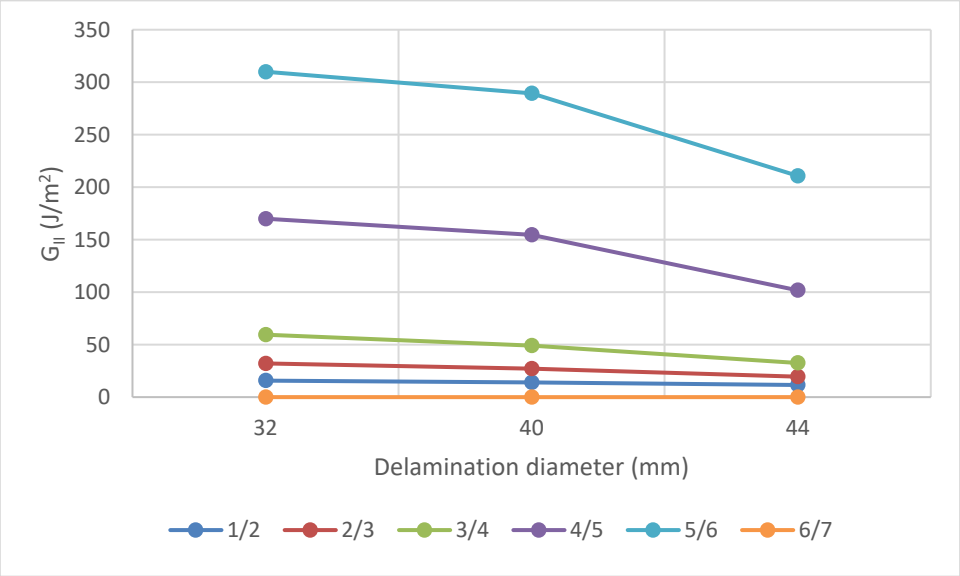

Figure 8-16 maximum G_{II} value of three different delamination sizes at a noted interface from 1st/2nd to 6th/7th at the load of 64.4 kN, 70. 9 kN and 88.3 kN (77% of RCS from 12/20/25J) respectively

Another point worth mentioning is that with the same nominal fraction of its RCS, the SERR value behaves differently. Even though the 32-mm group had the smallest delamination area, by applying the highest load, a larger SERR can be achieved. From these results, the case with a smaller delamination seems more

likely to propagate earlier or have a shorter fatigue life than those with a larger delamination. However, this is very contradictive to the experimental results we collected from the post-impact fatigue testing. One explanation is that the model calculated the SERR at the delamination front where only one delamination existed. This ideal scenario is much different from the real-world case, and the difference in larger impacted samples is higher. The existence of multiple delaminations would not only cause the A decrease in the overall stiffness was observed in more impacted samples which would influence the SERR value and the critical value.

Mode I and Mode II SERR Distribution

The distribution of SERR was similar in the three different delamination size models. The direction of maximum SERR and the distribution was dependent on the interface direction. In Figure 8-18 and Figure 8-19, Mode I and Mode II SERR are plotted at the circumference of the circle from the model with a 40mm circular delamination. The loading direction is along the 0º and 180º direction with a value of 64.4kN. A schematic drawing of the load direction and the delamination angle are shown in Figure 8-17.

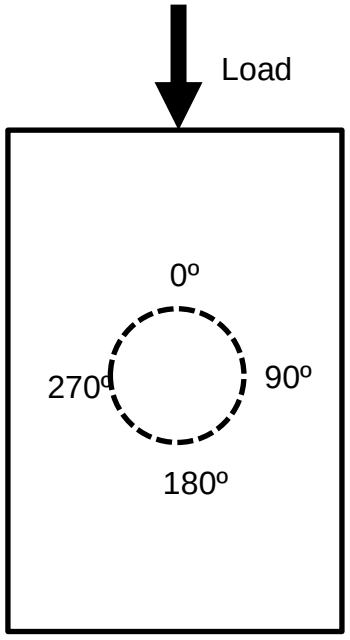

Figure 8-17 Schematic drawing of load and angle on the delamination front

From both graphs, it can be seen the maximum G value (from $1^{st}/2^{nd}$ to $5^{th}/6^{th}$ interface) are located on the two ends of the delamination area perpendicular to the load direction. The locations of the maximum SERR direction is identical to the propagation direction observed in the fatigue experimental testing. Although the low SERR value interfaces (from $6^{th}/7^{th}$ to $9^{th}/10^{th}$ interface) had their highest value in either 0º and 180º or the 90º and 270º, those values were so minimal that with which has no influence on the delamination propagation.

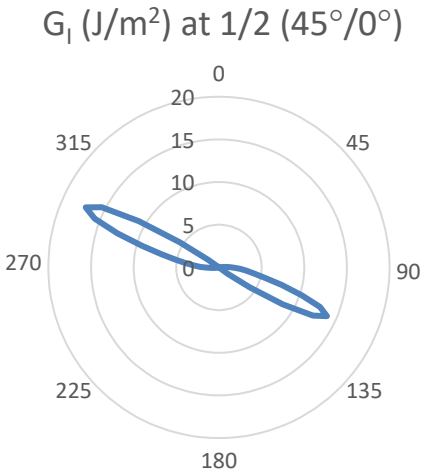
G_I (J/m²) at 1/2 (45°/0°)
0
20
15
10
5
0
45
90
135
180
225
270
315

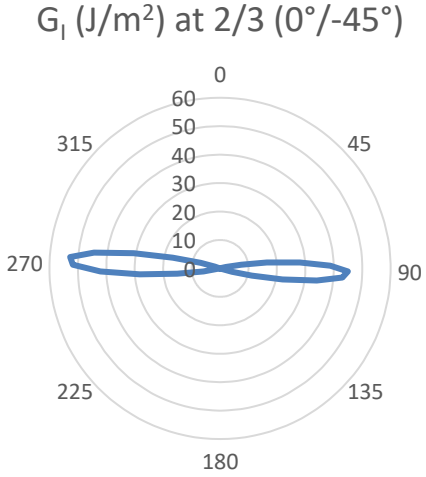
G_I (J/m²) at 2/3 (0°/-45°)
0
60
50
40
30
20
10
0
45
90
135
180
225
270
315

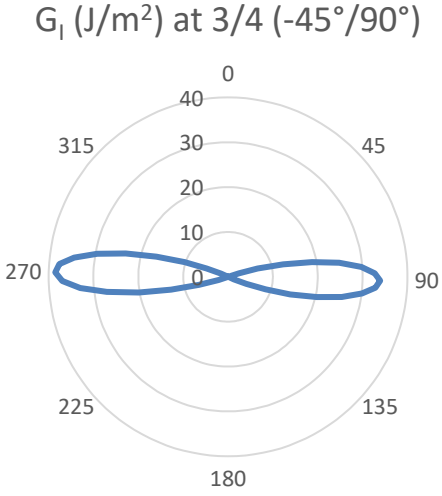
G_I (J/m²) at 3/4 (-45°/90°)
0
40
30
20
10
0
45
90
135
180
225
270
315

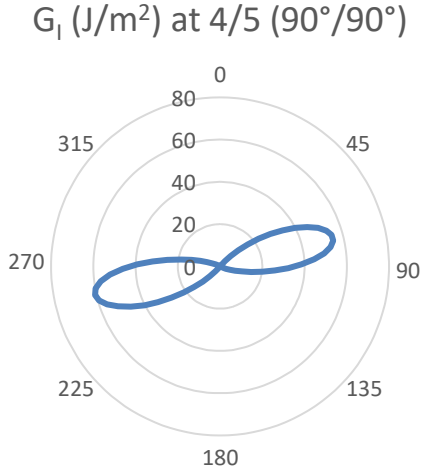
G_I (J/m²) at 4/5 (90°/90°)
0
80
60
40
20
0
45
90
135
180
225
270
315

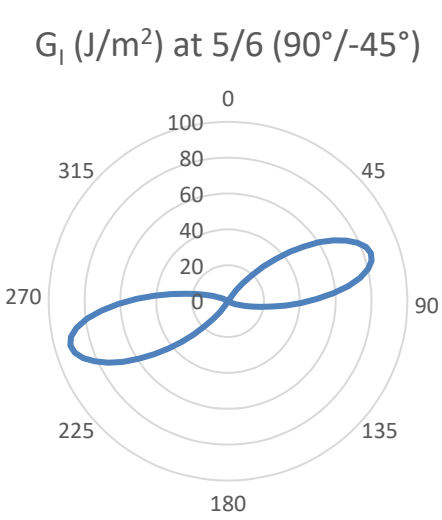
G_I (J/m²) at 5/6 (90°/-45°)
0
100
80
60
40
20
0
45
90
135
180
225
270
315

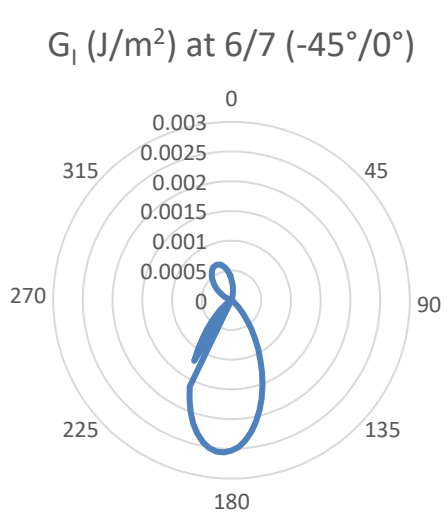
G_I (J/m²) at 6/7 (-45°/0°)
0
0.003
0.0025
0.002
0.0015
0.001
0.0005
0
45
90
135
180
225
270
315

Figure 8-18 G_I value at the 40 mm delamination front at a noted interface under 64.4 kN

G_{II} (J/m^2) at 1/2 (45°/0°)

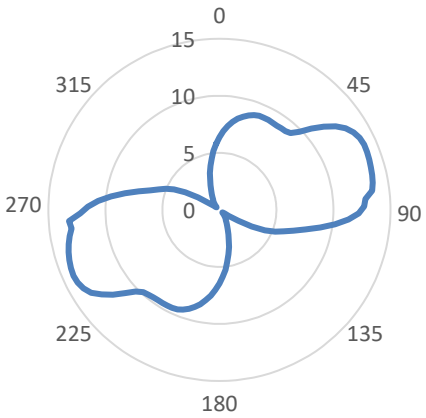

G_{II} (J/m^2) at 2/3 (0°/-45°)

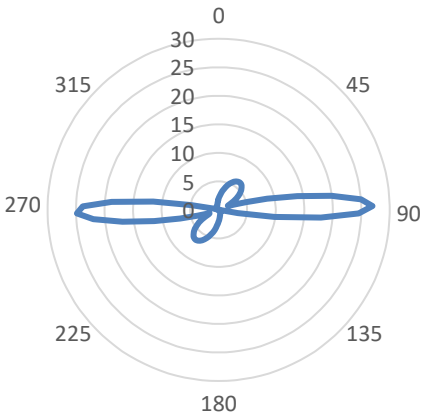

G_{II} (J/m^2) at 3/4 (-45°/90°)

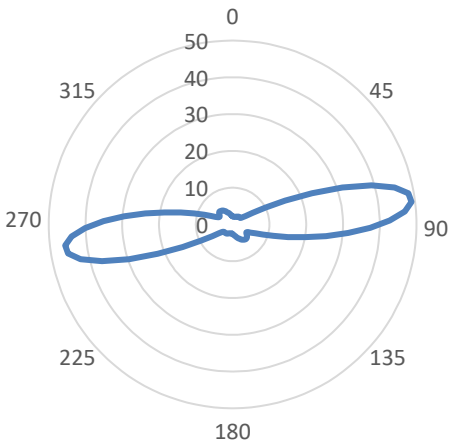

G_{II} (J/m^2) at 4/5 (90°/90°)

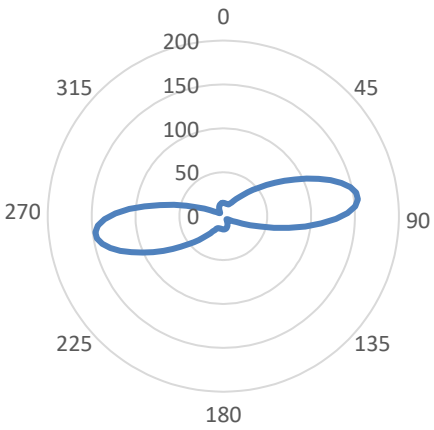

G_{II} (J/m^2) at 5/6 (90°/-45°)

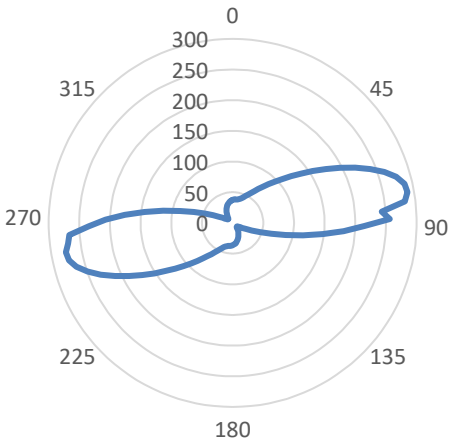

G_{II} (J/m^2) at 6/7 (-45°/0°)

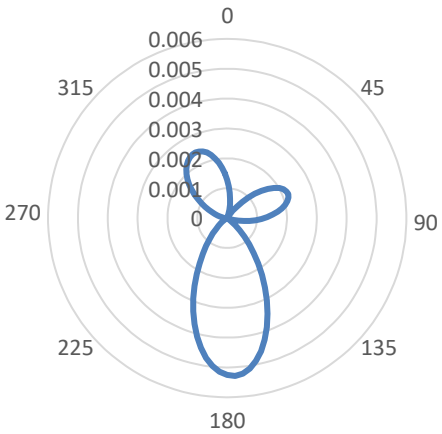

Figure 8-19 G_{II} value at 40 mm delamination front at a noted interface under 64.4 kN

8.3.5 Delamination Growth Rate Comparison between Experimental and Numerical Results

With the strain energy release rate values obtained, the study of comparing the delamination growth rate between experimental work and the numerical results can be performed.

Due to the limit amount of data obtained from numerical modelling and the sudden growth fact of most samples during experimental testing, a slow growth sample Q12-7 was selected in this comparison (see Figure 7-41). A transversal delamination length ranging from 32 mm to 44 mm was selected to correspond the numerical output. The experimental da/dN curve were derived by obtaining the slope of the delamination versus fatigue cycle curve.

Numerical wise, well accepted Paris Law (see Equation 2-5) was adopted to present the delamination propagation trend. The two parameters for Paris Law, c and m were determined by B-K Law (see Equation 2-8 and 2-9). Parameters in the B-K Law were obtained via basic fatigue fracture testing including DCB and MMB using the same material AS7/8552 at Cranfield (Chen 2015). By Chen (2015)'s contribution, c and m were given through the measurement from the testing. The two expressions were given in equations (8-1) and (8-2):

$$\log C = -15.96 - 15.4\left(1 - \frac{G_{II}}{G_T}\right)^{1.72} \quad \textbf{(8-1)}$$

$$m = 12.8 - 7.38\left(\frac{G_{II}}{G_T}\right)^{0.767} \quad \textbf{(8-2)}$$

Taking C and m back to equation (2-5), a Paris Law propagation model can be derived in the term of $\frac{G_{II}}{G_T}$. G_{II} values were obtained from the single delamination model and the maximum value were selected from the pool. G_T is the mathematical addition of G_I and G_{II}.

Comparison between the growth rate from experimental results and numerical results are presented in Figure 8-20. It can be found two curves hold the same trend that the growth rate accelerates as the delamination grows. The experimental and numerical results were similar when early stage of the delamination. The increase in growth rate from testing shows a slow acceleration whereas the acceleration from numerical result was significantly faster than the experimental one.

The results show the Paris Law is good fit with the initial delamination growth rate but would overestimate rate when the propagation starts. The differences are regarded being come from the following reasons. The parameters for Paris Law and B-K Law were derived and determined by basic fracture testing like DCB, ENF and MMB Thus the results are a good fit for all 0-degress layup and with a single delamination existed. But the real-world case would be more complicated by having multiple layup interfaces and multiple delamination. The slower growth rate than numerical prediction could come from the larger energy needed for the simultaneous multiple delamination growth.

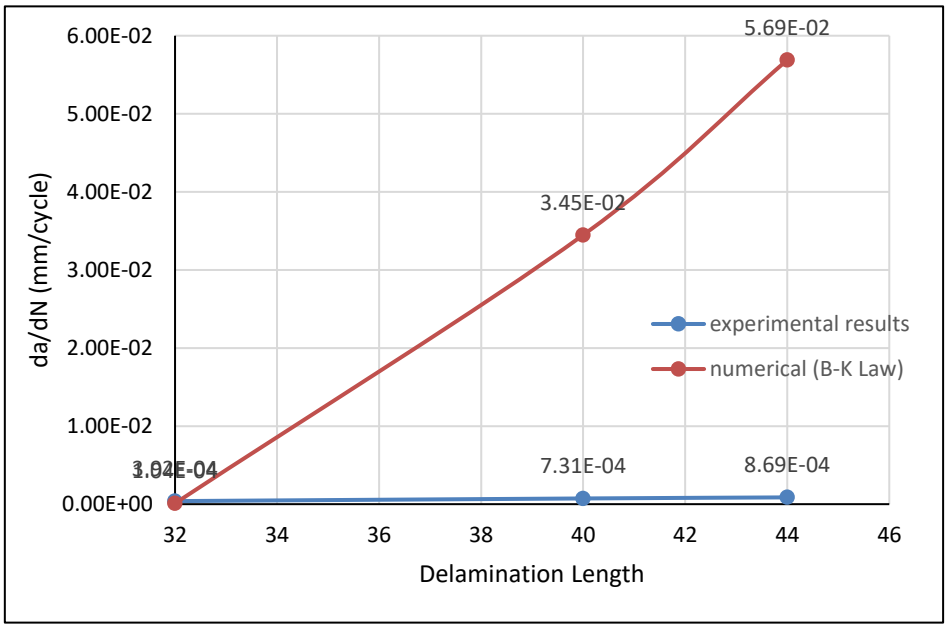

Figure 8-20 Comparison of delamination growth rate from experimental results and numerical results

8.4 Double-Layer Delamination Model

To examine the influence of the introduction of another delamination in another interface, in the FE model for fracture analysis, a second delamination with a smaller size of delamination (32 mm) was inserted between the fifth and sixth plies besides the pre-existed 40 mm delamination located between $1^{st}/2^{nd}$ interface. A same 64.4 kN was applied at the shorter end. SERRs at 2 delaminations front were calculated by VCCT (see Figure 8-21).

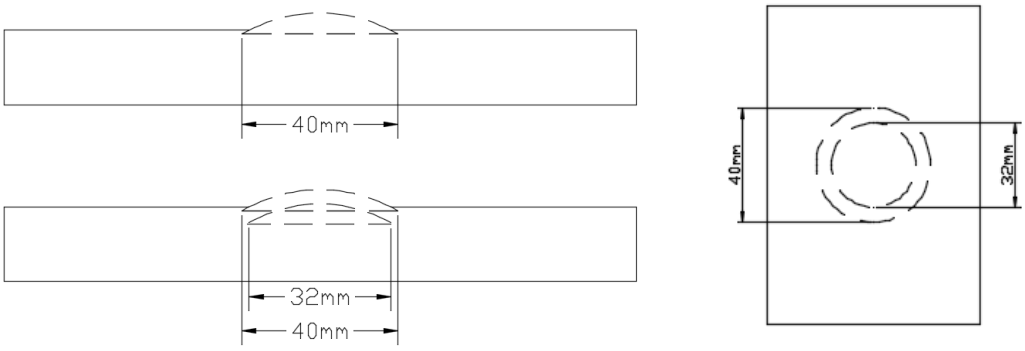

Figure 8-21 Schematic of the two-layer model (left: sectioned view; right: top view)

Although the thin sub-laminate with the delamination at the first ply interface buckled first, the G_I and G_{II} at the delamination tip were only, respectively, 36% and 10% of the thick sub-laminate with the delamination at the $5^{th}/6^{th}$ ply interface (see Figure 8-22). This result could explain that during fatigue tests, the deep damage grew first because, under cyclic loading, the range of ΔG would be higher in the deep delamination surface, as the G_{min} calculated for both cases approaching zero can be ignored. Hence, the crack growth occurs earlier than the delamination towards the surface of the laminate.

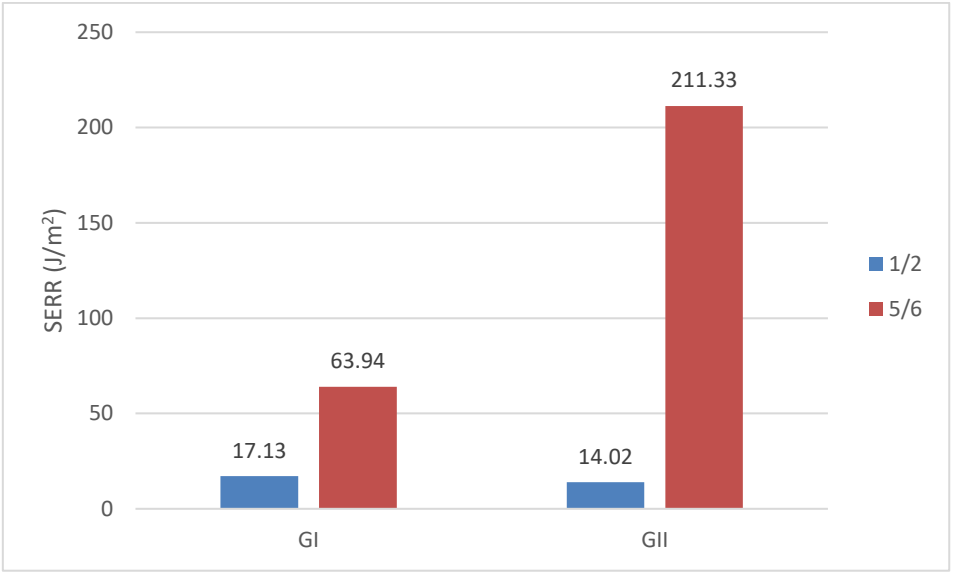

Figure 8-22 Comparison of Mode I and Mode II SERR between two interfaces at the load of 64.4kN from the double-layer model

8.5 Summary

In this chapter, finite element models were validated to help explain the experimental observations from the post-impact fatigue tests. The DCB and MMB models were validated by comparing their findings with experimental work and an established FEA model to correct the parameters for the subsequent static compression model with initial circular delamination. The buckling model was validated by comparing it with an analytical method. For the static model under compressive load, the differences in local buckling load and morphology were reported. It was found that a drastic increase in the buckling load increased the difficulty in propagation while the later presentation of SERRs at the delamination front showed a SERR of 0 after the quick increase of the buckling load. The reported direction of maximum SERR is in accordance with the real delamination propagation path. The single layer delamination model helped to explain the acceleration in delamination growth once the propagation starts. Further study revealed the strain level to propagate for three cases with different delamination areas. Finally, the study on double delamination model revealed the SERR value in smaller sized but deeper located delamination was significantly higher than the delamination which had a larger size and adjacent to the much severe damaged

back face, which could explain the experimental observation in the previous chapter.

9 DISCUSSION

Low-velocity impact, compression after impact and compressive fatigue under a constant loading spectrum on carbon fibre composite samples with different impact damage was studied in the chapters above. The initial velocity impact, the measurement of residual compressive strength through the CAI test, compressive fatigue testing on various samples and finite element analysis to interpret the experimental observation were all discussed. Although some concise summaries were included at the end of each chapter, further major discussions are presented in this chapter.

9.1 Low-velocity Impact

Low-velocity impact was performed mainly to introduce the initial damage to the test samples. Six energy levels were performed on QI samples and four energy levels were performed on CP samples. Some findings can also be presented.

The relationship between damage area and impact damage introduced in Section 5.4.1 and Figure 7-1 shows a positive correlation. This section demonstrated that with an increase in impact energy, more severe damage will appear. This behaviour is commonly reported in many previous literature (Cantewell et al. 1991, Davies and Zhang 1995, Cartié and Irving 2002).

Besides the well-studied aforementioned point, the effect of stacking layup and three key forces are studied. By comparing Figure 5-5 and Figure 5-6, it can be found that the difference between the P_c and P_r of the CP panel is lower than that of the QI panel. The difference between P_c and P_r implies the required energy for delamination initiation. CP panels need less energy for the onset of delamination. The observation is attributed to the greater fibre mismatch in the CP panel than in the QI panel, as fibre mismatch is widely regarded the main contributor to interlaminar delamination.

It can be found the maximum load P_m is lower in the CP specimen than in the QI specimen. P_m is the indicator of the energy transferred from the impactor to the specimen. The CP specimen absorbed less energy than the QI specimen. As

shown in Table 9-1, under the same impact energy, CP samples absorb 25% less energy than the QI specimens. The low energy absorption can be attributed to the higher laminate stiffness of CP specimens, making it “harder” for the impactor to bounce off the samples. The higher laminate stiffness (see Table 4-2) can be attributed to the higher content of 0° fibre.

Table 9-1 Comparison of absorbed energy for the specimen under 20-J impact energy

Specimen	Impact Energy (J)	Actual Energy (J)	Absorbed Energy (J)
C2	20	19.86	9.51
C3	20	20.36	9.43
Q2	20	19.86	12.21
Q5	20	19.37	11.07

Furthermore, severe damage within a small area is another explanation for the result. Figure 5-11 shows the back face of C5 and Q3 both of which underwent a 25-J impact. The larger elongated lump of the CP sample indicates that larger fibre mismatch causes severe internal damage and not just delamination.

A further comparison can be made using the delamination morphology from the C-scan for those two specimens (Figure 5-9). The damage shape for the CP is an elongated ellipse and a circular shape for QI. The shape for the CP comes from the difference in stiffness in 0° and 90° directions. The support fixture of the impact machine only supports the outer line of the specimen with a width of 25 mm. This may cause different stiffness owing to different “arm” lengths. The round shape for QI is more understandable as the specimen is equal in content in four directions, so the shape is an accumulative projection of the “peanut”-shaped damage in each ply induced by the transverse shear stress, as suggested in previous studies. Sanchez-Saez et al. (2005) found that 45° and -45° fibres could help the 0° and 90° ply to bear impact-induced load.

9.2 Compression after Impact

Compression after impact tests were conducted on samples at five different levels of impact damage. Comparing to the undamaged strength, an over 60% reduction

in residual strength was observed, which agrees with the previous results from some literature (Cantwell et al., 1984; Abrate, 1998; Cartié and Irving, 2002).

The obtained results are then compared with other published results as shown in Figure 9-1. It is found that, in terms of the residual compressive strength after impact. The performance of AS7/8552 was not superior to that recorded in previous research. This can be attributed to both fibre and matrix aspects. Cartié and Irving (2002) and Krutop (2007) used a fibre stronger than AS7 while Pichard and Hogg (1990) and Bishop (1985)'s matrix was thermoplastic rather than thermoset raisin, which is known for its higher fracture toughness.

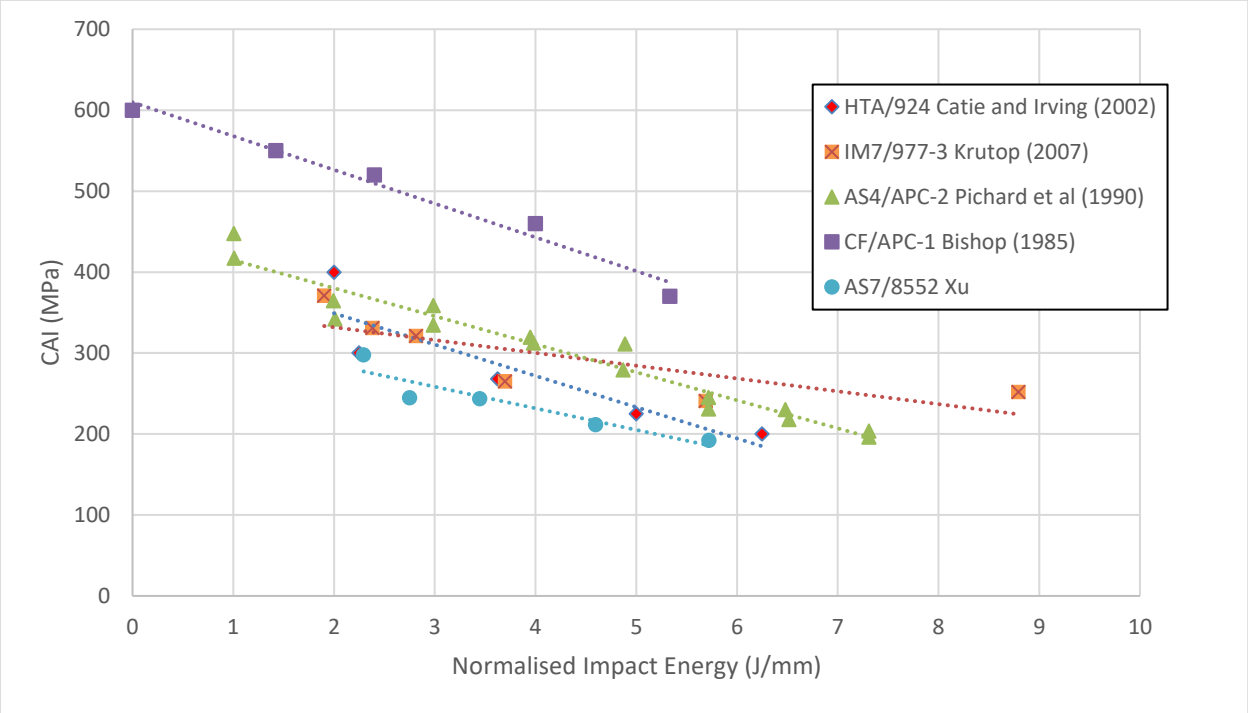

Figure 9-1 CAI versus normalised impact energy of AS7/8552 compared with that of other material

The lower RCS in the samples impacted by a higher energy could be explained in the prospective of fracture mechanics. Higher impact energy will result in a larger delamination area. The calculated SERR values in mode I and mode II shows a higher value in the larger delamination.

With the same loading rate through the test, it also can be understood that the sample impacted at a higher load would be

Besides the RCS obtained from CAI test, the out-of-plane displacement approaching failure presented a drastic change in cross-section morphology when approaching the final compressive failure with the appearance of two half-wavelengths local buckling mode. The occurrence of such mode can only be observed in static compression when the load almost reaches the RCS while during fatigue testing, such mode could be achieved by a fraction of RCS after certain cycles of fatigue load.

9.3 Compressive Post-Impact Fatigue Failure

Fatigue after impact is the main component in this project. The understanding of its failure mechanism would not only be beneficial to the design side to further utilise the full performance of carbon fibre composites but also indicates some new prospect to achieve a longer inspection window than before. A total19 samples were tested in this project and the fatigue life, applied maximum fatigue load, out-of-plane displacement and delamination size during the test session were recorded.

9.3.1 Failure Mechanism

The compressive fatigue progression after impact of CFRP at different energy levels were reported in chapter 7. Among all the test results, fatigue failure mechanism can be abstracted from the experimental observation and other supportive evidence.

There were two types of initial deformation observed in the fatigue test, inwards bending and outwards bending. Inwards bending was mostly observed among the test samples. Thus, it was determined to be the common process of fatigue failure. A transition between three distinguishable stages within the failure damage progression was identified by applying the smaller inspection step length.

Impact damaged CFRP samples, under the compressive cyclic load, at a constant amplitude went through three stages of surface deformation. The first was local bending at the impact damage site, the second was local buckling mode changes and the third was buckling area propagation. The sample Q25-2 was taken as an example for illustration.

At stage 1, the impact-induced delaminations grow in a slow pace. During this stage, the deformation under the fatigue load was a simple bending, which is similar to the responsive behaviour of a pristine sample with compression applied (see Figure 9-2b N=1, Figure 9-3). Meanwhile, the cyclic load would cause growth in those initially smaller sized delaminations. The study on a double delamination model, shown in Section.8.4, revealed that the SERR value in smaller but deeper delamination was significantly higher than in delamination which had a larger size and was opposite to the impacted surface. Given a larger driving force (larger SERR value), those smaller delaminations grew within the projected delamination area. The growth of these multiple delaminations can be observed in the sectioning view shown in Figure 7-53.

With more of these multiple delamination propagations, slight decreases in stiffness could be observed. However, the more significant criterion was the appearance of local buckling mode changes (see Figure 9-2b N=5000). The local buckling changes indicated the commencement of stage 2. The appearance of the buckling shape was due to the delamination propagation mentioned above. The surface deformation had changed from a single half-wavelength bending, to the two half-wavelengths buckling. As seen in Figure 8-11, delaminations located in the interfaces near the mid-plane were more likely to buckle in a two-half-wavelengths shape as such modes could be achieved at a lower eigenvalue. With the degradation of the layers near the back face, the buckling load would not be as high as the value stated in Figure 8-11. Another phenomenon supporting the prior growth was the initial delamination size of around 44mm in the longitudinal direction (y-direction) (see Figure 9-2a). The pre-rupture cycle plot illustrates an ‘envelope’ of the same size, even though the buckling mode has changed (see Figure 9-3).

The arrival of stage 3 has two clear signs, the initial delamination propagation under c-scan detection (see Figure 9-2a N=6150) and the extension of the local buckling area on the surface (see Figure 9-2b N=6150). At this stage, c-scan could detect the change in the accumulative delamination area, as the delamination broke the previous overall boundary. The progression of fatigue

damage was quick to the final failure. This was the same period reported in previous research, described as ‘quick progression’ to the final failure. The detected delamination area and the buckled area spread to one vertical edge, while sometimes subtle propagation into another vertical edge was observed (see Figure 9-2). When the damage grew to one side edge, the stiffness during those cycles decreased significantly. Final failure would happen when the rest of the structure could not sustain the load and sudden rupture occurred.

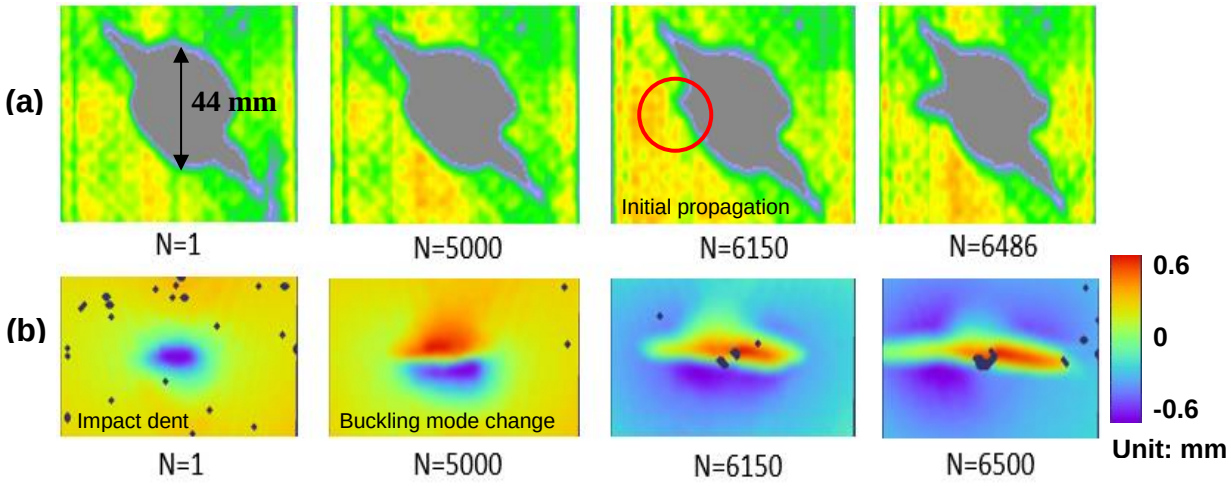

Figure 9-2 (a) Delamination area detected from c-scan at 1, 5000, 6150, 6486 cycle(s); (b) Out-of-displacement of sample Q25-2 from DIC measurement at 1, 5000, 6150 and 6500 cycle(s)

Evidence provided by the buckling area included changes in delamination buckling shape and stiffness degradation obtained by DIC measurements. SERR values calculated in the double delamination model at the delamination front showed that the smaller sized but deeper located delaminations were significantly higher than the delaminations which had a larger size and were adjacent to the much more severely damaged back face. Sectioned samples using microscope observation showed a delamination distribution with equal length, rather than the traditional “pine tree” distribution when comparing a fatigued sample to an unfatigued one.

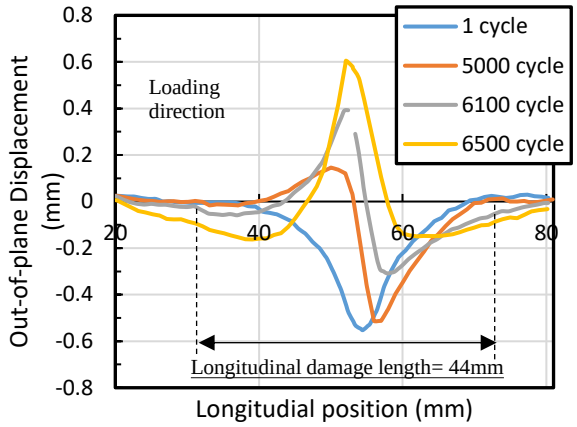

Figure 9-3 Out-of-plane displacement of sample Q25-2 on the midline along the loading direction (section selected of a ±25 mm range)

9.3.2 Fatigue Life of Impacted Composites

In this section, the fatigue life of impacted composites under cyclic compression will be discussed. The fatigue life is affected by the following factors, delamination area, maximum compressive load and strain energy release rate values.

As stated in the low-velocity impact section, it found the higher energy group in the fatigue testing had a larger initial delamination area than the less impacted group. By examining Figure 7-1 closely, the positive relationship between impact energy and initial delamination area was not linear. After some point, the delamination area increase will slow down, as there is always a limit for the delamination area caused by impact load. The limit appears when the impact velocity is high enough to cause penetration into the material. The penetration only happens in high-velocity impacts, which will not be discussed and considered in this project. From Figure 7-1, it can be found that the slope starts to slow down after 20J of impact energy. The difference in delamination size between 25J and 20J was smaller than the differences between 12J and 15J and between 15J and 20J. This phenomenon suggests that after a certain impact energy threshold, the increase in delamination slows down. The reason behind is believed as more resin and fibre breakage absorb the excessive energy rather than initiate more and larger delaminations.

A similar ‘threshold’ could be seen in the S-N curve shown in Figure 7-2. The trendlines were plotted for all the samples which failed within 5×10^5 cycles. It can be seen from the graph that the trendlines for the 20J and 25J group have a similar slope, while the slope of the 15J group is gentler. The trendline for the 12J group could not be plotted, as there was only one sample which achieved its fatigue life within the designed cycle number. However, if the trendline existed for 12J, it could be seen from the figure that the slope would not be steeper than the one for the 15J group. Even more obvious demonstrations of these slopes can be found in Figure 7-3, in terms of the maximum compressive load presented in the form of fracture of RCS. The 20J and 25J groups have a steeper reduction in maximum compressive load, to achieve a longer fatigue life. The interpretation of this could be attribute to the SERR value. The SERR values of modes I and II were shown for three cases in Figure 8-18 and Figure 8-19. It can be found that under the same load, the larger delamination size has a larger G value, which represents the high tendency for delamination growth. Although under the same fracture of RCS as its maximum load, the G_I and G_{II} value were higher in the smallest delamination (see Figure 8-15 and Figure 8-16), which seems contradictory to the experimental observation. However, this could suggest that the single delamination could not represent the real situation fully. Due to the internal delamination distribution, the critical threshold for fatigue delamination propagation is smaller than the static critical value, which is also highly size/length depended.

From Figure 7-2 and Figure 7-3, it can be found that the change in maximum compressive load has more effect in the more severe impact damaged cases, which means that the larger delamination is more sensitive to load changes. This may raise a concern for the impact structure in a real-life flight loading spectrum, as the load amplitude may vary.

9.3.3 Delamination Propagation Detection Sensitivity of DIC and C-scan

Most previous research stated that the short period between fatigue failure and the initiation of delamination propagation could be identified as the criteria they

used was c-scan detection. As discussed in the last section, subtle changes can be identified by DIC equipment between stage 1 and stage 2, which is significantly earlier than the c-scan detection at stage 3. Table 9-2 summarises the detection cycle number using DIC and c-scan for all the failed testing samples. For each sample, total fatigue life (N_f) was provided. The detection cycle number N_d was presented for the two methods. The ratio of detection cycle to the total fatigue life ($N_{d/}$ N_f) was given for each sample.

Table 9-2 Cycle of detection from DIC and c-scan

Sample	N_f	N_d (DIC)	N_d/N_f	N_d (c-scan)	N_d/N_f
Q12-7	146785	100000	68.1%	101600	69.2%
Q15-2	3560	3000	84.3%	3360	94.4%
Q15-4	274821	274600	99.9%	274600	99.9%
Q15-5	61865	50000	80.8%	60650	98.0%
Q20-2	6142	5000	81.4%	5000	81.4%
Q20-3	16497	10000	60.6%	15000	90.9%
Q20-4	31814	20000	62.9%	25000	78.6%
Q20-5	11300	10500	92.9%	11120	98.4%
Q25-2	6501	5000	76.9%	6150	94.6%
Q25-3	8966	5000	55.8%	8911	99.4%
	Average		76.4%		90.5%

It can be found that the N_d/N_f using c-scan usually reached over 90% and achieved an overall average of 90.5%. This average value agreed with the previous research (Chen, et al., 2002, Isa, et al., 2011 and Mitrovich, et al., 1999) about the quick progression of the fatigue failure and left a short window of time for inspection. However, the average N_d by DIC showed an enhancement in the detection time. N_d/N_f by DIC was at least the same as by c-scan, if not smaller. Due to the nature of the compressive fatigue failure mechanism discussed in Section 9.3, on-surface local buckling mode changes will always happen before detection by c-scan of the overall delamination. Using this method to monitor the out-of-plane displacement can identify the fatigue damage change much earlier than the ultrasonic c-scan. In this study, a significant period (14.1% of the total

fatigue lifetime) was obtained. The data plotted in Figure 9-4 shows that the detection ratio points from DIC stay under the c-scan detection points, which indicates the earlier detection of fatigue delamination progression using the DIC method.

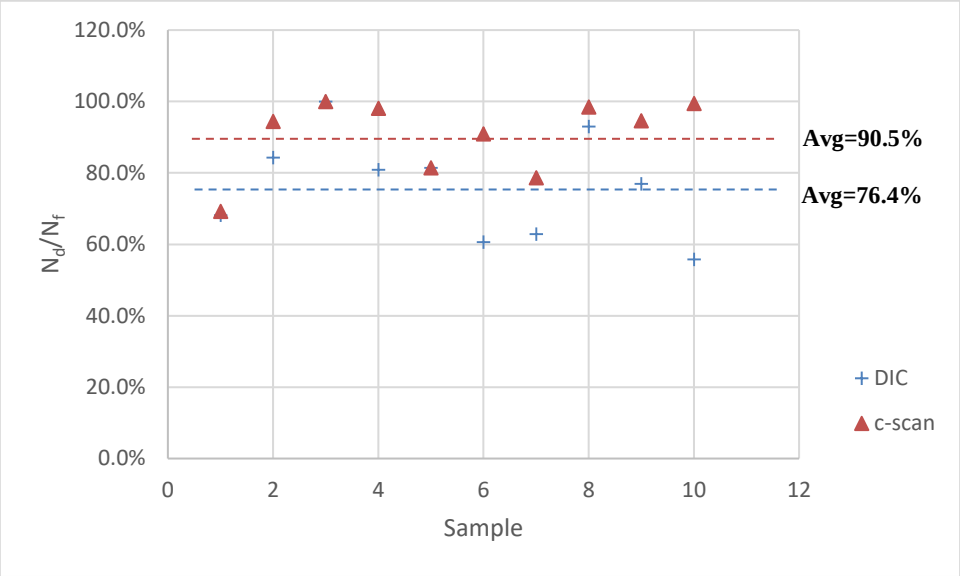

Figure 9-4 Cycle number on the first detection

9.3.4 Delamination Non-Growth Strain Level

In the damage tolerance design, empirically derived strain limits at ultimate levels are used to ensure no growth for BVID. These damage tolerance strain limits usually take 4500 μstrain. Curtis, et al. (1993) have shown that there is a wide variation in threshold strain, ranging from 3100 μstrain to a fatigue strain of 5000 μstrain for different type of laminas. Rhead, et al. (2008) proposed a 3500 μstrain by the analytical and numerical method. The model simplified the complex damage morphology by a single circular delamination at a critical level and calculates the strain at which thin-film buckling of the circular delaminated region occurs

In this section, non-growth strain level is discussed. The samples which were loaded at highest load and sustained the whole 5×10^5 lifetime will be presented. Sample Q12-4, Q15-8, Q20-7 and Q25-6 impacted at 12/15/20/25J and loaded at 82%, 73%, 70% and 70% of their nominal RCS were chosen. Figure 9-5 shows

the non-growth strain level is negatively correlated with impact energy in a linear relationship.

Another point worth mentioning here is the non-growth strain for 25J should be lower than the noted 2287 µstrain, as some deformation changes were observed (see section 7.3.4). The sample had a high possibility of failing if loaded with further fatigue progression. The true non-growth strain should be lower than the figure given. Overall a recommendation of 2000 µstrain is given for design allowance for BVID non-growth, though samples which were less impact damaged could sustain up to 3723 µstrain.

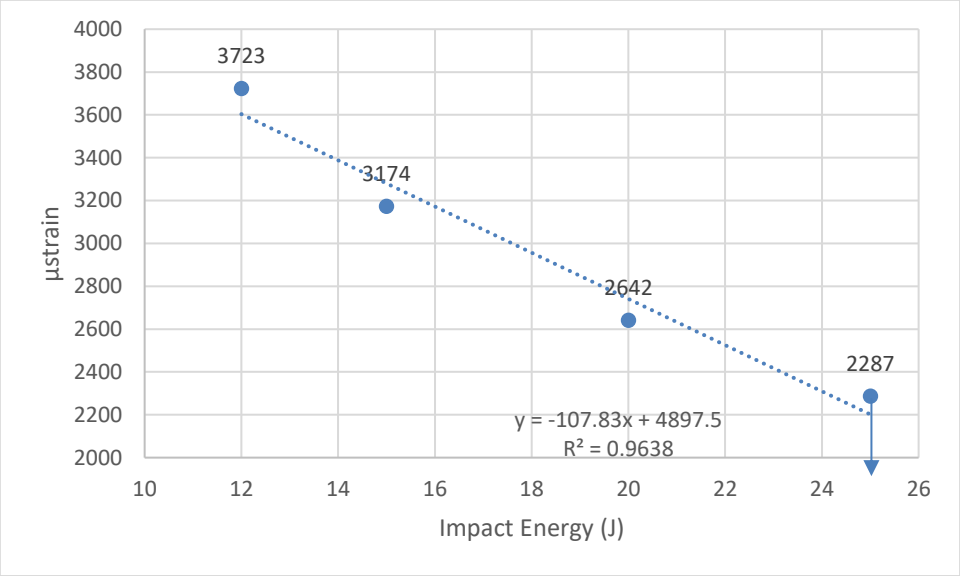

Figure 9-5 Non-growth strain level vs impact energy

9.3.5 Comparison of out-of-plane Displacement Approaching Failure between Static Compression and Compressive Fatigue

Out-of-plane displacement is discussed in the previous chapters and is regarded as an important parameter to describe the fatigue progression of CFRP samples. However, the maximum and minimum z-displacement varied among samples significantly (see Section 7.3). Some samples presented with a low positive z-displacement but with a high negative z-displacement, while others had a similar positive and negative z-displacement value. The difference of these maximum and minimum z-displacement values was used to quantify the behaviour. In addition, the displacement differences from the static testing samples were also

introduced for comparison. The results can be found in Figure 9-6. From the plot, it can be found that the failure would not happen until the difference of the maximum and minimum values exceeded 0.8 mm, while some extreme case could reach as high as 1.6mm. For the static test results, it was found that the difference was correlated with the impact energy. The sample impacted by higher level energy would deform more drastically than that which was less impacted. However, the trend did not pass onto the fatigue results, as the deformation is highly dependent on the internal delamination growth and morphology. Another trend which can be identified from the figure is the stiffness degradation. Loaded with a fraction of the RCS, fatigue samples were still able to obtain a difference value similar to the static testing samples. Furthermore, it can be found that in general, those samples loaded with a lower maximum fatigue load were deformed more significantly, independent of the initial impact damage, which can be attributed to degradation by the longer fatigue cycles.

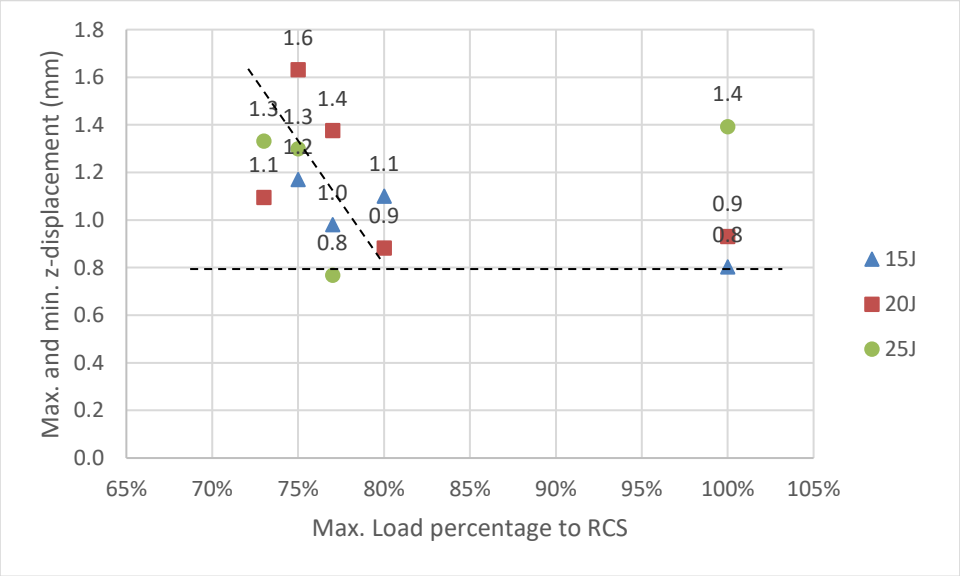

Figure 9-6 Max. and min. the z-displacement difference before failure

10 CONCLUSIONS AND FUTURE WORKS

Based on the previous chapters, some conclusions regarding the low-velocity impact, the static compression after impact and the compressive fatigue on carbon fibre composites and suggestions for future works will also be given in this chapter.

10.1 Conclusions

Samples of impacted carbon fibre composites were tested through low-velocity impact, static compression after impact and compressive fatigue testing to explore and identify the damage tolerance behaviour of carbon fibre composites. Stress levels at the growth/non-growth transition for different levels of impact energy were recorded, and the relationship between fatigue life and initial damage area was quantified. Some conclusions found are:

- The higher portion of 45° and -45° fibres could cause the delamination in larger overall size but could reduce the severity on the deformed panel.
- The lower RCS in the samples impacted by a higher energy could be explained in the prospective of fracture mechanics. The static SERR values in mode I and mode II shows a higher value in larger delaminations.
- 70% nominal RCS stress is the stress level required to ensure a 5×10^5 lifetime, while for the less impact damaged cases (12J) the stress level to ensure no failure can be lifted to as high as 82%.
- All the samples which underwent eventual failure had similar failure progression. The compressive fatigue failure can be categorised into three stages: (1) local bending at impact damage sites (2) local buckling mode changes and (3) buckling propagation.
- Monitoring of normal local displacement at the impact damage sites provides earlier indications of fatigue-induced changes in delamination buckling than observations of delamination area growth. An average 14.1% of the total fatigue life gives the potential for a longer inspection window.

- Delamination at deeper interfaces away from the mid-plane propagates at an early stage of fatigue. The smaller sized delaminations grow within the boundary of the overall delamination area.
- Non-growth strain level is negatively correlated with impact energy in a linear relationship. A recommendation of 3500 μstrain is given for design allowance for BVID non-growth, though samples which were less impact damaged could sustain a larger strain level.
- It could be useful to use the total out-of-plane displacement as another failure design criteria for post impact fatigue.

10.2 Future Works

The following recommendations are given to improve the future study on damage tolerance behaviour of carbon fibre composites:

- The fatigue test was only conducted on QI layup samples. As known the delamination initiates due to the fibre mismatch and the driving factor for the subsequent propagation, SERR are all dependent on the interface angles. The alternation of ply angles or a different QI layup is recommended. Similarly, an alternation of a different type of material is also recommended, as the fracture toughness varies. Furthermore, similar testing could be carried out in elements and detailed structure level.
- Testing methods could also be modified to ensure the capture of the fatigue failure. DIC capture evaluation could be conducted at each checkpoint, thus giving a clear reference as to which stage the testing sample is at. Based on the stage, the next checkpoint step length could be altered accordingly.
- The sectioning observation in this study came from two different samples, though the input parameters were strictly kept the same. The sectioning results can only be supportive evidence for the delamination growth during fatigue. It is recommended to use the CT technique and focus on one sample at different stages during the fatigue testing to obtain a direct result of how those delaminations propagate.

- Development of an enhanced numerical model is recommended based on the real delamination morphology.
- A model of delamination area/length propagation rate could be proposed for multiple delaminations in different angle orientations. Prior to that, a simpler multiple delamination in pure mode I or mode II could be performed. The comparison could be made from the delamination growth rate abstracted from those fracture tests to the fatigue delamination growth in an impacted sample.

REFERENCES

Abrate, S. (1998) *Impact on Composite Structures*. Cambridge: Cambridge University Press. doi: DOI: 10.1017/CBO9780511574504.

Abrate, S. and Schoeppner, G. (1999) 'Identification of two force thresholds for lowvelocity impact damage on laminated composites', in *31st International SAMPETechnical Conference*. Chicago, pp. 557–567.

Al-Khudairi, O. *et al.* (2015) 'Characterising mode I/mode II fatigue delamination growth in unidirectional fibre reinforced polymer laminates', *Materials & Design (1980-2015)*, 66(Part A), pp. 93–102.

Anderson, T. L. and Anderson, T. L. (2005) *Fracture Mechanics: Fundamentals and Applications, Third Edition*. Taylor & Francis. Available at: https://books.google.co.uk/books?id=MxrtsC-ZooQC.

Andersons, J., Hojo, M. and Ochiai, S. (2001) 'Model of delamination propagation in brittle-matrix composites under cyclic loading', *Journal of reinforced plastics and composites*. Sage Publications Sage CA: Thousand Oaks, CA, 20(5), pp. 431–450.

Avery, W. and Grande, D. (1990) 'Influence of materials and layup parameters on impact damage mechanisms', in *22nd International SAMPE Technical Conference*. Boston, MA, pp. 470–483.

Beghini, M., Bertini, L. and Forte, P. (2006) 'Experimental investigation on the influence of crack front to fiber orientation on fatigue delamination growth rate under mode II', *Composites Science and Technology*, 66(2), pp. 240–247. doi: https://doi.org/10.1016/j.compscitech.2005.04.033.

Beheshty, M. H., Harris, B. and Adam, T. (1999) 'Empirical fatigue-life model for high-performance fibre composites with and without impact damage', *Composites Part A: Applied Science and Manufacturing*. 30(8), pp. 971–987. doi: 10.1016/S1359-835X(99)00009-3.

Beheshty, M. H., & Harris, B. (1998). A constant-life model of fatigue behaviour for carbon-fibre composites: the effect of impact damage. Composites Science and Technology, 58(97), 9–18.

Bennati, S. and Valvo, P. S. (2006) 'Delamination growth in composite plates under compressive fatigue loads', *Composites Science and Technology*, 66(2), pp. 248–254. doi: https://doi.org/10.1016/j.compscitech.2005.04.035.

Benzeggagh, M. L. and Kenane, M. (1996) 'Measurement of mixed-mode delamination fracture toughness of unidirectional glass/epoxy composites with mixed-mode bending apparatus', *Composites Science and Technology*, 56(4), pp. 439–449. doi: https://doi.org/10.1016/0266-3538(96)00005-X.

Bibo, G. a., Hogg, P. J. and Kemp, M. (1995) 'High-temperature damage tolerance of carbon fibre-reinforced plastics':, *Composites*, 26(2), pp. 91–102. doi: 10.1016/0010-4361(95)90408-R.

Bishop, S. M. (1985) 'The mechanical performance and impact behaviour of carbon-fibre reinforced PEEK', *Composite structures*, 3, pp. 295–318. Available at: http://www.sciencedirect.com/science/article/pii/0263822385900595.

Blanco, N. *et al.* (2004) 'Mixed-mode delamination growth in carbon–fibre composite laminates under cyclic loading', *International Journal of Solids and Structures*, 41(15), pp. 4219–4235. doi: https://doi.org/10.1016/j.ijsolstr.2004.02.040.

Boeing Document D888-10026 (no date) *Test Methods for Advanced Composites, Revision A, Section 7.4*. Washington.

Butler, R., Rhead, A.T., Liu, W. and Knotis, N. (2012). Compressive strength of delaminated aerospace composites. Philosophical Transactions of the Royal Society A: Mathematical, Physical and Engineering Sciences, 370(1965), pp.1759–1779.

Cantwell, W. J., Curtis, P. T. and Morton, J. (1984) 'Impact and subsequent fatigue damage growth in carbon fibre laminates', *International Journal of Fatigue*. 6(2), pp. 113–118. doi: 10.1016/0142-1123(84)90022-7.

Cantwell, W. J. J. and Morton, J. (1991) ‘The impact resistance of composite materials — a review’, *Composites*. 22(5), pp. 347–362. doi: 10.1016/0010-4361(91)90549-V.

Cartié, D. D. R. and Irving, P. E. (2002) ‘Effect of resin and fibre properties on impact and compression after impact performance of CFRP’, *Composites - Part A: Applied Science and Manufacturing*. 33(4), pp. 483–493. doi: 10.1016/S1359-835X(01)00141-5.

Chen, A. S., Almond, D. P. and Harris, B. (2002) ‘Impact damage growth in composites under fatigue conditions monitored by acoustography’, *International Journal of Fatigue*. 24(2-4), pp. 257–261. doi: 10.1016/S0142-1123(01)00080-9.

Chen, Y. (2015) *Mixed Mode Delamination static and Fatigue Crack Growth of Unidirectional CFRP Composite Laminates*. MSc thesis, Cranfied University.

Crews Jr, J. H. and Reeder, J. R. (1988) ‘A mixed-mode bending apparatus for delamination testing’.

Cristescu, N., Malvern, L. and Sierakowski, R. (1975) ‘Failure mechanisms in composite plates impacted by blunt-ended penetrators’, *ASTM Special Technical Publication*, 568, pp. 159–172.

Curtis, P. T., Gates, J. and Molyneux, C. G. (1993) ‘Impact damage growth in carbon fibre composites. Defence Research Agency, Farnborough’, *Hampshire, Technical Report*, 93009.

Dahlen, C. and Springer, G. (1994) *Delamination Growth in Composites under Cyclic Loads*, *Journal of Composite Materials - J COMPOS MATER*. doi: 10.1177/002199839402800803.

Davies, G. A. O. and Olsson, R. (2004) ‘Impact on composite structures’, *The Aeronautical Journal*. 2016/02/01 edn. Cambridge University Press, 108(1089), pp. 541–563. doi: DOI: 10.1017/S0001924000000385.

Davies, G. A. O. and Zhang, X. (1995) ‘Impact damage prediction in carbon composite structures’, *International Journal of Impact Engineering*, 16(1), pp. 149–170. doi: https://doi.org/10.1016/0734-743X(94)00039-Y.

Davies, G. and Irving, P. (2014) ‘Impact, post-impact strength and post-impact fatigue behaviour of polymer composites’, in *Polymer Composites in the Aerospace Industry*. Imperial College, London, United Kingdom: Elsevier Inc., pp. 231–259. doi: 10.1016/B978-0-85709-523-7.00009-8.

de Freitas, M. and Reis, L. (1998) ‘Failure mechanisms on composite specimens subjected to compression after impact’, *Composite Structures*, 42(4), pp. 365–373. doi: https://doi.org/10.1016/S0263-8223(98)00081-6.

European Aviation Safety Agency (EASA) (2014) Engineering Decision 2010/003/R Annex II AMC 20-29 Composite Aircraft Structure. Effective 26 July 2014.

Federal Aviation Administration (1998) *Enhanced Reliability Prediction Methodology*. Virginia.

Fleck, N. A. (1997) ‘Compressive Failure of Fiber Composites’, *Advances in Applied Mechanics*, 33(C), pp. 43–117. doi: 10.1016/S0065-2156(08)70385-5.

Garnier, C. *et al.* (2013) ‘Fatigue behavior of impacted composite structures’, *Composite Structures*. 100, pp. 443–450. doi: 10.1016/j.compstruct.2012.12.025.

Gerharz, J. J., Idelberger, H. and Huth, H. (1989) ‘Impact damage in fatigue loaded composite structures’, in *Proceedings of the 15th Sym- posium of the International Committee on Aeronautical Fatigue*. Israel, pp. 497–516.

Glaessgen, E. H., Riddell, W. T. and Raju, I. S. (2002) ‘Nodal constraint, shear deformation and continuity effects related to the modeling of debonding of laminates, using plate elements’, *Computer Modeling in Engineering and Sciences*. TECH SCIENCE PRESS, 3(1), pp. 103–116.

Gong, W., Chen, J. and Patterson, E. A. (2015) ‘An experimental study of the behaviour of delaminations in composite panels subjected to bending’,

Composite Structures, 123(Supplement C), pp. 9–18. doi: https://doi.org/10.1016/j.compstruct.2014.12.008.

Gower, M.R.L., Shaw, R.M. and Sims, G.D., (2005). Evaluation of the Repeatability Under Static Loading of a Compression-After-Impact Test Method Proposed for ISO Standardisation. National Physics Laboratory [JG 4].

Guo, S. (2015) *Design and Analysis of Composite Structures*. Lecture notes, Cranfield University.

Gustafson, C.-G. and Hojo, M. (1987) 'Delamination Fatigue Crack Growth in Unidirectional Graphite/Epoxy Laminates', *Journal of Reinforced Plastics and Composites*. SAGE Publications Ltd STM, 6(1), pp. 36–52. doi: 10.1177/073168448700600104.

Hadcock, R. N. (1982) 'Design and Analysis of Advanced Composite Structures BT - Handbook of Composites', in Lubin, G. (ed.). Boston, MA: Springer US, pp. 533–556. doi: 10.1007/978-1-4615-7139-1_20.

Hashemi, S., Kinloch, A. J. and Williams, J. M. (1990) 'The analysis of interlaminar fracture in uniaxial fibre-polymer composites', *Proceedings of the Royal Society of London. A. Mathematical and Physical Sciences*, 427(1872), p. 173 LP – 199. Available at: http://rspa.royalsocietypublishing.org/content/427/1872/173.abstract.

HexPly, H. (2007) '8552, Epoxy Matrix Product Datasheet', *Hexcel Corporation, Stamford, CT*.

Hojo, M. *et al.* (2006) 'Modes I and II interlaminar fracture toughness and fatigue delamination of CF/epoxy laminates with self-same epoxy interleaf', *International Journal of Fatigue*, 28(10), pp. 1154–1165. doi: https://doi.org/10.1016/j.ijfatigue.2006.02.004.

Hojo, M. *et al.* (2010) 'Mode I fatigue delamination of Zanchor-reinforced CF/epoxy laminates', *International Journal of Fatigue*, 32(1), pp. 37–45. doi: https://doi.org/10.1016/j.ijfatigue.2009.02.025.

Hounslow, L. E. (2000) *The influence of z-pinning on low velocity impact performance of laminated carbon composites*. MSc. Thesis, Cranfield University.

Hull, D. and Shi, Y. B. (1993) 'Damage mechanism characterization in composite damage tolerance investigations', *Composite Structures*, 23(2), pp. 99–120. doi: https://doi.org/10.1016/0263-8223(93)90015-I.

Irving, P. E. (2013) *Damage Tolerance in Aircraft*. Lecture notes, Cranfield University.

Isa, M. D., Feih, S. and Mouritz, A. P. (2011) 'Compression fatigue properties of z-pinned quasi-isotropic carbon/epoxy laminate with barely visible impact damage', *Composite Structures*. 93(9), pp. 2269–2276. doi: 10.1016/j.compstruct.2011.03.015.

Juntti, M., Asp, L. E. and Olsson, R. (1999) 'Assessment of evaluation methods for the mixed-mode bending test', *Journal of Composites, Technology and Research*. ASTM International, 21(1), pp. 37–48.

Kardomateas, G. A., Pelegri, A. A. and Malik, B. (1995) 'Growth of internal delaminations under cyclic compression in composite plates', *Journal of the Mechanics and Physics of Solids*, 43(6), pp. 847–868. doi: https://doi.org/10.1016/0022-5096(95)00012-8.

Katerelos, D. G., Paipetis, A. and Kostopoulos, V. (2004) 'A simple model for the prediction of the fatigue delamination growth of impacted composite panels', *Fatigue & Fracture of Engineering Materials & Structures*. Blackwell Science Ltd, 27(10), pp. 911–922. doi: 10.1111/j.1460-2695.2004.00798.x.

Krueger, R. (2004) 'Virtual crack closure technique: History, approach, and applications', *Applied Mechanics Reviews*. 57(1-6), pp. 109–143. doi: 10.1115/1.1595677.

Krueger, R. (2012) 'Development and Application of Benchmark Examples for Mixed-Mode I / II Quasi-Static Delamination Propagation Predictions', pp. 1–19.

Krutop, B. (2006) Effect of impact damage and subsequent fatigue damage development in carbon fibre polymer composites for aircraft. MSc thesis, Cranfield University.

Levin, K. (1992) 'WS2i2 - Characterization of delamination and fibre fractures in carbon fibre reinforced plastics induced from impact' Oxford: Pergamon, pp. 519–524. doi: https://doi.org/10.1016/B978-0-08-037890-9.50089-2.

Liu, D. (1988) 'Impact-Induced Delamination—A View of Bending Stiffness Mismatching', *Journal of Composite Materials*. SAGE Publications Ltd STM, 22(7), pp. 674–692. doi: 10.1177/002199838802200706.

Mathieu, F., Hild, F. and Roux, S. (2012) 'Identification of a crack propagation law by digital image correlation', *International Journal of Fatigue*, 36(1), pp. 146–154. doi: https://doi.org/10.1016/j.ijfatigue.2011.08.004.

McGowan, D.M. and Ambur, D.R., (1997). Damage-Tolerance Characteristics of Composite Fuselage Sandwich Structures with Thick Facesheets. NASA Technical Report

Melin, L. G., Schön, J. (2001) 'Buckling behaviour and delamination growth in impacted composite specimens under fatigue load: An experimental study', *Composites Science and Technology*. 61(13), pp. 1841–1852. doi: 10.1016/S0266-3538(01)00085-9.

Melin, L. G., Schön, J. and Nyman, T. (2002) 'Fatigue testing and buckling characteristics of impacted composite specimens', *International Journal of Fatigue*. 24(2-4), pp. 263–272. doi: 10.1016/S0142-1123(01)00081-0.

Miracle, D. B., Committe, A. I. H. Donaldson, S. L. and BROWN, J. (2001) *Composites*. US.

Mitrovic, M. (1999) 'Effect of loading parameters on the fatigue behavior of impact damaged composite laminates', *Composites Science and Technology*. 59(14), pp. 2059–2078. doi: 10.1016/S0266-3538(99)00061-5.

Nettles, A., Hodge, A. and Jackson, J. (2011) ‘An Examination of the Compressive Cyclic Loading Aspects of Damage Tolerance for Polymer Matrix Launch Vehicle Hardware’, *Journal of Composite Materials*, 45(4), pp. 437–458. doi: 10.1177/0021998310376117.

Nilsson, K.-F. *et al.* (2001) ‘Delamination buckling and growth for delaminations at different depths in a slender composite panel’, *International journal of Solids and Structures*. Elsevier, 38(17), pp. 3039–3071.

Ogasawara, T. *et al.* (2013) ‘Fatigue behavior and lifetime distribution of impact-damaged carbon fiber/toughened epoxy composites under compressive loading’, *Advanced Composite Materials*. 22(2), pp. 65–78. doi: 10.1080/09243046.2013.768324.

Ong, C. L. and Llou, Y. Y. (1993) ‘Characterization of mechanical behaviors of advanced thermoplastic composites after impact’, *Acta Astronautica*, 29(2), pp. 99–108.

Pavier, M. J. and Chester, W. T. (1990) ‘Compression failure of carbon fibre-reinforced coupons containing central delaminations’, *Composites*, 21(1), pp. 23–31. doi: https://doi.org/10.1016/0010-4361(90)90095-E.

Prichard, J. C. and Hogg, P. J. (1990) ‘The role of impact damage in post-impact compression testing’, *Composites*, 21(6), pp. 503–511. doi: https://doi.org/10.1016/0010-4361(90)90423-T.

Ramkumar, L.R. and Whitcomb, J.D. (1985) *Characterization of Mode I and mixed-mode delamination growth in T300/5208 graphite/epoxy*, *Delamination and Debonding of Materials*.

Reeder, J. R. *et al.* (2002) ‘Postbuckling and growth of delaminations in composite plates subjected to axial compression’, in *The 43rd AIAA/ASME/ASCE/AHS/ASC Structures, Structural Dynamics, and Materials Conference*.

Rees, D. W. A. (2009) ‘Appendix C: Plate Buckling Under Biaxial Compression and Shear’, *Mechanics of Optimal Structural Design: Minimum Weight Structures*. Wiley Online Library, pp. 537–541.

Reu, P. (2012) ‘Introduction to Digital Image Correlation: Best Practices and Applications’, *Experimental Techniques*. Blackwell Publishing Ltd, 36(1), pp. 3–4. doi: 10.1111/j.1747-1567.2011.00798.x.

Reu, P. (2015) ‘All about speckles: speckle density’, *Experimental Techniques*. Wiley Online Library, 39(3), pp. 1–2.

Reu, P. (2014) ‘All about speckles: speckle size measurement’, *Experimental Techniques*. Wiley Online Library, 38(6), pp. 1–2.

Reu, P. (2015) ‘All about speckles: Contrast’, *Experimental Techniques*. Wiley Online Library, 39(1), pp. 1–2.

Reu, P. (2014) ‘All about speckles: aliasing’, *Experimental Techniques*. Springer, 38(5), pp. 1–3.

Rhead, A. T., Butler, R. and Hunt, G. W. (2008) ‘Post-buckled propagation model for compressive fatigue of impact damaged laminates’, *International Journal of Solids and Structures*. 45(16), pp. 4349–4361. doi: 10.1016/j.ijsolstr.2008.03.014.

Richardson, M. O. W. and Wisheart, M. J. (1996) ‘Review of low-velocity impact properties of composite materials’, *Composites Part A: Applied Science and Manufacturing* 27(12 PART A), pp. 1123–1133. doi: 10.1016/1359-835X(96)00074-7.

Robinson, P. and Hodgkinson, J. M. (2000) *Interlaminar fracture toughness*. CRC Press, New York.

Russell, A. J. and Street, K. N. (1989) ‘Predicting interlaminar fatigue crack growth rates in compressively loaded laminates’, in *Composite materials: fatigue and fracture, second volume*. ASTM International.

Sala, G. (1997) ‘Post-impact behaviour of aerospace composites for high-temperature applications: experiments and simulations’, *Composites Part B: Engineering*, 28(5), pp. 651–665. doi: https://doi.org/10.1016/S1359-8368(96)00078-9.

Sanchez-Saez, S. *et al.* (2005) ‘Compression after impact of thin composite laminates’, *Composites Science and Technology*. 65(13), pp. 1911–1919. doi: 10.1016/j.compscitech.2005.04.009.

Shen, F., Lee, K. H. and Tay, T. E. (2001) ‘Modeling delamination growth in laminated composites’, *Composites Science and Technology*, 61(9), pp. 1239–1251. doi: https://doi.org/10.1016/S0266-3538(01)00023-9.

Soutis, C. and Irving, P. (2014) *Polymer Composites in the Aerospace Industry*, *Polymer Composites in the Aerospace Industry*. The University of Manchester, Manchester, United Kingdom: Elsevier Inc.

Standard, ASTM D7136-12. (2005) ‘Standard Test Method for Measuring the Damage Resistance of a Fiber-Reinforced Polymer Matrix Composite to a Drop-Weight Impact Event’, *ASTM International*, i(C), pp. 1–16. doi: 10.1520/

Standard, ASTM. D7137/D7137M-12. (2012) ‘Standard Test Method for Compressive Residual Strength Properties of Damaged Polymer Matrix Composite Plates’, *ASTM International*, i, pp. 1–17. doi: 10.1520/D7137.

Standard, N. F. ‘EN ISO 527-5.“’, *Plastics-Determination of tensile properties-Part*, 5.

Stelzer, S. *et al.* (2012) ‘Mode I delamination fatigue crack growth in unidirectional fiber reinforced composites: Development of a standardized test procedure’, *Composites Science and Technology*, 72(10), pp. 1102–1107. doi: https://doi.org/10.1016/j.compscitech.2011.11.033.

Strait, L. H., Karasek, M. L. and Amateau, M. F. (1992) ‘Effects of Stacking Sequence on the Impact Resistance of Carbon Fiber Reinforced Thermoplastic Toughened Epoxy Laminates’, *Journal of Composite Materials*. SAGE

Publications Ltd STM, 26(12), pp. 1725–1740. doi: 10.1177/002199839202601202.

Suemasu, H. and Majima, O. (1998) ‘Multiple Delaminations and their Severity in Nonlinear Circular Plates Subjected to Concentrated Loading’, *Journal of Composite Materials*. SAGE Publications Ltd STM, 32(2), pp. 123–140. doi: 10.1177/002199839803200202.

Tai, N.-H. and Yu, H.-C. (1998) ‘Effects of low-energy impact and thermal cycling loadings on fatigue behavior of the quasi-isotropic carbon/epoxy composites’, *Journal of Polymer Research*. 5(3), pp. 143–151.

U.S. Government Accountability Office (2011) ‘Status of FAA’s actions to oversee the safety of composite airplanes’.

Wu, E. M. and Reuter Jr, R. C. (1965) *Crack extension in fiberglass reinforced plastics*. ILLINOIS UNIV AT URBANA DEPT OF THEORETICAL AND APPLIED MECHANICS.

Xu, Y. G. et al. (2013) ‘Delamination threshold load of composite laminates under low-velocity impact’, in *Key Engineering Materials*. Trans Tech Publ, pp. 521–524.

Yates, J. R., Zanganeh, M. and Tai, Y. H. (2010) ‘Quantifying crack tip displacement fields with DIC’, *Engineering Fracture Mechanics*, 77(11), pp. 2063–2076. doi: https://doi.org/10.1016/j.engfracmech.2010.03.025.

Zhang, X. (2013) *Fatigue and Fracture of Composite Materials*. Lecture notes, Cranfield University.

APPENDICES

Appendix A Out-of-Plane Displacement of CAI samples

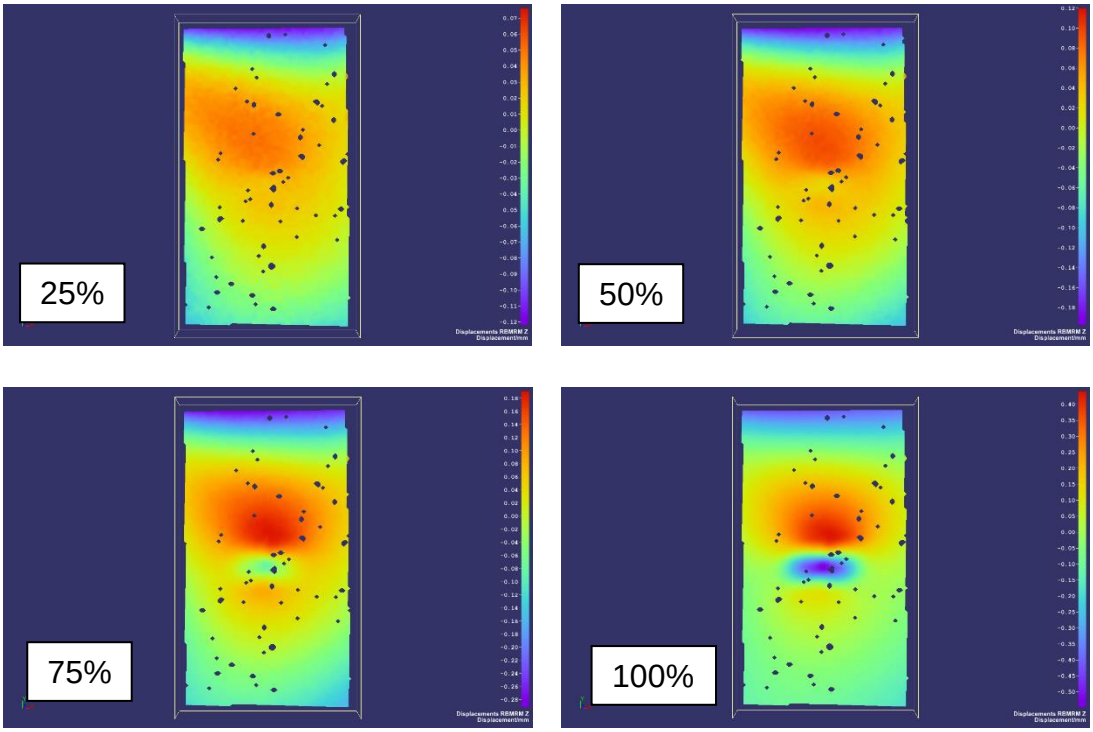

Figure A-1 Out-of-plane displacement of sample Q5 at noted fraction of RCS

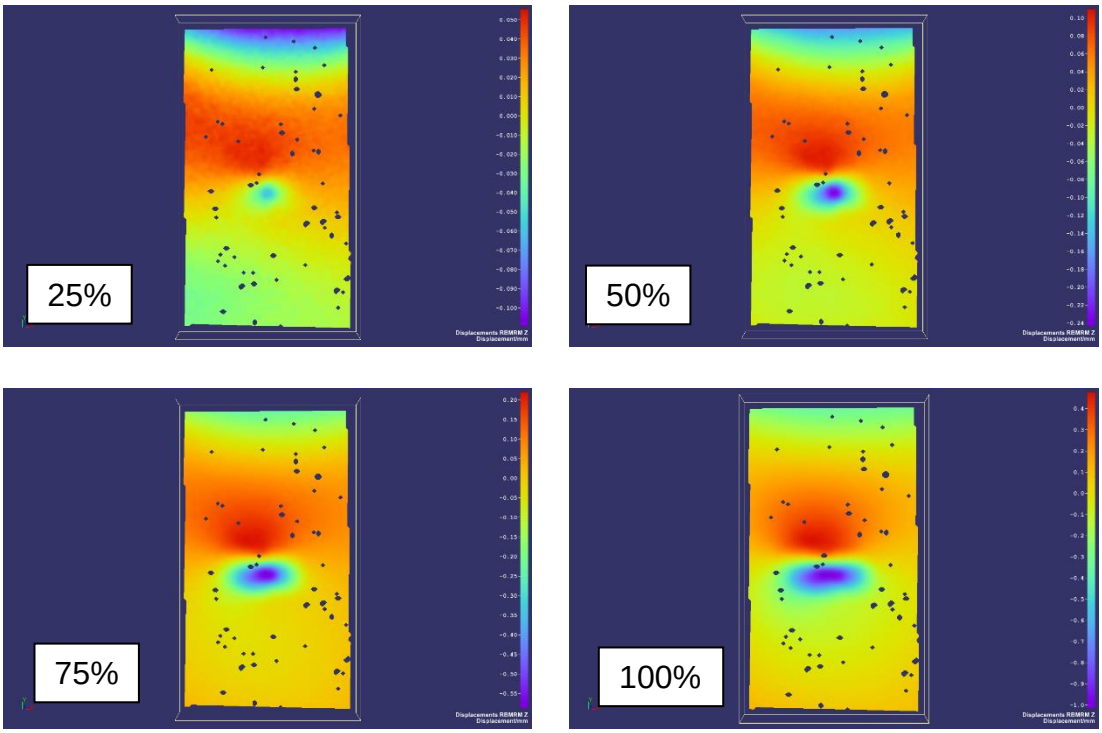

Figure A-2 Out-of-plane displacement of sample Q6 at noted fraction of RCS

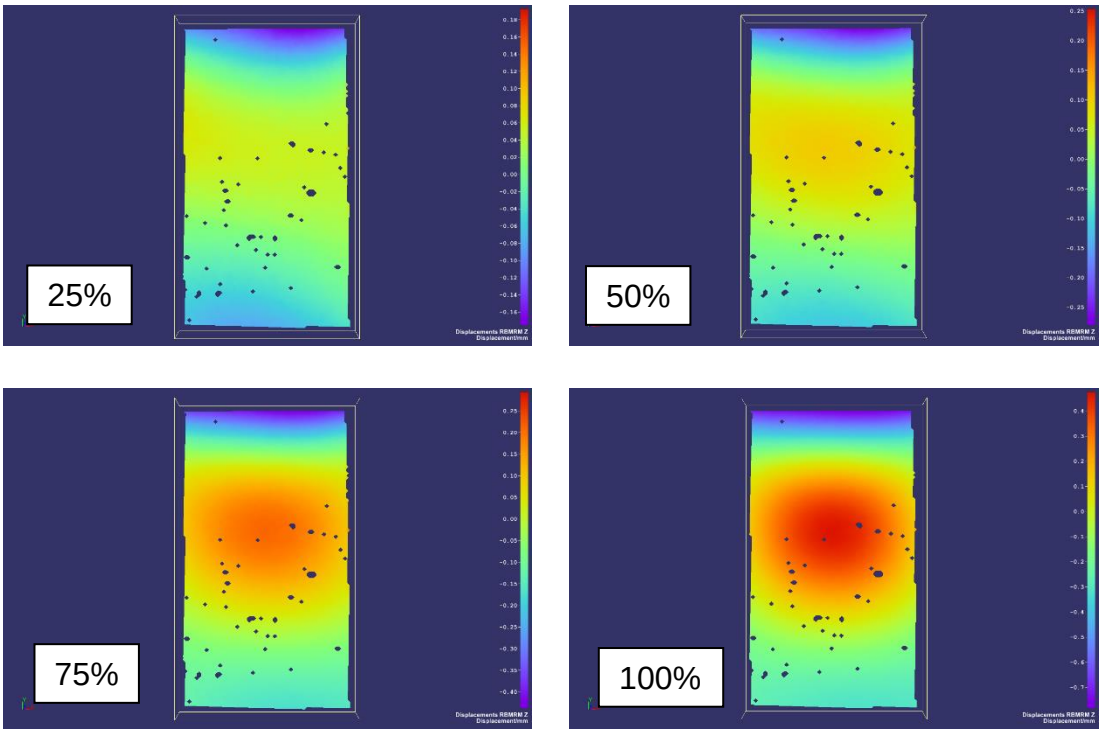

Figure A-3 Out-of-plane displacement of sample Q8 at noted fraction of RCS

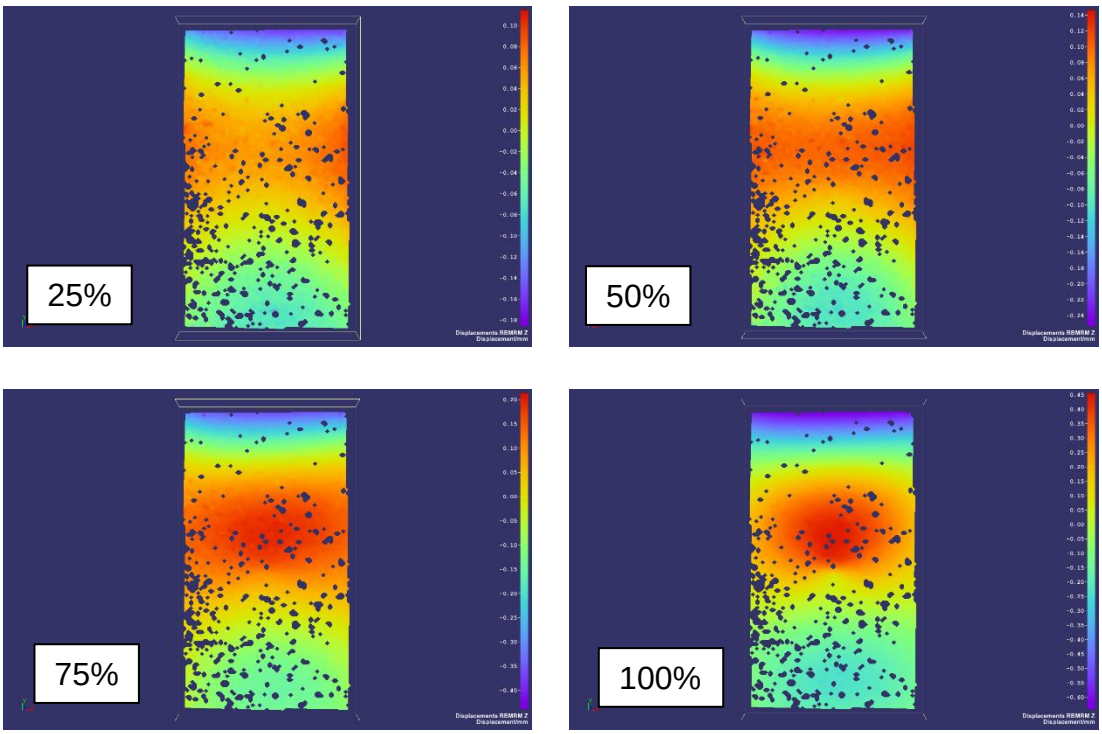

Figure A-4 Out-of-plane displacement of sample Q9 at noted fraction of RCS

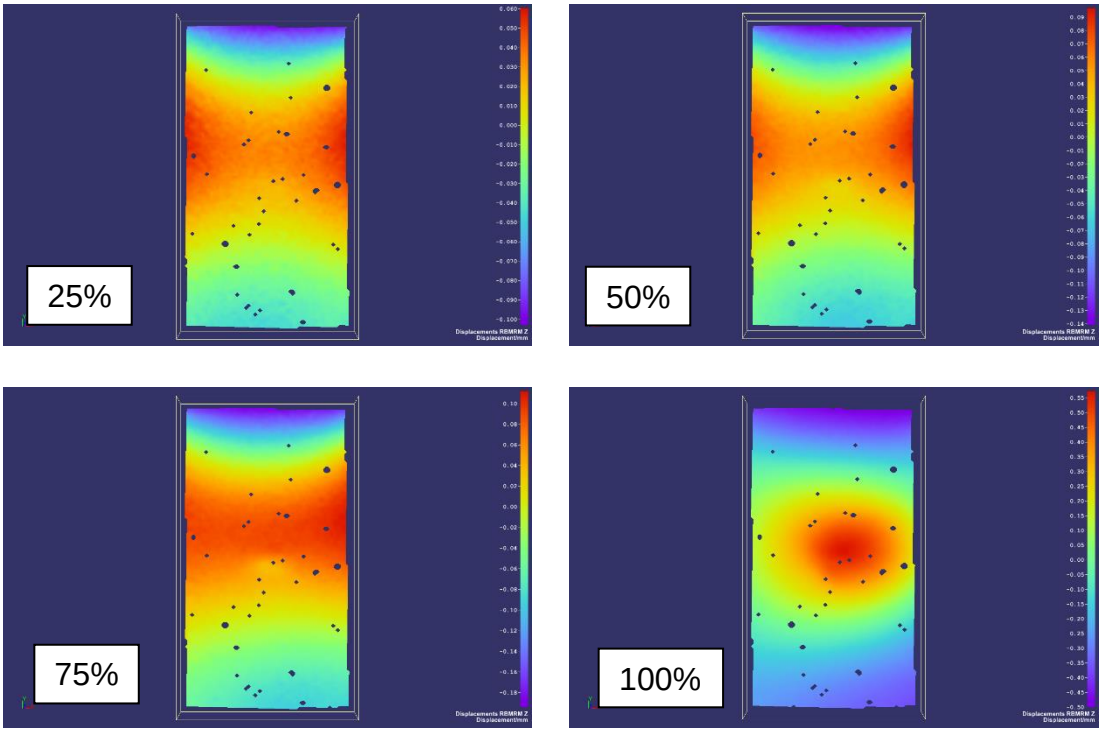

Figure A-5 Out-of-plane displacement of sample Q12 at noted fraction of RCS

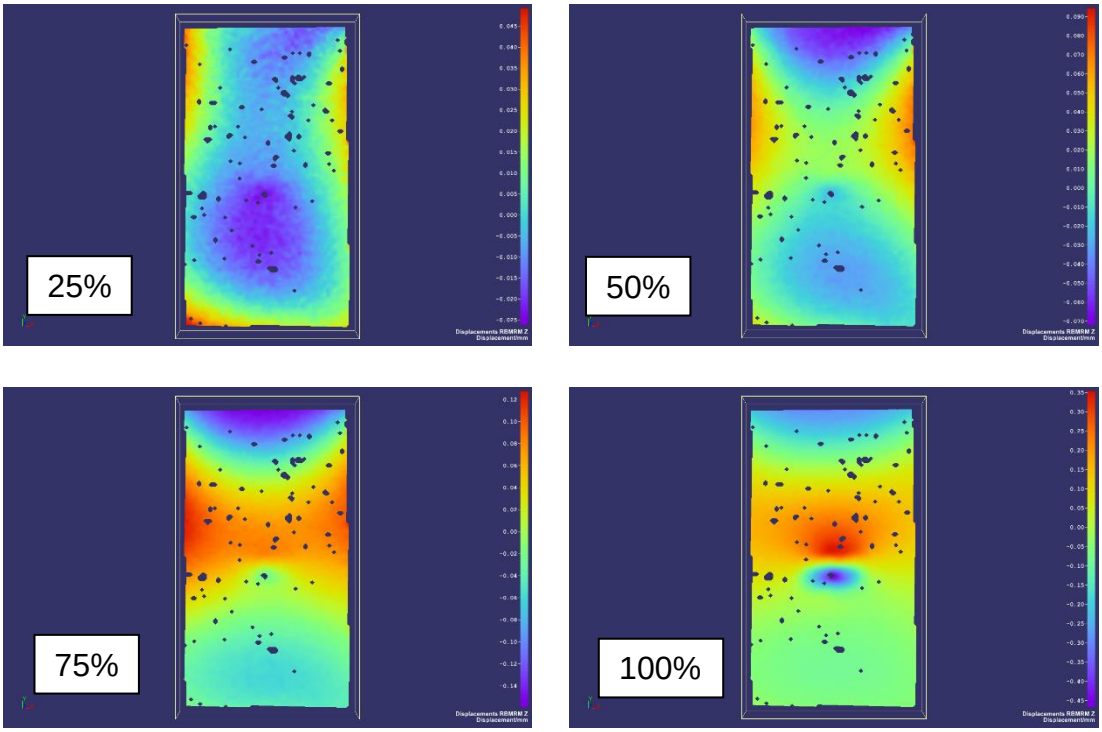

Figure A-6 Out-of-plane displacement of sample Q13 at noted fraction of RCS

Appendix B Delamination Area Growth in Fatigue

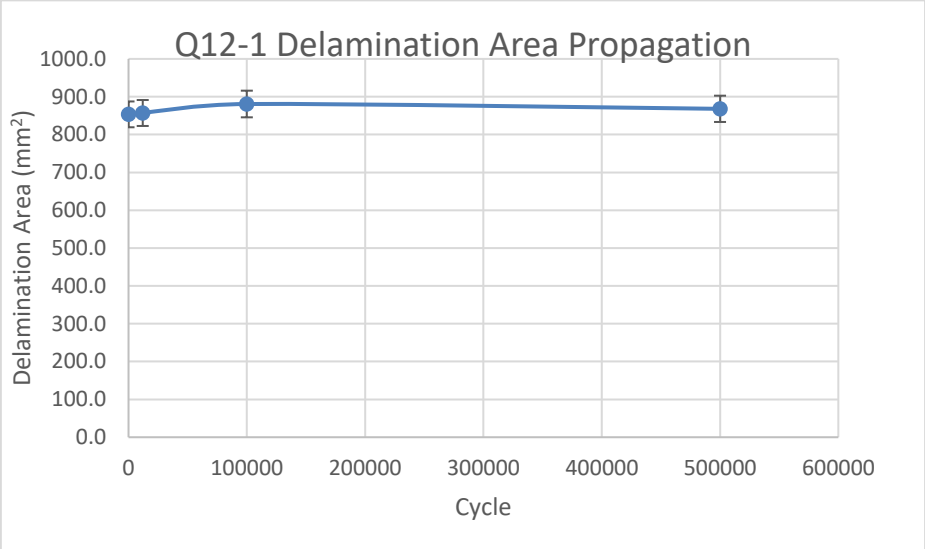

Figure B-1 Delamination area in sample Q12-1

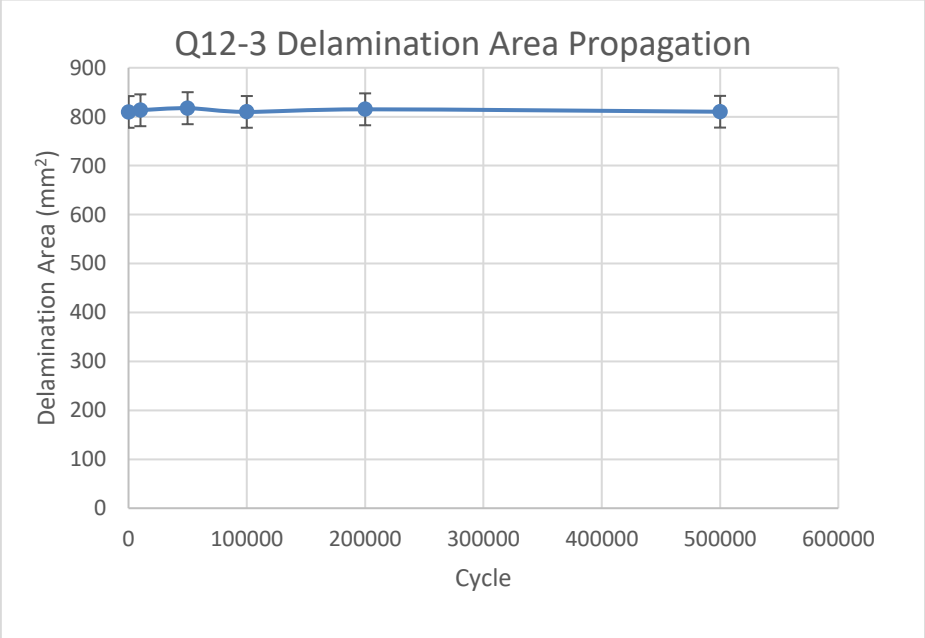

Figure B-2 Delamination area in sample Q12-3

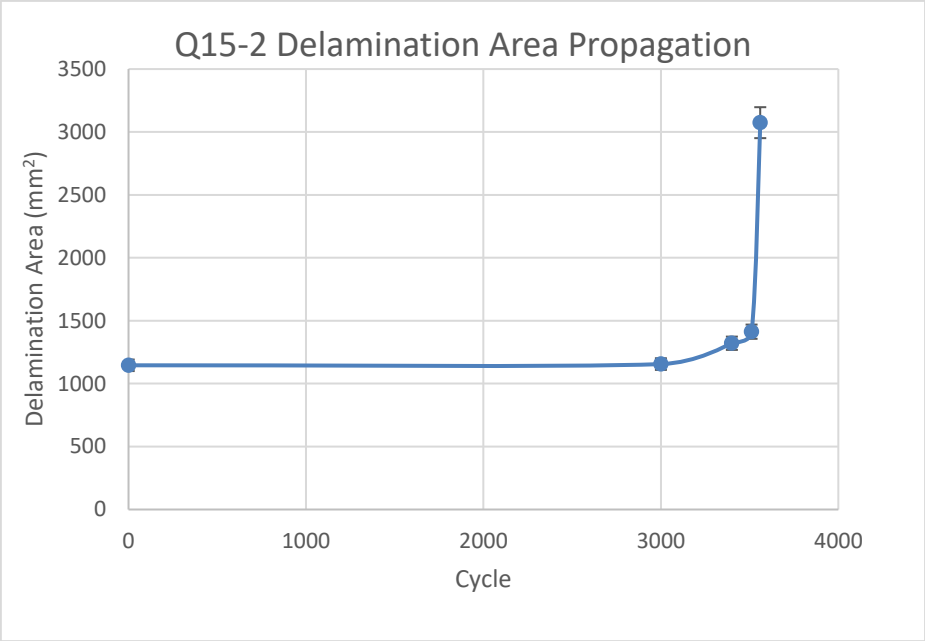

Figure B-3 Delamination area in sample Q15-2

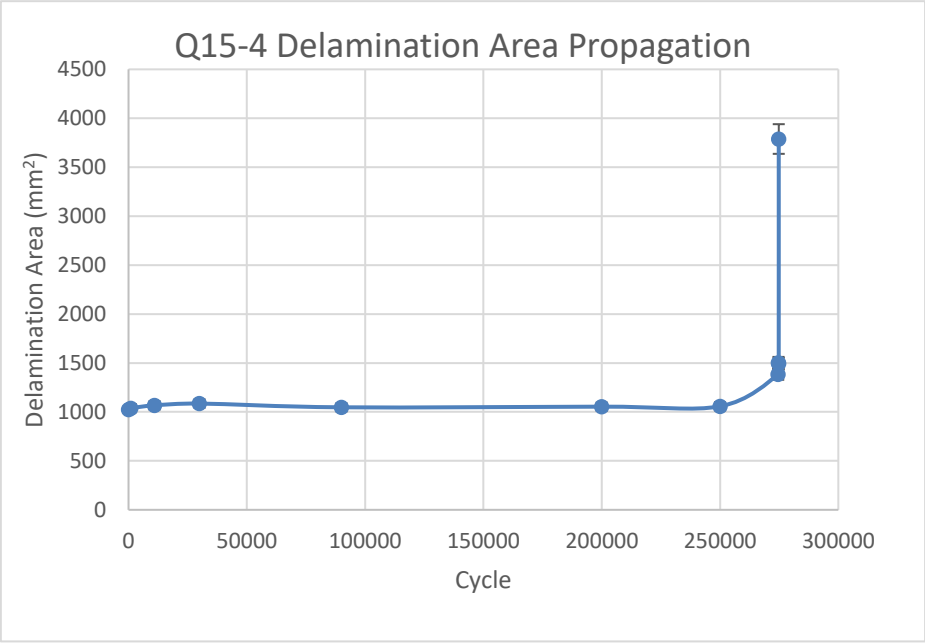

Figure B-4 Delamination area in sample Q15-4

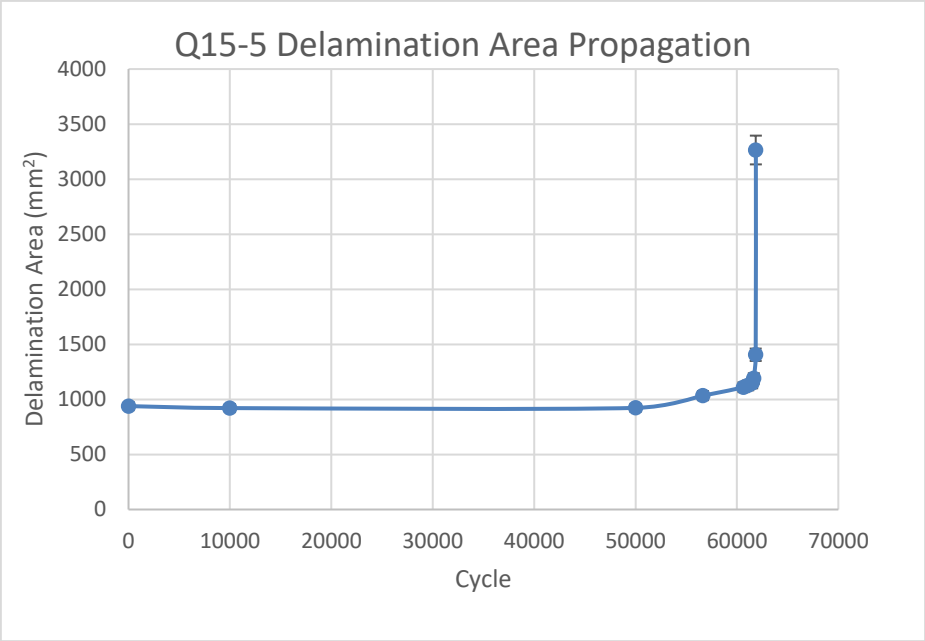

Figure B-5 Delamination area in sample Q15-5

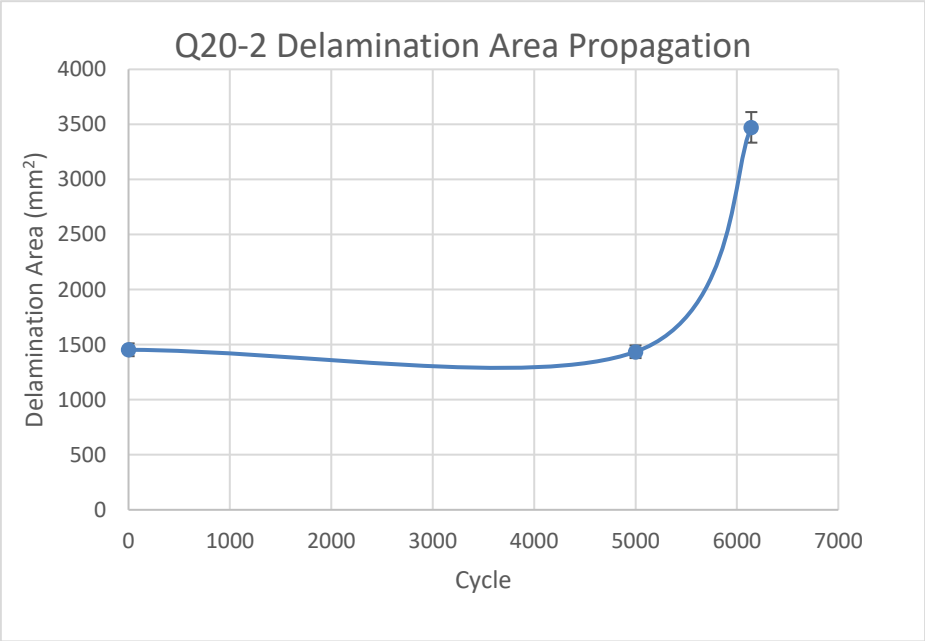

Figure B-6 Delamination area in sample Q20-2

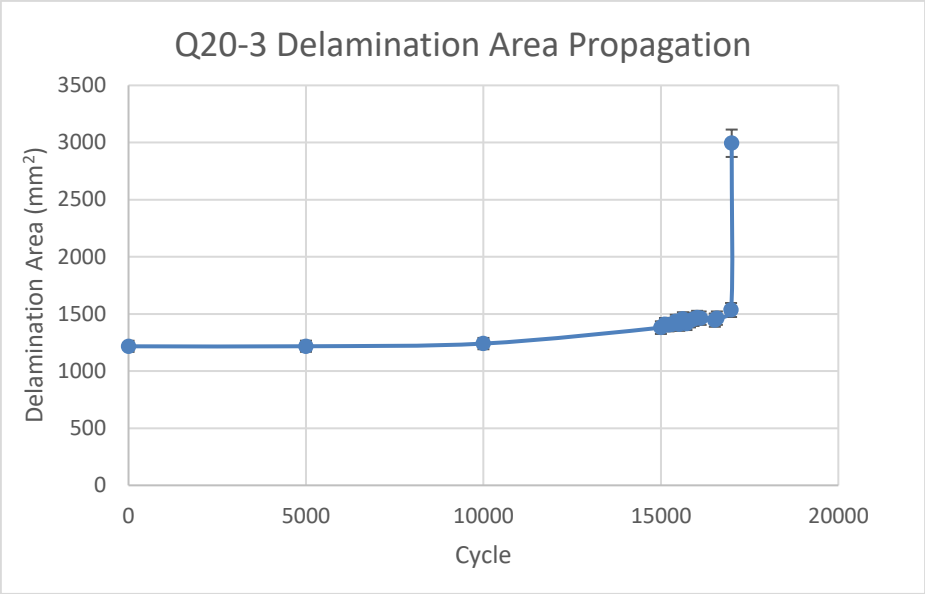

Figure B-7 Delamination area in sample Q20-3

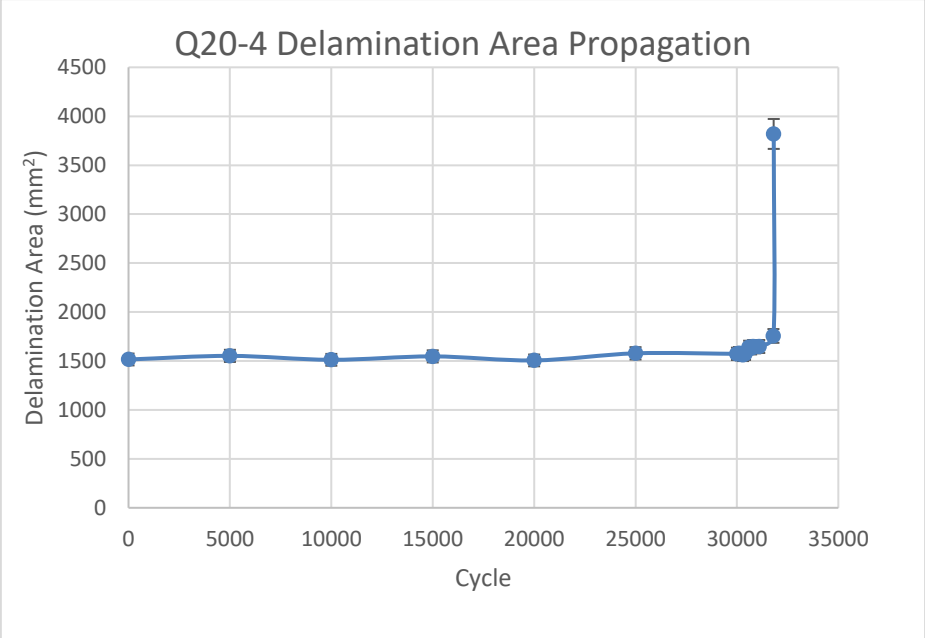

Figure B-8 Delamination area in sample Q20-4

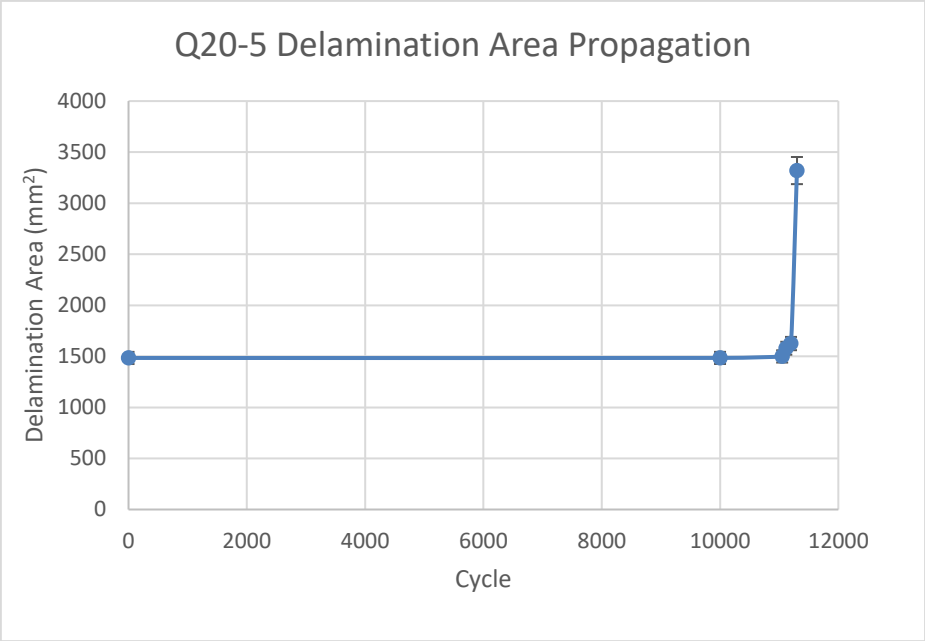

Figure B-9 Delamination area in sample Q20-5

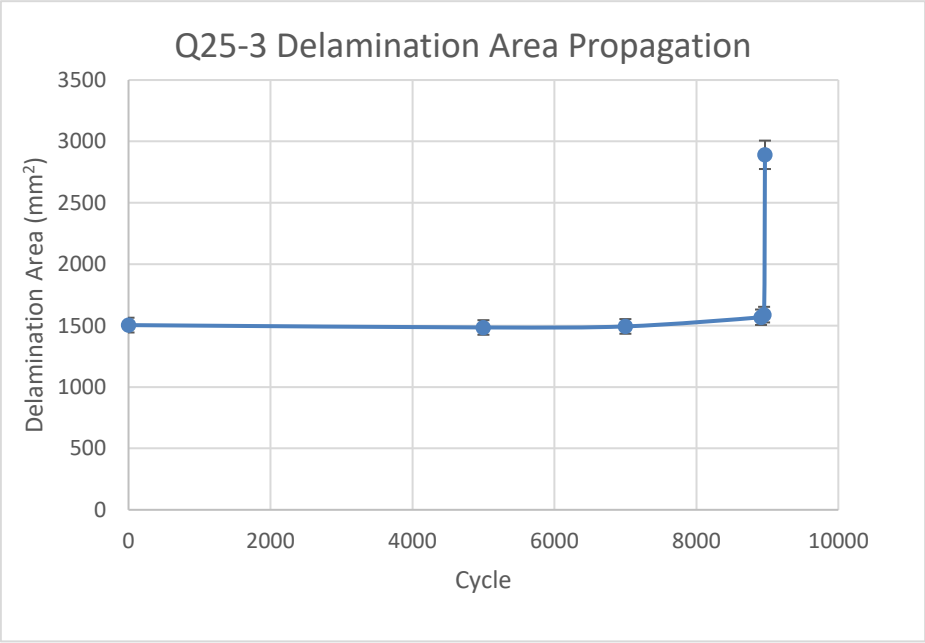

Figure B-10 Delamination area in sample Q25-3

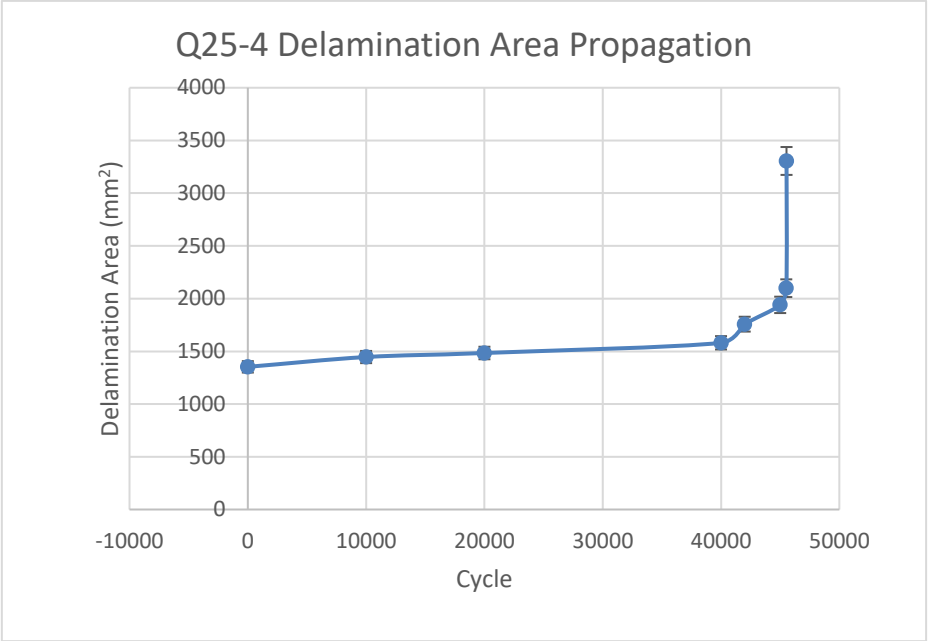

Figure B-11 Delamination area in sample Q25-4

Appendix C Stiffness Degradation during Fatigue

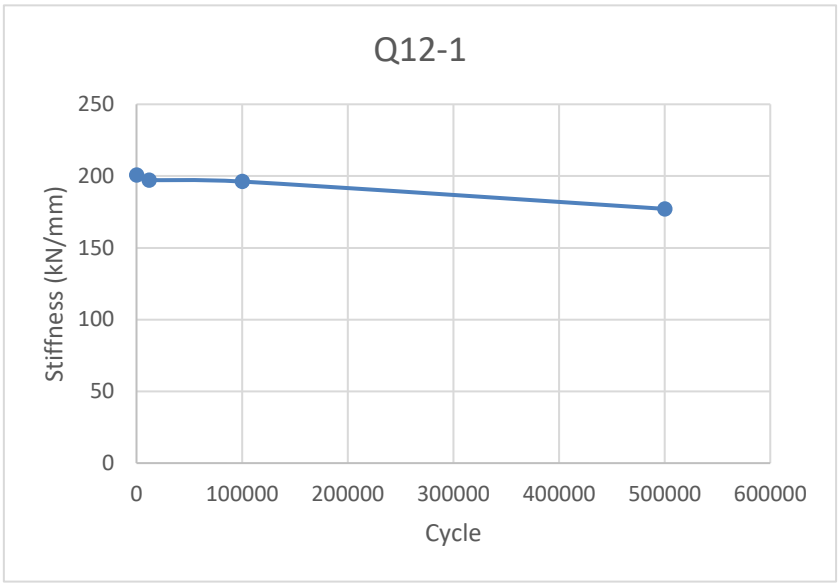

Figure C-1 Calculated stiffness of sample Q12-1 during fatigue session

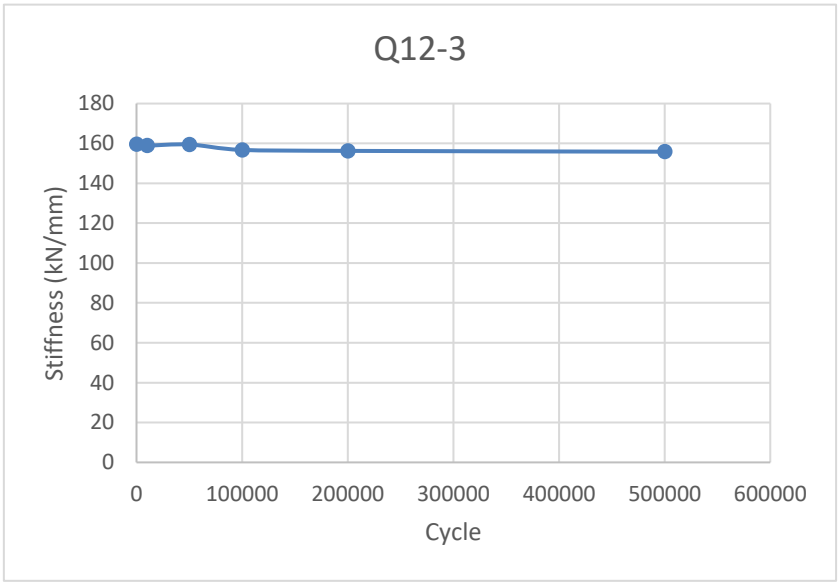

Figure C-2 Calculated stiffness of sample Q12-3 during fatigue session

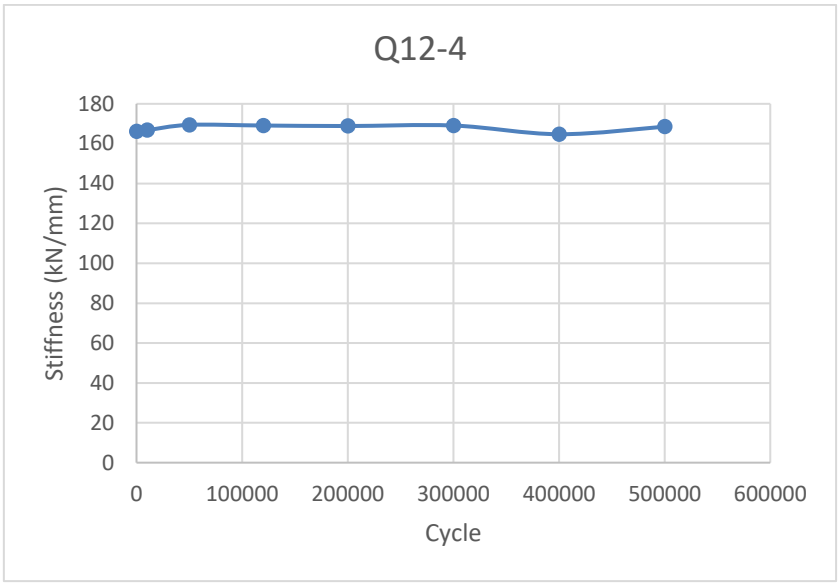

Figure C-3 Calculated stiffness of sample Q12-4 during fatigue session

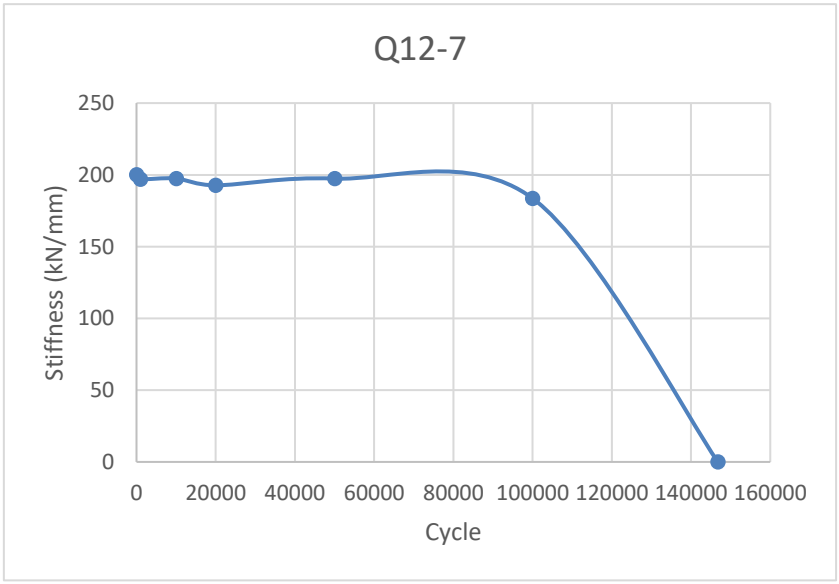

Figure C-4 Calculated stiffness of sample Q12-7 during fatigue session

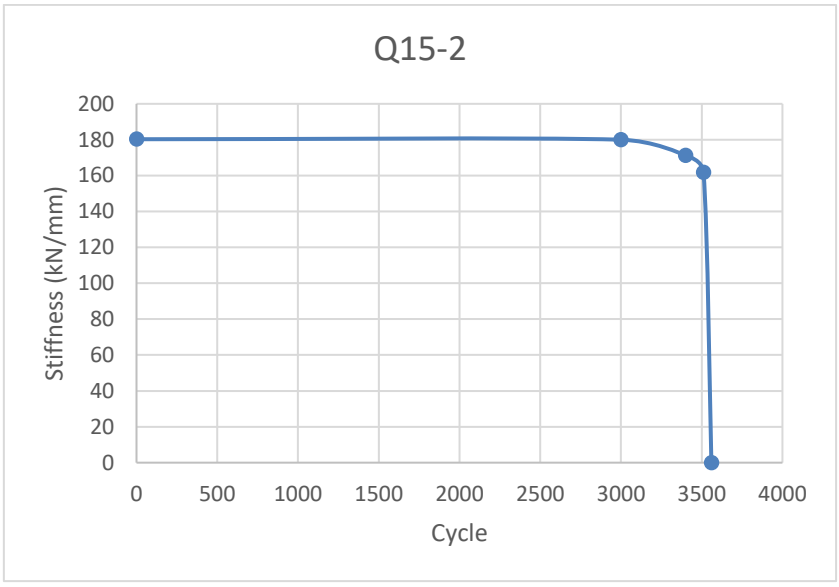

Figure C-5 Calculated stiffness of sample Q15-2 during fatigue session

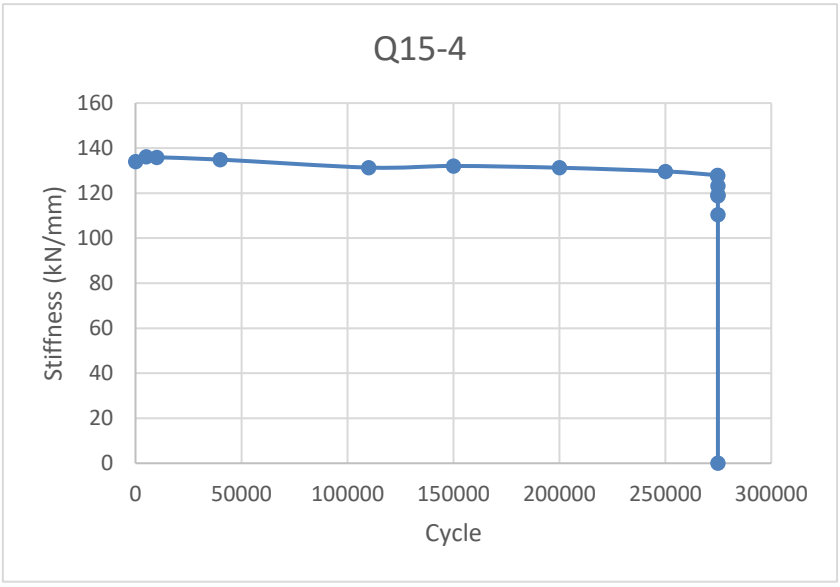

Figure C-6 Calculated stiffness of sample Q15-4 during fatigue session

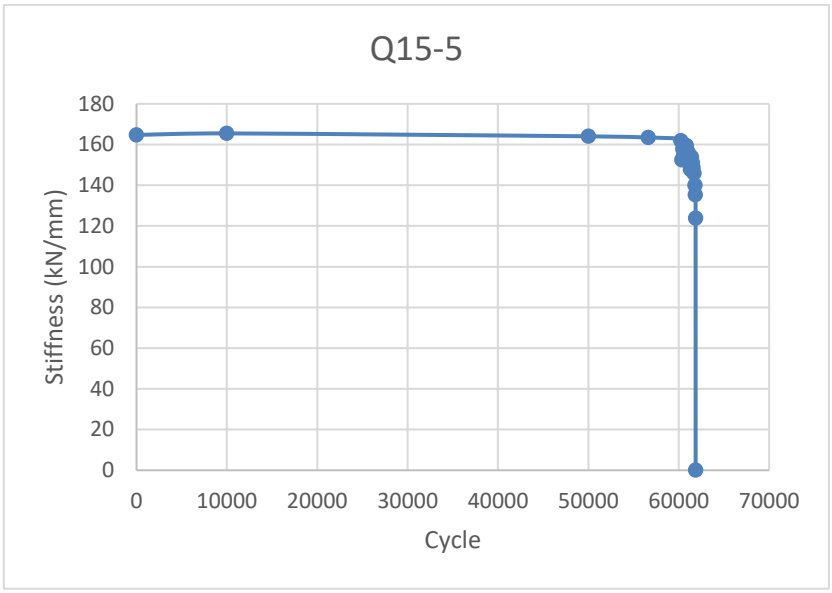

Figure C-7 Calculated stiffness of sample Q15-5 during fatigue session

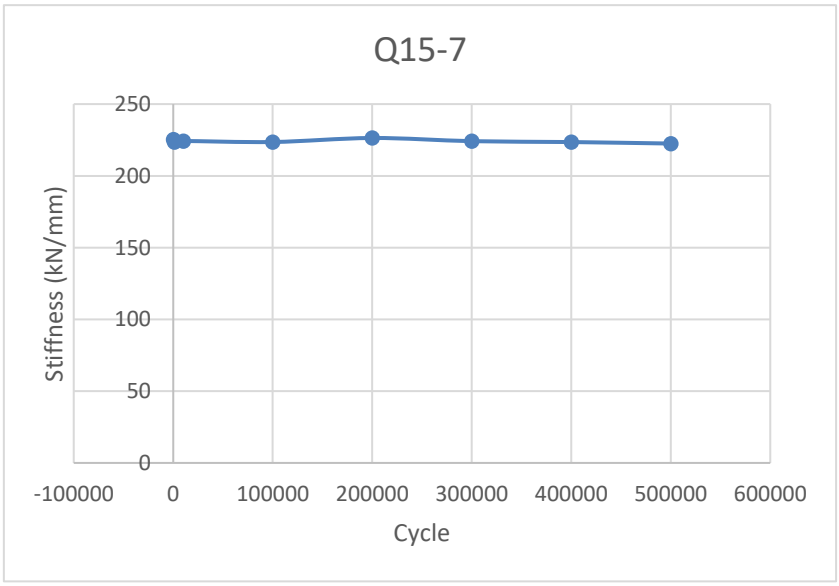

Figure C-8 Calculated stiffness of sample Q15-7 during fatigue session

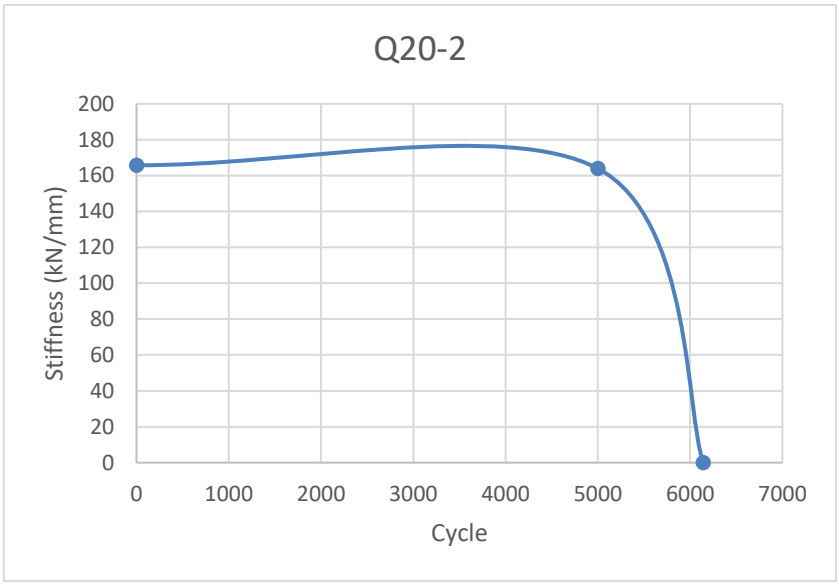

Figure C-9 Calculated stiffness of sample Q20-2 during fatigue session

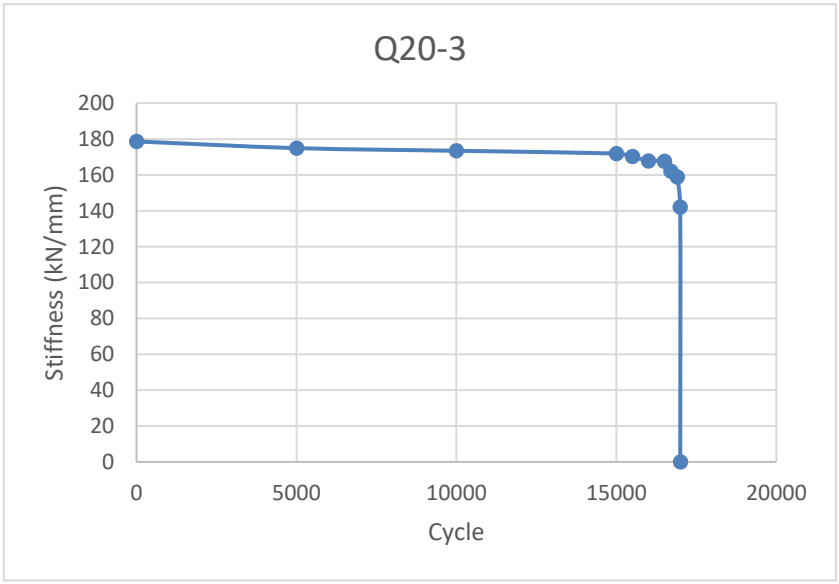

Figure C-10 Calculated stiffness of sample Q20-3 during fatigue session

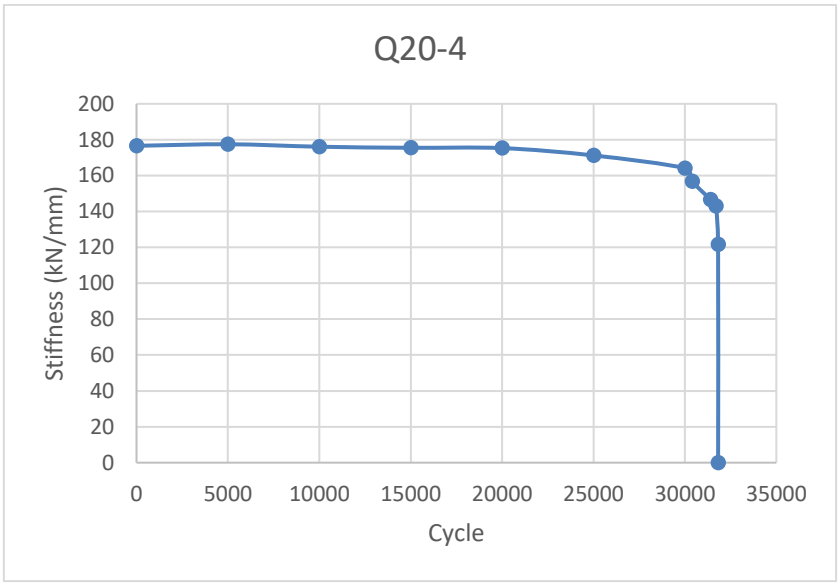

Figure C-11 Calculated stiffness of sample Q20-4 during fatigue session

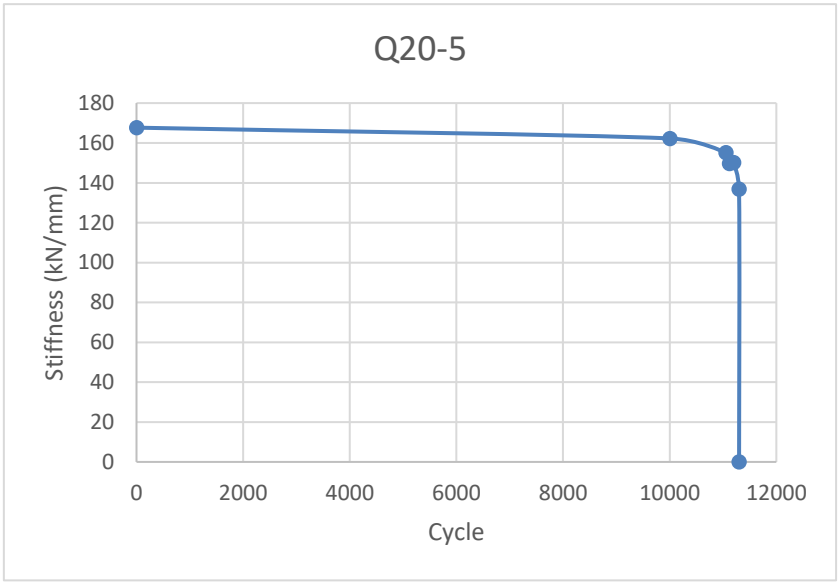

Figure C-12 Calculated stiffness of sample Q20-5 during fatigue session

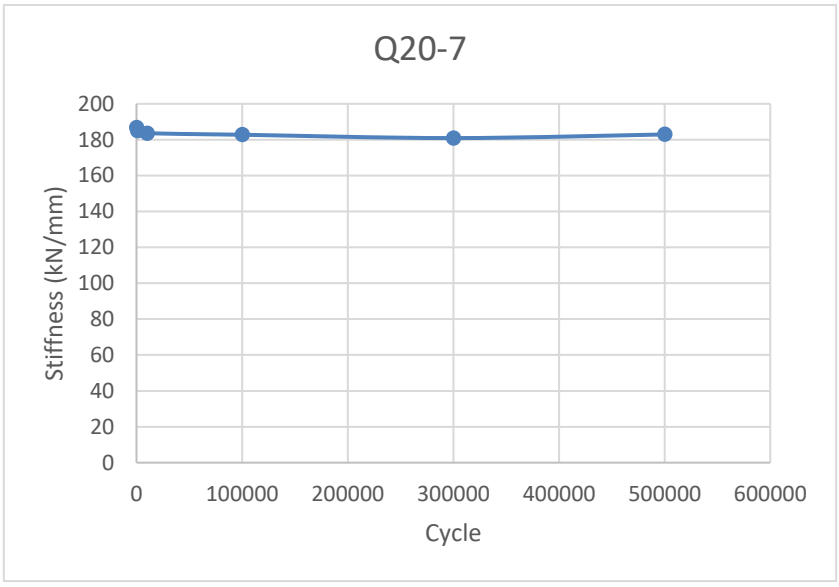

Figure C-13 Calculated stiffness of sample Q20-7 during fatigue session

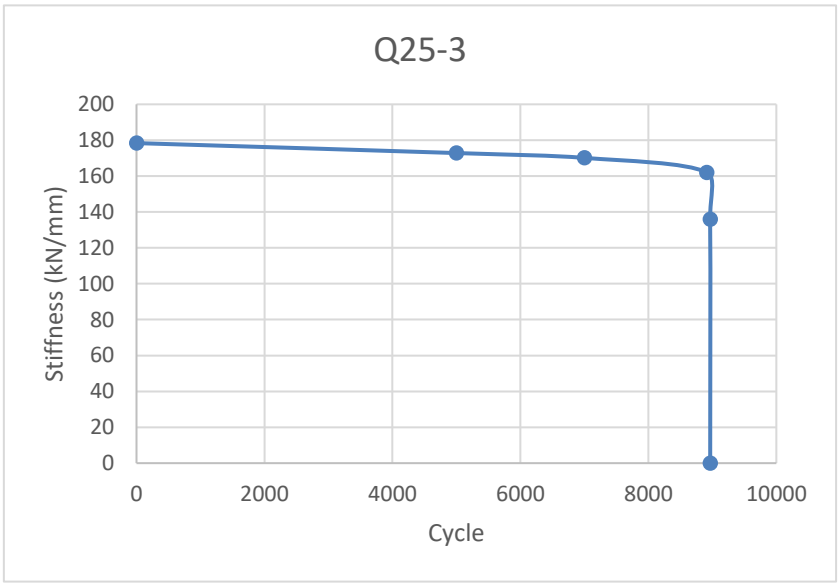

Figure C-14 Calculated stiffness of sample Q25-3 during fatigue session

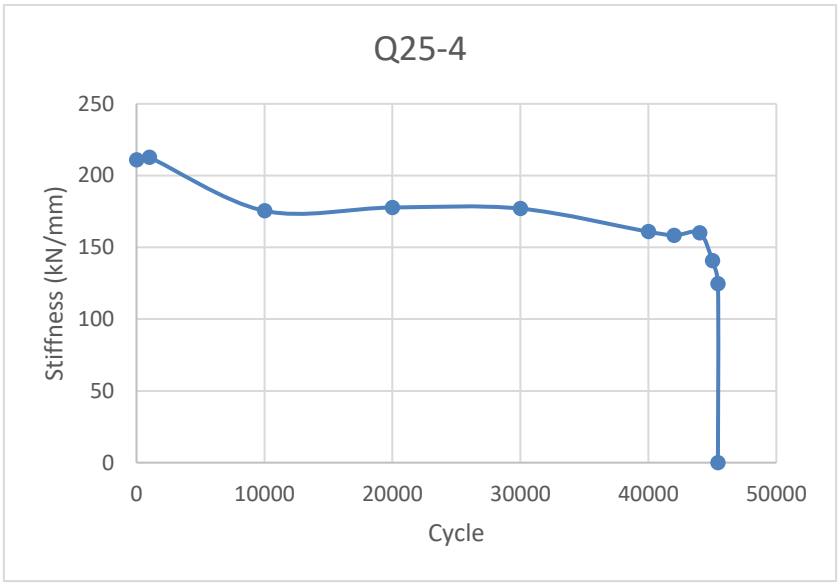

Figure C-15 Calculated stiffness of sample Q25-4 during fatigue session

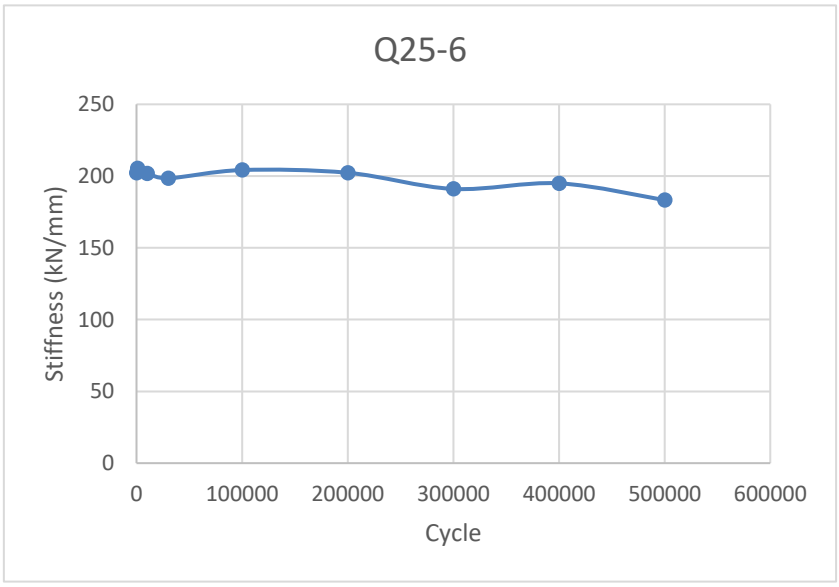

Figure C-16 Calculated stiffness of sample Q25-6 during fatigue session